

Distribution Agreement

In presenting this thesis or dissertation as a partial fulfillment of the requirements for an advanced degree from Emory University, I hereby grant to Emory University and its agents the non-exclusive license to archive, make accessible, and display my thesis or dissertation in whole or in part in all forms of media, now or hereafter known, including display on the world wide web. I understand that I may select some access restrictions as part of the online submission of this thesis or dissertation. I retain all ownership rights to the copyright of the thesis or dissertation. I also retain the right to use in future works (such as articles or books) all or part of this thesis or dissertation.

Signature:

Kirsten A. Cottrill

Date

Determining the mechanism and clinical relevance of sphingomyelinase-mediated decreases in transepithelial CFTR current in primary bronchial epithelial cells

By

Kirsten A. Cottrill
Doctor of Philosophy
Graduate Division of Biological and Biomedical Science
Molecular and Systems Pharmacology

Nael A. McCarty, Ph. D.
Advisor

Michael Koval, Ph. D.
Committee Member

Eric A. Ortlund, Ph. D.
Committee Member

Andrew Jenkins, Ph. D.
Committee Member

Joshua D. Chandler, Ph. D.
Committee Member

Accepted:

Lisa A. Tedesco, Ph.D.
Dean of the James T. Laney School of Graduate Studies

Date

Determining the mechanism and clinical relevance of sphingomyelinase-mediated decreases in transepithelial CFTR current in primary bronchial epithelial cells

By

Kirsten A. Cottrill
B.S., Mercer University, 2016

Advisor: Nael A. McCarty, Ph. D.

An abstract of
A dissertation submitted to the Faculty of
the James T. Laney School of Graduate Studies of Emory University
in partial fulfillment of the requirements for the degree of
Doctor of Philosophy
in Molecular and Systems Pharmacology
2021

Abstract

Determining the mechanism and clinical relevance of sphingomyelinase-mediated decreases in transepithelial CFTR current in primary bronchial epithelial cells

By Kirsten A. Cottrill

The Cystic Fibrosis transmembrane conductance regulator (CFTR) is an anion channel whose dysfunction causes Cystic Fibrosis (CF). Loss of CFTR function in pulmonary epithelial cells causes surface dehydration, mucus accumulation, inflammation, and bacterial infections resulting in lung failure. Little has been done to evaluate the effects of lipid perturbation on CFTR activity, despite CFTR residing in the plasma membrane. This work focuses on the acute effects of sphingomyelinase (SMase), a bacterial virulence factor secreted by CF-relevant airway bacteria which degrades sphingomyelin into ceramide, on the electrical circuitry of pulmonary epithelial monolayers. We report that basolateral SMase decreases CFTR-mediated transepithelial anion secretion in primary airway epithelial cells from explant tissue, with current CFTR modulators unable to rescue this effect. Using a holistic ion homeostasis approach, we determined that basolateral SMase inhibits apical and basolateral conductance in non-CF primary cells without affecting paracellular permeability. In CF cells ($\Delta F508/\Delta F508$), SMase was found to inhibit only apical conductance. We then explored the mechanisms underlying this effect. SMase increased the abundance of dihydroceramides, a result mimicked by blockade of ceramidase enzyme using ceranib-1, which also decreased CFTR currents. The SMase-mediated inhibitory mechanism did not involve removal of CFTR from the apical surface relative to total CFTR, nor did it involve activation of 5' adenosine monophosphate-activated protein kinase. To determine the pathological relevance of these sphingolipid imbalances, we evaluated the sphingolipid profiles of CF cells as compared to non-CF controls. Sphingomyelins, ceramides, and dihydroceramides largely were increased in CF cells. Correction of $\Delta F508$ -CFTR trafficking with VX445+VX661 decreased some sphingomyelins and all ceramides, but exacerbated increases in dihydroceramides. Additional treatment with the CFTR potentiator VX770 did not affect these changes, suggesting rescue of misfolded CFTR was sufficient. We furthermore determined that CF cells express more acid-SMase protein than non-CF cells. Lastly, we determined that airway-like neutrophils, which are increased in the CF lung, secrete acid-SMase. Identifying the complete mechanism of SMase-mediated inhibition of CFTR will be important, given the imbalance of sphingolipids in CF cells and the secretion of acid-SMase from cell types relevant to CF pathophysiology.

Determining the mechanism and clinical relevance of sphingomyelinase-mediated decreases in transepithelial CFTR current in primary bronchial epithelial cells

By

Kirsten A. Cottrill
B.S., Mercer University, 2016

Advisor: Nael A. McCarty, Ph. D.

A dissertation submitted to the Faculty of
the James T. Laney School of Graduate Studies of Emory University
in partial fulfillment of the requirements for the degree of
Doctor of Philosophy
in Molecular and Systems Pharmacology
2021

Acknowledgements

There are many people to thank for helping me reach this point in my scientific career. Of course, the first of these would be my parents, who raised and cared for me and my siblings. They instilled the powerful drive for learning and service that has led me into a career in biomedical research, and helped me become a functioning adult. My parents were assisted by their own parents, whom I also have to thank for their influence on my life. In addition to all of these family members, I have my brothers, who were and are still annoying, but with whom I share an unconditional love.

In addition to those who are related to me, there are others who have shaped who I am today. These include my educators, in particular my Kindergarten teacher Ms. Morris who always believed in me and pushed me to do my best, all of my math and science teachers in middle and high school who were patient with my incessant questioning, and my theater instructors who helped develop my presentation skills. There were also my afterschool mentors in the SSTRIDE program in Tallahassee, who first introduced me to biomedical research and to my high school research advisor Dr. Susan Cappendijk. Most formative, though, were my professors at Mercer University, in particular Dr. Garland Crawford who served as my research as well as my life mentor through all four years. These professors, and in particular those of the Chemistry Department, helped me learn about myself as well as the world around me. They inspired me to ask questions, figure out the answer to those questions, and then recognize the beauty and power in the answers.

My path to Emory, as well as my path within Emory, can be attributed largely to my wonderful mentor Dr. Nael McCarty. Nael took the time to learn about who I was, how I operated, and what my goals were. Based on that, he was able to provide recommendations for additional programs and opportunities that have allowed me to build a portfolio of experiences that push me closer to my ultimate goal of bridging basic and clinical research. He even figured out the perfect post-doctoral research opportunity for me, which checked every single one of my boxes. He has been patient as I

have gone through highs and lows of research as well as life. I cannot imagine having any other advisor for graduate school, and I look forward to his guidance as I continue my research career.

But ultimately, my graduate education probably could not have been completed without the support of my community of friends, who laughed, cried, and just existed with me through this whole process. Most of all, though, I must thank my husband, Ryan. He has helped me overcome many things and has pushed me to believe in myself, my hard work, and my dreams. He has listened attentively to me explain my work, frequently asking questions with a level of understanding that surprised me. He has reminded me to take care of myself instead of only taking care of the people around me, and he has shown me how to enjoy life more deeply and more faithfully. We cannot wait to welcome our first child, Cassidy, into the world soon after I defend this dissertation. Hopefully she is absorbing some of the information contained in these pages as I write them, as education can never start too early.

Table of Contents

CHAPTER 1 – INTRODUCTION 1

1.1 Cystic Fibrosis: an overview of the disease..... 1

 1.1.1 *European folklore and salty sweat.....1*

 1.1.2 *Dr. Dorothy Anderson and cystic fibrosis of the pancreas4*

 1.1.3 *The issue today – pulmonary manifestations of CF.....5*

 1.1.4 *Other organs affected by CF.....9*

1.2 CFTR: an overview of the protein..... 10

 1.2.1 *Protein structure and activity..... 10*

 1.2.2 *CF-causing mutations..... 14*

1.3 Highly effective modulator therapies and other developing therapies 20

 1.3.1 *The potentiator – VX770..... 20*

 1.3.2 *The correctors –VX809, VX661, and VX445..... 22*

 1.3.3 *Other emerging therapies..... 24*

1.4 CF animal and cell models..... 25

 1.4.1 *CF mouse models 25*

 1.4.2 *CF ferret models..... 28*

 1.4.3 *CF pig models..... 29*

 1.4.4 *CF cell models..... 31*

1.5 Lipid imbalances in CF epithelia..... 33

 1.5.1 *Fatty acids are imbalanced in CF epithelia 35*

 1.5.2 *Cholesterol is increased in CF epithelia 37*

 1.5.3 *Ceramides are imbalanced in CF epithelia 40*

 1.5.4 *Gangliosides are imbalanced in CF epithelia..... 47*

 1.5.5 *Sphingosine and sphingosine-1-phosphate are imbalanced in CF epithelia 47*

1.6 How lipids generally affect membrane protein activity..... 49

 1.6.1 *Lipid-dependent membrane mechanics affect membrane protein activity..... 51*

 1.6.2 *Direct allosteric lipid interactions affect membrane protein activity..... 52*

 1.6.3 *Lipid-mediated membrane surface localization affects membrane protein activity..... 53*

 1.6.4 *Lipid-mediated signaling cascades affect membrane protein activity..... 54*

 1.6.5 *How lipids interact with ABC transporters..... 54*

1.7 How lipids can affect CFTR 57

1.7.1	<i>Detergents and membrane lipids affect CFTR stability and ATPase activity</i>	57
1.7.2	<i>Arachidonic acid affects CFTR activity</i>	61
1.7.3	<i>Ceramide and its derivatives affect CFTR activity</i>	62
1.7.4	<i>Lipid rafts affect CFTR activity</i>	65
1.8	Summary	66

CHAPTER 2 – SPHINGOMYELINASE DECREASES TRANSEPITHELIAL ANION SECRETION IN AIRWAY EPITHELIAL CELLS IN PART BY INHIBITING CFTR-MEDIATED APICAL CONDUCTANCE..... 68

2.1	Introduction	69
2.2	Materials and methods	70
2.2.1	<i>Airway epithelial cells from human donors</i>	70
2.2.2	<i>Calu-3 and 16HBE bronchial epithelial cell culture</i>	72
2.2.3	<i>Purification of bacterial SMase</i>	73
2.2.4	<i>Lipidomics mass spectrometry</i>	73
2.2.5	<i>Short-circuit current measurements</i>	75
2.2.6	<i>Impedance measurements</i>	77
2.2.7	<i>Calcein flux assay</i>	79
2.2.8	<i>Statistical analyses</i>	80
2.3	Results	80
2.3.1	<i>WT SMase affects the sphingolipid profile in nHBE cells</i>	80
2.3.2	<i>WT SMase decreases short-circuit CFTR current in nHBE cells and nHTE cells</i>	87
2.3.3	<i>Differential effect of WT SMase on immortalized Calu-3 and 16HBE cells</i>	91
2.3.4	<i>WT SMase affects impedance-derived apical and basolateral conductance in nHBE cells</i>	93
2.3.5	<i>WT SMase does not affect paracellular permeability in nHBE cells</i>	96
2.3.6	<i>WT SMase inhibits CFTR current and conductance in cfHBE cells</i>	102
2.4	Discussion	108

CHAPTER 3 – MECHANISTIC ANALYSIS AND SIGNIFICANCE OF SMASE-MEDIATED DECREASES IN TRANSEPITHELIAL CFTR CURRENTS IN HBE CELLS..... 113

3.1	Introduction	113
3.2	Materials and methods	115
3.2.1	<i>Airway epithelial cells from human donors</i>	115
3.2.2	<i>Purification of bacterial SMase</i>	115
3.2.3	<i>Lipidomics mass spectrometry</i>	116

3.2.4	<i>Short-circuit current measurements</i>	116
3.2.5	<i>Analysis of surface expression of CFTR in nHBE cells</i>	116
3.2.6	<i>Neutrophil transmigration</i>	117
3.2.7	<i>Western blot analysis</i>	118
3.2.8	<i>Statistical analyses</i>	119
3.3	Results	119
3.3.1	<i>Inhibiting CDases with ceranib-1 affects CFTR currents similarly to WT SMase</i>	119
3.3.2	<i>Ceranib-1 affects total cellular dihydroceramides, as does SMase</i>	123
3.3.3	<i>No decrease in relative CFTR surface expression was detected following SMase treatment</i>	123
3.3.4	<i>AMPK is not involved in the WT SMase-mediated decrease in transepithelial CFTR currents</i>	126
3.3.5	<i>Ceramide and dihydroceramide levels in cfHBE compared to nHBE cells</i>	130
3.3.6	<i>Effects of modulator therapy on sphingolipids in cfHBE cells</i>	135
3.3.7	<i>Imbalance of acid-SMase in cfHBE cells and the effects of modulators</i>	138
3.3.8	<i>LTB₄-transmigrated neutrophils secrete acid-SMase</i>	138
3.4	Discussion	140
3.4.1	<i>Limitations</i>	145
CHAPTER 4 – DETERMINING THE EFFECTS OF CHOLESTEROL EXTRACTION ON CFTR CHANNEL ACTIVITY		147
4.1	Introduction	147
4.2	Methods	148
4.2.1	<i>FRT cells</i>	148
4.2.2	<i>Primary bronchial epithelial cells</i>	149
4.2.3	<i>Transepithelial short-circuit current analysis</i>	149
4.2.4	<i>Cholesterol staining with filipin III</i>	149
4.2.5	<i>Mass spectrometry analysis of cholesterol</i>	150
4.3	Results	151
4.3.1	<i>MβCD extracts cholesterol from FRT and nHBE cells</i>	151
4.3.2	<i>MβCD shifts the forskolin dose-response curve of CFTR to the right in FRT cells</i>	151
4.3.3	<i>MβCD shifts the forskolin dose-response curve of CFTR to the right in nHBE cells</i>	155
4.4	Discussion	158
CHAPTER 5 – UTILIZATION OF THE PLANAR LIPID BILAYER TECHNIQUE TO STUDY SINGLE-CHANNEL CFTR ACTIVITY		160
5.1	Introduction	161

5.2	Methods	161
5.2.1	<i>Growth and maintenance of BHK cells stably expressing His-tagged CFTR</i>	161
5.2.2	<i>Generation of His-tagged CFTR microsomes from BHK cells</i>	162
5.2.3	<i>Purification of His-tagged CFTR from BHK cells and generation of proteoliposomes</i>	162
5.2.4	<i>Planar Lipid Bilayer</i>	164
5.3	Results	168
5.3.1	<i>A CFTR-like current can be detected in His-CFTR-expressing BHK microsomes</i>	168
5.3.2	<i>The CFTR current from His-CFTR-expressing BHK Microsomes is sensitive to INH172</i>	171
5.3.3	<i>Purified CFTR proteoliposomes can be analyzed by PLB but are not as sensitive to INH172</i>	171
5.4	Discussion	174
CHAPTER 6 – THE EFFECTS OF LONG-TERM HYPERGLYCEMIA ON TIGHT JUNCTION FIDELITY IN NON-CF AND CF 16HBE CELLS		178
6.1	Introduction	178
6.2	Methods	180
6.2.1	<i>16HBE cells</i>	180
6.2.2	<i>Transepithelial short-circuit current analysis</i>	180
6.2.3	<i>Transcriptional expression analysis</i>	181
6.2.4	<i>Immunofluorescence staining</i>	183
6.3	Results	184
6.3.1	<i>CFTR mutation and long-term glucose growth affect TER in 16HBE cells</i>	184
6.3.2	<i>CFTR mutation and chronic hyperglycemia affect mRNA expression of tight junction proteins</i>	184
6.3.3	<i>CFTR mutation and long-term hyperglycemia affect CLDN1 protein expression</i>	186
6.3.4	<i>CFTR mutation and long-term glucose growth affect CLDN3 protein expression and localization</i>	189
6.3.5	<i>CFTR mutation and long-term glucose growth affect CLDN4 protein expression and localization</i>	194
6.3.6	<i>CFTR mutation and long-term glucose growth affect CLDN7 protein expression and localization</i>	197
6.4	Discussion	197
CHAPTER 7 – CONCLUSIONS		202
CHAPTER 8 – APPENDIX OF ADDITIONAL PROJECTS		207
8.1	Identification of CFTR in lamprey intestine	207
8.2	Development of the Programmable Automated Cell Culture System (PACCS)	207
8.3	Expanding the applicability of a new impedance analysis technology	209

8.4	Determining the impacts of β 2AR agonists on VX770-mediated potentiation of CFTR	210
8.5	Evaluating the importance of cholesterol on CLC channels	211
CHAPTER 9 – APPENDIX OF DETAILED ELECTROPHYSIOLOGY METHODS		213
9.1	Ussing chamber analysis.....	213
9.1.1	<i>Recording solutions</i>	<i>213</i>
9.1.2	<i>Sources of reagents and equipment.....</i>	<i>214</i>
9.1.3	<i>Setting up and running the experiment.....</i>	<i>214</i>
9.1.4	<i>Application notes.....</i>	<i>217</i>
9.2	PLB analysis.....	217
9.2.1	<i>Sources of reagents and equipment</i>	<i>217</i>
9.2.2	<i>Electrophysiology Physical Setup</i>	<i>218</i>
9.2.3	<i>Running an Experiment.....</i>	<i>219</i>
REFERENCES		224

List of Abbreviations

3-keto-dhSph	3-keto-dihydrosphingosine
ABC transporter	ATP-binding cassette transporter
ABS	ATP binding Site
ACN	acetonitrile
ALI	air-liquid interface
Amil	amiloride
AMPK	5' adenosine monophosphate-activated protein kinase
ANO1	anoctamin 1; also known as TMEM16A
APO-1	apoptosis antigen 1
ATP	adenosine triphosphate
BCA	bicinchoninic acid
BHK	baby hamster kidney
C_a	apical capacitance
CaCC	calcium-activated chloride channel
cAMP	cyclic adenosine monophosphate
C_b	basolateral capacitance
CDase	ceramidase
cDNA	complementary DNA
Cer	ceramide
CerS	ceramide synthases
CERT	ceramide transport protein
CF	Cystic Fibrosis
cfHBE	CF human bronchial epithelial cells from explant tissue

cfHNE	CF human nasal epithelial cells from explant tissue
cfHTE	CF human tracheal epithelial cells from explant tissue
CFTR	Cystic Fibrosis transmembrane conductance regulator
CFRD	Cystic Fibrosis-related diabetes
CHO	chinese hamster ovary
CHS	cholesteryl hemisuccinate
CLDN	claudin
CRAC	cholesterol recognition amino acid consensus
Cryo-EM	cryogenic electron microscopy
C _T	cycle threshold
CT	computerized tomography
DAPI	4',6-diamidino-2-phenylindole
DDM	n-dodecyl β-D-maltoside
DhC DES	dihydroceramide desaturase
dhCer	dihydroceramide
dhSph	dihydrosphingosine, also known as sphinganine
DMPC	1,2-dimyristoyl-sn-glycero-3-phosphocholine
DMPE	1,2-dimyristoyl-sn-glycero-phosphoethanolamine
DOPC	1,2-dioleoyl-sn-glycero-3-phosphocholine
DOPE	1,2-dioleoyl-sn-glycero-phosphoethanolamine
DPPE	2-dipalmitoyl-sn-glycero-phosphoethanolamine
EC ₅₀	effective concentration for half-maximal activation
EDTA	ethylene-diaminetetraacetic acid
EGTA	ethylene-bis(oxyethylenitrilo)tetraacetic acid

ENaC	epithelial sodium channel
ER	endoplasmic reticulum
EtOAc	ethyl acetate
FA	formic acid
FBS	fetal bovine serum
FDA	Food and Drug Administration
FFA	free fatty acid
FEV1	forced expiratory volume in the first second
FRT	Fischer rat thyroid
FSK	forskolin
G	conductance
G_a	apical conductance
G_b	basolateral conductance
G_c	transcellular conductance
GJ	gap junction protein
GM1	monosialotetrahexosylganglioside
G_p	paracellular conductance
GPCR	G protein-coupled receptors
G_T	transepithelial conductance
H322A SMase	enzyme-dead sphingomyelinase from <i>S. aureus</i>
HAE	human airway epithelial cells from explant tissue
HBE	human bronchial epithelial cells from explant tissue
HEMT	highly effective modulator therapy
HNE	human nasal epithelial cells from explant tissue

HTE	human tracheal epithelial cells from explant tissue
IBMX	3-isobutyl-1-methylxanthine
I_{cap}	capacitive current
IF	immunofluorescence
IL	interleukin
IPA	isopropyl alcohol
IRB	institutional review board
I_{sc}	transepithelial short-circuit current
KDSR	3-ketodihydrosphingosine reductase
K_i	inhibitory constant
Kir2	inwardly-rectifying potassium channel 2
KRH	Krebbs Ringers HEPES buffer
KRT16	keratin-16
LMNG	2,2-didecylpropane-1,3-bis- β -D-maltopyranoside
M β CD	methyl β cyclodextrin
MOPS	3-(N-morpholino)propanesulfonic acid
MS	mass spectrometry
NBD	nucleotide binding domain
nHBE	non-CF human bronchial epithelial cells from explant tissue
NHERF1	sodium-hydrogen antiporter 3 regulator 1
nHNE	non-CF human nasal epithelial cells from explant tissue
nHTE	non-CF human tracheal epithelial cells from explant tissue
NKCC	sodium potassium two-chloride symporter
N/K pump	sodium-potassium ATPase

NPC	Niemann-Pick Disease type C
PACCS	Programable Automated Cell Culture System
PBS	phosphate-buffered saline
PBS ^{-/-}	phosphate buffered saline without calcium or magnesium
PC	phosphatidylcholine
PCR	polymerase chain reaction
pen/strep	penicillin/streptomycin
PI	phosphatidylinositol
PKA	protein kinase A
PKC	protein kinase C
PLB	planar lipid bilayer
P(o)	open probability
POPC	1-palmitoyl-2-oleoyl-sn-glycero-3-phosphocholine
POPE	1-palmitoyl-2-oleoyl-sn-glycero-3-phosphoethanolamine
POPS	1-palmitoyl-2-oleoyl-sn-glycero-3-phospho-L-serine
PP2A	protein phosphatase 2A
PP2C	protein phosphatase 2C
ppFEV1	percent predicted forced expiratory volume in the first second
PS	phosphatidylserine
qRT-PCR	real-time quantitative reverse transcription polymerase chain reaction
R _a	apical resistance
R-domain	regulatory domain
R _b	basolateral resistance
R _p	paracellular resistance

R_s	series resistance
R_T	transepithelial resistance
SERCA1	sarco(endoplasmic reticulum Ca^{2+} ATPase
S1P	sphingosine-1-phosphate
S1PR	sphingosine-1-phosphate receptor
SM	sphingomyelin
SMase	sphingomyelinase
SMS1	sphingomyelin synthase 1
SOX7	SRY-box transcription factor 7
Sph	sphingosine
SphK	sphingosine kinase
τ_a	apical time constant
τ_b	basolateral time constant
TER	transepithelial resistance
TM	transmembrane helix
TMD	transmembrane domain
TMEM16A	transmembrane member 16A
UPLC-MS	ultra-performance liquid chromatography
VIP	vasoactive intestinal peptide
WT	wild-type

List of Figures

Figure 1.1: A graphical representation of sweat glands, and the defective ion transport in CF.

Figure 1.2: A graphical representation of pulmonary epithelial cells, and the defective ion transport in CF.

Figure 1.3. Some of the cryo-EM structures of human CFTR.

Figure 1.4: A graphical representation of CFTR and its gating cycle.

Figure 1.5: The cryo-EM structure for PKA-phosphorylated, ATP-bound CFTR bound to VX770.

Figure 1.6: A graphical representation of cellular ceramide synthesis pathways.

Figure 1.7: A graphical representation of the ways by which lipids can affect membrane protein activity.

Figure 1.8: Cryo-EM structures of CFTR with resolved lipids bound.

Figure 2.1. A model of a bronchial epithelial monolayer (A) is shown alongside the representative circuit diagram (B).

Figure 2.2. A graphical model of transepithelial short-circuit current analysis with an Ussing chamber.

Figure 2.3. Mutant H322A SMase is a good negative control for WT SMase.

Figure 2.4. IPA extracts sphingolipids more efficiently than ethyl acetate extraction.

Figure 2.5. SMase reduces all sphingomyelins and increases all ceramides in nHBE cells.

Figure 2.6. Short-circuit current analysis revealed a reduction of transepithelial CFTR current in nHBE cells after WT SMase treatment.

Figure 2.7. SMase affects nHTE cells similarly to nHBE cells.

Figure 2.8. Short-circuit current analysis revealed an increase in CFTR currents in Calu-3 cells after WT SMase treatment.

Figure 2.9: SMase affects the transepithelial short-circuit currents of 16HBE cells, but differently than nHBE cells.

Figure 2.10. Impedance measurements of nHBE cells (a single biological replicate) showed a reduction in both apical and basolateral conductance after WT SMase treatment, alongside a reduction of basolateral capacitance but an increase in apical capacitance.

Figure 2.11. SMase does not affect baseline transepithelial conductance or calcein flux.

Figure 2.12. SMase modulates sphingolipids and transepithelial currents similarly in VX809-corrected cfHBE cells as in nHBE cells.

Figure 2.13. SMase modulates transepithelial currents similarly in VX445/VX661-corrected cfHBE cells as in nHBE cells.

Figure 2.14. Apical conductance was decreased but basolateral conductances was unaffected by WT SMase in C18-corrected cfHBE cells, as determined by impedance analysis.

Figure 3.1. Inhibiting CDases with ceranib-1 caused a decrease in CFTR currents and enhanced the WT SMase-mediated inhibition of CFTR.

Figure 3.2. Lipidomics mass spectrometry analysis indicated that ceranib-1 increased dihydroceramides.

Figure 3.3. Surface biotinylation followed by a CFTR pull-down indicated that SMase did not decrease CFTR surface expression.

Figure 3.4. Inhibiting AMPK does not prevent WT SMase-mediated decreases in transepithelial CFTR currents but does have other effects on currents.

Figure 3.5. Lipidomics analysis reveals that time on the Transwell affects the ceramides and dihydroceramide profiles of nHBE cells.

Figure 3.6. Lipidomics analysis of sphingolipid species in HBE and HNE cells indicate many increased sphingomyelins, ceramides, and dihydroceramides in the CF group.

Figure 3.7. Lipidomics analysis indicates that the newest FDA-approved correctors can affect the sphingolipid imbalances in cfHBE cells.

Figure 3.8. Western blot and densitometry analyses indicate imbalances in acid-SMase protein expression and secretion in cfHBE as compared to nHBE cells.

Figure 3.9. Neutrophils transmigrated through H441 cells by LTB4 stimulation secrete acid-SMase.

Figure 4.1: M β CD extracts cholesterol from FRT and nHBE cells.

Figure 4.2: M β CD affects the forskolin dose-response curve in FRT cells expressing CFTR.

Figure 4.3: M β CD affects ENaC and CFTR currents in nHBE cells.

Figure 5.1: Diagram of the PLB setup, viewed from above.

Figure 5.2: A CFTR-like current can be detected in His-CFTR-expressing BHK microsomes.

Figure 5.3: The CFTR-like current from His-CFTR-expressing BHK Microsomes is sensitive to INH172.

Figure 5.4: Purified CFTR proteoliposomes can be analyzed by PLB but are not as sensitive to INH172.

Figure 6.1: TER is lower in CF cells and following hyperglycemic conditions, as determined by an Ussing Chamber.

Figure 6.2: PCR analysis of WT- and Δ F508-CFTR-expressing 16HBE cells indicate different gene expression in CF cells and differential adaptations to hyperglycemia.

Figure 6.3: CLDN1 fluorescence is affected by CFTR expression and glucose growth.

Figure 6.4: CLDN3 fluorescence is affected by CFTR expression and glucose growth.

Figure 6.5: CLDN4 fluorescence is affected by CFTR expression and glucose growth.

List of Tables

Table 1.1: The seven classes of CFTR defects, with examples

Table 1.2. The different classes of lipids, with examples.

Table 1.3 A list of some ABC transporters, their lipid substrates, and their associated diseases

Table 1.4. The current high-resolution structures of CFTR from the Chen lab

CHAPTER 1 – INTRODUCTION

Preface: Some of the text and figures presented here are reproduced from a review paper published in *Communications Biology* in April 2020. The goal of this review paper was to compile and analyze the literature regarding lipid imbalances in Cystic Fibrosis (CF), to review the mechanisms by which lipids are known to affect membrane protein activity, and to compile and analyze the literature regarding the effects of specific lipids on CFTR structure and function. I wrote the review.

- **Cottrill KA**, Farinha CM, McCarty NA. 2020. The bidirectional relationship between CFTR and lipids. *Commun Biol* 3:179

1.1 Cystic Fibrosis: an overview of the disease

CF is a lethal genetic disease that affects more than 70,000 individuals worldwide (1). It is a progressive disease affecting many organs, though this has only become more apparent as interventions to extend the lives of people with CF have developed. The disease appears typically, but not exclusively, in the white population descendant from northern Europe. Approximately 4% of non-Hispanic white people are carriers of a CF-causing mutation. These mutations exist in the gene encoding the CF transmembrane conductance regulator (CFTR), an anion channel present in cell types throughout the body, and cause loss of function to this protein. This section will provide an overview of the historical context of CF, as well as important clinical manifestations, and the physiological effects of loss of CFTR that cause these clinical outcomes.

1.1.1 European folklore and salty sweat

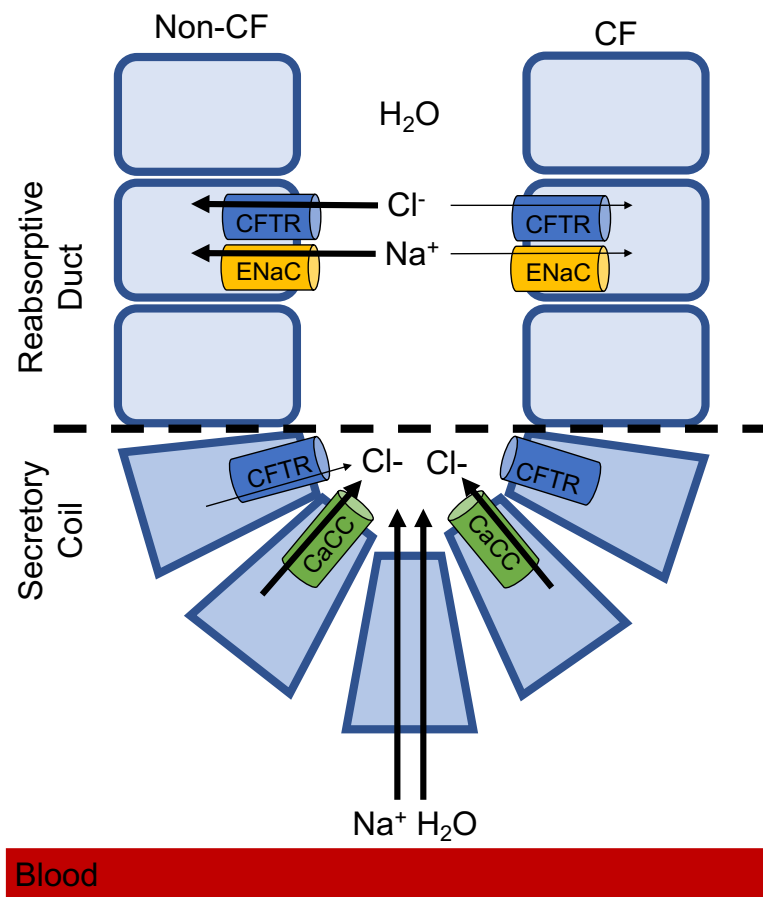
Descriptions of CF may have appeared originally in ancient Europe, in folklore such as “Woe to that child which when kissed on the forehead tastes salty. He is bewitched and soon must die,” (2). This references two important aspects of CF: excessively salty sweat, and infant mortality in the absence of

intervention. Increased sweat chloride was first linked to CF during a 1948 heatwave in New York, during which a high proportion of the infants presenting with heat stroke also had CF. Dr. Paul di Sant'Agnes noticed this phenomenon and hypothesized that it was due to excessive salt loss from sweating. Further experimentation confirmed that people with CF do indeed have increased sweat chloride levels (3). In fact, the discovery of this phenomenon led to an easy diagnostic method for CF that is still utilized today. A test resulting in a sweat chloride >60 mM, which is 3-5x higher than the non-CF population, strongly suggests CF (4; 5).

The mechanism for this increased sweat chloride is straight-forward. The sweat gland can be divided into two parts, a secretory coil and a reabsorptive duct. In the secretory coil, sodium, chloride, and water move isotonicly from the blood stream through and between the epithelial cells into the luminal sweat gland space (Figure 1.1). Chloride secretion through this region is controlled mostly by cholinergic innervation, and thus is mediated predominantly by calcium-activated chloride channels (CaCCs) (6). As this isotonic saltwater progresses toward the surface of the body, it enters the reabsorptive duct. The epithelial cells of this region are capable of reabsorbing sodium and chloride, but not water, thus leading to a hypotonic (relative to blood) saltwater solution upon final release onto the surface of the skin. In this region, chloride reabsorption is controlled by CFTR, and sodium reabsorption is controlled by the epithelial sodium channel (ENaC) (6). Thus, in people with CF in which CFTR has reduced or completely absent function, chloride reabsorption is vastly reduced. Interestingly, ENaC activity also has been found to be decreased in CF sweat glands, suggesting cooperation between ENaC and CFTR channels (7; 8). Overall, this lack of sodium and chloride reabsorption causes the sweat to remain largely isotonic to the blood, resulting in saltier sweat compared to non-CF subjects.

In fact, it was evaluation of these sweat chloride abnormalities that eventually lead to the discovery that a defective anion channel is the cause of CF. Specifically, experiments with sweat glands determined that while substitution of chloride with impermeant anions in the luminal space hyperpolarized the transepithelial potential in non-CF tissue, the same was not true in CF tissue. Thus, CF sweat glands exhibited a lack of chloride conductance (9). This discovery led to the logical conclusion that the later-

Figure 1.1: A graphical representation of sweat glands, and the defective ion transport in CF. The sweat gland can be divided into two sections, the secretory coil (bottom) and the reabsorptive duct (top). In the secretory coil, sodium, chloride, and water are secreted such that the concentrations remain isotonic to the blood (red rectangle). Chloride secretion in this region mainly is mediated by calcium-activated chloride channels (CaCC, green cylinder), though a small amount is mediated by CFTR (blue cylinder). In the reabsorptive duct, sodium and chloride reabsorption occurs without reabsorption of water, leading to a hypotonic solution that is ultimately released onto the surface of the skin. In this region, chloride reabsorption is mediated by CFTR and sodium reabsorption is mediated by ENaC (yellow cylinder). In CF (right), CFTR is defective and cannot reabsorb chloride. Simultaneously, this loss of CFTR function results in a loss of activity of ENaC, resulting in a lack of reabsorption of sodium as well. Thus, the sweat does not become as hypotonic, remaining salty.



discovered CFTR gene associated with CF encoded an anion channel.

1.1.2 Dr. Dorothy Anderson and cystic fibrosis of the pancreas

Though salty sweat is an externally recognizable symptom of CF, and though this salty sweat helped elucidate the function of CFTR, infant death is not caused by this phenomenon. Rather intestinal obstruction due to meconium ileus and malnutrition due to pancreatic insufficiency cause infant mortality if no proper intervention is administered. In fact, the first formal description of CF was based in part on observations of pancreatic fibrotic damage in infants who died of malnutrition, as noted by Dr. Dorothy Anderson in 1938 (10). These infants had extensive mucus plugging of their pancreatic ducts, along with malabsorption of many nutrients, failure to grow, and steatorrhea. Dr. Anderson also found this disease to be autosomal recessive (11).

Since this initial discovery, more has been learned about the effect of CF on the pancreas. CFTR localizes to the proximal duct epithelial cells of the pancreas (12). Lack of CFTR activity in the pancreas leads to decreased water and bicarbonate secretion, with the former causing thicker pancreatic secretions and the later causing decreased pH of those secretions (13-15). These altered secretion characteristics lead to macromolecular precipitation and plugging of the pancreas. Together, the decreased pH and buildup of pancreatic enzymes lead to tissue damage and pancreatic insufficiency, the inability of the pancreas to secrete enough digestive enzymes to adequately break down food (16; 17).

Importantly, not all people with CF are pancreatic insufficient, largely based on the severity of the CFTR mutation, as will be discussed below. However, a large portion of people with CF do present with pancreatic insufficiency. In fact, newborn bloodspot screening for CF involves analysis of immunoreactive trypsin, which indicates pancreatic insufficiency (18). This screening will miss pancreatic sufficient people with CF, unfortunately, but can still identify a large portion of those with CF (19). To extend the lives of these pancreatic insufficient people with CF, doctors implement nutrient repletion therapies that must be used at every meal or snack. This includes high-calorie and high-fat diets along with administration of pancreatic enzymes and critical vitamins, among other things (17).

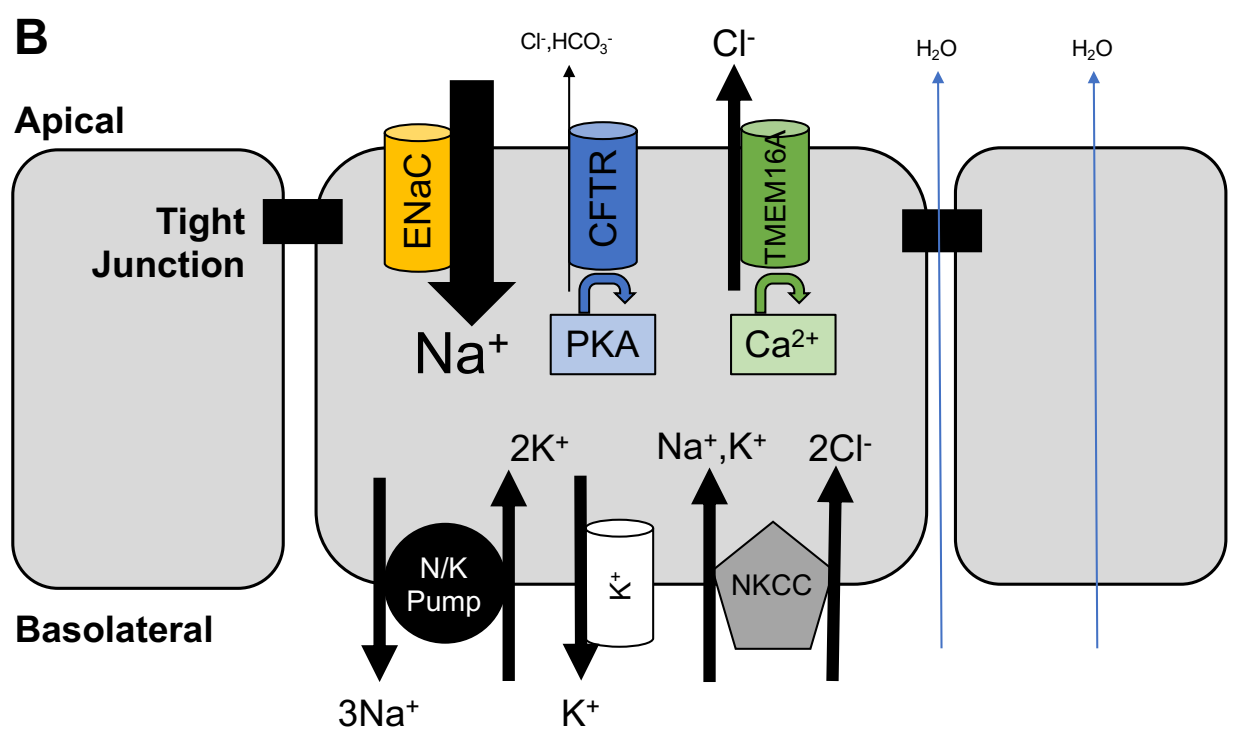
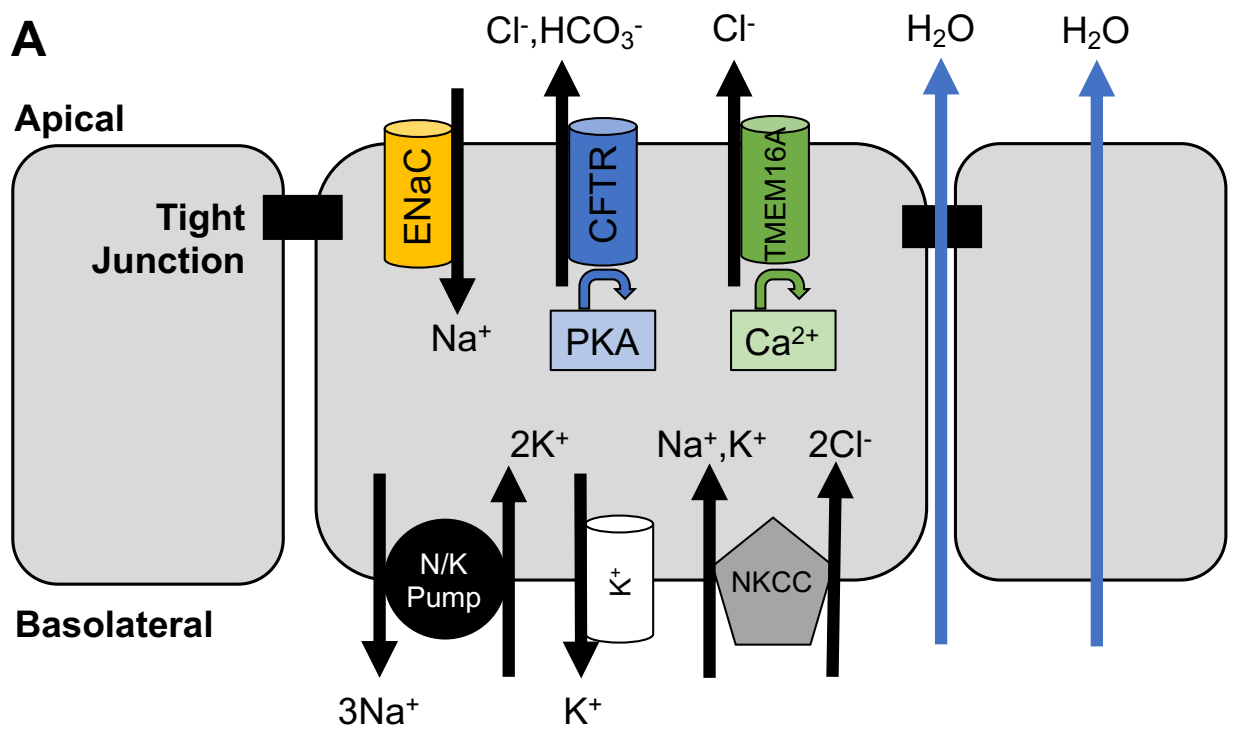
1.1.3 *The issue today – pulmonary manifestations of CF*

Although meconium ileus and malnutrition due to pancreatic insufficiency were the main causes of death in the early years of CF research, Dr. Dorothy Anderson did also note the presence of pulmonary infection during her post-mortem analyses of people with CF. Given the effective treatment strategies that have been implemented to address pancreatic insufficiency, people with CF now live longer, meaning that these pulmonary manifestations have become more problematic. Currently, lung failure is the leading cause of death among people with CF, caused by persistent inflammation and immune cell infiltration, mucus plugging of the airways, and colonization with bacteria (20). The most commonly found bacteria in the CF lung are *Pseudomonas aeruginosa* and *Staphylococcus aureus* (21).

First, it is important to understand CF in the lungs on a cellular physiology level (15). CFTR has been found to localize to serous cells in the submucosal glands (22), ciliated cells in the superficial and gland regions (23), and most recently pulmonary ionocytes which mostly localize to the submucosal glands (24). In pulmonary epithelial cells, CFTR is located at the apical membrane, which faces the lumen of the lungs, and facilitates chloride movement into the lumen (Figure 1.2A). Note that this is the opposite directionality as is seen in the reabsorptive duct of the sweat gland, where chloride moves into the cell from the lumen through CFTR. In pulmonary epithelial cells, a basolateral-to-apical (body-to-air) driving force for chloride is established by many components of the basolateral membrane. Firstly, the sodium-potassium ATPase (N/K pump) pumps sodium out of and potassium into the cell, creating a gradient for each of these ions in which sodium is higher outside of the cell and potassium is higher inside of the cells. This pump is the main consumer of ATP in the cell. The basolateral potassium gradient established by N/K pump facilitates potassium leak out of the cell through potassium channels, resulting in a negative membrane potential. When CFTR is activated by protein kinase A (PKA), the membrane voltage moves closer to that of the chloride reversal potential, which would eventually lead to a loss of driving force for chloride secretion. However, the signaling mechanisms that activate CFTR also activate a subset of the basolateral potassium channels, which maintains a basolateral-to-apical driving force. The basolateral sodium gradient established by the N/K pump facilitates cellular uptake of sodium, potassium, and chloride through the

Figure 1.2: A graphical representation of pulmonary epithelial cells, and the defective ion transport

in CF. A monolayer of airway epithelial cells (grey curved rectangles) connected by tight junctions (black rectangles) is shown, both for **(A)** non-CF and **(B)** CF lungs. The resting membrane potential is set by the N/K Pump (black circle) along with potassium channels (white cylinder) at the basolateral side of the cells. The NKCC (grey pentagon) facilitates basolateral chloride uptake into the cell. Apically located CFTR (blue cylinder), activated by PKA (light blue rectangle), releases chloride and bicarbonate into the airspace. TMEM16A (green cylinder), activated by calcium (light green rectangle), can also release chloride into the airspace. Apically located ENaC facilitates sodium movement into the cell, balancing basolateral sodium loss from the N/K Pump. Water can move paracellularly and transcellularly into the airspace, based on the concentrations of sodium and chloride.



sodium potassium two-chloride symporter (NKCC), again at the basolateral side of these cells. This is a major mechanism for basolateral chloride uptake and establishes a high intracellular concentration of chloride. Coupled with the negative membrane potential, apical chloride secretion through CFTR is encouraged.

Importantly, in pulmonary epithelial cells CFTR is not the only apically located channel and is not even the only apically located chloride channel (15). The calcium-activated chloride channel TMEM16A (transmembrane member 16A) is also present and can facilitate chloride secretion into the airspace upon increases in intracellular calcium. Because of this, some work has been done to explore whether it may be possible to bypass CFTR and utilize TMEM16A activation to induce chloride secretion and thus alleviate CF (25). This work into TMEM16A potentiators is ongoing but would be particularly beneficial for people with CF who are not approved for current CFTR modulators (as will be discussed below). However, it must be considered that endogenously, CFTR is activated by beta adrenergic receptors while TMEM16A is activated by purinergic receptors and muscarinic acetylcholine receptors. Thus, endogenously, these channels are activated via completely different methods, so potentiation of TMEM16A may not be relevant enough to substantially improve CF symptoms, and may lead to harmful side effects.

Aside from TMEM16A, ENaC must also be considered when studying CFTR in pulmonary epithelial cells. ENaC facilitates sodium movement into the cells from the apical side. While this specific directionality of ion movement is the same as the reabsorptive duct of the sweat gland, the relative directionalities of ion movement through CFTR and ENaC are not consistent. The overall apical-to-basolateral movement of sodium through ENaC results in a current of the same directionality as a basolateral-to-apical movement of chloride through CFTR (or TMEM16A). Thus, it is important to always inhibit ENaC prior to activating CFTR when studying these epithelial cells.

Ultimately, based on the sodium and chloride concentrations in the airspace, there is a driving force for water movement into the airspace. This water movement occurs predominantly between the cells, through tight junctions, and through cells via aquaporins (15). This hydration of the apical space of airway epithelial cells forms what is called the periciliary liquid layer. The cilia project into this periciliary liquid

layer, and when they beat, the resulting movement of this liquid layer moves the mucus layer above it. If the periciliary liquid layer is too deep, ciliary movement will not cause sufficient movement of this layer to facilitate movement of the mucus layer (26; 27). Contrarily, if the periciliary liquid layer is too thin, the cilia cannot move at all, which again results in a lack of movement of the mucus layer on top.

In CF, CFTR does not sufficiently conduct chloride, bicarbonate, or thiocyanide into the apical space (Figure 1.2B). Simultaneously, ENaC becomes overactive, resulting in increased apical uptake of sodium (28; 29). Again, note that the relative effects of loss of CFTR function on ENaC activity differ from those of the pancreas, in which decreased CFTR activity results in decreased ENaC activity. However, the phenomenon of their activities being linked is consistent. In the lung, inhibiting this overactive ENaC has been a target for therapeutics, again proposed as a method for circumventing modulation of CFTR to combat CF. However, there are mixed results from clinical trials, with some showing that inhibiting ENaC with amiloride actually worsens lung function (30). Regardless, in the pulmonary epithelial cells, the combination of decreased chloride secretion into and increased sodium absorption from the airspace results in dehydration and a decreased aqueous layer at the apical surface of the cells (31). This ultimately leads to dysfunction of the cilia, resulting in stagnation of the airway mucus. One current, effective treatment strategy for CF is to administer aerosolized hypertonic saline to try and replete this liquid (32).

1.1.4 Other organs affected by CF

As mentioned above, in infancy, people with CF can die of meconium ileus, the neonatal form of intestinal obstruction. This generally can be treated by an enema to deliver a non-absorbable osmolyte solution, but occasionally surgery is necessary to remove this blockage (33). Intestinal obstruction can occur at any stage in CF, though, as the CF intestines are chronically dehydrated, acidic, and mucus-ridden due to loss of CFTR activity in these organs. Non-neonatal intestinal blockages are treated very similarly to meconium ileus. While these intestinal obstructions are relatively rare, people with CF do experience persistent constipation. This can be treated with laxatives such as polyethylene glycol (33).

Something not mentioned so far has been the effects of CF on fertility. Typically, this discussion

revolves around male fertility, though female fertility may also be affected in CF. Regarding male fertility, the majority of males with CF present with congenital bilateral absence of the vas deferens, the connective tube that transports sperm from the testis to the ejaculatory organs of the penis (34-36). The effects of CF on female fertility are more complex and multifactorial. Women with CF have approximately 2.5-fold higher rates of infertility and subfertility as compared to the non-CF population. However, it is not clear which symptoms and complications are due to the primary CFTR defect rather than other factors related to life with CF, such as malnutrition. For example, women with CF do have thickened and dehydrated cervical mucus, blocking adequate sperm entry into the uterus (37). This is likely a direct effect of loss of CFTR activity, as thickened mucus and dehydration occurs in many organs in CF. However, women with CF may also have anovulation caused by hypothalamic suppression due to malnutrition (37). Clearly more work is necessary to ascertain the effects of CF on female fertility.

1.2 CFTR: an overview of the protein

As stated above, CF is caused by loss-of-function mutations in the CFTR gene. There are many different mutations that can cause loss of function of CFTR. Furthermore, there are many different effects these mutations can have on CFTR production, structure, and activity that can ultimately cause a loss of function. This section will provide an overview of the CFTR protein, and the classifications of CFTR mutations to the gene/protein that cause CF.

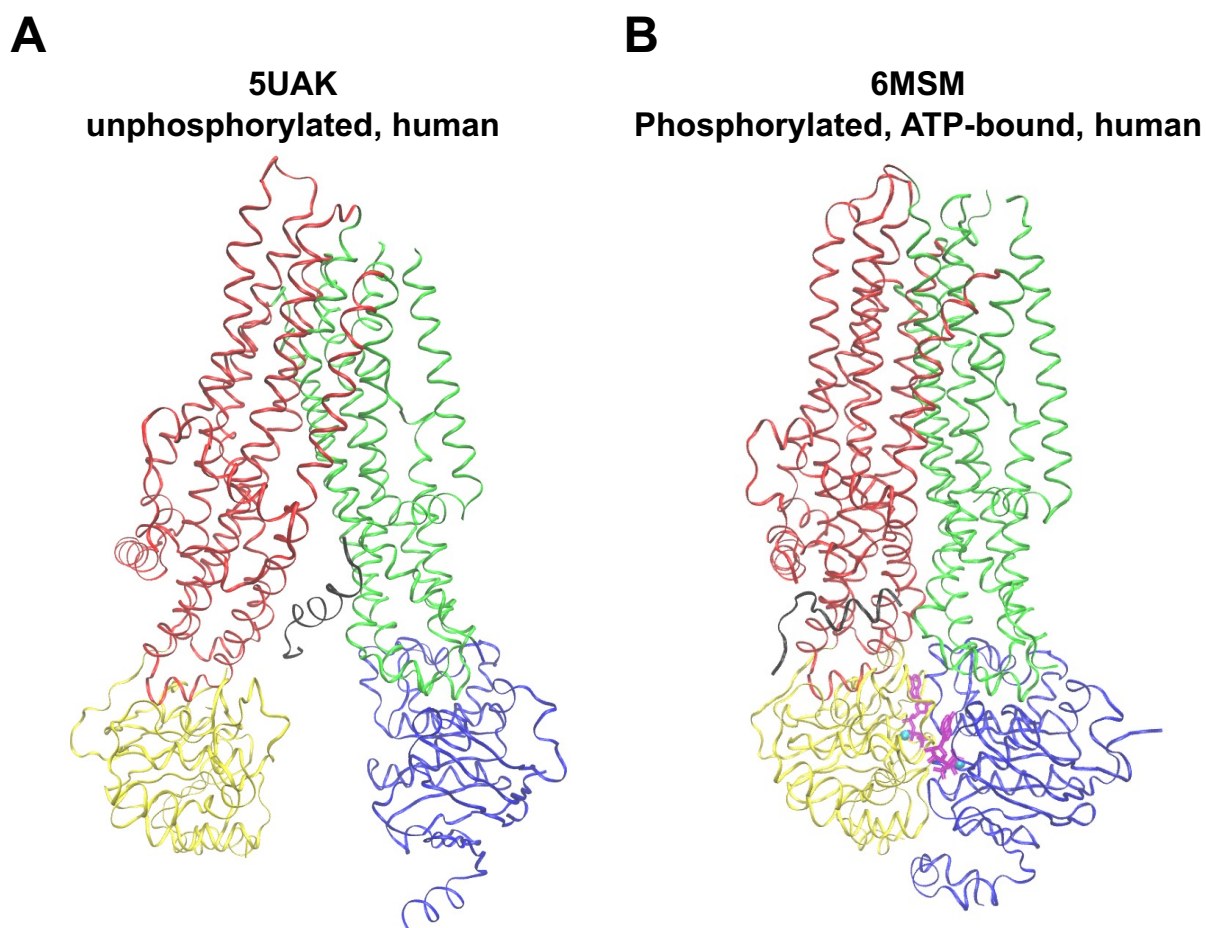
1.2.1 Protein structure and activity

In 1989, the gene and protein associated with CF were identified and named CFTR (38-40). CFTR is a member of the ATP-Binding Cassette (ABC) transporter superfamily, and thus alternatively is referred to as ABCC7. However, while all other ABC transporters use ATP to power an enzymatic function, most commonly leading to active transport of substrates across a membrane, CFTR is the only ABC transporter that functions at least primarily as an ion channel. CFTR conducts chloride, bicarbonate, and thiocyanate anions, which flow across the membrane according to their electrochemical gradients. As an ABC

transporter, CFTR contains two transmembrane domains (TMDs) (each with six transmembrane helices), two nucleotide binding domains (NBDs), and a regulatory R-domain, with a tertiary sequence in the following order: N-term → TMD1 → NBD1 → R-domain → TMD2 → NBD2 → C-term (Figure 1.3). Note however that TMD1 and TMD2 actually are composed of transmembrane helices encoded both before and after the NBD1 sequence. CFTR channel opening requires two related processes: phosphorylation of the R-domain by PKA, and binding and subsequent hydrolysis of ATP at the NBDs (41). Closure is regulated by ATP hydrolysis at the NBDs. Importantly, as will be discussed below, dephosphorylation of the R-domain as well as phosphorylation of inhibitory sites can also affect CFTR channel activity.

The R-domain is a highly disordered region of CFTR, and thus only a small portion of it has ever been resolved. Specifically, a short alpha helix was occluding what could represent the ion conductance pathway between the two TMDs in the dephosphorylated, ATP-free human CFTR cryogenic electron microscopy (cryo-EM) structure (PDB 5UAK) (Figure 1.3A) (42). What specific portion of the R-domain this helix was composed of is uncertain due to the low resolution of this region. A helix belonging to the R-domain also was resolved in the PKA-phosphorylated, ATP-bound human CFTR structure (PDB 6MSM). However, this helix, again of an unknown portion of the R-domain, was located at an outside interface of the protein, not occluding the potential conducting pore (Figure 1.3B). This indicates that part of the dimerization of the NBDs and the activation of CFTR involves the translocation of at least portions of the R-domain (43). How exactly PKA-phosphorylation of the R-domain alone affects the structure and localization of this domain and how this movement affects CFTR activity is still unclear. Many have speculated that electrostatic repulsion following phosphorylation results in movement of the R-domain from an occluding position to a position that does not prohibit anion conductance (44). This is supported by the apparent occlusion in the cryo-EM structure, the fact that phosphomimetic mutation of predicted PKA-phosphorylation sites results in active CFTR (45), as well as the fact that deletion of the R-domain (split- Δ R-CFTR) results in a constitutively active and PKA-insensitive CFTR (46). However, evidence against this theory comes from data showing that treatment of split- Δ R-CFTR with unphosphorylated R-domain

Figure 1.3. Some of the cryo-EM structures of human CFTR. The structures are (A) unphosphorylated (PDB ID: 5UAK) (42) or (B) PKA-phosphorylated and ATP-bound (PDB ID: 6MSM) (43) are shown as ribbon structures. TMD1 is red, NBD1 is yellow, TMD2 is green, NBD2 is blue, and the resolved portion of the R-domain is black. If ATP is present, it is colored as magenta lines and the coordinating magnesium is a cyan VDW sphere.



does not inhibit channel activity. Rather, treatment with PKA-phosphorylated R-domain further stimulates CFTR channel activity, suggesting that a portion of the phosphorylated R-domain may serve as a CFTR activator (47). This theory is supported by other cryo-EM data, in which the R-domain is resolved in the PKA-phosphorylated and ATP-bound CFTR. It is possible that both theories are true; the R-domain could be inhibitory when unphosphorylated, and stimulatory when PKA-phosphorylated. More work is necessary to fully understand the R-domain of CFTR.

Regardless of the exact structural mechanisms dictating CFTR activation, it is well known that activating the R-domain predominantly occurs through PKA-mediated phosphorylation, for which there are 10 predicted PKA phosphorylation sites (48; 49). Notably, though, full CFTR activity additionally is dependent on PKC-mediated phosphorylation, with PKC being activated by calcium (50). PKA is activated by cAMP, and thus pharmacological interventions that increase cellular cAMP levels result in CFTR activation. Endogenously, generation of cAMP is initiated by activation of G_s-coupled G protein coupled receptors (GPCRs), which results in activation of adenylyl cyclase, which generates cAMP. Endogenously, these GPCR agonists include epinephrin activation of beta-adrenergic receptors, acetylcholine activation of some muscarinic receptors, vasoactive intestinal peptide activation of some of its receptors, and adenosine activation of some of its receptors (49). Importantly, cholera toxin increases cAMP levels leading to activation of CFTR which explains the severe intestinal water loss during cholera infection. Pharmacologically, cAMP also can be generated by synthetic beta-adrenergic agonists (or other G_s-coupled GPCR agonists), by direct activation of adenylyl cyclase with forskolin, by the cell-permeable cAMP analog 8Br-cAMP, or by inhibition of phosphodiesterase (which breaks down cAMP) with 3-isobutyl-1-methylxanthine (IBMX).

As mentioned, an additional critical step of CFTR gating is the binding and hydrolysis of ATP. Each of the two ATP binding sites (ABSs) in CFTR's NBDs is comprised of several conserved motifs including Walker A, Walker B, and signature (LSGGQ) motifs. Importantly, each ABS is comprised of components from both NBDs. An ATP molecule at each ABS is bound in part by the Walker A and B

motifs of one NBD, and the signature motif of the other NBD. Thus, two molecules of ATP are sandwiched in opposite directions between the two NBDs, as can be seen in the PKA-phosphorylated, ATP-bound CFTR cryo-EM structures (PDB 6MSM (human) and 5W81 (zebrafish)) (Figure 1.3B) (43; 51). A lysine in the Walker A motif is critical for hydrolysis, and an aspartic acid in the Walker B motif is critical for magnesium coordination and thus hydrolysis. The signature sequence is also critical for hydrolysis. Importantly, the signature sequence in NBD2 is degenerate (LSHGH), leading to ineffective hydrolysis of ATP at this site (ABS1). Thus, essentially only one of the two ABSs catalyzes ATP hydrolysis, whereas the other mainly contributes ATP binding only (52). The remaining ATP hydrolysis functionality is critical, as mutations to the NBDs that decrease ATP hydrolysis rates affect the burst frequency and burst duration of CFTR channels, though single-channel conductance remains the same (53). The effects of these mutations were highly dependent on which NBD was mutated, suggesting that each ATP binding site has a specific role in CFTR gating. Specifically, mutations that decreased the catalytic efficiency of the fully functional ATP hydrolysis site (ABS2) increased the open state stability of CFTR (53). Similarly, addition of the non-hydrolysable ATP analog AMP-PNP results in significantly increased CFTR single-channel open durations. Together, these data suggest that ATP binding facilitates channel opening, whereas ATP hydrolysis facilitates channel closure. Thus, an overall gating scheme can be proposed (Figure 1.4).

1.2.2 *CF-causing mutations*

Interestingly, although the NBDs and the R-domain regulate channel opening, the entirety of the CFTR protein is sensitive to mutation. Over 2000 variants have been described with over 350 identified as disease-causing mutations. These mutations do not cluster in one particular region, but are distributed throughout the gene (54). Even the ultimate effect of these mutations on CFTR is complex, which is why there are seven different classes of mutations (Table 1.1) (55; 56). However, it is important to note that class V-VII are not completely agreed upon. Furthermore, many mutations fall into multiple classes, and not all mutations in the same class result in the same morbidities and mortalities. Thus, while these classes are important for a basic understanding and categorization of CFTR mutations, they are imperfect.

Figure 1.4: A graphical representation of CFTR and its gating cycle. CFTR is composed of TMD1 (red rectangle), NBD1 (yellow half-circle), R-domain (black line), TMD2 (green rectangle), and NBD2 (blue half-circle). Two ATP binding sites exist between the two NBDs, with one site capable of efficient ATP hydrolysis (ABS2, light red semi-circle and triangle) and the other degenerate site not (ABS1, light green semi-circle and triangle). The gating cycle of CFTR involves first PKA-mediated phosphorylation and ATP (purple semi-circle and triangle) binding at the degenerate ABS1 site (C0-C1). The next step involves ATP binding at the functional ABS2 site (C1-C2). This facilitates movement of the CFTR structure such that an anion pore is opened (C2-O). Hydrolysis of the ATP at the functional ABS2 site then results in channel closure (C3). Release of the ADP and inorganic phosphate returns the channel to the original closed state (C3-C1).

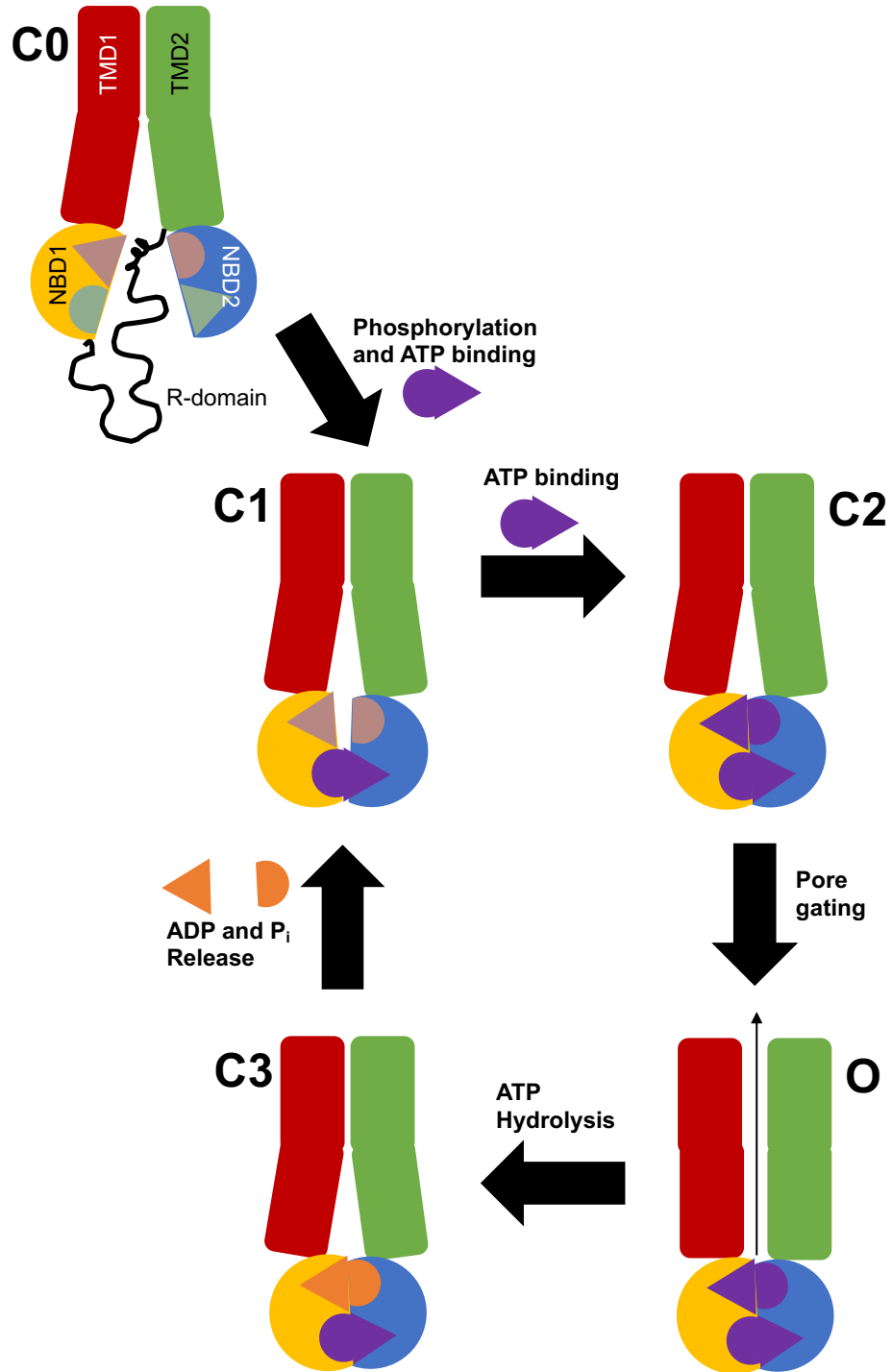


Table 1.1: The seven classes of CFTR defects, with examples

Class	Explanation	Example
I	defective synthesis of the protein	G542X
II	defective trafficking to the cell membrane	Δ F508
III	decreased ability to open	G551D
IV	decreased ability to conduct ions	R347P
V	decreased amount of CFTR protein	A455E
VI	decreased stability at the surface	N287Y
VII	absence of mRNA	3849 + 10kB C \rightarrow T

Class I mutations result in inadequate protein production caused by mutations that result in premature stop codons, mutations causing splicing variations, or frame shift mutations. Class I mutations result in very small amounts of mRNA, likely due to nonsense-mediated decay, and therefore low abundance of protein (57; 58). Even this small amount of protein that is produced is so severely altered that it is completely nonfunctional, resulting in a very severe phenotype. The most commonly found mutation of this class is G542X, in which a stop codon causes a loss of the amino acid chain following residue 542. Specifically, 2.5% of people with CF have at least one copy of this mutation (54). However, other common mutations of this class include W1282X and R553X.

Class II mutations result in improper trafficking of CFTR to the cell membrane, where it could elicit its effects. By far the most commonly found mutation in this class, and in fact the most commonly found mutation in the CF population, is the Δ F508 mutation, in which the phenylalanine at position 508 has been deleted. Approximately 70% of people with CF carry at least one Δ F508 allele (54). This Δ F508 mutation causes improper folding of CFTR due to improper contacts between TMD1 and NBD1, which results in its targeting for degradation (59). This loss of trafficking can be detected by simple biochemical methods. Typically, CFTR receives core glycosylation in the endoplasmic reticulum (ER). This CFTR then is trafficked to the Golgi, where it undergoes additional complex glycosylation. Following this final glycosylation, CFTR is trafficked to the cell membrane. When probed on a western blot, this results in CFTR bands of three molecular weights – un-glycosylated, core-glycosylated, and complex-glycosylated termed bands A, B, and C respectively. While the majority of wild-type (WT) CFTR exists as band C, the majority of Δ F508-CFTR exists as band B, indicating that it never traffics to the Golgi and instead is targeted immediately for degradation (60). This phenomenon of predominant band B expression rather than band C is a definable feature of Class II mutations.

Class III mutations result in CFTR protein that is localized correctly and in adequate amounts, but that has a reduced capacity to open. The most commonly found mutation in this class is G551D, in which the glycine at position 551 is substituted with an aspartic acid. This mutation is present in at least one allele

in approximately 2% of people with CF (54). This G551D mutation is in the signature sequence of NBD1 and results in substantially decreased binding of ATP to this binding site (61). This decreased ATP binding causes significantly decreased channel opening. However, when G551D-CFTR does open, its single-channel properties are very similar to WT-CFTR (62). Thus, for the G551D mutation, not all CFTR ion channel activity is lost.

Class IV mutations result in CFTR protein that is localized correctly, in adequate amounts, and with the ability to open, but that does not conduct ions sufficiently. A major mutation in this class is R347H, which occurs in only 0.14% of people with CF (54). In WT-CFTR, this arginine forms a salt bridge with an aspartic acid on the opposite face of the pore to stabilize the conducting pathway. Loss of this salt bridge results in a reduction of CFTR channel activity, but certainly not a complete loss of conduction for this specific mutation (63). Another important mutation, R117H, is present in about 1.3% of people with CF and also does not result in a complete loss of conduction. However, this R117H mutation does seem to have some additional characteristics of Class III mutants.

Class V mutations result in insufficient amounts of total cellular CFTR protein. One important mutation of this class is A455E, which is present in 0.35% of people with CF (54). The decreased amount of protein in this mutant is caused by rapid degradation of the fully glycosylated form, as well as the partially glycosylated form (64). Similar to Class V, but on a more subcellularly localized scale, class VI mutations result in decreased cell surface stability of the CFTR protein. A representative mutation of this class is N287Y, which is fully functional aside from its increased internalization rate and thus decreased surface expression (65). Class VII mutations result in decreased amounts of mRNA, generally due to changes in the promoter regions for CFTR. The most commonly found mutation of this class is 3849 + 10kB C → T, which is present in approximately 0.8% of people with CF (54). Because of this defect in the promoter region, there is an insufficient amount of CFTR mRNA, and thus of CFTR protein as well.

Importantly, as mentioned above, not all mutations fall into a single class. As will be discussed below, intervention to rescue one aspect of a CFTR mutant frequently reveals subsequent abnormalities with the mutant that categorize it within a different class. The most well-studied example of this is the

$\Delta F508$ mutation, which while typically considered Class II also has characteristics of Class III and VI mutations. Even more so, not all mutations within a class respond to modulators to the same degree, with some mutations not responding at all to modulators that positively affect most other mutations in the same class. So, again, this classification scheme is imperfect, though it is still useful for a basic understanding of CFTR mutations.

1.3 Highly effective modulator therapies and other developing therapies

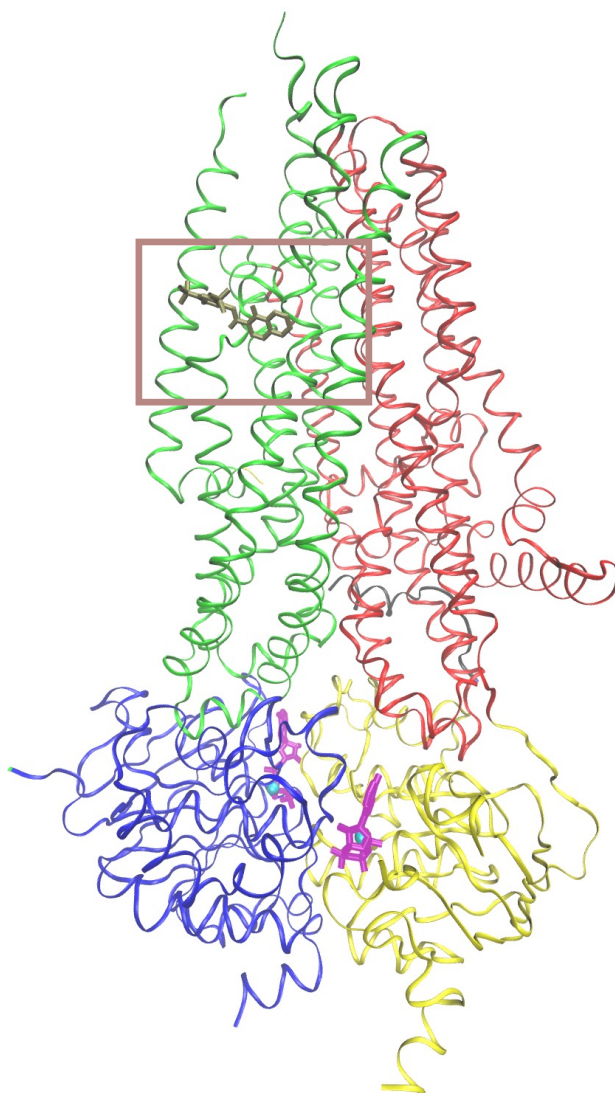
1.3.1 The potentiator – VX770

The first highly effective modulator therapy (HEMT) to achieve Food and Drug Administration (FDA) approval was the compound VX770 from Vertex Pharmaceuticals in 2012 (drug name ivacaftor, brand name Kalydeco[®] in the U.S.). This compound was identified by high-throughput screening to increase the ion channel activity of the Class III G551D-CFTR in Fisher rat thyroid (FRT) cells by stabilizing the open state after it had already been pre-activated by forskolin (state “O” of Figure 1.4) (66-69). The effects of VX770 on G551D-CFTR were confirmed in bronchial epithelial cells from human explant tissue (HBEs). This requirement for an additional activating compound (forskolin in this case) is what designates VX770 as a potentiator rather than an activator of CFTR. Recent cryo-EM studies have found that VX770 binds in the break point of one of the transmembrane helices in TMD2 (Figure 1.5) (70). The relevance of this binding site is debated since it has not been determined if this break in the transmembrane helix of CFTR is physiological or an artifact of harsh purification conditions. Furthermore, hydrogen-deuterium exchange experiments on detergent-purified, thermo-stabilized CFTR did not identify this or any nearby site as being protected by VX770, though importantly the transmembrane domain had minimal exchange under control conditions anyways (71). In support of the VX770 binding site on CFTR determined by cryo-EM, though, recent click chemistry experiments on membrane-bound CFTR determined a similarly located binding site (72). However, this paper also identified a binding site in the fourth intracellular loop of CFTR (72), which is supported by the hydrogen-deuterium exchange experiments which indicate reduced exchange at this loop in the presence of VX770 (71). This is important, given that the most commonly found CFTR mutation,

Figure 1.5: The cryo-EM structure for PKA-phosphorylated, ATP-bound CFTR bound to VX770.

The cryo-EM structure of the protein (PDB ID: 6o2p) is shown as a ribbon structure. TMD1 is red, NBD1 is yellow, TMD2 is green, NBD2 is blue, and the resolved portion of the R-domain is black. ATP is colored as purple lines and the coordinating magnesium is a cyan VDW sphere. VX770, drawn as tan lines and highlighted by a tan box, is associated with TMD2.

6o2p
Phosphorylated, ATP-bound, human
VX770-bound



$\Delta F508$, is due to the loss of a phenylalanine in NBD1 that interfaces with the fourth intracellular loop. In support of these data indicating an additional binding site for VX770, data from our own lab indicate that VX770 has multiple binding sites (73). So, while the TMD2 binding site identified by cryo-EM and click chemistry could be a true binding site, along with the fourth intracellular loop binding site, more work is necessary to determine definitively all binding sites. Furthermore, it is necessary to characterize the specific effects of each binding site on VX770-mediated potentiation of CFTR in order to logically design more effective drugs of this class.

Regardless of the lack of knowledge of the molecular bases for VX770's mechanism of action, clinical trials were conducted to evaluate its efficacy. Phase 2 and 3 trials of VX770 in patients at least heterozygous for the G551D mutation indicated a good safety profile as well as significant improvements in sweat chloride, lung function measured by the percent predicted for the forced expiratory volume in the first second (ppFEV1), frequency of pulmonary exacerbations, and body weight (74; 75). At this point, Kalydeco[®] is approved for 97 CFTR mutations, including mostly Class III and Class IV. Not all Class III or Class IV mutations respond to VX770, though (63), indicating that more work is necessary to understand the interactions between VX770 and those specific mutations. Furthermore, the majority of people with CF have mutations of different classes for which VX770 alone is ineffective. However, as is discussed below, ivacaftor is used in combination therapies with other drugs to treat many more people with CF.

1.3.2 *The correctors – VX809, VX661, and VX445*

Unfortunately, because VX770 works by stabilizing the open state of CFTR, it alone is ineffective at treating the most common CFTR mutation, $\Delta F508$, which is a Class II misfolding and mistrafficking mutant. Another class of HEMTs that stabilize misfolded CFTR in order to accomplish effective trafficking to the plasma membrane, ultimately termed correctors, is required to treat the majority of people with CF. The first drug of this class, VX809 (drug name lumacaftor), was approved as a combination therapy with ivacaftor (brand name Orkambi[®]) by the FDA in 2015 for people with CF homozygous for the $\Delta F508$

mutation. Like VX770, VX809 was identified by Vertex Pharmaceuticals using a high-throughput screening process, though this time the focus was on FRT cells expressing the Δ F508-CFTR mutation (76). VX809 is thought to bind near the F508 residue at the interface between NBD1 and the fourth intracellular loop, as determined by computational docking, nuclear magnetic resonance experiments, and thermostability assays (77-80). However, there is conflicting data and potentially additional binding sites for this small molecule. This small molecule corrector was found to increase the fraction of CFTR in the fully glycosylated band C form, suggesting improved trafficking from the ER to the Golgi. VX809 also increased the amount of transepithelial current through CFTR, suggesting improved surface expression of this mutant protein. This improvement was translated into a clinically meaningful outcome, as Phase 3 trials showed that people homozygous for Δ F508-CFTR treated with a combination of lumacaftor and ivacaftor had moderately improved ppFEV1 and reduced pulmonary exacerbations as compared to the placebo group (81). However, discontinuation due to adverse events was higher in the intervention group. Furthermore, continued research determined that VX770 negatively affected VX809-mediated correction in chronic treatment conditions due to destabilization and increased turnover of CFTR (82; 83). Biochemically, this could be seen as a reversion back to predominantly band B CFTR upon treatment of VX809-rescued Δ F508-CFTR cells with chronic VX770, as well as an overall decrease in total WT-CFTR protein upon chronic VX770 treatment. Clearly a different treatment was necessary.

This different treatment came first in 2018 as a substitution of VX809 for VX661 (drug name tezacaftor), which when combined with ivacaftor was given the brand name Symdeko[®]. Just like all of the current HEMTs thus far, VX661 came from Vertex Pharmaceuticals. It has the same basic structure as VX809 and is thought to bind in the same location at the interface between NBD1 and the fourth intracellular loop (80). Phase 3 clinical trials in people homozygous for Δ F508-CFTR treated with a combination of tezacaftor and ivacaftor had moderately improved ppFEV1 and reduced pulmonary exacerbations as compared to the placebo group (84). Importantly, though, fewer people discontinued this intervention due to adverse events, indicating an improvement from Orkambi[®]. Unfortunately, just as with

VX809, chronic VX770 negatively impacted VX661-mediated correction of CFTR (82).

This Symdeko[®] therapy was not utilized for very long, as it was very quickly replaced in 2019 by the triple-combination therapy Trikafta[®] from Vertex, which consists of ivacaftor, tezacaftor, and elexacaftor (VX445). Elexacaftor is a distinct corrector compound that synergizes with tezacaftor, stabilizing CFTR and increasing the amount of band C through a congruent mechanism with an unknown binding site separate from the tezacaftor binding site (85-87). Importantly, in bronchial epithelial cells from explant lung tissue from people with CF, though chronic VX770 was found to decrease the amount of band C CFTR rescued by VX445 and VX661 in combination, the amount of band C CFTR remained significantly higher than with either drug alone with chronic VX770. This triple-combination therapy also significantly increased the transepithelial chloride transport in these cells over the VX661/VX770 treatment alone. In Phase 2 and 3 clinical trials, in people either homozygous for $\Delta F508$ -CFTR or heterozygous for $\Delta F508$ -CFTR with an additional minimal function mutation, triple-combination therapy resulted in a significant (both statistically and clinically) improvement in sweat chloride, ppFEV1, and other lung function measurements over patients on Symdeko[®] for the homozygous $\Delta F508$ -CFTR group and over placebo for the heterozygous $\Delta F508$ -CFTR group (85; 88; 89). Adverse events leading to discontinuation of the treatment were rare. Trikafta[®] has been a breakthrough therapy both because of its high efficacy and because of its approval for people heterozygous for $\Delta F508$ -CFTR, which includes a large proportion of the CF population. Between Kalydeco[®] and Trikafta[®], 90% of people with CF currently have a HEMT intervention available to them.

1.3.3 Other emerging therapies

There is still a remaining 10% of people with CF for whom there is no current HEMT, though. This includes, but is not limited to, people who express CFTR alleles that do not lead to the generation of full-length protein, including alleles bearing nonsense mutations. New therapeutic strategies are necessary to address the primary CFTR defect in these people. Novel strategies such as read-through compounds for

people with Class I mutations (90; 91), gene therapy for any mutation (92), and even more are being explored (93). Ultimately, CF treatments are becoming much more about personalized medicine, where the specific genetic mutation(s) and disease manifestations guide the specific therapies that are administered.

1.4 CF animal and cell models

There are myriad animal models that have been developed to study CF, each with its own unique set of benefits and pitfalls. For the purposes of this section, we will focus only on mouse, ferret, and pig models. There also is an abundance of airway epithelial cells lines that have been developed, many of which will be explored here.

1.4.1 CF mouse models

Mice are frequently the default animal model for biomedical research since they are relatively cheap, easy to breed, and have short lifespans. However, mice do not always recapitulate the disease phenotype of interest, so care must be taken when developing, evaluating, and selecting mouse models. Mice were found to possess a CFTR gene with 78% sequence homology to human CFTR (94), and to express CFTR mRNA in intestinal and pulmonary tissues (95). Since this discovery, much work has been done to develop CF mouse models. The most commonly used CFTR knockout mouse models can be divided into a few groups including total CFTR knockout, CFTR knockout with regained gut expression, low-CFTR expression, and $\Delta F508$ - (and other mutants) CFTR-expressing. In addition, a mouse model overexpressing the β -subunit of ENaC in the lungs is frequently used. We will examine a representative model of each of these classes, though many models within each class exist with variations in the method of generation and the genetic background (96-98).

Cftr^{*tm1Unc*}, one of the most commonly used CFTR knockout mouse model, was developed in 1992 by the Koller laboratory (95). These mice are in a C57BL/6 background and contain a functional CFTR knockout mutation due to a stop codon insertion (S489X, Class I mutation), which results in extremely low

levels of CFTR mRNA production. While this mutation did not affect fetal viability, it did result in runting and increased rates of death in the first five postnatal days and in the seven days following weaning. It also was associated with decreased body mass. Death was likely due to the extensive intestinal blockage found in these mice, particularly in the ileum and large intestine. This phenomenon occurs in humans as well and previously was the major cause of death for CF in humans (10). In order to extend the lifespan of these CFTR knockout mice, they must be fed either a diet of liquid nutrients, Peptamen (99), or water with the laxative polyethylene glycol (100). In regards to the pulmonary phenotype, these CFTR knockout mice had increased nasal potential differences, generally attributed to increased activity of ENaC. This ENaC involvement was confirmed, as knockout mice showed increased magnitudes of effect of the ENaC inhibitor amiloride on the nasal potential differences as compared to the WT mice (101). Similarly increased magnitudes of amiloride-sensitive nasal potential differences in CF are seen in humans as well (102). However, unlike human tissue, forskolin still elicited an effect on transepithelial currents in these CFTR knockout mice trachea (103). This has been suggested to be calcium activated chloride channels activated through a cross-talk mechanism between cAMP generation and calcium release (103-105).

In order to address the lethal intestinal dysfunction of the CFTR knockout mouse, a gut-corrected CFTR knockout model, *Cftr*^{Tg(FABPCFTR)}, was developed in 1994 by the Whitsett laboratory (106). In this transgenic model, human CFTR is expressed in the intestinal tract, as controlled by the rat fatty acid binding protein gene promoter. These mice lived much longer than their non-gut-corrected controls, and most of the intestinal defects were not present. Thus, an altered diet was not necessary for these mice, removing a potential confounding variable.

As an alternative CFTR knockout model, the *Cftr*^{tm1Hgu} model was developed in 1992 by the Hooper laboratory, still on the C57BL/6 background (107). This knockout was made via a different method (insertional rather than genetic replacement), resulting in a model that retained low levels of CFTR activity. This slight CFTR activity leads to decreased mortality compared to the other CFTR knockout model, *Cftr*^{tm1Unc}, and thus an altered diet was not necessary for these mice either. These knockout mice still had increased nasal potential differences like the total CFTR knockout model. They also retained forskolin-

elicited changes in potential differences, though these changes were significantly less than their WT counterparts. Histologically, there were some intestinal abnormalities in the CF mice, but not to the degree of the total CFTR knockout mouse model.

Importantly, most people with CF have at least one mutation that results in misfolding and mistrafficking of CFTR (Class II, most notably $\Delta F508$ -CFTR). A CFTR knockout model does not recapitulate the potential cellular effects of this misfolding and mistrafficking. Thus, following these CFTR knockout mouse models, the *Cftr*^{*tm1Eur*} model was developed in 1995 by the Scholte laboratory in which CFTR was mutated to the $\Delta F508$ genotype, rather than being fully knocked out, using an insertional method (108; 109). These mice did not experience runting or intestinal blockage like the knockout mice, and thus did not require an altered diet. However, these mice still did have significantly decreased weight as compared to their WT controls as they aged. Like the knockout mice, these mice had increased nasal potential differences, increased magnitudes of amiloride-sensitive nasal potential differences, and retained a forskolin-elicited current in the trachea. The reason these $\Delta F508$ -CFTR mice have a less severe phenotype than the total CFTR knockout model could be because the $\Delta F508$ mutation in mouse CFTR has been found to be less severe in regard to both trafficking and channel activity than the human mutation (110).

Importantly, none of these mouse models focusing on CFTR develop notable spontaneous lung disease. Instead, spontaneous lung disease is seen in the *Snn1b* mice, a transgenic model overexpressing β -ENaC in the airway, which was developed in 2004 by the Boucher laboratory (111). Surprisingly, this model most closely resembled the lung phenotype of human CF, including mucus obstruction, airway inflammation, infiltration of immune cells, and epithelial cell death among other things (112). These mice even died prematurely from their lung disease. However, note that some of the phenotypes seen are not associated with CF, including emphysema (112). Also, importantly, since the β -ENaC overexpression is localized to the airway, no altered diet is necessary to prevent death from intestinal obstruction. However, simultaneously, this model loses the complexity of inter-organ effects of CF.

Still, none of these models develop a spontaneous lung infection, as occurs in humans. It is

hypothesized that this is due to pulmonary expression of alternative chloride channels such as TMEM16A, the channel thought to be activated by forskolin in the CFTR knockout models. Furthermore, when CF bacteria such as *P. aeruginosa* are introduced to the CF mice lungs, the mice experience both increased mortality and prolonged bacterial clearance relative to their WT counterparts. Still, of the CF mice that do survive this bacterial challenge, they do ultimately clear the infection, unlike many people with CF (96-98). Overall, while mouse models are indeed beneficial, they clearly do not represent the pulmonary phenotype of CF very well. Furthermore, dietary interventions to keep CF mice alive for longer may act as a confounder in some research studies, and thus must be considered when reviewing data. Lastly, to date, no chronic infection CF mouse model has been developed, leading to extreme limitations in our understanding of chronic infections in CF. Other animal models must be utilized in addition to these mouse models.

1.4.2 *CF ferret models*

Thankfully, there are other animal models that more closely mimic the pulmonary phenotype of CF, though these models do still have limitations. Specifically, ferret and pig models will be discussed.

In 2008, a CFTR knockout ferret model was developed in the Engelhardt laboratory using a recombinant adeno-associated virus and somatic cell nuclear transfer cloning (113). Ferret lungs are more similar than mouse to human lungs and have been used historically to model pulmonary viral infections. Specifically, pulmonary CFTR expression is more similar to humans in ferrets than in mice (summarized elsewhere (113; 114)), and ferret CFTR also shares 92% sequence identity with human CFTR (42). As another benefit, though the lifespan of ferrets is indeed longer than mice, their lifespans are still relatively short, allowing for rapid research.

These CFTR knockout ferrets experience intestinal obstruction, similarly to their mouse counterparts, along with decreased intestinal absorption of nutrients, leading to significantly decreased body weight relative to their WT controls (114). To prevent premature death from intestinal disease and malnutrition, a polyethylene glycol gavage can be performed to clear blockages, and ursodeoxycholic acid (a bile acid), omeprazole (a proton-pump inhibitor, increasing gut pH), and supplemental pancreatic

enzymes and amino acids can be administered (114; 115). Alternatively, a gut-corrected CFTR knockout ferret model was developed to circumvent the intestinal disease (114). Despite these interventions, CFTR knockout ferrets have decreased body mass compared to their WT controls.

Importantly, and unlike their CFTR knockout mouse counterparts, CF ferrets develop spontaneous lung disease (114; 115). In fact, these ferrets are so susceptible to lung infections at an early age that they must be reared on a cocktail of antibiotics to prevent death from pulmonary failure (114; 115), though these antibiotics do not prevent pulmonary neutrophilic inflammation (116). Importantly, neutrophilic inflammation seems to precede infection in people with CF as well (117). In addition to all of this, CFTR knockout ferrets experience severe pulmonary mucus plugging, as is seen in humans. Upon electrophysiological examination, the knockout ferrets showed no forskolin-elicited changes in potential differences in excised tracheal sections, suggesting no alternative chloride channel is present in ferret lungs in contrast to mouse lungs (114). Upon maturing, the lung infections in these ferrets are less life-threatening, but chronic infection and persistent pulmonary decline still occur (115). Interestingly, the type of bacteria colonizing the lung of the CF ferrets was different than people with CF. Ultimately, though, this is a good animal model to study CF lung disease. It can be improved upon by introducing actual CFTR mutations rather than just knocking out CFTR and by intentionally establishing chronic infections with bacteria commonly found in the human CF lung.

1.4.3 CF pig models

As an alternative to ferrets, it is known that pig lungs also are very similar to human lungs in many regards (118), suggesting they could serve as another model for CF disease. Furthermore, pig CFTR shares 92% sequence homology with human CFTR (42; 119). In 2008, the Prather/Welsh laboratory established the first pig model of CF using adeno-associated virus and somatic cell nuclear transfer (120). Birthweight did not differ between CFTR knockout and WT pigs. As in the other CFTR knockout animal models, intestinal obstruction was an issue immediately after birth. Administration of pancreatic enzymes and fat-soluble vitamins was necessary to prevent malnutrition, as in ferrets and humans. To overcome the intestinal

defects, a gut-corrected CFTR pig model was developed in 2013 in the Welsh laboratory, which was confirmed to maintain similar pulmonary phenotypes to total CFTR knockout pigs as newborns (121).

In regard to pulmonary phenotype, these CFTR knockout pigs had hyperpolarized baseline nasal potential differences associated with increased magnitudes of the effect of amiloride, suggesting ENaC overactivity as seen in humans. Unlike mice, but similarly to ferrets and humans, increasing cAMP levels with isoproterenol did not trigger a change in nasal potential difference in the CF pigs, suggesting a lack of CFTR and no redundant channels to compensate for this loss. CFTR knockout pigs did not show infection or inflammation immediately after birth (120).

A Δ F508-CFTR-expressing model also was made in the Prather/Welsh lab in 2008 (120). These Δ F508-CFTR pigs were similar to the CFTR knockout pigs in regards to intestinal defects and pulmonary electrophysiology characteristics (122), and thus were evaluated alongside CFTR knockout mice when determining longer-term lung pathologies of CF pigs (123). By two months, chest CT (computerized tomography) scans indicated thickening of the airway walls, similar to human chest CT scans. Furthermore, upon dissection, CF pig lungs showed mucus plugging, with these plugs containing neutrophils along with some macrophages and bacteria. These phenomena were shown in gut-corrected CFTR knockout pigs as well (121). Microscopic examination of CFTR knockout and Δ F508-CFTR pigs also revealed occasional neutrophilic infiltration. Interestingly, though, by this point, CF pigs did not have differences in cell counts or cytokines in their bronchoalveolar lavages, as compared to their WT controls. Bronchoalveolar lavages and lung sections from CF pigs did tend to culture bacteria more frequently than their WT counterparts. Interestingly, inoculation with *S. aureus*, a commonly found bacteria in the CF lung (21), indicated that newborn CF pigs could not clear bacteria as well as their WT controls.

Ultimately, pigs are an excellent model for CF lung disease. However, an important caveat to consider is that they are extremely difficult to keep alive. Furthermore, since they are larger and longer-lived than mice and ferrets, they are already more expensive to care for, both regarding money and time.

1.4.4 *CF cell models*

Cell models in CF research can be divided into three broad categories: immortalized cell lines, cancer cell lines, and primary cells. Immortalized cells (having the potential for indefinite replication) can be generated from non-cancerous tissue using a variety of methods, while cancer cell lines are obtained from excised tumors and are already immortalized by nature. In laboratory-immortalized and cancer cells, only one original patient sample is represented, and each cell line tends to require slightly different culture conditions. In contrast, primary cells are isolated from human tissue but are not modified, and thus cannot be propagated indefinitely in culture. Primary cells originate from any patient, and thus can capture population-level heterogeneity. All cells discussed within this section are mentioned in future sections.

Numerous immortalized pulmonary cell lines have come out of the Gruenert laboratory. All these cell lines end with the suffix “o-,” to indicate that the cells were immortalized by the origin-of-replication defective SV40 plasmid. Frequently, the cell lines are referred to without this “o-” suffix. In 1992, 9HTEo-cells were developed (124; 125). These are tracheal epithelial cells originating from non-CF patient lung explant submucosal glands showing cAMP- and calcium-mediated anion currents, suggesting the presence of CFTR and TMEM16A, respectively. These cells appear to have both serous cell and mucous cell phenotypes in culture (126). In 1994, the 16HBEO- cell line was developed from bronchial surface epithelial cells from lung explant tissue of a 1-year-old male without CF (127). These cells occasionally formed small cilia at their apical side. Surprisingly, 16HBEO- cells did not show any amiloride-sensitive current, suggesting the cells do not express ENaC for some still unknown reason. However, the cells did exhibit cAMP-mediated chloride currents following the depletion of chloride from the apical buffer, as well as calcium-activated currents regardless of apical chloride depletion. 16HBEO- cells also have been found to express CFTR protein. Comparative CF-representing 16HBEO- cells bearing one of a suite of CFTR mutations have been developed by the CF Foundation Therapeutics Laboratory using CRISPR/Cas9 editing (128). Importantly, during development of these mutants, it was discovered that the SV40 sequence used to originally immortalize these cells was inserted into one of the CFTR alleles, rendering them monoallelic for CFTR. Also in the early 1990s in the Gruenert laboratory, the CFBE41o- cell line was developed from

bronchial epithelial cells from a patient homozygous for the $\Delta F508$ mutation (129). Importantly, though, the $\Delta F508$ -CFTR expressed by these cells could not be rescued by traditional means, thus representing a hybrid between a $\Delta F508$ -CFTR and a CFTR knockout cell line model (130). As such, non-CF comparison cells can be generated by stably transducing in CFTR (130). Though these non-CF models are still not ideal due to the presence of the $\Delta F508$ -CFTR which unfolds and could trigger feedback pathways in these cells, they are still useful for research purposes.

In addition to the cells from the Gruenert laboratory, another important cell line, IB3-1, was established in 1991 by the Guggino laboratory (131). These bronchial epithelial cells originated from a 7-year-old white male patient with CF ($\Delta F508/W1282X$ genotype) and were immortalized via adeno-12-SV40 infection. In 1993, S9 cells and C38 cells were generated in the Carter laboratory by stable transduction of CFTR complementary DNA (cDNA) into IB3-1 cells via adeno-associated virus, with S9 having full-length CFTR and C38 having CFTR with a short truncation at the N-terminus (132). Thus, these S9 and C38 cells are considered the non-CF counterparts of IB3-1 cells. Importantly, though, while these non-CF cells do have recovered CFTR protein production and channel activity, they are not true representations of the non-CF phenotype, as they do still express $\Delta F508$ -CFTR much like the transduced CFBE41o- cells discussed above. Furthermore, these IB3-1 cells, and thus the S9 and C38 cells derived from them, are chromosomally unstable (131).

Calu-3 cells were established by ATCC and were characterized by the Widdicombe laboratory in 1994 (133-135). These cells originated from the adenocarcinoma of a 25-year-old white male without CF. Interestingly, despite being male, the cells are disomic for the X chromosome. Furthermore, these cells are missing chromosomes 1, 13, 15, and 17 (135). Calu-3s have granules characteristic of secretory cells. Calu-3 cells showed cAMP-mediated anion secretion that was amplified by depletion of chloride from the apical buffer, along with calcium-mediated anion secretion. This suggested that the cells were expressing CFTR and TMEM16A, respectively. Interestingly, similar to the 16HBEo- cells, Calu-3 cells did not have any amiloride-sensitive current, suggesting a lack of ENaC activity. None of the ENaC subunits are located on

any of the missing chromosomes, so this cannot explain the loss of ENaC activity.

Lastly in regard to cell lines, in 2003, NuLi and CuFi cells were developed in the Klingelutz laboratory using bronchial epithelial cells isolated from explant lung tissue of people without and with CF, respectively (136). Importantly, the authors designate these cells only as airway, not specifically bronchial epithelial cells. In a method varying from the others discussed so far, these cells were immortalized by the reverse transcriptase component of telomerase and human papillomavirus type 16 E6 and E7 genes. A few different CuLi lines were established, including genotypes $\Delta F508/\Delta F508$, $\Delta F508/R553X$, and $\Delta F508/G551D$. Cells were a mixture of ciliated and goblet, with the exact ratio varying by passage number. The NuLi cells exhibited amiloride-sensitive and cAMP-mediated currents, suggesting the presence of ENaC and CFTR. While CuFi cells maintained that amiloride-sensitive current, they had no cAMP-mediated anion currents unless recombinant CFTR was reintroduced to the cells.

Overall, there are clearly plenty of airway epithelial cell line models to choose from, each with their own caveat. In addition to these, and serving as a more physiologically relevant model, primary airway epithelial cells are also available, including nasal (HNE), tracheal (HTE), and bronchial (HBE). In this case, cells are isolated from lung explant tissue and are grown without immortalization techniques, then differentiated from basal to epithelial cells. Overall, there are two main methods for culturing primary airway cells, including one from the Randell laboratory and one from Vertex Laboratories (137; 138). These methods will be described in more detail in future sections. These primary cell models, while more physiologically relevant, are more difficult to work with, and certainly cannot be propagated for as long.

1.5 Lipid imbalances in CF epithelia

Lipids are divided into eight categories based on their structure (Table 1.2). These lipids can take on diverse roles, including energy storage, signaling, and membrane composition. Focusing in on the membrane composition role of lipids, it is important to point out the complexity of membranes. Different subcellular compartments differ in their lipid composition. For example, cardiolipin is found almost

Table 1.2. The different classes of lipids, with examples.

Lipid	Description	Example
Fatty Acid	Acyl chain ending in a carboxylic acid	Arachidonic Acid
Glycerolipid	Glycerol in which any number of its hydroxyls are substituted with a fatty acid	Triacyl glyceride (body fat)
Phosphoglyceride (aka Phospholipid)	Glycerolipid in which the first or third hydroxyl group is a phosphate potentially leading to a head group	Phosphatidylcholine Phosphatidylserine
Sterol	Four-ring hydrocarbon with a hydroxyl on carbon 3 and numerous other possible side chains elsewhere	Cholesterol Estrogen, Testosterone
Sphingolipid	Sphingoid base with numerous possible side chains	Sphingomyelin
Prenol	Composed of repeat units of 3-methyl-2-buten-1-ol	Geraniol (citronella)
Saccharolipid	Glycerolipid in which the first or third hydroxyl group is a sugar	lipopolysaccharide
Polyketide	Repeating carbonyl and methylene groups	Doxycyclin

exclusively in mitochondria, and the lipids comprising the endoplasmic reticulum membrane are predominantly PCs (139). Even within a compartment, the inner and outer leaflets of the bilayer typically are not composed of lipids in the same ratios.

Lipids are not simply a uniform boundary of a cell or cellular organelles. In fact, the diverse lipid composition of cells, organelles within these cells, and even the specific leaflets within these bilayers can contribute to the structure and function of these components, as well as the structure and function of the proteins that reside within them. As such, it is important to consider lipid imbalances in disease, and to determine the effects these imbalances have on pathophysiology.

An imbalance of lipids in the blood has frequently been reported in CF, especially in relation to pancreatic insufficiency and CF-Related Diabetes (CFRD), to be discussed in a future section. These data, reviewed elsewhere (140; 141), are extensive, frequently conflicting, and can be confounded by the altered diet which people with CF are prescribed. Here we focus mainly on lipid imbalances in CF airways as well as airway epithelial cells in human and mouse models in an effort to understand the roles lipids may play in the lung disease of CF patients and the lipid environment that CFTR experiences in these cells.

1.5.1 Fatty acids are imbalanced in CF epithelia

Linoleic acid and arachidonic acid are omega-6 fatty acids. Linoleic acid is an essential fatty acid, meaning it must be absorbed through the diet. Arachidonic acid can be absorbed through the diet or catabolized from linoleic acid. Docosahexaenoic acid is an omega-3 fatty acid that can be absorbed through the diet or produced from metabolism of eicosapentaenoic acid or α -linoleic acid. While each of these fatty acids play a vital physiological role, imbalances between them can affect health, with an increased ratio of omega-6/omega-3 fatty acids inducing a pro-inflammatory state (142).

Arachidonic acid was increased and docosahexaenoic acid was decreased in nasal epithelial cells collected from people with CF, compared to control (143). Importantly, this imbalance was observed regardless of pancreatic sufficiency status, indicating that the modified high-calorie/high-fat diet of pancreatic insufficient people with CF was not the cause of this lipid imbalance. In support of this,

experiments were performed in the commonly-used 16HBE cells with and without CFTR transiently knocked down (CF and non-CF, respectively) and in IB3-1 CF cells with and without viral transduction to express WT-CFTR (non-CF and CF C38 cells, respectively) (144; 145). Both sets of CF cells indicated increased arachidonic acid concentrations alongside decreased linoleic and docosahexaenoic acid levels as compared to their control.

However, it is important to note that cell lines are an imperfect model due to their genetic instability. Cells collected directly from people and cultured in a laboratory setting without genetic modification (primary cells) are considered the gold standard. Even more so, though, the specific 16HBE pairing in this case is not perfect since the CF model is represented only by a CFTR knockdown. Most people with CF express the trafficking mutant $\Delta F508$ -CFTR, which adds complexity not captured by using a cell line that produces no CFTR. The misfolded $\Delta F508$ -CFTR may induce an unfolded protein response that elicits effects on the cells, which will not occur in a cell line simply not expressing CFTR. Conversely, the C38 control cells express both two mutated CFTR proteins and WT-CFTR protein. Thus, this WT-CFTR-expressing cell line is not truly representative of non-CF cells, as the cells potentially are still burdened by the unfolded $\Delta F508$ -CFTR. Still, though both sets of cell lines have limitations, used together, they can add insight into the mechanism of the effect. These two sets of cell lines revealed similar data, which matched data gathered directly from patient cells. Furthermore, in HBE cells from human explant tissue, docosahexaenoic acid was decreased and arachidonic acid was increased in CF cells (cFHBEs) relative to non-CF controls (nHBEs) (146). This was found in cultured bronchial epithelial cells from a pig model as well as the total lung homogenate of a mouse model of CF (146). Thus, this fatty acid imbalance is well supported by many models.

Despite the overall decreased presence of linoleic and docosahexaenoic acid, CF cell lines showed an increased uptake of these lipids (144; 147). To explain the decrease in linoleic acid abundance, further investigation found increased metabolism of linoleic acid into arachidonic acid via $\Delta 5$ - and $\Delta 6$ -desaturase in CF cells. This increase in $\Delta 5$ - and $\Delta 6$ -desaturase activity could be due to a loss of proper CFTR function,

which leads to an increase in intracellular calcium that activates calcium/calmodulin-dependent protein kinase kinase β , which activates 5' adenosine monophosphate-activated protein kinase (AMPK), which is known to affect lipid synthesis and metabolism. Inhibiting either of these kinases returns $\Delta 5$ - and $\Delta 6$ -desaturase activity to control levels (148). The decreased levels of docosahexaenoic acid were found likely to be due to increased retroconversion of docosahexaenoic acid to its precursor molecule, eicosapentaenoate (147).

Overall, it seems that CF epithelial cells have reduced levels of docosahexaenoic acid and increased levels of arachidonic acid, leading to an imbalanced ratio of the two that indicates a pro-inflammatory state. Supplementation of docosahexaenoic acid, which is known to downregulate expression of the $\Delta 5$ - and $\Delta 6$ -desaturases, reversed the overall metabolic profile in CF cells but did not affect non-CF cells, (144; 145; 147). There have been many clinical trials to evaluate the efficacy of supplementation by docosahexaenoic acid (and other omega-3 fatty acids) in CF (149; 150). While a couple of studies report slight improvements in some of the clinical outcomes measured, overall, there was no benefit to omega-3 fatty acid supplementation in CF. However, the benefits of modifying the overall diet to favor omega-3 rather than omega-6 fatty acids, rather than additional omega-3 supplementation on top of the fats already consumed by people with CF, have yet to be determined.

Excitingly, Trikafta[®] was found to partially correct the docosahexaenoic acid and arachidonic acid imbalances in CF primary bronchial epithelial cells (146). Future work should determine the effects that this specific lipid modulation has on CF cells, including the effects of various inflammatory markers. Furthermore, it is important to determine if the effects found in these primary bronchial epithelial cells translates to the lungs of actual people with CF.

1.5.2 Cholesterol is increased in CF epithelia

Cholesterol, the precursor for many vitamins and hormones, constitutes a large percentage of the lipid mass of the plasma membrane, has a large influence on the fluidity of the membrane, and clusters with sphingomyelin to form lipid rafts (151). It is an extremely important lipid that is imbalanced in many

diseases, especially neurological diseases (152). While cholesterol imbalance is implicated in the pathogenesis of some diseases, its involvement in some others remains unknown.

There is evidence that cholesterol is imbalanced in CF-representing cells. For example, HeLa cells (cervical epithelial) were transfected with a construct encoding $\Delta F508$ -CFTR, which has improper folding and trafficking. These cells were stained with the cholesterol probe filipin, which showed an accumulation of cholesterol in the $\Delta F508$ -CFTR-expressing cells (153). Similarly, baby hamster kidney (BHK) and Chinese hamster ovary (CHO) cells were transfected with constructs encoding $\Delta F508$ - or C1410X-CFTR mutants and were compared to cells transfected with constructs encoding WT-CFTR (154). Both of these mutants are typically trafficked from the ER to the lysosome for degradation, and thus are Class II trafficking defect mutants. However, these mutants can traffic through the Golgi to the ultimate destination of the cell surface when the cells are shifted to 27°C for 24-48 hr. This altered temperature treatment is called temperature shift correction. In the cells expressing these mutants of CFTR, there was an increase in free cholesterol, as detected by thin-layer chromatography, accompanied by a redistribution of cholesterol from the Golgi to non-Golgi vesicles thought to be late endosomes, as detected by filipin staining (154). These two CFTR mutants are usually trafficked from the ER to the lysosome, but can traffic to the Golgi and cell surface when rescued by temperature shift to 27°C. Interestingly, the redistribution of cholesterol was intensified by this temperature shift rescue of mutant CFTR trafficking, rather than being normalized, leading the authors to believe that the distal secretory pathway was involved (154). For comparison, cells also were transfected with constructs encoding G551D- or D572N-CFTR. G551D-CFTR is a gating defect mutation that has no trafficking defect. D572N-CFTR is another Class II trafficking defect mutant like $\Delta F508$ - or C1410X-CFTR, but this mutant cannot be rescued by temperature shift correction. Importantly, neither G551D- nor D572N-CFTR transfections affected cellular cholesterol levels as compared to WT-CFTR transfected cells. Furthermore, overall cholesteryl esters were decreased, indicating decreased transfer from endosomes to the ER and Golgi (154). These data cumulatively suggest that when CFTR mutants such as $\Delta F508$ - or C1410X-CFTR escape the ER quality control mechanisms, traffic to the surface,

and are quickly targeted for degradation – which occurs to a small degree without temperature shift correction – these mutants are trafficked through the endosomal pathway to the lysosome. This may disturb the activity of the established endosomal pathways which process cholesterol, leading to cholesterol accumulation in endosomal structures. While this theory is plausible, these studies were conducted in cells that do not normally express CFTR, raising questions about the validity of translating these findings into relevant cells that do normally express CFTR.

More physiologically relevant data were gathered in CF airway cell lines and in the pulmonary epithelia of CF mice. The CF airway cell lines were IB3-1 cells along with 9/HTEo- cells transfected to overexpress the CFTR R-domain, which will inhibit CFTR activity. Non-CF comparison cells were S9 cells along with 9/HTEo- cells with a mock transfection. The CF mice either were total CFTR knockouts, which were fed a liquid diet to prevent early death from intestinal blockage, or were expressing Δ F508-CFTR, which were given water with polyethylene glycol plus electrolytes to prevent early death from intestinal blockage. Filipin staining, fluorescent NBD-cholesterol, and electrochemical measurements using a modified microelectrode doped with cholesterol oxidase were used to quantify and qualify cholesterol in these cells. Data indicated that cholesterol accumulated intracellularly and in the plasma membrane of the CF models as compared to the non-CF models (155; 156). Correction of CFTR either by treating with VX809 in CFBE cells (expressing Δ F508-CFTR) or by inducing CFTR expression in knockout mice reduced this cholesterol accumulation (157). The CF models also showed inflammatory imbalances common to CF, such as decreased nitric oxide synthase and SMAD3 protein expression, as well as decreased signal transducer and activator of transcription-1 activity (156; 158). Interestingly, decreasing cholesterol levels by treating cells with HMG-CoA reductase inhibitor resolved these imbalances, suggesting that cholesterol accumulation caused this inflammation (156; 158). Importantly, the degree of cholesterol accumulation seemed to correlate with the severity of CFTR genotype, with mouse epithelial cells expressing Δ F508-CFTR (unfolded protein, high severity) accumulating more cholesterol than cells expressing R117H-CFTR (reduced function CFTR, mild severity) (159). These data may be confounded by the fact that the R117H-CFTR mice were fed a standard chow diet up until one week prior to the

experiment, at which point they were fed the Peptamen diet like the $\Delta F508$ -CFTR mice.

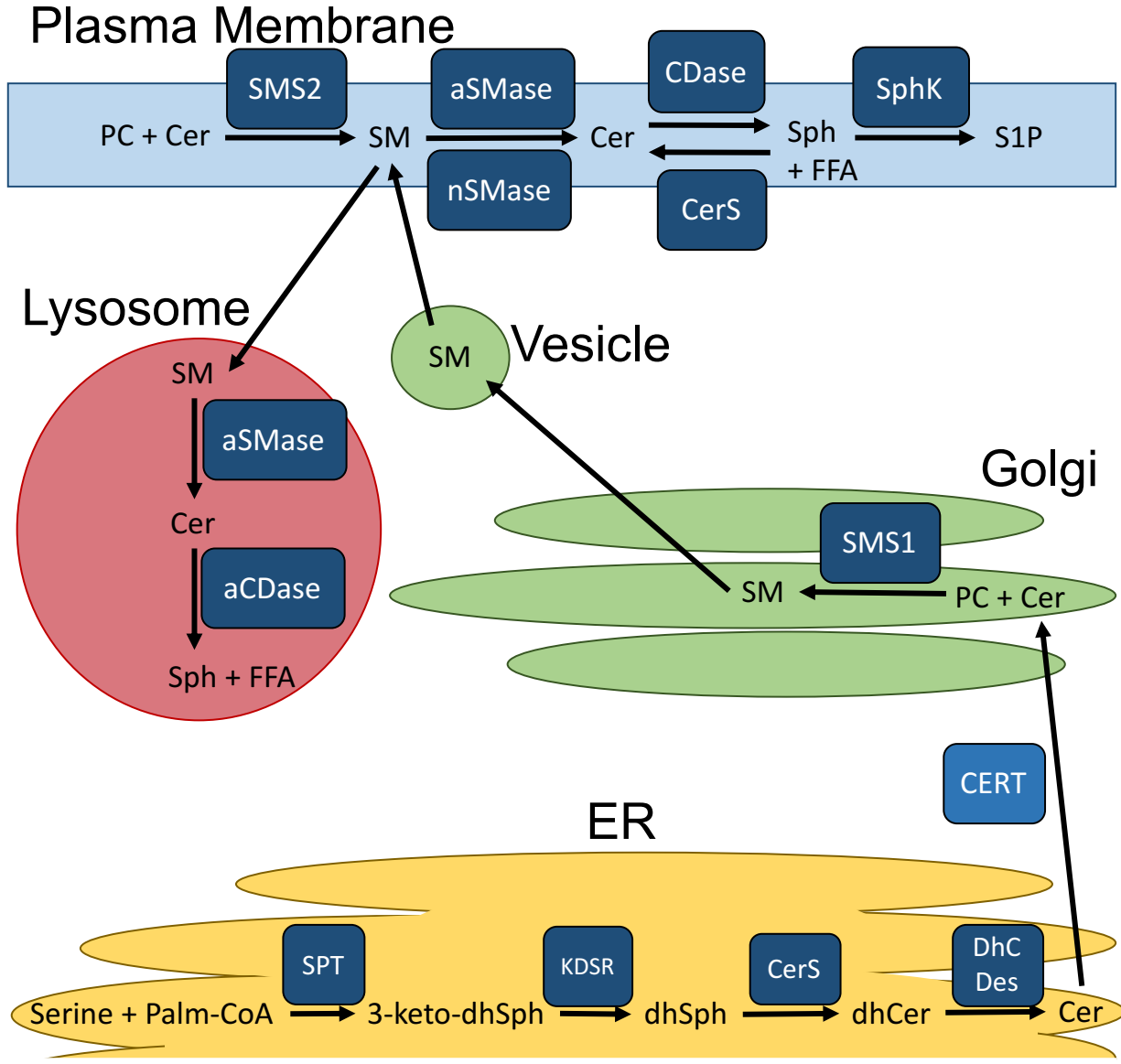
The CFTR knockout mouse data presented above may be confounded by results showing that Peptamen, the liquid diet used in these studies, causes a 300% increase of cholesterol in the lungs of mice with either residual CFTR activity or intestinal CFTR expression (160). However, the $\Delta F508$ -CFTR-expressing mouse model fed a normal diet showed the same effects. Furthermore, within the cell lines studied above, the non-CF and CF counterparts were maintained in the same media with the same nutrient composition, yet still the CF cells showed similarly increased cholesterol levels. This suggests that in the CF mice, the cholesterol imbalance and its resulting inflammatory imbalance are likely caused by the primary CFTR defect and not by the diet.

Still, little work has been done to quantify the relative levels of cholesterol in lung epithelial cells from people with CF, which is vital to confirm the relevance of this observed imbalance. A thin-layer chromatography analysis of lipids extracted from tracheobronchial sections revealed that human CF lung sections had increased cholesterol levels compared to non-CF lung sections (161). However, people living with CF are encouraged to eat a high-calorie, high-fat diet. Thus, it is difficult to distinguish in actual patient samples an imbalance caused by the primary CFTR defect from an imbalance caused by altered diet. Thus, though cell lines, mouse tissue, and some patient data indicate that cholesterol is increased in airway epithelia, more work is necessary to confirm that this imbalance is due to the primary CFTR defect, to confirm that the mechanism established in non-epithelial cell lines is consistent with the mechanism in cells collected from people living with CF, and to understand the pathology of how this imbalance affects the wellbeing of people with CF.

1.5.3 *Ceramides are imbalanced in CF epithelia*

Ceramide is a sphingolipid implicated in pro-inflammatory and pro-apoptotic signaling, but also in proliferative signaling. Which signaling pathways are activated depends upon the acyl chain length (162). Ceramide concentrations in cells are controlled by the direct synthesis of ceramide and production by the salvage pathway (Figure 1.6) (163). This balance between ceramide and sphingomyelin is important, as

Figure 1.6: A graphical representation of cellular ceramide synthesis pathways. *De novo* ceramide synthesis begins in the ER, with the synthesis of a serine and a palmitoyl-CoA (C16:0) into 3-keto-dihydrosphingosine (3-keto-dhSph) and a CoA via serine palmitoyl transferase (SPT) (164; 165). This is the rate-limiting step of *de novo* ceramide synthesis. The 3-ketoSpha species is then reduced by 3-ketodihydrosphingosine reductase (KDSR) into dihydrosphingosine (dhSph), also known as sphinganine (164; 165). dhSph is then *N*-acylated into dihydroceramide (dhCer) by one of six ceramide synthases (CerS) (164; 165). These CerS enzymes homo- and heterodimerize, and the combination of enzymes in the dimer control the length of the acyl chain added to form dhCer (166). dhCer is then desaturated by dihydroceramide desaturase (DhC DES) to form ceramide (Cer), which has a 4,5-*trans*-double bond, to end the *de novo* synthesis pathway (164; 165). CerS2 and CerS5 seem to be the most predominantly expressed CerS enzymes in pulmonary epithelial cells (BEAS2B and primary small airway epithelial cells from human lung explants) (167). Cer can then be used to synthesize more complex sphingolipids via headgroup additions. For the purposes of this figure, the focus will remain on the generation of sphingomyelin (SM). Cer is transported via the ceramide transport protein (CERT) to the Golgi (168). Once here, Cer can be modified to form glycosphingolipids (sugar headgroup added, includes gangliosides) or SM. To form SM, a phosphocholine headgroup is added from a phosphatidylcholine (PC) to ceramide by sphingomyelin synthase 1 (SMS1), with diacyl glycerol as an additional product of this reaction (168). SM is then trafficked through vesicles to the cell membrane. Once at the membrane, acid-sphingomyelinase (aSMase) and neutral-SMase (nSMase) enzymes on the external and internal leaflet, respectively, can break SM back down into Cer and phosphocholine (169; 170). This Cer can be converted back into SM at the cell surface via sphingomyelin synthase 2 (SMS2) or can be further broken down into sphingosine (Sph) and a free fatty acid (FFA) by ceramidase (CDase) enzymes (168; 171). This Sph can then enter the “salvage” pathway to generate sphingolipids (165). Sph can be converted back into Cer by CerS enzymes or can be phosphorylated into sphingosine-1-phosphate (S1P) by sphingosine kinase (SphK) (171; 172). Plasma membrane SM can also be trafficked to the lysosome for breakdown by acid-SMase and acid-CDase into Cer and Sph (172).



sphingomyelin and cholesterol cluster to form lipid rafts whereas ceramide clusters with itself to form larger lipid platforms that exclude cholesterol (151; 173). Many different proteins localize preferentially into these sphingomyelin rafts or ceramide platforms, bringing them into proximity to each other to increase the efficiency of their interactions (173-175). Generally, these protein clusters involve various partners of a signaling mechanism, increasing the efficiency of their influence on their specific signaling pathways. Importantly, CFTR clusters into both sphingolipid rafts and ceramide platforms; the impact of this on channel mobility and activity will be discussed below (176-178).

The activity of CFTR in these different microdomains is relevant to CF, as ceramide levels are imbalanced in CF. Originally, evidence from the Gulbins lab indicated that ceramide levels were increased in lung epithelia from CF patients grown on microscopy slides (160). However, the ceramide antibody used in this study was found to non-specifically bind many other types of lipids, leading to doubt about the validity of these results (179). The theory posited from these original studies was that ceramide accumulation occurred because of alkylation of lysosomes from pH 4.5 to 5.9 (180). At pH 5.9, acid-SMase in the lysosome still functions to convert sphingomyelin into ceramide (181). However, at this pH, acid-CDase is incapable of converting ceramide into sphingosine and a fatty acid (in fact, it catalyzes the reverse reaction to synthesize more ceramide) (182). Alkylation of the lysosome, knockout of acid-SMase, or functional inhibition of acid-SMase decreased ceramide levels to non-CF concentrations, suggesting a role for acid-SMase in ceramide accumulation. However, the idea that defective CFTR results in alkylation of the lysosome (or any organelle) is highly contested (183; 184).

Alternative to these findings in which ceramide was increased in the CF model, multiple publications from a multi-institution collaboration (consisting of the De Sanctis and Radzioch groups, frequently along with the Scholte group) revealed decreased ceramide content in the total lung homogenate as compared to control mice (146; 185-187). These studies utilized more accurate mass spectrometry methods (coupled to an initial thin-layer chromatography step) and both whole-animal CFTR knockout and a $\Delta F508$ -CFTR-expressing strain of mice. This decreased ceramide occurred alongside an increase in the ratio of long chain ceramides to very long chain ceramides. Importantly, this imbalance was found

regardless of whether the mice were fed the liquid Peptamen diet or the standard chow diet like the non-CF control mice, indicating that altered diet was not the cause for the ceramide imbalance. This ceramide imbalance could contribute to the chronic inflammation seen in CF patient lungs as long-chain ceramides are pro-inflammatory while very-long-chain ceramides are anti-inflammatory (188). Importantly, total lung homogenate includes much more than just epithelial cells, so these data must be considered carefully since it is unclear what cell types contribute to this imbalance.

To focus on epithelial cells, the multi-institution collaborative discussed in the previous paragraph also conducted studies comparing CFBE41o- cells (CF) and CFBE41o- cells transduced with lentiviral vector containing WT-CFTR (non-CF). These studies indicated a ceramide imbalance similar to what this collaborative found in CF mice (186). However, as mentioned previously, these cells do not represent the trafficking defect of the most common CFTR mutation, which is important to consider since this trafficking mutation could even further worsen the imbalance seen by a simple loss of CFTR. To address this, the same collaborative utilized their method coupling thin-layer chromatography to mass spectrometry to evaluate ceramides in cfHBE cells (n=5, at least heterozygous for $\Delta F508$ -CFTR, 12-32 years old, 60% male) and nHBE cells (n=4, ex-smokers, 58-76 years old, 100% male; one additional subject of unknown demographics). As in their previous mouse models, this group found an overall decrease in ceramides in the CF cells, with a concurrent increase in long-chain ceramides and decrease in very-long-chain ceramides (146). This was confirmed in cultured bronchial epithelial cells from CFTR knockout pigs paired to WT pigs (146).

Alternative to these data, there is much support for the original data in which ceramide is increased in CF epithelial cells compared to non-CF cells, and this support comes from multiple groups independently. Ceramide levels were increased via *de novo* synthesis in CFTR knockdown 16HBE cells as compared to control 16HBE cells, as determined by thin-layer chromatography (189). IB3-1 cells (CF) were found by mass spectrometry analysis to have increased ceramide levels compared to C38 cells and 16HBE cells (non-CF) (190; 191). Using immunohistochemistry, the lower airway epithelium of explant lungs from people living with CF (varying and unknown genotypes) had increased ceramide staining

compared to control lungs from unused donors, people with pulmonary hypertension, and people with emphysema (192). Tissue homogenate from these CF lungs also showed increased levels of ceramide as compared to lungs from people with pulmonary hypertension, as determined by mass spectrometry (192). In addition, using both thin-layer chromatography(193) and mass spectrometry separately (194), cfHBE cells were found to have increased ceramides relative to nHBE controls. Co-culture with *P. aeruginosa* increased ceramide levels in both nHBE and cfHBE cells (194). Importantly, these studies evaluated cfHBE cells both homozygous and heterozygous for the $\Delta F508$ -CFTR mutation. Instead of the original theory regarding lysosomal pH, these newest data in primary human bronchial epithelial cells suggest an increase in surface CDase activity and protein expression with a simultaneous decrease in surface sphingomyelinase activity in CF cells, both of which could explain increased ceramide levels (194). However, an increase in the *de novo* synthesis of ceramide, as identified in CFTR knockdown 16HBE cells (189), was not ruled out.

Clearly discrepancies exist in the literature regarding ceramide imbalances in CF cells. Given that multiple groups have found by different methods that ceramides are increased in CF cells, this seems more likely to be the true phenomenon. It is possible that the multi-institutional collaborative consistently finds decreased overall ceramides with an increased ratio of long-chain to very-long-chain ceramides due to their thin layer chromatography coupled to mass spectrometry method, which may somehow introduce biases into the sample. More work should be done to determine the reason for their consistently conflicting results.

Determining the true imbalance is especially important given that two different drugs are currently in clinical trials targeting these two different conclusions regarding ceramide imbalances. Based on the data showing that ceramide is increased in CF and led by the group that initially found this increase, amitriptyline is being explored as a functional acid-SMase inhibitor that decreases ceramide levels. Interestingly, amitriptyline increased FEV₁ and body mass index in people with CF (195; 196). However, amitriptyline is a tricyclic antidepressant with many effects. Furthermore, amitriptyline inhibits acid-SMase by accumulating in the lysosome and inducing its dissociation from the lysosomal membrane, causing its degradation (197). This very nonspecific mechanism likely affects other lysosomal membrane-associated proteins, as has been shown with other tricyclic antidepressants (198).

Based on the data showing that ceramides overall are decreased but the long-chain to very-long-chain ratio is increased in CF, led by the multi-institutional collaborative, the retinoic acid derivative fenretinide is being explored as a novel treatment mechanism for CF. In Phase I trials, fenretinide restored the ceramide imbalance detected in blood samples (186). In mice, it was found to decrease the bacterial burden of CF mice acutely infected with *P. aeruginosa* (185). In CFBE41o- cells, fenretinide re-balances ceramide levels by decreasing ceramide synthase 5 activity while maintaining ceramide synthase 2 activity. However, the study does not report any differential expression of ceramide synthases in CF cells compared to non-CF controls, leaving the underlying mechanism still unclear.

Understanding the mechanism by which loss of CFTR function leads to an imbalance in ceramide species, how this imbalance affects the disease state, and how to correct the imbalance are important future steps toward developing new alternative treatments for CF. This is especially true given studies that show that ceramide accumulation can explain many of the symptoms of CF. For example, ceramide is known to trigger apoptosis by inducing release of cytochrome c from the mitochondrial membrane, and thus increased basal levels of ceramide could lead to a state of increased apoptosis (176; 199-201). Ceramide is thought to be a major cause of fibrosis, as decreasing ceramide levels via genetic deletion of acid-SMase or functional inhibition of acid-SMase with amitriptyline (limitations discussed above) decreases lung fibrosis in CF mice (202). Normalization of ceramide levels via genetic or pharmacological functional inhibition of acid-SMase negates some of the CF phenotypes in mice, leading to a recovery of macrophage-mediated killing of bacteria, a decrease in the number of neutrophils in the lung, decreased cell death, decreased DNA deposition in the airway, and decreased interleukin-1 β (IL-1 β) levels (160; 203; 204). Furthermore, decreasing ceramide concentrations by treating CF cells with recombinant acid-CDase decreased tumor necrosis factor α and IL-8 levels, again suggesting an anti-inflammatory effect of reducing ceramide levels via this enzyme (194). Importantly, though, note that these studies were all conducted by the same group. Lastly, blocking ceramide synthesis (but also synthesis of its down-stream molecules) by inhibiting sphingosine palmitoyl transferase with myriocin decreases NF- κ B activation, suggesting an anti-

inflammatory effect of decreasing ceramide levels (190).

1.5.4 *Gangliosides are imbalanced in CF epithelia*

Gangliosides are a type of sphingolipid comprised of a ceramide base and an oligosaccharide headgroup. Importantly, *P. aeruginosa* binds to asialo-monosialotetrahexosylganglioside (asialo-GM1) (205). Asialo-GM1 is increased in the 9HTEo⁻ tracheal epithelial cell line overexpressing the R-domain (functionally inhibiting CFTR, mimicking but not replicating CF), as determined by an anti-asialo-GM1 antibody, as compared to control 9HTEo⁻ cells (206). This could explain the increased adherence of *P. aeruginosa* to these CF epithelial cells (206). Potentially complementary data come from Calu-3 bronchial epithelial cells treated with short hairpin RNA against CFTR (functional knockout, not accounting for defective protein folding or trafficking), which show reduced GM1 levels as compared to the control Calu-3 cells, as detected by thin-layer chromatography and cholera toxin B staining (207). It is possible that the GM1 levels were reduced because there was an increased conversion into asialo-GM1, but experiments have not been conducted to determine the mechanism of either the decrease in GM1 or the increase in asialo-GM1. Importantly, though, this reduction of GM1 seemed to cause decreased β 1-integrin signaling and delayed wound repair in the Calu-3 cells, as treatment with exogenous GM1 recovered this signaling and delayed repair (207). More work is necessary to better understand the imbalance of these lipids, the mechanism by which loss of CFTR function leads to the imbalance, and the clinical relevance of this imbalance.

1.5.5 *Sphingosine and sphingosine-1-phosphate are imbalanced in CF epithelia*

Ceramide is degraded by CDase into a free fatty acid and sphingosine, an antimicrobial lipid (Figure 1.6) (208). Based on anti-sphingosine antibody staining, *in situ* kinase assays, and mass spectrometry analysis sphingosine is decreased in freshly-isolated human nasal epithelial cells from people with CF compared to non-CF cells and in both gut-corrected and total CFTR knockout (with residual CFTR function) mouse trachea as compared to WT controls (208; 209). Mass spectrometry analysis found

similarly decreased sphingosine levels in whole lung tissue of $\Delta F508$ -CFTR-expressing mice as compared to WT-CFTR-expressing mice (210). Again, analysis of whole lung mouse tissue and mouse models in general should be considered lightly, given the diverse cellular composition of tissue homogenate as well as the limitations of mouse models for representing human CF disease. In support of all of these data, recent mass spectrometry analysis in HBE cells as well as pig explant tissue found decreased sphingosine levels in CF cells (a heterozygous or homozygous $\Delta F508$ -CFTR for human, CFTR knockout for pig) as compared to non-CF cells, which was partially corrected by 24 hr VX770/VX809 treatment in the human cells (146).

The mechanism for the observed decreased sphingosine mass has not been determined. Part of the reason for this reduced sphingosine may be the increased levels of its precursor, ceramide. Ceramide platforms cluster and modify the activity of beta-1-integrin, causing a downregulation of acid-CDase (209). Importantly, rescue of sphingosine levels by inhalation of acid-CDase or sphingosine itself prevented pulmonary *P. aeruginosa* infection in CFTR knockout mice, indicating that it is an important molecule for antibacterial resistance (208).

Contrary to these data, recent work from the same laboratory that identified decreased sphingosine in CFTR knockout mice and freshly isolated human nasal epithelial cells found no difference in sphingosine levels (as detected by mass spectrometry) between cfHBE and nHBE cells, until the introduction of *P. aeruginosa* (194). However, in nHBE cells, *P. aeruginosa* infection resulted in an increase in sphingosine levels, which was not detected in cfHBE cells. This loss of sphingosine accumulation following infection in cfHBE cells could be explained by a loss of increased acid-CDase protein expression that was detectable in nHBE cells. As mentioned above, though, treating nHBE or cfHBE cells with recombinant acid-CDase did not affect sphingosine levels, regardless of infection status (194). This could be due to rapid metabolism of sphingosine into another lipid.

Sphingosine is phosphorylated by sphingosine kinases into S1P (Figure 1.6), a signaling lipid generally associated with proliferation and antagonization of apoptosis (211). S1P initiates many different signaling cascades via extracellular activation of its five GPCR receptors (S1PR₁-S1PR₅), with S1PR₃ being

the most highly expressed receptor in HBE cells (211; 212). S1P is decreased in total lung homogenate of Δ F508-CFTR-expressing mice as compared to WT-CFTR-expressing mice (210).

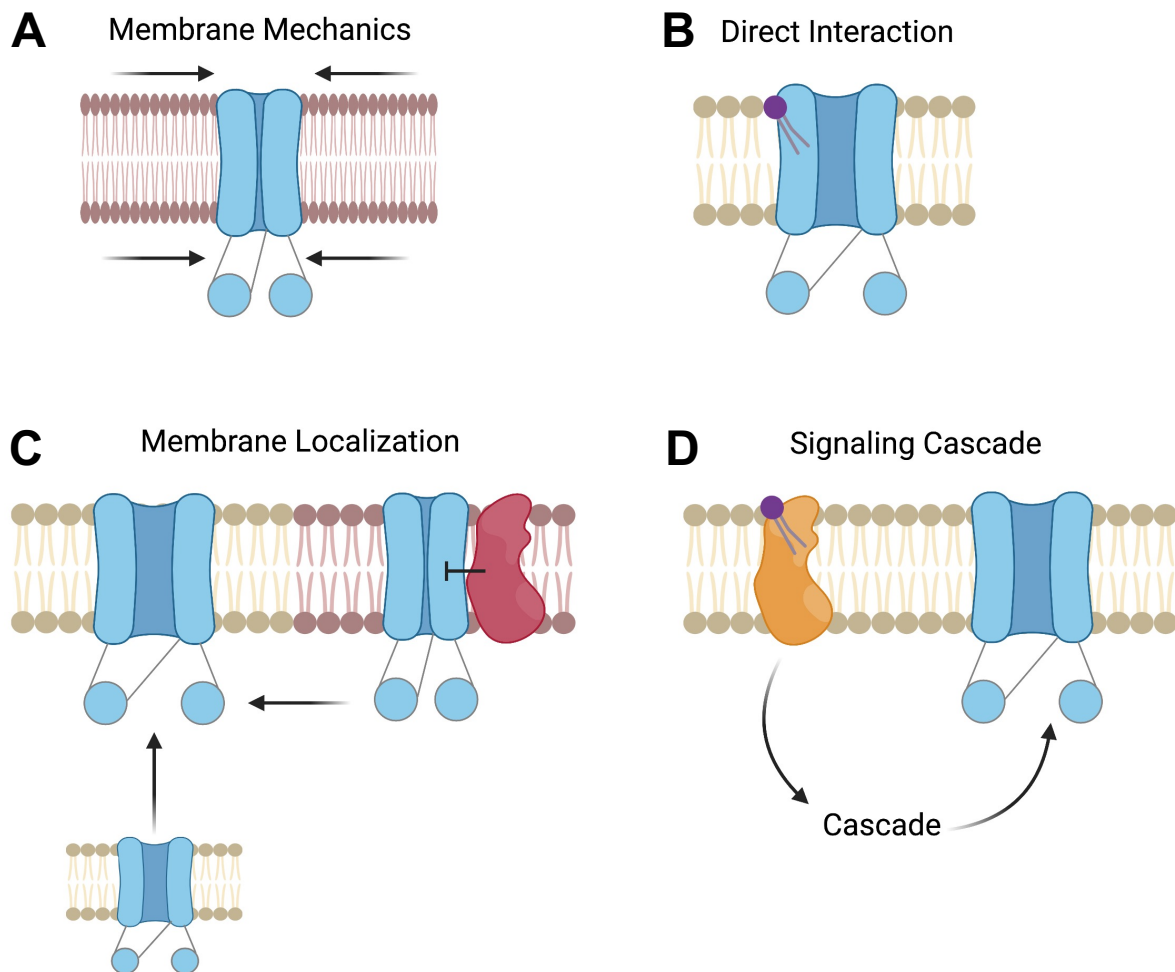
Importantly, CFTR is thought to import S1P, sequestering it from its S1PRs. CFTR transports S1P into the cell independently of its chloride channel function in C127 mouse mammary epithelial cells (213). Unfortunately, this study did not test the S1P transport of a gating mutant such as G551D-CFTR, but rather focused on the trafficking mutant Δ F508-CFTR. If S1P transport occurs independently of the chloride channel activity, it is important to know if S1P transport is altered in CFTR gating mutants as well, and whether this function is sensitive to the known small-molecule CFTR modulators described above. Furthermore, it was not determined whether CFTR directly transported S1P or if it facilitated S1P transport via another mechanism. S1P has been found to be decreased in the Δ F508-CFTR-expressing mouse model, as compared to the WT-CFTR-expressing model, as determined by mass spectrometry (210). Increasing S1P levels by inhibiting its breakdown via a S1P lyase inhibitor led to decreases in inflammatory cytokines such as interferon γ and IL-10 back to non-CF levels.

Given all of the information laid out in this section, it is important to understand if current modulator therapies rebalance sphingosine and/or S1P levels and whether rebalancing of these lipids reduces susceptibility to bacterial infection, which is a major concern for people with CF.

1.6 How lipids generally affect membrane protein activity

It is important to discuss well-characterized interactions between lipids and membrane proteins, which could hint at possible lipid-CFTR interactions that have yet to be characterized. There are four main ways by which lipids can affect ion channels: through alterations of membrane mechanics such as fluidity, by direct allosteric interactions, by changing their surface localization, and by changing signaling cascades that modify the protein (Figure 1.7). Frequently, these mechanisms overlap, making it hard to define the system fully. Still, we will attempt to explore each individually using representative examples that illustrate the concept.

Figure 1.7: A graphical representation of the ways by which lipids can affect membrane protein activity. These mechanisms include **(A)** mechanical properties of the membrane, such as its stiffness, **(B)** direct interactions between lipids and the channel, **(C)** the localization of the channel either within the cell or the plasma membrane, and **(D)** initiation of a signaling cascade that affects channel activity. The membrane protein of interest in this case is drawn to look like a CFTR channel (light blue) that can be active (open) or inactive (closed). This figure was made using BioRender.



1.6.1 *Lipid-dependent membrane mechanics affect membrane protein activity*

Lipids can affect membrane protein activity by altering characteristics of the membrane environment such as hydrophobic thickness, curvature, and flexibility. All membrane proteins have an optimal transmembrane-domain length. Bilayers that are too thick or too thin can shift the hydrophobic contacts of the protein, causing either the protein, the lipid bilayer, or both to deform to minimize exposure of hydrophobic surfaces to water (214; 215). Besides thickness, deformation can occur by pressure exerted by the curvature of the membrane as well. Deformation of the protein may cause a change in the activity of that protein, perhaps by promoting protein conformations that enhance or decrease function. Furthermore, ion channels are conformationally dynamic proteins; whenever a channel opens, it deforms the membrane around it to make room for a pore through the channel. These membrane deformations include stretching, compressing, or bending the bilayer or protein (215-217). Deformation of the membrane or protein requires energy, and the amount of energy depends in part on the flexibility of the “annular lipids” immediately surrounding and interacting with the membrane protein. Thus, the immediate lipid environment of a transmembrane protein may affect protein activity based on the mechanical stress it encounters.

This is exemplified by the bilayer deformations associated with the conformational movements of the sarco endoplasmic reticulum Ca^{2+} -ATPase (SERCA1) (218). X-ray crystallography studies of SERCA1 incubated with soybean PC and octaethyleneglycol mono-*n*-dodecyl ether detergent were integrated with solvent contrast modulation experiments to resolve the protein and its surrounding bilayer in four different reaction states (1: two Ca^{2+} associated, 2: two Ca^{2+} and ATP associated, 3: transition state where two Ca^{2+} and ADP and P_i are associated, and 4: phosphorylated protein stabilized with inhibitor thapsigargin). The resulting SERCA1 structures were then simulated in a 1,2-dioleoyl-sn-glycero-phosphocholine (DOPC) bilayer. Transitioning between State1 and State3, the protein tilts 18°. The tilting between each state causes distortion of the surrounding membrane. A certain amount of membrane flexibility is required to accommodate this massive movement of SERCA1 while maintaining hydrophobic contacts. Lack of flexibility therefore theoretically would lead to an inhibition of SERCA1 function.

The interplay between SERCA1 and membrane flexibility serves an example of the overarching

principle that membrane mechanics, dictated by the lipids comprising the membrane, affect membrane protein activity. This concept has not yet been applied to CFTR when studying its activity but is of vital importance to gathering a more complete understanding of CFTR.

1.6.2 Direct allosteric lipid interactions affect membrane protein activity

In addition to affecting membrane mechanics, lipids can affect membrane proteins by directly binding to them. One interesting example of direct lipid interactions affecting ion channel activity involves the inwardly rectifying potassium channel 2 (Kir2), as studied by the Levitan laboratory. These channels localize to cholesterol-rich microdomains (219). However, cholesterol seems to inhibit these channels, as enriching cells with cholesterol by treating them with cholesterol-loaded methyl- β -cyclodextrin (M β CD) caused whole-cell Kir2 currents to decrease. Inversely, depleting cells of cholesterol by treating them with empty M β CD caused whole-cell Kir2 currents to increase (219; 220). Based on single-channel recordings, the overall decrease in current caused by cholesterol is due to some channels being locked closed, as the surface expression and single-channel properties seemed not to be drastically affected. Instead, the number of patches apparently containing a channel decreased, implying that some of the patches had channels that simply never opened (219; 220).

To determine if the inhibitory effects of cholesterol were specific, cholesterol was exchanged with its stereoisomer epicholesterol by treating cells with epicholesterol-loaded M β CD. Epicholesterol will maintain the mechanical properties but not the direct binding properties of cholesterol. This replacement of cholesterol with epicholesterol caused an increase in whole-cell Kir2 currents, similar to simply removing cholesterol, implicating a stereo-specific inhibitory interaction between cholesterol and Kir2 channels (220). This inhibition of Kir2 by cholesterol is based on a direct interaction of cholesterol with the channel, likely in the middle of the transmembrane domain based on docking simulations, molecular dynamics simulations, and mutational studies (221). Interestingly, this binding domain varies from the cholesterol recognition amino acid consensus (CRAC) sites found in other ion channels and from the other cholesterol binding sites identified in other membrane proteins (222-224).

Cholesterol's direct binding and effect on activity of Kir2 channels exemplifies one of many direct allosteric interactions that lipids can have with membrane proteins, how that interaction can affect a protein's activity, and how experiments can be set up to determine the interaction.

1.6.3 Lipid-mediated membrane surface localization affects membrane protein activity

Additional to what has been discussed thus far, lipids can affect surface localization of proteins. Surface localization of a protein involves at least two major concepts: (1) the total amount of protein in the plasma membrane to elicit its effect, and (2) the relative distribution of the protein within specific microdomains of the plasma membrane, which can affect colocalization with modulator and/or effector proteins. Cholesterol, as an example, impacts both of these properties for many membrane proteins. Regarding the first concept, removal of cholesterol in mouse cortical collecting ducts with M β CD caused a decrease in basal ENaC activity due to a decrease in the number of channels present at the cell surface, as determined by surface biotinylation experiments (225).

Regarding the second concept, cholesterol affects the localization of PDZ domain-containing proteins within the plasma membrane. A PDZ domain binds the PDZ binding-domain motif of another target protein (226-228). Generally, there are multiple PDZ domains within a single protein, allowing the PDZ-domain-containing protein to act as a scaffold to bring two or more proteins with PDZ binding-domain motifs into proximity. Frequently, these PDZ domains contain a CRAC cholesterol-binding sequence, and those that do bind cholesterol tend to depend upon this lipid to localize to the plasma membrane (229). Thus, cholesterol is important for localizing some PDZ-interacting proteins such that they can perform their intended scaffolding function in the correct membrane. One important PDZ domain-containing scaffold protein to consider is the sodium-hydrogen antiporter 3 regulator 1 (NHERF1), which binds CFTR (among other proteins) and stabilizes its localization to cholesterol-rich microdomains (230; 231).

Again, cholesterol serves just as an example of one way in which lipids can affect membrane protein localization, and how that membrane localization can affect the apparent activity of the protein. This is an important concept to keep in mind in studying the effects of lipids on CFTR.

1.6.4 Lipid-mediated signaling cascades affect membrane protein activity

An extremely important mechanism by which lipids can affect membrane protein activity is by initiating signaling cascades. To examine this concept, ceramide platforms will be discussed. Ceramide platforms are related to lipid rafts, which are enriched in sphingomyelin and cholesterol, in that ceramide can be generated from sphingomyelin and these ceramide platforms exclude cholesterol (173). Localization to these platforms can alter protein activity. For example, apoptosis antigen 1 (APO-1) is activated when localized to ceramide-rich platforms (174). Activation of APO-1 initiates a signaling cascade ultimately leading to cell apoptosis. Ceramide and some of its derivatives activate many different signaling cascades. For example, in oligodendrocytes, ceramide inhibits Kir channels via Ras and protein kinase C (PKC), both of which interact with Raf-1 (232). The ceramide derivative S1P can bind to and activate one of five GPCR proteins to initiate a signaling cascade as well (211).

As seen by these examples, since lipids are able to affect membrane protein activity by activating signaling cascades, it is important to study the potential lipid imbalances in CF and how they can affect the signaling cascades involved in modulating CFTR activity. The literature regarding this subject will be reviewed in section 1.7.

1.6.5 How lipids interact with ABC transporters

Since CFTR is an ABC transporter (ABCC7), knowledge about the lipid interaction of the larger ATP transporter family may be useful to understanding lipid interactions with CFTR. Many ABC transporters transport lipids, including cholesterol, phospholipids, and sphingolipids. Importantly, these lipid transporters come from all different subfamilies; a subset of these transporters and their substrates are listed in Table 1.3 (233; 234).

Aside from serving as transported substrates, lipids can have a large impact on ABC transporter stability and function (235). Focusing on ABCB1 (multidrug resistance protein 1, P-glycoprotein 1) as an example, it is known that specific phospholipids have differential effects on ABCB1's ATPase activity.

Table 1.3 A list of some ABC transporters, their lipid substrates, and their associated diseases

Name	Substrate(s)	Disease
ABCA1	cholesterol and phospholipids	Tangier
ABCA4	N-retinylidene-phosphatidylethanolamine	Stargardt
ABCA7	phosphocholine and sphingomyelin	Alzheimer's
ABCB1	glucosylceramides and phospholipids	Inflammatory Bowel Disease
ABCB4	phosphatidylcholine	Progressive Familial Intrahepatic Cholestasis 3
ABCC1	glucosylceramide, sphingomyelin, and sphingosine-1-phosphate	
ABCC1-ABCC4	bile salts	ABCC2: Dubin-Johnson Syndrome
ABCD1-3	fatty acyl-CoA	ABCD1: Adrenoleukodystrophy
ABCG1 ABCG2	sterols	

The ATPase activity of ABCB1 protein extracted from CHO cells (to 90% purity) was determined by a colorimetric assay measuring production of inorganic phosphate. Specifically, some uncharged phospholipids (1,2-dimyristoyl-sn-glycero-phosphoethanolamine (DMPE), 2-dipalmitoyl-sn-glycero-phosphoethanolamine (DPPE), and egg PC) had stimulatory effects while negatively charged phospholipids (phosphatidylserine (PS) and phosphatidylinositol (PI)) had inhibitory effects (236). Interestingly, using isotopic inorganic phosphate and two-dimensional high-performance thin-layer chromatography, this paper also identified that PS, PE, and a little PC (along with an unidentified lipid) were co-purified with ABCB1 protein. This relative composition varied greatly from the total plasma membrane lipid composition, indicating a tight and specific association of ABCB1 with these lipids. In another study using human ABCB1-containing membrane vesicles from Sf9 cells, depletion of cholesterol with M β CD treatment resulted in a significant decrease in basal ATPase activity of ABCB1 (237). Repletion of cholesterol recovered this ATPase activity. Further studies on purified human ABCB1 (95% pure) reconstituted into 4:4:2 PC:PE:PS liposomes with varying concentrations of cholesterol confirmed that cholesterol increased basal ATPase activity (238). These authors confirmed that isotopic cholesterol co-purified with ABCB1 through affinity pull-down and size exclusion chromatography. Interestingly, the cholesterol analogue cholesterol hemisuccinate was found to thermally stabilize ABCB1 (239). Thus, these data indicate that ABCB1 is tightly bound to many lipids, and that these lipids affect the activity of this ABC transporter protein.

ABCB1 is not the only ABC transporter affected by lipids, and not all ABC transporters are affected in the same way by the same lipids. ABCG1 has no activity in detergent, but recovers activity once reintroduced into liposomes (240; 241). Conversely, ABCA4 has less ATPase activity once introduced to lipids (242). ABCG2's ATPase activity is stimulated by cholesterol (243; 244). The exact mechanism by which these lipids affect the activity of ABC transporters is not fully understood. Structural data will be needed to confirm possible direct interactions. Currently, only a few structures of human ABC transporters other than CFTR have been solved at high resolution. Of the solved structures, ABCG2 (PDB 6HIJ) has cholesterol and 1,2-dioleoyl-sn-glycero-phosphoethanolamine (DOPE) bound (245), and ABCB10 has

cardiolipin (PDB 3ZDQ, 4AYT, 4AYX) or cholesterol (PDB 4AYW) and n-dodecyl β -D-maltoside (DDM) detergent bound (246). More work is required to improve methods of purifying and imaging other ABC transporters with potential lipid interactors. Since CFTR is an ABC transporter, the refinement of these methods will facilitate a better understanding of CFTR as well, which is important to understanding CFTR in its endogenous lipid environment.

1.7 How lipids can affect CFTR

1.7.1 *Detergents and membrane lipids affect CFTR stability and ATPase activity*

Whereas all ABC transporters are difficult to work with, CFTR is notoriously difficult to purify for biochemical and biophysical studies, in part because of its propensity to aggregate and its instability in solution (247-250). This instability is influenced by several factors. One issue is that CFTR is a membrane protein with 12 membrane-spanning helices. At the same time, CFTR has large intracellular domains that prefer the aqueous solvent that the hydrophobic regions reject. Nonetheless, some recent successes have led to important new structural insights for this channel.

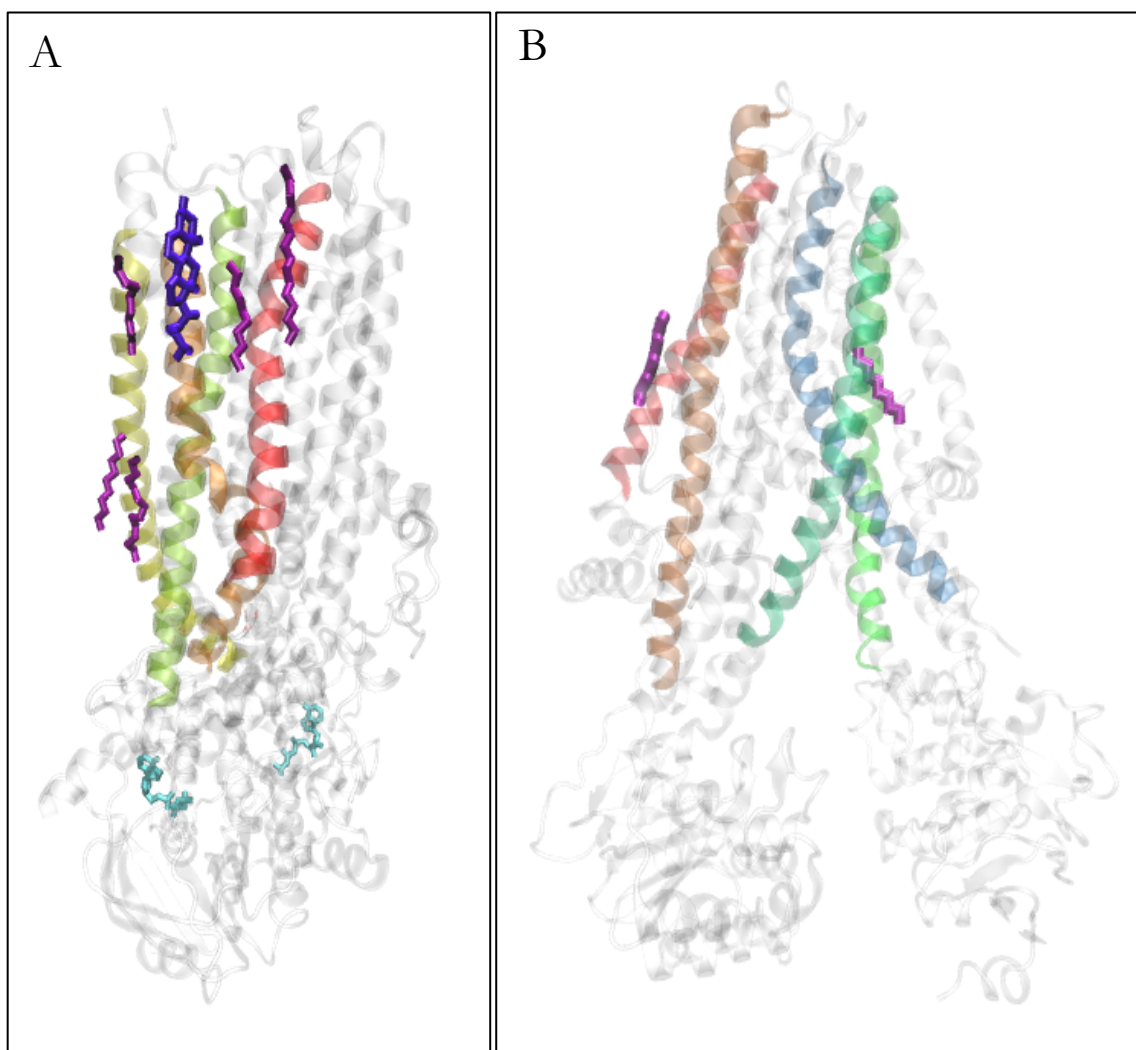
Currently, the highest-resolution structures of CFTR have come from the Chen lab using single-particle cryo-EM (Table 1.4). All six of these CFTR structures were purified initially in 0.2-0.25% cholesteryl hemisuccinate (CHS) and 1-1.25% 2,2-didecylpropane-1,3-bis- β -D-maltopyranoside (LMNG). It is important to note a critical downfall to these current CFTR structures – none of the outward-facing structures are actually open, as they do not have a conducting pore that spans the entire thickness of the membrane. This issue of these structures lacking a complete pore is compounded by the fact that the purified CFTR itself was never assessed for ion channel activity. It would make sense for the E1371Q-CFTR stabilized mutant to have incomplete channel activity, as this removes the ATP hydrolysis function which is required to reach the full conducting state (251). However, even the WT-CFTR that was used for the closed structures was not assessed for ion channel function or ATPase activity after purification. Thus, it is unknown whether the purification process denatured CFTR to any extent, and whether this explains the lack of a pore in the final structures.

Table 1.4. The current high-resolution structures of CFTR from the Chen lab

Origin	Mutation	State	Resolution	Year	PDB ID
Human	-	Dephosphorylated, Apo-ATP, inward-facing	3.87 Å	2017	5UAK (42)
Human	E1371Q	Phosphorylated, ATP-bound, outward-facing	3.2 Å	2018	6MSM (43)
Human	E1371Q	Phosphorylated, ATP-bound, outward-facing, Ivacaftor- bound	3.3 Å	2019	6O2P (70)
Human	E1371Q	Phosphorylated, ATP-bound, outward-facing, GLPG1837- bound	3.2 Å	2019	6O1V(70)
Zebrafish	-	Dephosphorylated, Apo-ATP, inward-facing	3.73 Å	2016	5UAR (252)
Zebrafish	E1372Q	Phosphorylated, ATP-bound, outward-facing	3.37 Å	2017	5W81 (51)

Interestingly, lipids appear in a few of the CFTR structures described above, either co-purified from the cell or introduced during purification. The phosphorylated, outward-facing human CFTR shows a cholesterol molecule bound toward the top of the transmembrane domain, associated with transmembrane helix 3 (TM3) (Figure 1.8A) (43). Importantly, the more recently released phosphorylated, outward-facing human CFTR bound to modulator GLPG1837 shows a cholesterol bound to the same spot (70). While CFTR is predicted to have eight cholesterol binding sites according to molecular docking simulations against the inward-facing zebrafish CFTR structure (253), none of these sites match the site of bound cholesterol observed in the outward-facing human CFTR structures. There are also five hydrocarbon chains of varying lengths bound to the outward-facing human CFTR structure that were also seen bound to the same pockets in the outward-facing human CFTR structure bound to the CFTR potentiator GLPG1837 (43; 70). Three of the hydrocarbons were bound toward the top of the transmembrane domain (thus likely from the outer leaflet of the plasma membrane), and two were bound toward the bottom (thus likely from the inner leaflet). There were also six hydrocarbon chains associated with the outward-facing human CFTR structure bound to VX770, with most of them in the same pockets as the other structures (70). The hydrocarbons are likely the only resolved portions of larger phospholipids, which would have had to come from the original human embryonic kidney cell plasma membrane from which CFTR was purified since phospholipids were not added during purification process. The inward-facing zebrafish CFTR structure also shows two hydrocarbon chains (Figure 1.8B) (252). One chain is external, associated with TM1 and TM2. The other chain is pushed into the second transmembrane domain a bit, interacting with TM9, TM10, and TM12. Neither of these hydrocarbon chains match any of the binding locations of the chains in the human structure discussed above. It should, however, be noted that the human structure is outward-facing, whereas the zebrafish structure is inward-facing. It is possible that the lipid interactions change based on the state of the channel, as noted above for SERCA1 (218). However, this remains uncertain as specific lipids were not seen in the inward-facing human or the outward-facing zebrafish CFTR structures. Future experiments should work toward understanding the effect(s) that these cholesterol molecules and acyl chains have on the structure and function of CFTR.

Figure 1.8: Cryo-EM structures of CFTR with resolved lipids bound. (A) A representation of phosphorylated, ATP-bound human CFTR (PDB: 6MSM), with TM1 in red, TM3 in orange, TM4 in yellow, TM6 in yellow-green, and ATP colored cyan. The lipids are opaque, with cholesterol colored violet, and other lipids colored purple. (B) A representation of dephosphorylated, apo-ATP zebrafish CFTR (PDB: 5UAR), with TM1 in red, TM2 in dark orange, TM9 in green, TM10 in blue-green, and TM12 in grey-blue. The lipids are opaque purple.



Further evidence of important lipid-CFTR interactions comes from the observation that adding a 4:1 (w/w) ratio of 1-palmitoyl-2-oleoyl-sn-glycero-3-phosphocholine (POPC) to 1-palmitoyl-2-oleoyl-sn-glycero-3-phosphoethanolamine (POPE) to anionic detergents helped stabilize isolated NBD1 of CFTR (254). Though POPC and POPE may stabilize NBD1, molecular docking simulations indicate that the NBDs preferentially bind the PS head group over the PC or PE headgroups (255). Furthermore, 1-palmitoyl-2-oleoyl-sn-glycero-3-phosphoserine (POPS) stabilized full-length CFTR more than POPC or POPE and conferred higher ATPase activity to CFTR than POPC or POPE (255). Interestingly, this study also demonstrated that brain PS, comprised of mostly C₁₈ acyl chain lengths, helped CFTR maintain an eight-fold higher ATPase activity than any previously reported and a 10-12°C higher thermal stability than detergent alone. Importantly, this increased stability seems to be the reason for the increased ATPase activity. Given that PS is prevalent in the plasma membrane, this interaction is likely physiologically relevant. This phenomenon is important to understand, as the most common CF mutation (Δ F508) is a deletion of a residue in NBD1 which causes destabilization of the entire protein (256; 257).

1.7.2 *Arachidonic acid affects CFTR activity*

As mentioned above, arachidonic acid levels are increased in CF cells as compared to control. This is an important context to consider, as the effect of arachidonic acid on CFTR activity is complex and still incompletely understood. In detached membrane patches from Calu-3 pulmonary epithelial cells, intracellularly applied arachidonic acid inhibited PKA-activated CFTR (258). Further studies suggested that arachidonic acid directly inhibited CFTR by inserting itself into the pore from the cytoplasmic face, interacting with the positively charged residues K95 and R303 (259). Identification of these amino acids required mutating residues into an uncharged alanine, a polar glutamine, and a negatively charged glutamate, and then determining the dissociation constant (K_d) for arachidonic acid-mediated inhibition of these mutant CFTRs. However, there is no information regarding the effect of these mutations on single-channel CFTR activity in the absence of arachidonic acid, which is important to consider. For example,

K95E, which induces the highest apparent K_d for arachidonic acid, may just stabilize the open state of CFTR rather than prevent arachidonic acid from blocking the pore. If arachidonic acid is not acting as a pore blocker but rather as an allosteric modulator, mutations stabilizing the open state would cause an apparent increase in K_d for arachidonic acid. Furthermore, K95 and R303 are known to be important for conducting anions through CFTR, along with R104, R117, K335, and R352, although these likely do not function as chloride binding sites, *per se* (260-262). Still, this proposed mechanism for arachidonic acid blocking may be plausible since five other open-channel blockers utilize the K95 residue as well (260).

To complicate the story further, arachidonic acid does not always inhibit CFTR. In polarized Calu-3 monolayers, extracellularly applied arachidonic acid slightly activated CFTR currents via a cyclooxygenase and/or arachidonate 5-lipoxygenase metabolite (263). This extracellular application of arachidonic acid is physiologically relevant, as arachidonic acid is released from the cell after activation with adenosine, which is present in sufficient levels in CF sputum (264). The mechanism by which activation occurs has not been determined. The validity and relevance of the activating and inhibiting effects of arachidonic acid on CFTR are vital to understand given that studies have found elevated arachidonic acid in CF cells (see section 1.5.1). Furthermore, it is important to determine if docosahexaenoic acid has the inverse effect on CFTR. Understanding these effects will help researchers determine the lipid feedback loops present in CF, potentially uncovering new therapeutic targets that address multiple aspects of the disease and that interrupt detrimental feedback loops or support helpful feedback loops.

1.7.3 *Ceramide and its derivatives affect CFTR activity*

The effect of ceramide on CFTR activity is also complex and incompletely understood, in part because ceramide and its derivatives are involved in so many signaling cascades, depending in part on the fatty acid chain length, which also controls the effects on membrane mechanics. Whereas data discussed earlier indicate that there may be a ceramide chain length imbalance in CF, unfortunately research up to this point has not specifically accounted for ceramide chain length when evaluating the direct effects of ceramide on CFTR activity. This is something the field should consider moving forward. Regardless of this,

the majority of data suggest that ceramide is increased in CF pulmonary epithelial cells. Thus, the effects of ceramide on CFTR are extremely relevant to understand.

In *Xenopus* oocytes, bacterial SMase inhibits WT-CFTR and, to a lesser degree, CFTR with the R-domain deleted (265; 266). In studies from our lab, bath-applied SMase inhibited CFTR-mediated chloride currents in a cell-attached patch clamp configuration, that is when the electrode pipet was sealed to the plasma membrane, thus isolating those channels within the membrane patch from the bath solution while the currents through the patch were recorded (266). Importantly, in this experiment, SMase never came into direct contact with the CFTR in the patch, or with the lipids surrounding CFTR, yet SMase still caused an inhibition of CFTR currents. However, when we performed an excised patch experiment, that is when the patch of plasma membrane was pulled off from the rest of the cell, thus isolating the recorded membrane patch from the intracellular components, application of SMase to the solution within the pipet directly contacting the external leaflet of the plasma membrane caused no inhibition of CFTR (266). If ceramide or phosphocholine directly inhibited CFTR, or if removal of sphingomyelin directly inhibited CFTR, or if SMase itself directly inhibited CFTR, there would have been inhibition of CFTR currents in the isolated membrane in the excised patch experiments. Given that the cell-attached configuration seems to be important for inhibition, we hypothesized that SMase interacting with lipids outside of the patch induced a signaling mechanism that was transmitted to the CFTR channels within the patch. Furthermore, we found that the efficacy of SMase-mediated inhibition of CFTR decreased as the level of phosphorylation-mediated activation increased, and SMase-mediated inhibition was hindered by mutations stabilizing the open-state of CFTR (265; 266). This led us to hypothesize that in this *Xenopus* oocyte system, SMase acts on a closed state of CFTR, not the open state. Yet still, VX770, the only clinically approved CFTR potentiator, could not recover SMase-mediated inhibition of CFTR.

Importantly, we also showed that SMase decreases transepithelial CFTR currents in primary mixed bronchial/tracheal epithelial cells collected from human non-CF lung explant tissue and primary bronchial epithelial cells from human CF (homozygous $\Delta F508$ -CFTR) lungs (266). Furthermore, VX770 could not recover SMase-mediated inhibition of CFTR currents in these cells (266). The mechanism evaluated in the

Xenopus oocyte studies may not translate to this primary airway epithelial cell model, as the mechanism of inhibition of CFTR by SMase and its metabolites seems to be highly dependent on the cell type. For example, in T84 colonic epithelial cells, ceramide seemed to decrease apical anion secretion by activating c-Jun N-terminal kinase (JNK) which inhibited basolateral cAMP-gated potassium channels (267), which provide a driving force for apical anion secretion (268). In Calu-3 cells, though, ceramide seemed to inhibit cAMP-dependent chloride currents via inhibition of CFTR itself at the apical membrane without affecting basolateral potassium channels (269). This was determined by permeabilizing either the apical or the basolateral membrane to monovalent ions with the pore-forming antibiotic nystatin. When apically permeabilized (circumventing the need for CFTR), ceramide did not inhibit chloride secretion. When basolaterally permeabilized (with CFTR still being required), ceramide still inhibited chloride secretion. The authors for this Calu-3 study ruled out the involvement of protein phosphatase 2A (PP2A), protein phosphatase 1 (PP1), and PKC using inhibitors and activators of these enzymes. PP2A and PP1 are activated by ceramide and are known to inhibit CFTR by dephosphorylating the R-domain (270-273), PKC is generally inhibited by ceramide and can both potentiate and inhibit CFTR, depending on which serine of the R-domain it phosphorylates (45; 274). No definite mechanism for inhibition of CFTR by ceramide in Calu-3 cells has been identified.

In contrast to both T84 and Calu-3 cells, in BHK cells, the ceramide metabolite S1P inhibits CFTR (275). In this system, S1P activates AMPK, which phosphorylates S737 of the R-domain of CFTR, a known inhibitory post-translational modification (275-277). The involvement of AMPK along with other canonical signaling pathways is called into question in *Xenopus* oocytes, though, as SMase inhibits a CFTR construct without an R-domain (265; 266), which is the site of almost all known post-translational phosphorylation events regulating CFTR activity (44; 278; 279). Post-translational modifications outside of the R-domain or on accessory proteins become more likely mechanisms in this case. Clearly, if we are to understand the mechanism driving SMase-mediated inhibition in primary bronchial epithelial cells, the cell type of most relevance in CF, we need to carefully consider which cell lines and/or cell types we are using.

However, contrary to these studies finding inhibition of CFTR by ceramide, a recent study reports

activation of CFTR by ceramide. The authors found that treatment of nHBEs with vasoactive intestinal peptide (VIP) (triggering a cAMP and a calcium response) and carbachol (triggering a calcium response) led to both activation of CFTR and also generation of ceramide platforms, within which CFTR accumulated (280). Interestingly, the generation of these platforms appeared to be due to activation of acid-SMase on the surface of the cells. Treatment with amitriptyline to functionally inhibit acid-SMase (thus preventing an increase in ceramide) reduced CFTR activity, possibly due to decreased CFTR stability at the cell surface and therefore increased internalization. However, considering that the acid-SMase involved in ceramide platform generation was already located at the cell surface along with the understanding that amitriptyline acts by facilitating the degradation of lysosomal acid-SMase, the proposed mechanism by which amitriptyline affects surface acid-SMase activity and CFTR currents remains uncertain.

Ceramide and its derivatives activate many signaling cascades, but the specific enzymes involved in SMase-mediated inhibition of CFTR have not been determined in many cell types. The mechanism by which CFTR inhibition via SMase occurs in primary pulmonary epithelial cells is important to understand, especially since the clinical therapeutic VX770 cannot recover the channel activity. Furthermore, given that ceramide is imbalanced in CF and has an effect on the activity of CFTR, the cycle of CFTR dysfunction, ceramide imbalance, and the effect of ceramide on CFTR needs to be understood to elucidate any feedback loops that are disrupted in CF or other inflammatory lung diseases.

1.7.4 Lipid rafts affect CFTR activity

As mentioned previously, lipid rafts are microdomains in cell membranes that are enriched for cholesterol and sphingolipids. Cholera toxin frequently is used to probe for lipid rafts as it binds to GM1, which is abundant in lipid rafts. In murine tracheal epithelial cells, using fluorescent cholera toxin and CFTR antibody as probes, CFTR was found to cluster into GM1-positive lipid rafts or platforms. Importantly, this clustering of CFTR and GM1 remained upon *P. aeruginosa* infection, which seems to cause the conversion of lipid rafts into ceramide platforms at the site of contact at the cell (176).

In Madin-Darby canine kidney cells transfected with GFP-CFTR, CFTR was found by western

blot at a low percentage in the detergent-resistant fraction, which represents the lipid raft component of cell membranes (281). This CFTR was predominantly band C, the fully glycosylated and mature form of CFTR. CFTR also could be found in other fractions of the membrane, although these fractions seemed to have much more band B CFTR, the partially glycosylated form associated with the ER. Approximately 15 min after *P. aeruginosa* infection, the percentage of CFTR in the detergent-resistant fraction increased by approximately 50%, then by 30 min decreased below basal levels. These authors showed that removing cholesterol by treatment with cyclodextrin significantly decreased the amount of CFTR found in the detergent resistant fraction of these cells. This phenomenon also was seen in the Calu-3 bronchial epithelial cell line (282).

All of these data indicate that cholesterol is important for CFTR localization to lipid rafts. Cholesterol is also important for CFTR lateral mobility at the cell surface, in that decreasing cholesterol increases mobility and increasing cholesterol decreases mobility (178). One possible explanation for this involves NHERF1, a protein that binds CFTR via its PDZ domain and stabilizes and immobilizes it at the cell surface while also bringing important proteins such as PKA into proximity of CFTR (230; 231). NHERF1 binds cholesterol very tightly, and loss of this binding decreases the ability of NHERF1 to remain in the plasma membrane. While cholesterol binding does not greatly impact the ability of NHERF1 to bind CFTR, the instability of NHERF1 at the membrane decreases the time it has to interact with CFTR and PKA, thus minimizing their colocalization and ultimately minimizing PKA-mediated activation of CFTR (229). More research into this topic is necessary to fully understand cholesterol's impact on CFTR activity and on the disease severity of CF and other inflammatory lung diseases.

1.8 Summary

It is surprising that more work has not been done to characterize the effect of CFTR on cellular lipid compositions, and *vice versa*. Many other members of the ABC transporter superfamily transport lipids, and mutations in many of these can cause human disease (234). Furthermore, many other ion channels and membrane proteins display altered activity based on the surrounding lipid environment. Given

that many lipids appear to be altered in CF lung epithelial cells, it is of vital importance to identify all of the lipid imbalances in CF and to study the activity of CFTR in this altered lipid state.

In regard to lipid imbalances in CF, experiments should be conducted to identify global lipid imbalances in airway epithelial cells from people with CF as compared to controls, and to determine the mechanisms for these imbalances. These experiments should take into consideration the class of CFTR mutation, so as to parse apart the effects of loss of CFTR's ion channel function from a loss of proper CFTR trafficking. Furthermore, these experiments should determine the effects these lipid imbalances have on the health outcomes of people with CF, and whether any methods of correction of the imbalance could positively impact the health of people with CF. These experiments should also determine if the FDA-approved CFTR modulators rebalance the lipids. Even more specifically, though, experiments should be conducted that identify the specific lipid environment that CFTR experiences. Methods should be refined to purify CFTR in high-yield, high-quality batches that can be used to identify tightly associated lipids.

In regard to lipids affecting CFTR activity, experiments at every level—from the single channel all the way up to a tissue or patient level—are needed to determine how the identified lipid imbalances affect the ability of CFTR to function. It is important that these experiments be validated in a relevant cellular model as well, with bronchial epithelial cells from people being the current gold standard.

Even if CFTR modulators are able to help CFTR function better, if CFTR resides in a lipid environment that is not conducive to its functioning, those modulators are not going to work at their full potential. Improved treatment for CF is urgently needed. An enhanced understanding of CFTR-lipid interactions should not only provide a more accurate model of CF and other chronic lung diseases but may aid in the identification of new drug targets or lead to modulation of current therapies.

CHAPTER 2 – SPHINGOMYELINASE DECREASES TRANSEPITHELIAL ANION SECRETION IN AIRWAY EPITHELIAL CELLS IN PART BY INHIBITING CFTR- MEDIATED APICAL CONDUCTANCE

Preface: Much of the text and figures presented here are reproduced from a portion of a manuscript accepted to *Physiological Reports* in May 2021. There were multiple goals for this manuscript, including 1) determining if SMase decreased transepithelial CFTR currents equally in bronchial and tracheal epithelial cells, 2) screening cell line models to determine if any replicated the primary cell phenotype in response to SMase, 3) determining the apical, basolateral, and paracellular basis of SMase-mediated decreases in transepithelial CFTR current, and 4) determining if FDA-approved CFTR correctors could prevent SMase-mediated decreases in transepithelial currents. I performed all experiments, in some cases with assistance from co-authors or Cores. I also analyzed all data and wrote the manuscript.

It is important to acknowledge the lab of Dr. Joanna Goldberg for the use of their cooled incubator, sonicator, and centrifuge to purify SMase. This work was supported by Georgia Institute of Technology's Systems Mass Spectrometry Core Facility, which performed mass spectrometry lipidomics experiments that I then analyzed. This work also was supported by the CF@LANTA Biorepository and Experimental Models Core, which collected, grew, and differentiated primary pulmonary epithelial cells. These were the cells used for the vast majority of the experiments in this chapter, with the exception of the impedance analysis experiments which utilized cells grown in the Dr. Robert Bridges laboratory.

- **Cottrill KA**, Peterson RJ, Lewallen CF, Koval M, Bridges RJ, & McCarty NA. 2021. Sphingomyelinase decreases transepithelial anion secretion in airway epithelial cells in part by inhibiting CFTR-mediated apical conductance. *Physiol Report*. Accepted.

2.1 Introduction

As discussed above, CFTR is an anion channel present in epithelial cells throughout the human body. CFTR, located at the apical side of airway epithelial cells, is activated by phosphorylation by the cAMP-activated PKA, and is gated by the binding and hydrolysis of ATP (15; 41). Loss-of-function mutations in CFTR cause the lethal genetic disease known as CF (38; 39). Most commonly, people living with CF die of pulmonary failure caused by dehydration of the airspace, chronic inflammation, bronchiectasis, mucus buildup, and chronic lung infections (21; 283). While some therapeutics have been developed that target the primary CFTR defect, as discussed in section 1.3, these therapeutics do not fully recover CFTR channel function (284; 285). A better understanding of how CFTR functions in the pulmonary epithelial cell environment is necessary for the development of more efficacious treatment strategies for CF and other lung diseases.

Membrane proteins such as CFTR depend on their membrane lipid environment, a fact that is often neglected experimentally due to difficulties in controlling and examining this environment. It is possible that a perturbation of the cellular lipid environment could affect the function of CFTR, as has been seen in other ion channels and as is discussed in section 1.6 (225; 286; 287). Specifically, we and others have previously found that the bacterial virulence factor SMase, which breaks down membrane-localized sphingomyelin into ceramide and phosphocholine, has an inhibitory effect on CFTR-mediated transepithelial currents in airway epithelial cells (266; 269). We also found that the only clinically approved CFTR potentiator, VX770/ivacaftor, did not rescue this loss of channel activity in clinically relevant primary airway epithelial cells both from non-CF and CF donors (266). The precise mechanism by which SMase decreases these transepithelial currents is not known at present.

Sphingolipids are involved in regulation of cell physiology, including cell growth and apoptosis, among other things (288; 289), and their roles in inflammatory lung diseases have been reviewed in more detail elsewhere (289). Understanding the sphingolipid imbalance caused by SMase is clinically relevant to many chronic lung diseases. It has been found in bronchial epithelial cells that oxidative stress, present in many inflammatory lung diseases (290; 291), increases the activity of endogenous neutral-SMase (292;

293). Furthermore, proinflammatory factors such as tumor necrosis factor α and lipopolysaccharide promote the secretion and activation of acid-SMase from lung epithelial cells (294; 295). However, endogenous SMase is not the only source of this enzyme. The two bacteria most commonly found in the CF lung, *P. aeruginosa* and *S. aureus* (21), both secrete enzymes with SMase activity (296; 297).

Given the relevance of these sphingolipid imbalances, more work was needed to understand the mechanism of SMase-mediated inhibition of transepithelial CFTR currents. A monolayer of bronchial epithelial cells has many components that contribute to transepithelial currents (Figure 2.1). Decreased transepithelial anion currents such as observed after treatment with SMase could be due to a loss of chloride or bicarbonate conductivity through the apical side of the cell, a loss in the driving force facilitated by ion channels on the basolateral side of the cell, a change in the paracellular shunt pathway, or some combination of these. Furthermore, it is unknown whether this mechanism is consistent between nHBE and cHBE cells, and whether it is a robust effect that is observed across cells from many donors or from other regions of the lung. The goal of the work presented here was to understand in more detail the mechanism by which SMase decreases transepithelial anion currents in primary airway epithelial cells.

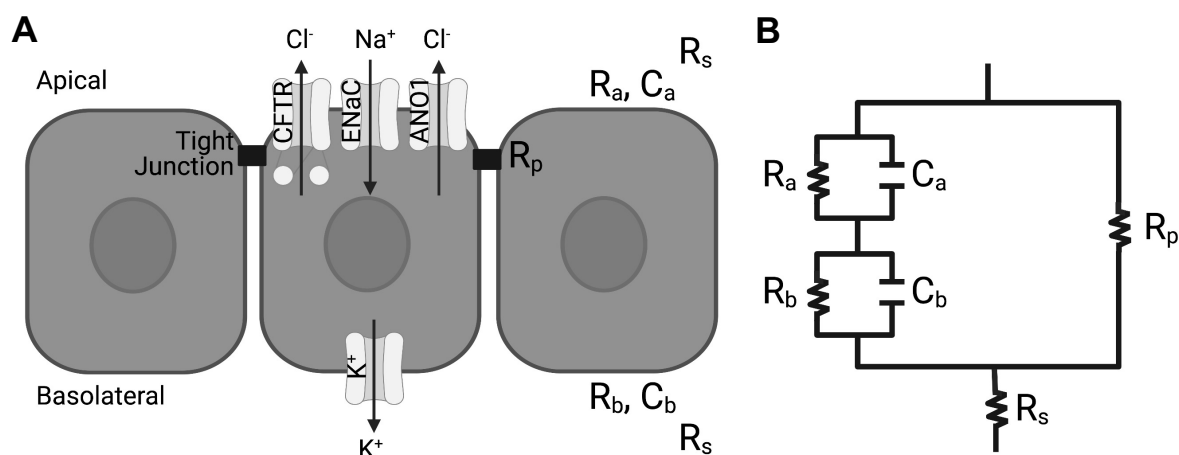
2.2 Materials and methods

Unless otherwise specified, chemical reagents were purchased from MilliporeSigma.

2.2.1 Airway epithelial cells from human donors

Two different methods for preparing and culturing primary airway epithelial cells were used. One of these methods is based on work from the Randell laboratory (137), and has been used previously in our laboratory (266). Primary bronchial (HBE), tracheal (HTE), and mixed bronchial/tracheal airway (HAE) cells were isolated from human donor lung explants under an institutional review board (IRB)-approved protocol through the CF@LANTA Experimental Models Core. Cells were plated on Costar 3470 plates (0.4 μ M pore size, polyester, Corning), and after two days were transitioned to air-liquid interface (ALI) and differentiated in medium based on the previously described ALI medium formulation (137),

Figure 2.1. A model of a bronchial epithelial monolayer (A) is shown alongside the representative circuit diagram (B). The cells are grey rectangles, the channels are light grey, the tight junctions are black rectangles, and the directionalities of ion flow are black arrows. The apical and basolateral capacitances are C_a and C_b , respectively. The apical resistance (R_a) is affected predominantly by the apical channels CFTR, ENaC, and anoctamin 1 (ANO1). The basolateral resistance (R_b) is affected predominantly by the basolateral potassium channels. The paracellular resistance (R_p) is due to tight junctions between the cells. The series resistance (R_s) is driven by the composition of the buffer and the resistance of the plastic filter on which the cells are supported. The apical resistor and capacitor are in parallel with one another, as are the basolateral resistor and capacitor. The apical components are in series with the basolateral components. The paracellular resistor is in parallel with both the apical and basolateral components, while the solution resistor is in series with the entire circuit. This figure was made using BioRender.



with modifications to glucose (150 mg/dL; 8.3 mM), CaCl₂ (1 mM), heparin (2 µg/ml), L-glutamine (2.5 mM), hydrocortisone 960 mg/ml, bovine pituitary extract (20 µg/ml) and Mg²⁺ (0.5 µM). Once cultures were at ALI, the medium was changed every 48-72 hr and cultures were allowed to differentiate for at least 3 weeks. For cfHBE cells, which were from donors homozygous for the ΔF508 mutation, CFTR was corrected either by temperature shift to 27 °C accompanied with addition of 3 µM VX809 (Selleckchem) for 24 hr, or by treatment with 18 µM VX661 (Selleckchem) and 5 µM VX445 (Selleckchem) for 48 hr.

Impedance measurement experiments described below were conducted using nHBE and cfHBE cells which were cultured using the Vertex method (138). The HBE cells were plated on Costar 24-well high-throughput screening filter plates (0.4 µm pore size, polyester, Corning) and grown at ALI in HBE differentiation medium containing 2% Ultrosor-G for five to seven weeks. Medium was replaced on the basolateral side three times a week. To remove accumulated mucus, the apical surface was washed with 70 µL of freshly made 3 mM dithiothreitol (DTT) in PBS for 30 min. Cells were washed 72 hr later with 70 µL of PBS for 30 min, 24 hours before the functional measurements. For impedance measurements, specifically, trafficking of ΔF508-CFTR in cfHBE cells was corrected with 6 µM C18 (VRT-534, an analog of VX809) for 24 hr prior to the experiment (298).

2.2.2 *Calu-3 and 16HBE bronchial epithelial cell culture*

For Ussing Chamber experiments, Calu-3 cells (ATCC[®] HTB-55[™]) were grown as described previously (269). Cells were plated at 150,000 cells/well on Costar 3470 plates using DMEM medium with 10% fetal bovine serum (FBS) (Atlanta Biologicals), 2 mM L-glutamine (Corning), 50 I.U./mL penicillin (Corning), and 50 µg/mL streptomycin (Corning). The apical medium was removed one day after plating, and the cells were allowed to continue to polarize for 5-7 days. The basolateral medium was replaced every 48-72 hr during this polarization period.

16HBE cells were grown similarly to Calu-3 cells, except that MEM medium (Gibco) was used as a base and the cells were grown in submersion culture on Transwells for 5-7 days.

2.2.3 Purification of bacterial SMase

WT and enzyme-dead H322A *S. aureus* SMase with an N-terminal 6x histidine tag were purified from BL21 (DE3) *E. coli* bacteria by recombinant expression from a pET28b vector (Novagen) similarly to previous methods (266). Bacteria were grown with 50 µg/mL kanamycin sulfate (Thermo Fisher), induced with 0.1 mM isopropyl β-d-1-thiogalactopyranoside, and incubated at 16 °C overnight. Bacteria were pelleted, then resuspended in PBS (Boston Bio Products) with 1:100 protease inhibitor cocktail. Bacteria were lysed by sonication, and insoluble material was pelleted at 11,000 x g for 30 min at 4 °C. The soluble material (supernatant) was incubated overnight at 4 °C with Roche cOmplete™ resin, washed, and equilibrated according to the manufacturer's protocol. The resin was washed five times with wash buffer at 4 °C. Resin was incubated for 30 min at 4 °C in three column volumes of elution buffer. This elution fraction was collected, and an additional three column volumes of elution buffer was added to the beads for 5 min at 4 °C. These elution fractions were pooled, diluted to 4 mg/mL, and dialyzed in 1 L wash buffer in 12-24 hr increments using Spectrum Labs Float-A-Lyzers® with 0.1 kDa molecular weight cutoff until the calculated concentration of imidazole was below 1 nM. SMase purity was evaluated by a Coomassie-Blue staining following sodium dodecyl sulfate-polyacrylamide gel electrophoresis. Final protein concentration was determined by a Thermo Scientific Pierce™ bicinchoninic acid assay kit in accordance with the manufacturer's protocol. Specific activity of 100 ng of SMase protein at room temperature over 30-40 min was determined by a Molecular Probes® Amplex® Red SMase activity assay in accordance with the manufacturer's protocol, using a plate reader (SpectraMax® M2e, Molecular Devices). Note that SMase is added basolaterally in this study, as we and others have shown that WT SMase has no effect when applied apically (266). We have shown that WT SMase does not hydrolyze apical sphingomyelin (266).

2.2.4 Lipidomics mass spectrometry

All chemical reagents in this section are from Thermo Fisher, unless otherwise noted. Polarized HBEs were collected from Transwell filters by scraping with a pipet tip, pelleted at 500 xg for 10 min, flash-frozen with liquid nitrogen, and stored at -80 °C. Pellets were resuspended in 100 µL isopropyl alcohol

and subjected to three freeze-thaw cycles using liquid nitrogen and ice bath sonication. After each extraction, samples were dried in a SpeedVac vacuum concentrator and reconstituted with the reconstitution solvent, detailed below, at a ratio of $3.33\text{E-}4$ $\mu\text{L}/\text{cell}$. Reconstituted samples were sonicated for 5 min and centrifuged at $21,100 \times g$ for 5 minutes. The supernatant was transferred to autosampler vials, sealed, and stored at $4\text{ }^{\circ}\text{C}$ until analysis. For quality control purposes, a pooled sample was created by mixing an equal volume from each sample. A sample blank was created by following the above procedure without cells.

Ultra-performance liquid chromatography coupled to mass spectrometry (UPLC-MS) was performed using a Vanquish system, an AccucoreTM C30 column (2.1×150 mm, $2.6\text{ }\mu\text{m}$ particle size), and an Orbitrap ID-X Tribrid mass spectrometer system. The chromatographic method for sample analysis involved elution with solutions including: Mobile Phase A (40:60 water:acetonitrile (ACN), 10 mM ammonium formate, 0.1% formic acid); Mobile Phase B (10:90 ACN:IPA (A461-4), 10 mM ammonium formate, 0.1% formic acid). The following gradient program was used at a flow rate of $0.40\text{ mL}/\text{min}$: 0 min 80% A, 1 min 40% A, 5 min 30% A, 5.5 min 15% A, 8 min 10% A, held 8.2 min to 10.5 min 0% A, 10.7 min 80% A, and held until 12 min. The column temperature was $50\text{ }^{\circ}\text{C}$, and the injection volume was $5\text{ }\mu\text{L}$. The heated electrospray ionization source was operated at a vaporizer temperature of $275\text{ }^{\circ}\text{C}$, spray voltage of 3.5 kV , and sheath, auxiliary, and sweep gas flows of 40, 8, and 1, respectively. The instrument acquired full MS data in the $150\text{-}2000\text{ m}/z$ range in positive ionization mode. UPLC-MS/MS experiments were performed by acquiring mass spectra in a data-dependent fashion. MS/MS were collected with a resolution of 120,000 and the dd-MS2 were collected at a resolution of 30,000, an isolation window of $0.8\text{ m}/z$, and a cycle time of 2 s. Stepped normalized collision energies of 15, 30, and 45 were used to fragment selected precursors in the HCD cell prior to combination of ion for analysis in the orbitrap. Dynamic exclusion was set at 2.5 s. Ions with charges >2 were omitted.

Data acquisition and processing were carried out using Compound DiscovererTM V3.0. After processing, peak areas were scaled by the median peak area of the sample. Annotation of the dataset was achieved by MS2 spectral matching to a local spectral database, built from curated experimental data. In addition, accurate mass, retention time, and isotopic pattern were matched to database entries.

Standards were obtained from Avanti Polar Lipids, Inc., including the following, listed with their final target concentration diluted in Optima™ chloroform: 160 µg/mL 15:0-18:1(d7); 5 µg/mL 15:0-18:1(d7) PE; 5 µg/mL 15:0-18:1(d7) PS; 30 µg/mL 15:0-18:1(d7) PG; 10 µg/mL 15:0-18:1(d7) PI; 25 µg/mL 18:1(d7) LPC; 5 µg/mL 18:1(d7) LPE; 350 µg/mL 18:1(d7) Chol Ester; 10 µg/mL 15:0-18:1(d7) DG; 55 µg/mL 15:0-18:1(d7)-15:0 TG; 30 µg/mL 18:1(d9) SM; 100 µg/mL Cholesterol (d7). The reconstitution solution was prepared by diluting the stock solution and Deuterated Ceramide LIPIDOMIX™ Mass Spec Standard (d18:1-d7/16:0, d18:1-d7/18:0, d18:1-d7/24:0, d18:1-d7/24:1(15Z)) to 1.66% and 0.22% v/v, respectively, in isopropanol.

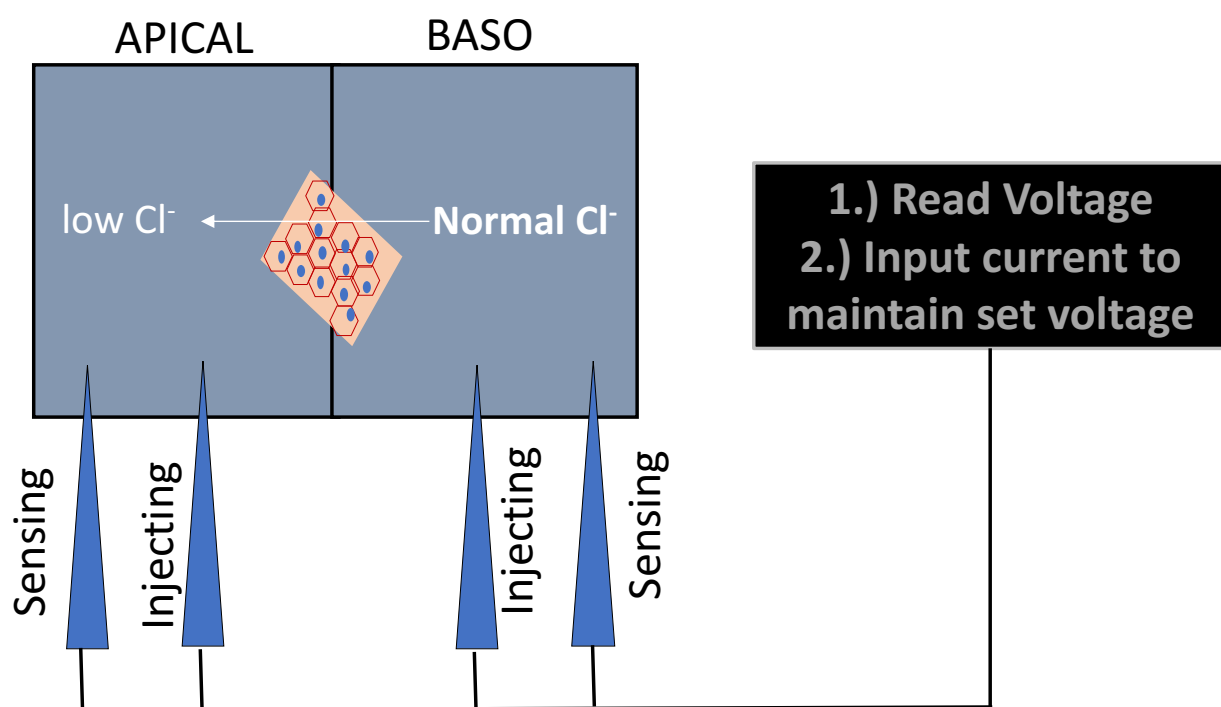
Peak areas were normalized to a blank tube, lipid standards, and the median peak intensity of all identified features. Data are reported either in bar graphs with the normalized peak area on the y-axis, or as volcano plots with the $-\log$ (unadjusted P value) on the y-axis and the difference in the normalized peak intensities on the x-axis. A 5% false discovery rate was applied using the two-stage step-up method of Benjamini, Krieger, and Yekutieli (299), as recommended by PRISM. Statistical values were considered significant if both the P value and the Q value were less than 0.05. In the volcano plots, points that had a significant P value but not a significant Q value are notated as open circles, rather than solid circles.

2.2.5 *Short-circuit current measurements*

Transepithelial short-circuit current experiments using an Ussing Chamber were performed as described previously (73; 266). The setup of these experiments is represented in Figure 2.2. Specifically, a monolayer of epithelial cells grown on permeable plastic supports are inserted into the chambers such that their basolateral side faces to the right and their apical side faces to the left. This monolayer separates the two chambers, so any ions – and thus any current – moving between the chambers must be moving through the monolayer (transepithelial). This movement can be paracellular (between cells) or transcellular (through cells). In the Ussing chamber, there are two electrodes on either side of the monolayer, with one sensing and the other manipulating the transepithelial voltage. The computer controlling these electrodes determines the current needed to maintain a transepithelial voltage of 0 mV, also known as short-circuit conditions.

Figure 2.2. A graphical model of transepithelial short-circuit current analysis with an Ussing chamber.

The monolayer of epithelial cells is represented in the light pink box, with connecting red-outlined hexagons defining the cell borders and blue circles defining the nucleus of the cells. The basolateral portion of the monolayer faces to the right, and the apical portion faces to the left. Each side of the cells has two electrodes, one sensing voltage and one injecting current. These electrodes are connected to a computer that monitors and manipulates the voltage with current injection. The basolateral side of the monolayer is exposed to a buffer with a biologically relevant concentration of chloride (described in more detail below). The apical side of the monolayer generally is exposed to a buffer with low concentrations of chloride, facilitating chloride movement from the basolateral to the apical side of the cells.



The negative value of this injected current is the transepithelial short-circuit current (I_{sc}). To obtain the transepithelial resistance, Ohm's Law is utilized, which states that voltage is equal to current multiplied by resistance ($\Delta V = \Delta I \times R$). The computer periodically applies a voltage clamping protocol (± 5 mV) to the system, monitoring the change in transepithelial current required to reach this new voltage, and then calculates the transepithelial resistance using Ohm's Law.

To perform transepithelial short-circuit current analyses A VCC MC6 multichannel voltage/current clamp with a U100 converter, EasyMount containment systems, P2300 chambers, DM MC6 input modules, P2024-40 electrode leads, P2020-S electrode sets, P2020 electrode tips, and P2302T Transwell sliders were obtained from Physiologic Instruments. Acquire & Analyze software was used to collect data. The amplifier was set to voltage-clamp at 0 mV to record short-circuit currents.

Bath buffer was prepared according to the recipe described previously (269). Normal chloride buffer was 115 mM NaCl, 5 mM KCl, 1 mM MgCl₂, 2 mM CaCl₂, 10 mM glucose, 10 mM HEPES, 25 mM NaHCO₃, pH 7.4. Low chloride buffer was 115 mM Na gluconate, 5 mM KCl, 1 mM MgCl₂, 4 mM CaCl₂, 10 mM glucose, 10 mM HEPES, 25 mM NaHCO₃, pH 7.4. In most cases, a chloride gradient was applied by adding the normal chloride buffer basolaterally and the low chloride buffer apically. Chambers were bubbled with O₂:CO₂ 95:5% and maintained at 37 °C during experiments.

Cells were stabilized for 30 min prior to treatment with 1 µg/mL WT or H322A (inactive mutant) SMase basolaterally for 30 min. To inhibit ENaC-mediated sodium currents, 20 µM amiloride was added to the apical side of cells. To generate cAMP to stimulate CFTR, 0.01-10 µM forskolin was added to both sides of the cells. To potentiate CFTR currents, 1 µM VX770 (Selleckchem) was added to both sides of the cells. To inhibit CFTR, 10 µM INH172 was added to the apical side of cells. The currents elicited by each treatment were calculated as the average of the final ten seconds prior to the next treatment.

2.2.6 Impedance measurements

Impedance analysis experiments were performed as described previously (300; 301). The goal of impedance analysis experiments is to determine apical and basolateral resistances and capacitances of an

epithelial cell monolayer in a non-destructive manner. This is superior to microelectrode experiments, in which an individual cell must be punctured with small electrodes, damaging the monolayer and providing only a single-cell measurement.

For impedance analysis experiments, 1 hr prior to experiments, cells were switched to HEPES-buffered (pH 7.4) F12 Coon's modified medium at 37°C without CO₂. This plate was transferred to a 37 °C plate warmer on an automated robotic platform. Transepithelial voltage (V_T) and resistance (R_T) of all 24 wells were measured simultaneously every 3 minutes using a MTECC24 (Multi Transepithelial Current Clamp (EP Design, Belgium)). A reference plate in a separate 37 °C plate warmer on the same robotic platform was used to measure the offset potential of the electrodes between measurements of the cell plate. Impedance was measured every 3 min at 126 frequencies ranging from 1 to 10,000 Hz, fitting only the 1-8,000 Hz range. Cells were stabilized for 15 min prior to basolateral addition of 1 µg/mL WT or H322A SMase. After 30 min of SMase treatment, at least 6 µM benzamil was added apically to inhibit ENaC. After 18 min, 10 µM forskolin and 1 µM VX770 were added to activate and potentiate CFTR currents. The values 30 min after addition of forskolin and VX770 are reported.

A monolayer of epithelial cells was modeled as in Figure 2.1. The impedance data were plotted as Nyquist diagrams. Custom software, developed in the Bridges Laboratory (300), was used to fit these Nyquist plots to solve for R_a , R_b , C_a , and C_b using the following system of equations

$$Z_t = R_s + \frac{A(j\omega)^{1-\theta} + B}{C(j\omega)^{2(1-\theta)} + D(j\omega)^{(1-\theta)} + 1}$$

$$A = \frac{R_p [R_a (R_b C_b)^{(1-\theta)} + R_b (R_a C_a)^{(1-\theta)}]}{R_a + R_b + R_p}$$

$$B = \frac{R_p (R_a + R_b)}{R_a + R_b + R_p}$$

$$C = \frac{R_p (R_a C_a R_b C_b)^{(1-\theta)}}{R_a + R_b + R_p}$$

$$D = \frac{\{R_b(R_a C_a)^{(1-\theta)} + R_a(R_b C_b)^{(1-\theta)} + R_p[(R_a C_a)^{(1-\theta)} + (R_b C_b)^{(1-\theta)}]\}}{R_a + R_b + R_p}$$

, where Z_t is the impedance at a given time, R_s is the solution resistance, j is $\sqrt{-1}$, ω is the frequency of the sine wave, θ is the phase angle of the sine wave, and R_p is the paracellular resistance (302).

In order to fit these equations to the Nyquist plot, an initial estimate value for R_p , the inverse of paracellular conductance (G_p), is needed. Many current-voltage relationship experiments performed previously in the Bridges laboratory revealed that in nHBE and cfHBE cells, following the addition of benzamil to inhibit ENaC and forskolin/VX770 to activate CFTR, (G_p) is 71% of the transepithelial conductance (G_T) (*data not shown*).

Lastly, it must be assumed that the basolateral membrane time constant (τ_b), equal to the product of resistance and capacitance, is larger than the apical membrane time constant (τ_a). Microelectrode experiments have determined that basolateral resistance is larger (301; 303). Furthermore, since membrane capacitance is based on membrane surface area, thickness, and lipid composition, and since the basolateral membrane has a larger surface area than the apical membrane, it is safe to assume that the basolateral capacitance is larger than the apical capacitance (304). These considerations, in addition to pharmacological studies targeting the apical and the basolateral membrane, indicate that τ_b is larger than τ_a (301).

With all of the assumptions discussed here, the software can successfully iteratively solve for the values of R_a , R_b , C_a , and C_b to determine the best fit for the impedance data. The bound for these values were 5-10000 $\Omega\text{-cm}^2$ for the resistances, 0.1-20 $\mu\text{F/cm}^2$ for C_a , and 0.1-60 $\mu\text{F/cm}^2$ for C_b . Seed values were 60 $\Omega\text{-cm}^2$ for R_a , 410 $\Omega\text{-cm}^2$ for R_b , 2.5 $\mu\text{F/cm}^2$ for C_a , and 19 $\mu\text{F/cm}^2$ for C_b . The best-fit values are reported within this manuscript.

2.2.7 Calcein flux assay

Paracellular flux was measured using calcein (305; 306). Krebs Ringers HEPES (KRH) buffer was 150 mM NaCl, 2 mM CaCl_2 , 1 mM MgCl_2 , 10 mM glucose, 10 mM HEPES, pH 7.4. Cells were washed

once with KRH, then left at 37 °C in fresh KRH buffer, with or without 3 mM EGTA to disrupt tight junctions for 90 min. To the basolateral side of the cells, 500 μ L of fresh KRH buffer (with or without 3 mM EGTA) with 1 μ g/mL H322A or WT SMase was added. From this, 100 μ L were immediately collected as the 0 min timepoint, and a fresh 100 μ L with the appropriate SMase treatment was added back to the basolateral side. To the apical side, 200 μ L of KRH with 20 μ g/mL calcein (Invitrogen) was added. Cells were maintained at 37 °C, and 100 μ L of basolateral buffer was collected and replaced every 15 min over the course of 1 hr. Collected basolateral buffer was maintained in a black well, clear bottom, Costar 96-well plate protected from light. After all time points were collected, the 96-well plate was read with a Spectromax[®] M2e plate reader with excitation and emission wavelengths of 485 and 515 nm, respectively, to determine the relative transepithelial flux of calcein.

2.2.8 Statistical analyses

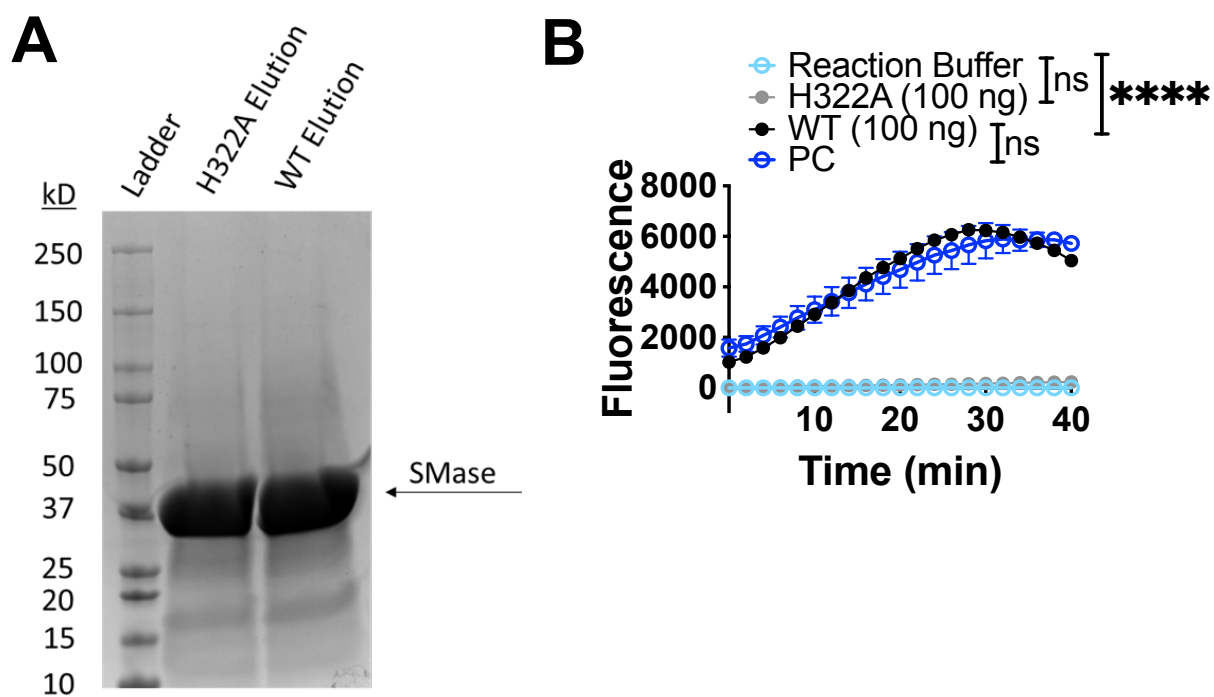
Data were exported to and processed in Excel, unless otherwise noted. Statistical analyses were conducted and graphs were made using GraphPad PRISM software, with α set at 0.05 according to common practice. Data were excluded based on Grubb's outlier tests with an α of 0.05, or in cases of technical experimental issues. In all cases, data are represented as the mean and standard deviation, unless otherwise noted. In many cases, the individual data points are also plotted. Specific statistical tests as well as the significance values are listed in the figure legends, including unpaired, two-tailed *t* tests; multiple *t* tests without correction; and two-way ANOVAs, utilizing the Tukey correction recommended by PRISM if multiple comparisons were used.

2.3 Results

2.3.1 WT SMase affects the sphingolipid profile in nHBE cells

As a control for our WT SMase treatment, enzyme-dead H322A SMase was purified in parallel to account for any co-purified proteins. The WT and H322A SMase preparations appear identical in purity, in which SMase is by far the most dominant band (Figure 2.3A). H322A SMase was confirmed to have no detectible

Figure 2.3. Mutant H322A SMase is a good negative control for WT SMase. (A) H322A or WT SMase, purified as described in section 2.2.3, was intentionally overloaded for an SDS-PAGE experiment to show impurities. Total protein in the gel was stained with Coomassie blue. SMase (37 kD) is the most prominent band by far, but there are other co-eluted proteins. (B) SMase activity was assessed by an Amplex Red assay. The generation of fluorescent product over time was compared between groups by multiple two-way ANOVAs. H322A SMase (filled grey circle, n= 4) had no detectible activity above the reaction buffer control (open light blue circle, n=4) ($p=0.0718$), while WT SMase activity (filled black circle, n=4) was detected over the reaction buffer ($****p<0.0001$), and WT SMase activity was not distinguishable from the phosphocholine positive control group (open dark blue circle, n=4) ($p=0.8478$).



SMase activity (Figure 2.3B). In order to determine the sphingolipid profile of polarized nHBE cells, and how that profile changes with SMase treatment, cells were treated basolaterally with 1 $\mu\text{g/ml}$ WT SMase or H322A SMase control for 30 min prior to extraction of cell lipids for analysis by lipidomics mass spectrometry (266). Preliminary experiments on polarized Calu-3 bronchial epithelial cells were performed to determine if a simple isopropyl alcohol extraction was as efficient at extracting sphingolipids of interest as the ethyl acetate method previously outlined (185; 307). In fact, we found that isopropyl alcohol was more efficient than ethyl acetate at extracting sphingomyelins and ceramides, and thus this method was used for the remainder of the experiments (Figure 2.4). Only sphingolipids confirmed at a Schymanski confidence level 3 or higher were assessed (308). The highest abundance sphingomyelins identified in nHBE cells were the d34:1, d42:2, and d36:1 species (Figure 2.5A).

Our mass spectrometry instrumentation did not allow for the distinction between the sphingosine tail and the fatty acid chain of the sphingomyelins studied. However, the highest abundance ceramide species (d18:1/16:0, d18:1/24:1, and d18:1/18:0) likely correspond to the highest abundance sphingomyelin species (d34:1, d42:2, and d36:1) (Figure 2.5C). This hypothesis is supported by correlating the decrease in sphingomyelin species to the increase in the corresponding ceramides after WT SMase treatment, which results in a 0.9806 R^2 value (Figure 2.5E). The relative abundance of these three species of ceramides in bronchial epithelial cells generated by WT SMase was similar, but not identical, to previous studies from other labs (186; 309; 310). In nHBE cells, WT SMase treatment decreased the abundance of all sphingomyelin species by $54.3 \pm 2.3\%$ (SEM) while increasing all ceramide species by $144.6\% \pm 9.6\%$ (SEM) (Figure 2.5B,D). Because WT SMase decreased all sphingomyelins and increased all ceramides, we could not parse out any specific sphingolipid interactions caused by WT SMase treatment. Note also that WT SMase added to the apical side of bronchial epithelial cells elicits no effect, and we have found previously that, for a yet undetermined reason, WT SMase does not hydrolyze sphingomyelin on the apical side of the cells (266).

Figure 2.4. Isopropyl alcohol (IPA) extracts sphingolipids more efficiently than ethyl acetate (EtOAc) extraction. Lipidomics mass spectrometry of Calu-3 bronchial epithelial cells treated basolaterally with 1 $\mu\text{g}/\text{mL}$ enzyme-dead H322A SMase identified **(A,B)** sphingomyelins and **(C,D)** ceramides. Sphingolipids either were extracted with the IPA method described in section 2.2.4 (black, $n=2$), or with ethyl acetate (EtOAc) method described previously (grey, $n=2$) (185; 311). **(A,C)** The peak amplitudes were normalized as described in section 2.2.4, and data were analyzed by multiple t tests with a 5% false discovery rate. **(B, D)** Volcano plots of the differences between the H322A and WT SMase treatments, with the $-\log(\text{P value})$ on the y-axis and the difference between the averages of the normalized peak areas on the x-axis are shown. The horizontal dotted line ($-\log(\text{P value})=1.30$) indicates the significance cutoff, above which a species is considered significantly different. This significance area is highlighted with a green box. All sphingomyelins and ceramides of interest were significantly more abundant when extracted with IPA. This method was thus what we used moving forward.

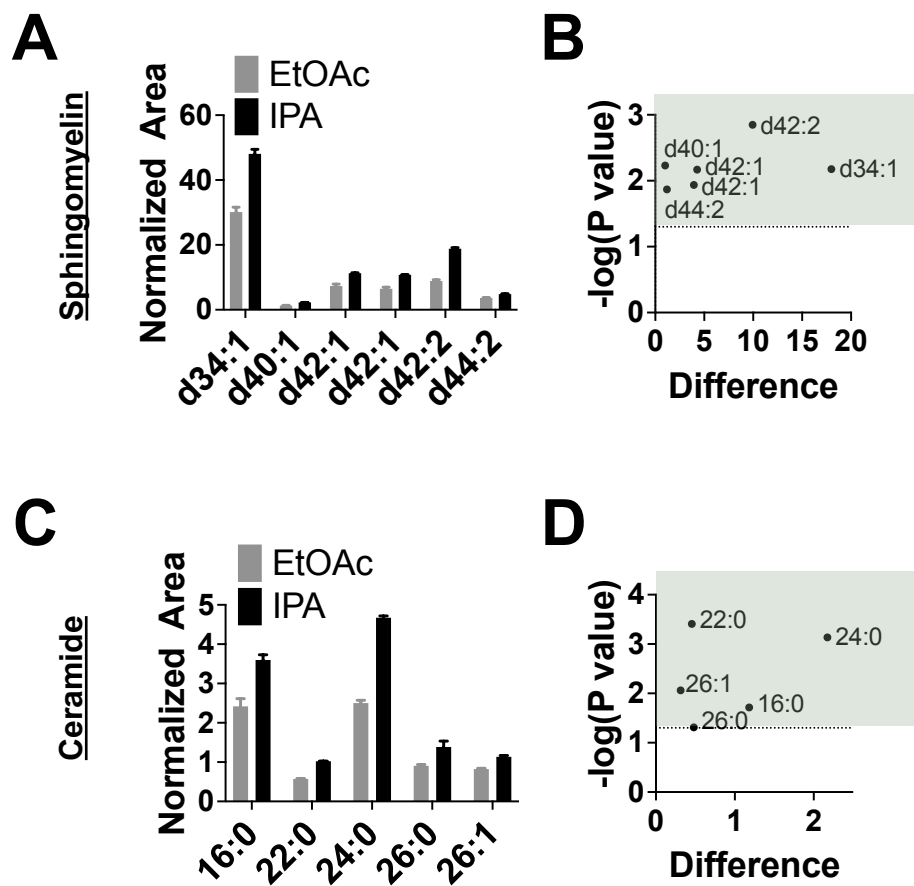
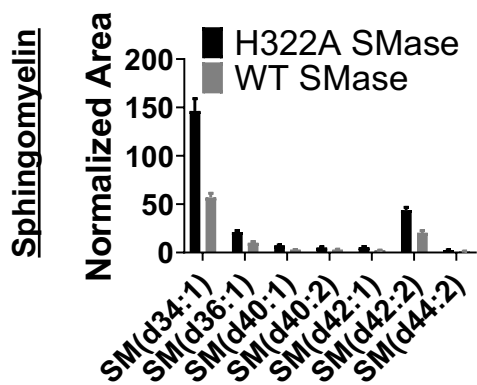
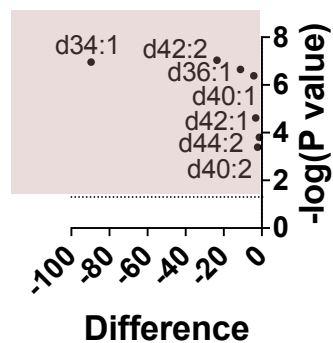
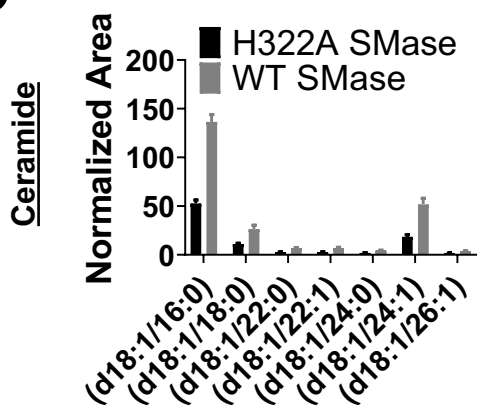
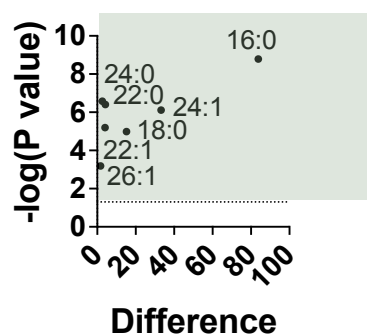
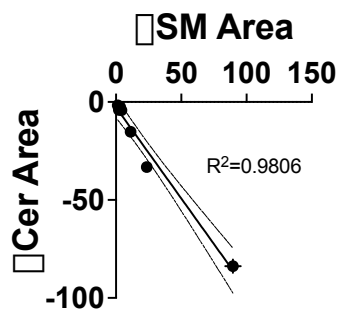


Figure 2.5. SMase reduces all sphingomyelins and increases all ceramides in nHBE cells. Lipidomics mass spectrometry revealed **(A, B)** a reduction of sphingomyelins (SM) and **(C, D)** an increase of ceramides nHBE cells (a single biological replicate is shown) treated basolaterally with WT SMase (grey, n=5), as compared to enzyme-dead H322A SMase control (black, n=6). **(A, C)** The means and standard deviations of the peak amplitudes (normalized as described in section 2.2.4) are shown. Data were analyzed by multiple *t* tests, applying a 5% false-discovery rate as described in section 2.2.4. **(B, D)** Volcano plots of the differences between the WT SMase and H322A SMase control treatments, with the $-\log(P \text{ value})$ on the y-axis and the difference in the normalized peak areas on the x-axis, are shown. The horizontal dotted line ($-\log(P \text{ value})=1.30$) indicates the significance cutoff for the P value, above which a species is considered significantly different so long as the Q value was also less than 0.05. All sphingomyelins of interest were significantly decreased by WT SMase treatment (within the pink box). Conversely, all ceramides of interest were significantly increased (within the green box). **(E)** The mean and SEM of the change in sphingomyelin was plotted against the mean and SEM of the change in the corresponding ceramide. A linear fit was applied and indicated high correlation between these two axes ($R^2=0.9806$).

A**B****C****D****E**

2.3.2 *WT SMase decreases short-circuit CFTR current in nHBE cells and nHTE cells*

We have shown previously that WT SMase added to the basolateral side of mixed bronchial/tracheal airway epithelial cells (nHAE) reduces forskolin-elicited and VX770-potentiated transepithelial short-circuit currents, defined as the change in current from the post-amiloride current to the post-forskolin or post-VX770 current (266). To further understand if these differences were due to a change in current through CFTR, we quantified the difference in the current sensitive to INH172, which inhibits CFTR channels (312). INH172 also has been found to inhibit the volume-sensitive outwardly rectifying chloride channel, but this channel is not expected to be activated by forskolin (313). Furthermore, we used INH172 at concentrations and exposure times that avoid pitfalls related to generation of reactive oxygen species and mitochondrial dysfunction (314). Thus, we have defined CFTR currents within this study as forskolin-elicited, VX770-potentiated, and INH172-sensitive transepithelial short-circuit currents.

Because of a refinement of our isolation techniques, we were able to evaluate bronchial and tracheal epithelial cells separately. Thus, in order to understand if WT SMase had a more dominant effect on bronchial or tracheal epithelial cells, we repeated our previous experiments in both. A representative experiment is shown (Figure 2.6A). Consistent with our previous work in nHAE cells, we found that WT SMase treatment of nHBE cells reduced forskolin-elicited currents (Figure 2.6E). VX770-potentiated currents also were reduced by WT SMase treatment from $75.8 \pm 5.1 \mu\text{A}/\text{cm}^2$ to $56.3 \pm 2.3 \mu\text{A}/\text{cm}^2$, a 25.8% decrease (Figure 2.6F). Similarly, WT SMase significantly decreased INH172-sensitive current from $71.7 \pm 2.4 \mu\text{A}/\text{cm}^2$ to $53.1 \pm 1.1 \mu\text{A}/\text{cm}^2$, (Figure 2.6H), a 25.9% decrease further indicating that CFTR currents were indeed reduced by WT SMase. This effect of WT SMase on forskolin-elicited and INH172-sensitive currents was found in nHBE cells from multiple donors (within this study, each figure represents a different unique subject, while the data within a figure represents technical replicates from that subject), indicating that this is not a patient-specific phenomenon. In nHTE cells, the forskolin-elicited, VX770-potentiated, and INH172-sensitive currents also were found to be decreased by WT SMase treatment (Figure 2.7), indicating that WT SMase affects CFTR-mediated anion secretion in multiple classes of airway epithelial cells. Note also that the effects of WT SMase on CFTR currents in nHBE cells remained consistent when

Figure 2.6. Short-circuit current analysis revealed a reduction of transepithelial CFTR current in nHBE cells after WT SMase treatment.

A single biological replicate is shown. **(A)** An example trace of area-corrected transepithelial short-circuit currents is shown. Cells were stabilized for 30 min, at which point *(a)* 1 $\mu\text{g}/\text{mL}$ enzyme-dead H322A (black) or WT SMase (grey) was added basolaterally. After 30 min, *(b)* 20 μM amiloride was added apically, followed by *(c-f)* 0.01, 0.1, 1, and 10 μM forskolin. Forskolin-elicited currents were potentiated by *(g)* 1 μM VX770. Finally, CFTR currents were inhibited by *(h)* 10 μM INH172 apically. **(B)** The absolute currents after 20 μM amiloride and **(G)** the absolute currents after 10 μM INH172 were analyzed by unpaired two-tailed t tests, which indicated no difference between SMase and control treatments ($p=0.6087$, $p=0.5550$). **(C)** The change from the pre- to the post-amiloride current was also analyzed by an unpaired two-tailed t test and indicated that SMase significantly decreased this amiloride-sensitive ENaC current (** $p=0.0074$). **(D)** The absolute currents elicited by forskolin, as well as **(E)** the changes in current from the post-amiloride current to these post-forskolin currents, were analyzed by a two-way ANOVA with repeated measures over the concentrations of forskolin. This analysis indicates that SMase significantly decreased the absolute forskolin currents as well as the forskolin-elicited currents in nHBE cells (* $p=0.0238$, ** $p=0.0037$). The absolute changes in current **(F)** from the post-amiloride current to the post-VX770 current and **(H)** from the post-VX770 current to the post-INH172 current, plotted as individual values along with the means and standard deviations, were analyzed by unpaired two-tailed t tests. These analyses indicate that SMase significantly decreased the VX770-potentiated current (** $p=0.0038$) and INH172-sensitive current (***) $p=0.0003$) in nHBE cells.

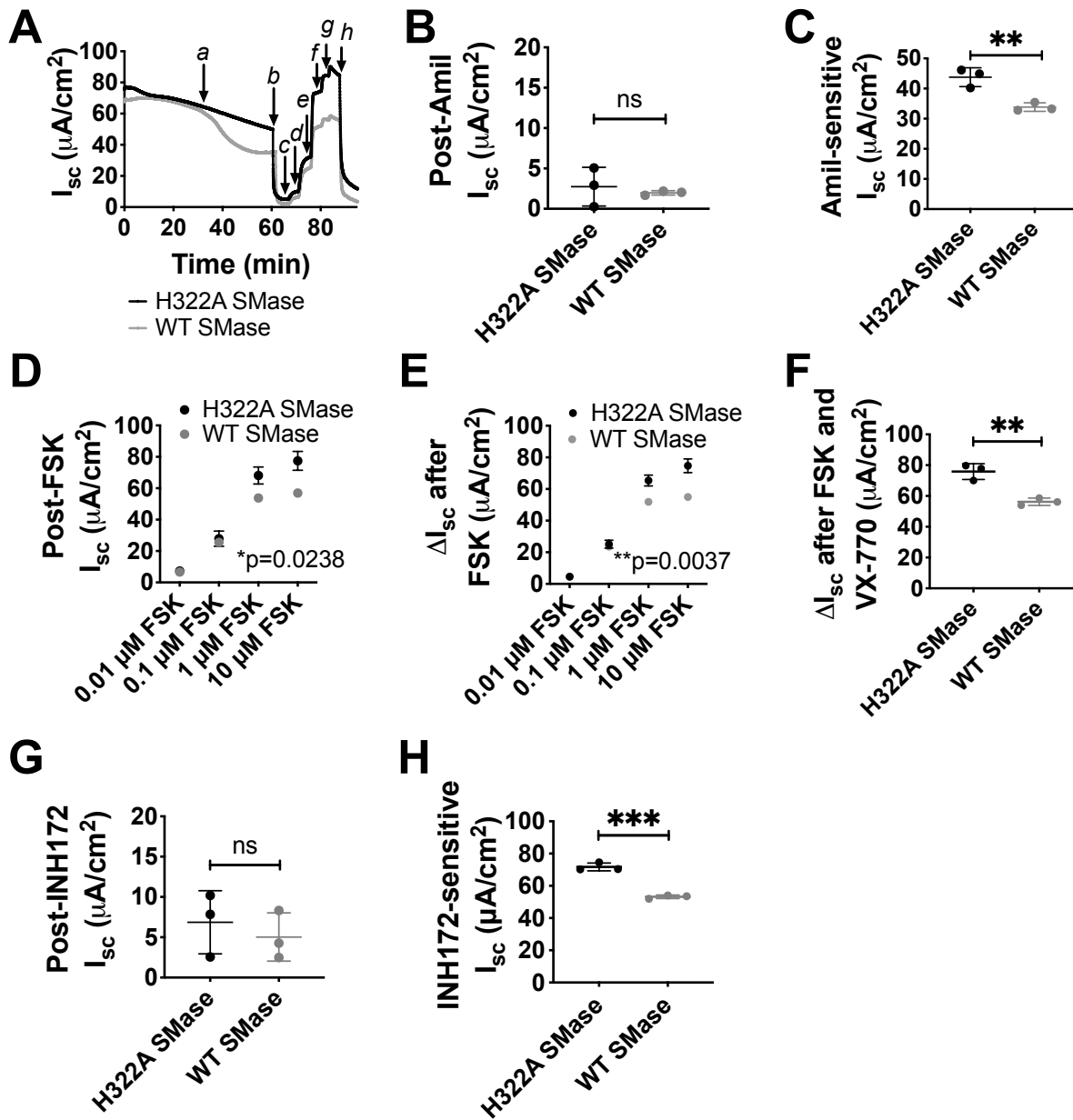
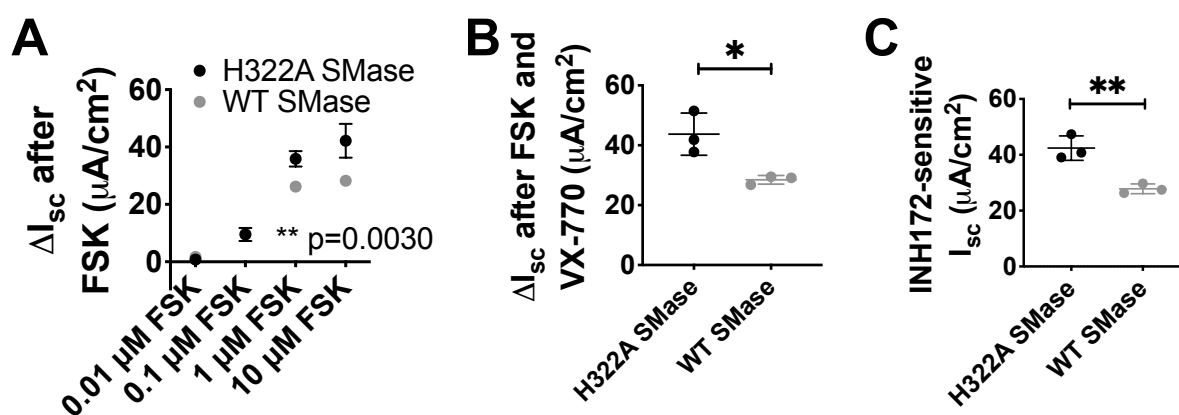


Figure 2.7. SMase affects nHTE cells similarly to nHBE cells. A reduction in CFTR short-circuit currents was seen in nHTE cells treated basolaterally with 1 $\mu\text{g}/\text{mL}$ WT SMase (grey, n=3) as compared to enzyme-dead H322A SMase (black, n=3) when measured using an Ussing Chamber. **(A)** The absolute changes in current from the post-amiloride current to the current elicited by various concentrations of forskolin were analyzed by a two-way ANOVA with repeated measures over the concentrations of forskolin. This analysis indicates that SMase significantly decreased the forskolin-elicited currents in nHTE cells (**p=0.0030). The absolute changes in current **(B)** from the post-amiloride current to the post-VX770 current and **(C)** from the post-VX770 current to the post-INH172 current were analyzed by unpaired two-tailed t tests. These analyses indicate that SMase significantly decreased the **(B)** VX770-potentiated current (*p=0.0213) and **(C)** INH172-sensitive current (**p=0.0058) in nHTE cells.



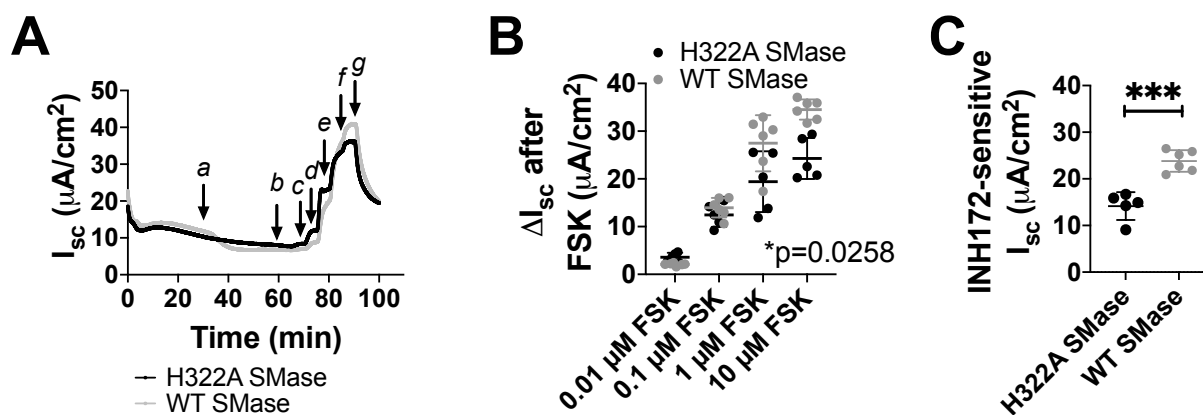
the short-circuit current analyses were performed under symmetric chloride conditions (*data not shown*).

The forskolin-elicited and VX770-potentiated current data were calculated as the change in current from the post-amiloride current. The INH172-sensitive current was calculated as the change in current from the post-VX770 current to the post-INH172 current. To confirm that these reduced forskolin-elicited, VX770-potentiated, and INH172-sensitive currents were not due to an increase in the post-amiloride or post-INH172 baselines currents, we quantified the absolute currents after amiloride and after INH172. These baseline currents were not significantly different after WT SMase treatment compared to control (Figure 2.6B,G). However, the absolute currents following forskolin addition were decreased by WT SMase (Figure 2.6D). This indicates that WT SMase specifically decreased currents through CFTR in nHBE cells. Interestingly, along with decreasing CFTR currents, WT SMase decreased ENaC-mediated currents, as indicated by reduced amiloride-sensitive current (Figure 2.6C). This phenomenon has been seen by others, for example when WT SMase and ceramide were shown to decrease ENaC open probability in renal cells (287). However, it cannot be ruled out that this decrease in ENaC current is partially due to decreased activity of basolateral potassium channels that facilitate the potential for sodium movement through ENaC.

2.3.3 *Differential effect of WT SMase on immortalized Calu-3 and 16HBE cells*

Previous work had reported that WT SMase decreased forskolin-elicited currents in the immortalized bronchial epithelial cell line Calu-3 under symmetric chloride conditions (269). We thus repeated our previous short-circuit current analyses on Calu-3 cells. In contrast to previous results, under a chloride gradient, Calu-3 bronchial epithelial cells did not replicate the phenotype seen in nHBE cells following WT SMase treatment. Rather, we found that WT SMase increased CFTR currents in Calu-3 cells, as indicated by increased forskolin-elicited and INH172-sensitive currents (Figure 2.8). This is the opposite of the decreases in CFTR currents seen in nHBE cells. We repeated our Calu-3 experiments in symmetric chloride conditions to replicate the experimental setup in previous literature. However, we found that while WT SMase had no significant effect on forskolin-elicited currents, it increased the INH172-sensitive currents similarly to the experiments performed under a chloride gradient (*data not shown*). The reason for

Figure 2.8. Short-circuit current analysis revealed an increase in CFTR currents in Calu-3 cells after WT SMase treatment. (A) An example trace of area-corrected transepithelial short-circuit currents is shown. Cells were treated as in Figure 2.6, except VX770 was not added prior to (g) INH172 addition. (B) The forskolin-elicited current was analyzed by a two-way ANOVA with repeated measures over the concentrations of forskolin, indicating that WT SMase (grey, n=6) significantly increased forskolin-elicited currents as compared to H322A SMase control (black, n=5) in Calu-3 cells (*p=0.0258). (C) INH172-sensitive currents were analyzed by an unpaired two-tailed *t* test, indicating that WT SMase significantly increased the INH172-sensitive currents in Calu-3 cells (**p=0.0003).



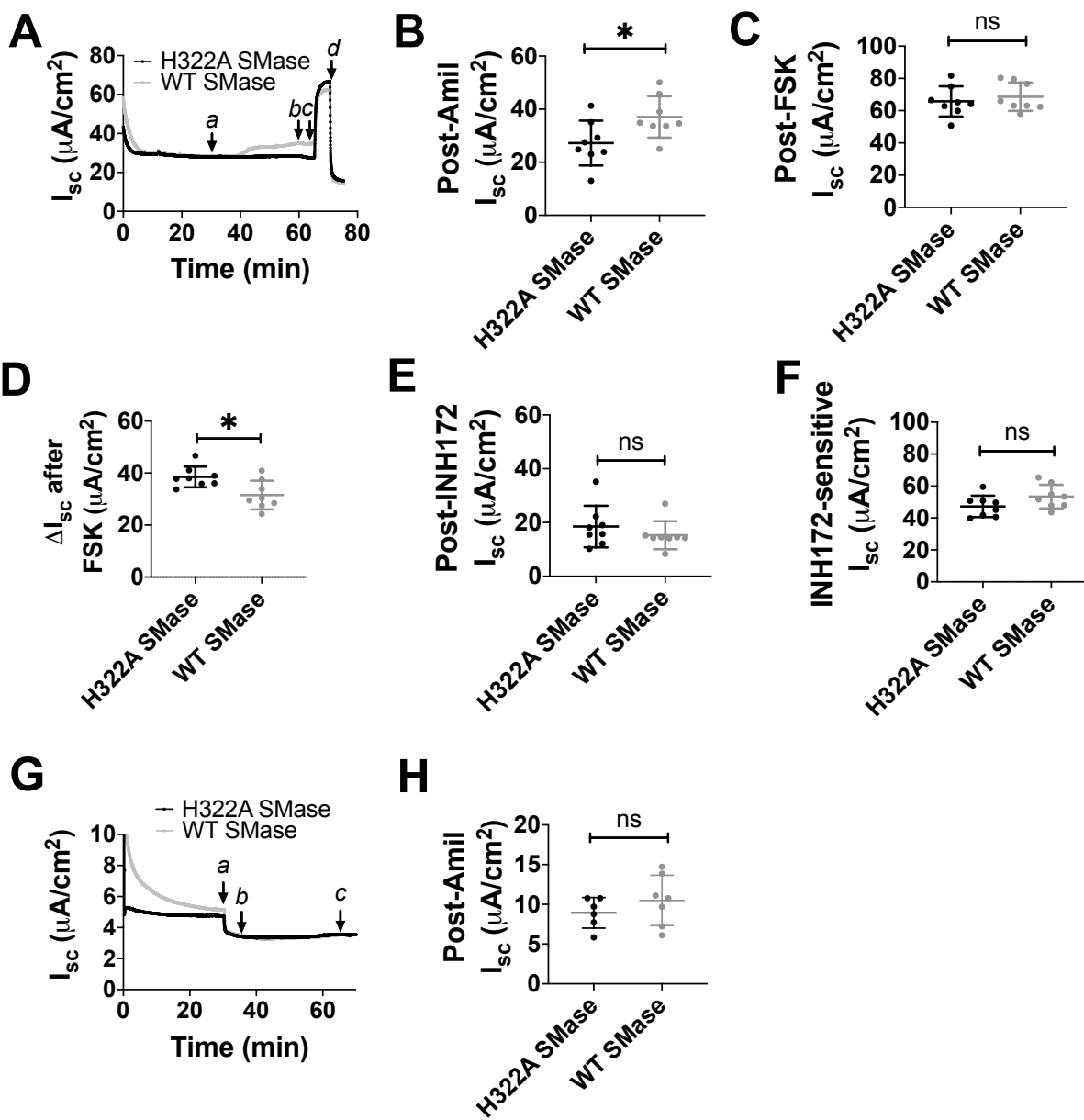
the inconsistency of our results as compared to previous literature are unknown at present but could reflect a significant heterogeneity to the Calu-3 cell line. Importantly, the previous analysis did not use a CFTR-specific inhibitor such as INH172 to verify that the currents were attributable to CFTR, instead using the non-specific inhibitor NPPB (269).

We then asked whether the immortalized 16HBE bronchial epithelial cell line was a suitable surrogate for nHBE cells. Interestingly, WT SMase treatment caused an elevated post-amiloride baseline current (Figure 2.9B). Given that the post-forskolin currents were not different between treatments (Figure 2.9C), the apparent decrease in forskolin-elicited currents following WT SMase treatment (Figure 2.9D) was due to this elevated post-amiloride current. Interestingly, the post-INH172 currents were not affected by WT SMase, nor were the INH172-sensitive currents (Figure 2.9E-F). Taken together, this suggests that WT SMase activates CFTR prior to forskolin addition. To test this hypothesis, we treated 16HBE cells with INH172 prior to amiloride to determine if the elevated post-amiloride currents remained in the SMase treated cells. This INH172 pre-treatment did eliminate the elevated post-amiloride currents in the WT SMase-treated cells, suggesting that in 16HBE cells, WT SMase treatment activates CFTR prior to forskolin addition (Figure 2.9G-H). This is different than what occurs in both the nHBE cells and the Calu-3 cells, suggesting that the effects of WT SMase are not consistent between cell types. Given that nHBE cells are a closer *in vitro* analog to native cells *in vivo*, we chose to perform all future experiments in nHBE cells.

2.3.4 *WT SMase affects impedance-derived apical and basolateral conductance in nHBE cells*

The results thus far establish that CFTR-mediated transepithelial short-circuit currents in nHBE cells are reduced by WT SMase treatment. However, transepithelial currents are controlled by basolateral and apical conductance of ions through channels, along with functionally related transporters, and paracellular conductance through tight junctions (Figure 2.1). It is important to note that conductance describes the ability for ions to move through a channel or across a membrane, independent of the net ion movement, which is current. In order to understand if basolateral WT SMase reduced transepithelial currents by inhibiting CFTR-mediated apical membrane conductance, by inhibiting basolateral

Figure 2.9: SMase affects the transepithelial short-circuit currents of 16HBE cells, but differently than nHBE cells. Short-circuit transepithelial currents of 16HBE cells were measured using an Ussing Chamber and a basolateral-to-apical chloride gradient. **(A)** An example trace is shown. Cells were stabilized for 30 min, at which point *(a)* 0.1 $\mu\text{g}/\text{mL}$ enzyme-dead H322A (black, $n=8$) or WT (grey, $n=8$) SMase was added basolaterally. After 30 min, *(b)* 20 μM amiloride was added apically to inhibit ENaC currents, then *(c)* 10 μM forskolin was added to activate CFTR currents. These forskolin-elicited CFTR currents were inhibited by *(d)* apical addition of 10 μM INH172. **(B)** The absolute currents after 20 μM amiloride was analyzed by an unpaired two-tailed t test and indicated a significant increase in current in the SMase-treated group as compared to the H322A SMase control ($*p=0.0296$). The amiloride-sensitive currents were very close to zero, and thus were not analyzed. **(C)** The absolute currents after 10 μM forskolin and **(D)** the changes in current from the post-amiloride current to this current were analyzed by unpaired two-tailed t tests. The absolute currents were not different, but the change in current was significantly decreased in the SMase-treated group as compared to control ($p=0.5359$, $*p=0.0116$). **(E)** The absolute currents after 10 μM INH172 and **(F)** the changes in current from the forskolin current to this current were analyzed by unpaired two-tailed t tests, indicating no significant difference between treatments in either ($p=0.3437$, $p=0.1065$). Taken together, these data suggest that in 16HBE cells, SMase activated CFTR prior to forskolin addition. Experiments were conducted in which CFTR was inhibited prior to SMase treatment, and **(G)** an example trace is shown. Cells were stabilized for 30 min, at which point *(a)* 10 μM INH172 was added apically to inhibit CFTR. Then *(b)* 0.1 $\mu\text{g}/\text{mL}$ enzyme-dead H322A (black, $n=6$) or WT (grey, $n=7$) SMase was added basolaterally. After 30 min, *(c)* 20 μM amiloride was added apically to inhibit ENaC currents **(H)** The absolute currents after 20 μM amiloride was analyzed by an unpaired two-tailed t test and indicated no change between treatment groups ($p=0.3154$).



conductance, or both, we utilized impedance analysis, which estimates apical and basolateral resistances (inverse of conductances) and capacitances separately (300; 303).

Impedance data were plotted as Nyquist plots (Figure 2.10A). The apical and basolateral resistances used to fit these Nyquist Plots were inverted into conductances, compiled, and analyzed (Figure 2.10B-C). WT SMase treatment decreased both the apical and basolateral conductance after addition of forskolin and VX770 in nHBE cells. Forskolin- and VX770-elicited apical conductance was reduced from 11.54 ± 0.35 mS/cm² to 9.93 ± 0.34 mS/cm², an approximate 14% decrease. Basolateral conductance was reduced from 3.53 ± 0.22 mS/cm² to 2.77 ± 0.20 mS/cm², an approximate 21% decrease. Since CFTR is the only apical channel activated after forskolin addition, this indicates that WT SMase decreases CFTR-mediated transepithelial currents in part by decreasing the total conductance through apical CFTR. Furthermore, the basolateral membrane conductance data indicate that WT SMase additionally could be reducing CFTR-mediated transepithelial currents by inhibiting a basolateral component of transepithelial flux, which is important for maintaining a driving force for apical anion secretion.

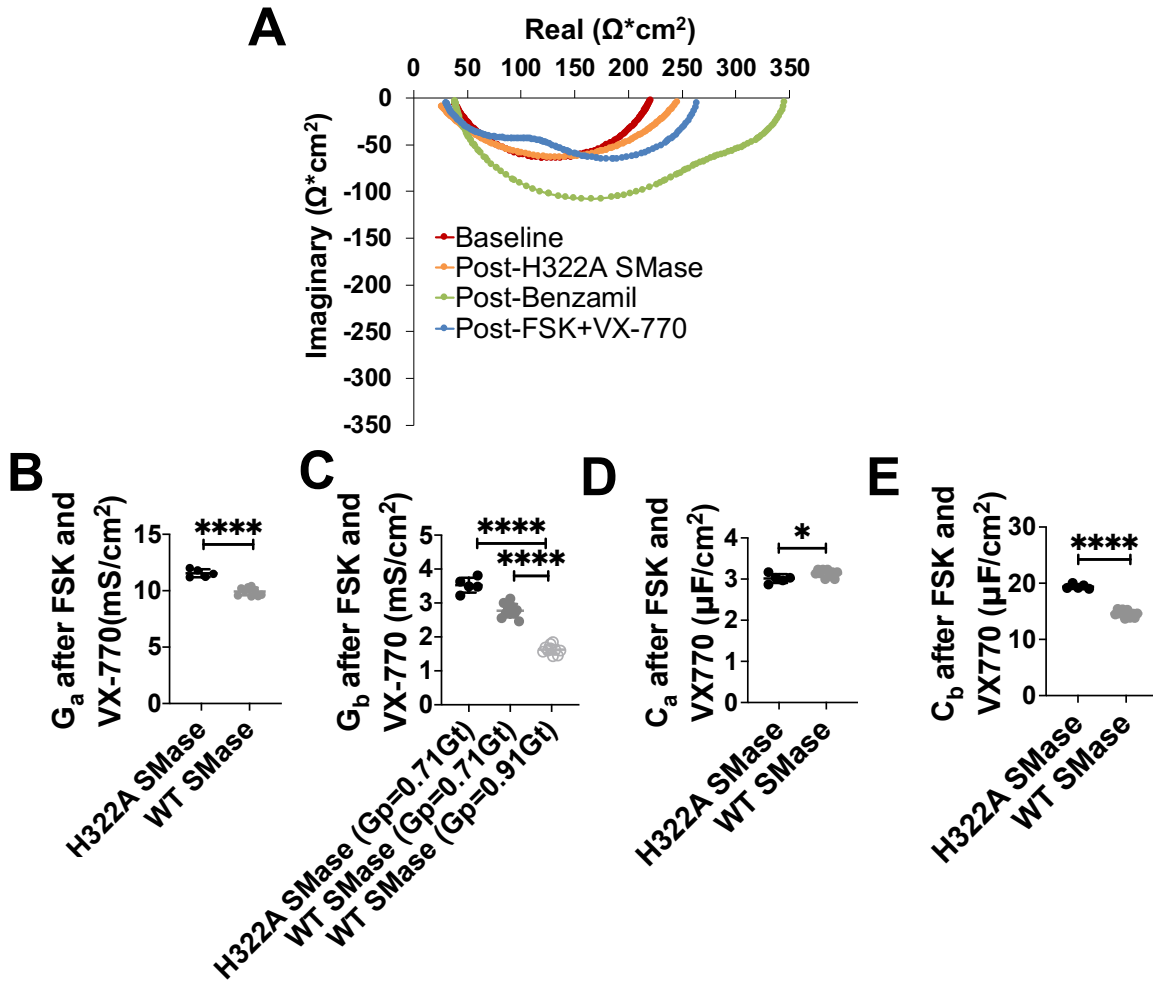
Along with conductance, the impedance analysis method also allowed for the determination of the apical and basolateral capacitances. Basolateral WT SMase decreased basolateral capacitance from 19.4 ± 0.42 μ F/cm² to 14.5 ± 0.74 μ F/cm², an approximate 25% decrease. WT SMase also increased apical capacitance from 3.01 ± 0.11 μ F/cm² to 3.10 ± 0.15 μ F/cm², an approximate 4% increase (Figure 2.10D-E).

2.3.5 *WT SMase does not affect paracellular permeability in nHBE cells*

Part of the procedure to fit impedance data requires knowledge of the relationship between the paracellular and transepithelial conductances. While the value for this assumption does not affect most of the calculated values, it can dramatically affect the value for the basolateral conductance (G_b) (300). Thus, we needed to confirm that the assumed value for the relationship between paracellular and transepithelial conductance (G_p , G_T) was warranted following WT SMase treatment.

Figure 2.10. Impedance measurements of nHBE cells (a single biological replicate) showed a reduction in both apical and basolateral conductance after WT SMase treatment, alongside a reduction of basolateral capacitance but an increase in apical capacitance.

(A) A representative fit of the Nyquist Plot at baseline (red), after 30 min of 1 $\mu\text{g}/\text{mL}$ enzyme-dead H322A SMase basolaterally (orange), after at least 6 μM benzamil apically (green), and after 10 μM forskolin and 1 μM VX770 (blue) is shown. These fits were created by assuming that G_p is 71% of G_T , and then iteratively determining the R_a , R_b , C_a , and C_b that fit the primary data best. R_a and R_b were inverted to obtain the G_a and G_b . (B) G_a and (C) G_b after forskolin and VX770 in cells treated basolaterally with either 1 $\mu\text{g}/\text{mL}$ H322A (black, $n=5$) or WT SMase (grey, $n=10$) were analyzed by unpaired two-tailed t tests. These analyses indicate that WT SMase significantly inhibited both G_a (**** $p<0.0001$) and G_b (**** $p<0.0001$) of nHBE cells when assuming $G_p = 0.71G_T$. Within G_b , when assuming $G_p = 0.91G_T$ (light grey, open circles), WT SMase appears to have an even more significant effect, with the G_b significantly decreased under these conditions as compared to the previous conditions (**** $p<0.0001$). The (D) C_a and (E) C_b were analyzed by unpaired two-tailed t tests. These analyses indicate that basolateral WT SMase significantly decreased C_b (**** $p<0.0001$), while significantly increasing C_a (* $p=0.0322$).

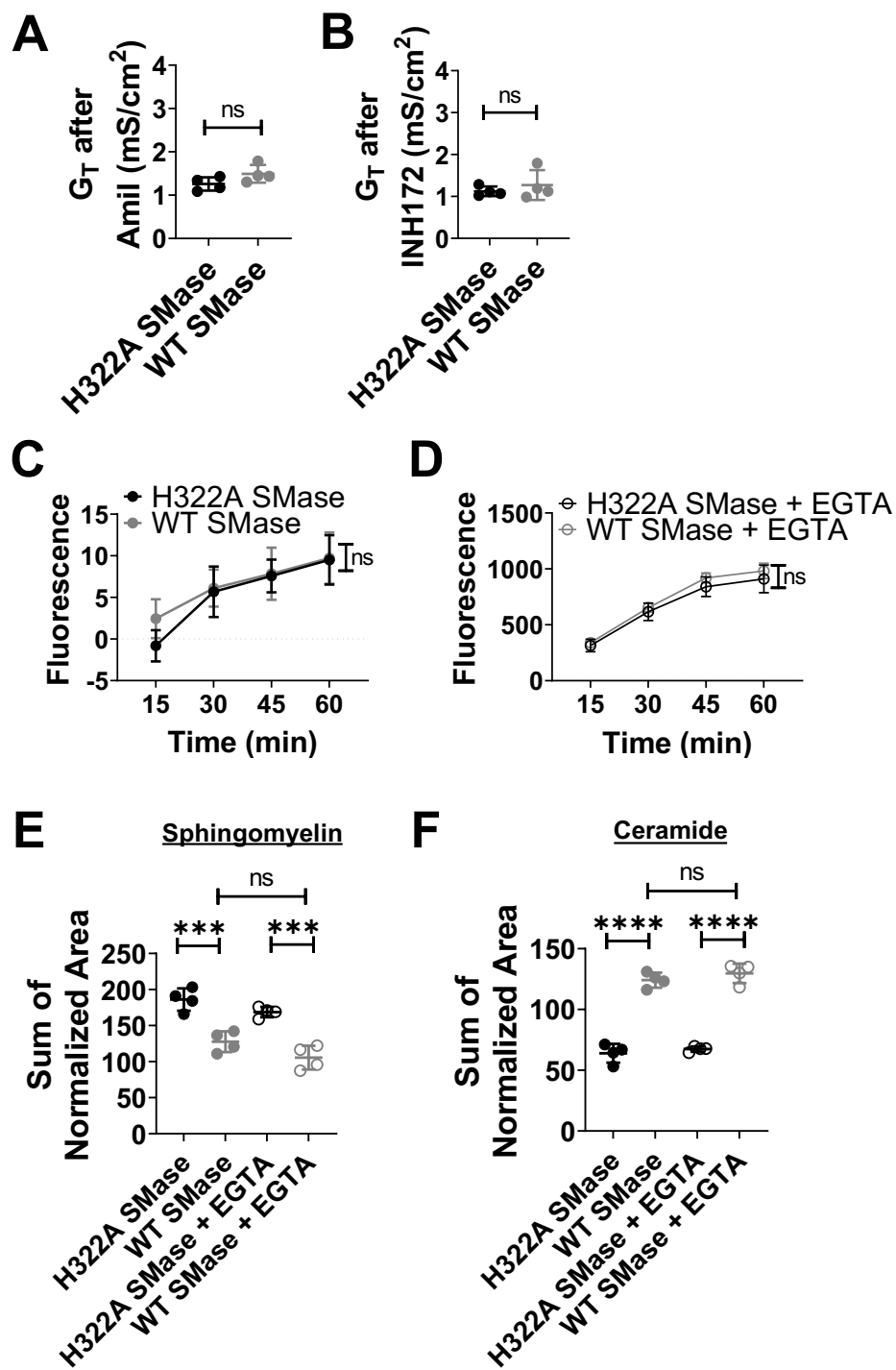


The assumed value relating G_p and G_T was based on prior experiments on nHBE cells not treated with WT SMase, which indicated that $G_p = 0.71G_T$ (*unpublished observations*). G_T is equal to the sum of G_p and transcellular conductance (G_c). Thus, it is clear that the relationship between G_p and G_T can be affected by changing G_p , G_c , or both. WT SMase treatment does decrease the G_c (at least through the apical membrane, Figure 2.10B), which would increase the relative contribution of G_p to G_T , assuming that G_p remained unchanged after WT SMase treatment. Fitting the WT SMase-treated cells with a higher relative contribution of G_p (a lower relative contribution of R_p) makes the observed decrease in G_b after WT SMase treatment more extreme than when assuming the same G_p for both treatments (Figure 2.10C, grey open circles, 54% decrease in G_b). Thus, we have biased our results toward the null by assuming $G_p = 0.71G_T$. However, this still assumes that G_p remains unchanged by WT SMase treatment. While there is some evidence that 0.1 μM (but not 1 μM) ceramide treatment for 24 hr may decrease the permeability of tight junctions in H441 small airway cells (315), we needed to determine whether WT SMase affected paracellular conductance under the conditions used here.

Under a chloride gradient, we found that there was no difference in the post-amiloride or post-INH172 short-circuit currents, which are predominantly (not exclusively) controlled by paracellular ion movements since ENaC and CFTR are both inhibited (or inactivated) at both points (Figure 2.6B,H). These data suggest that WT SMase does not affect paracellular chloride conductance. However, tight junctions in bronchial epithelia show differential ion selectivity (316). Therefore, to evaluate the paracellular conductance of all ions, the transepithelial conductance in the absence of an ion gradient was evaluated (normal chloride buffer on both sides). These data indicated no difference in the post-amiloride or post-INH172 conductance after treatment with SMase (Figure 2.11A-B). Thus, these data support the hypothesis that SMase does not affect paracellular conductance of any ion under the treatments explored in these experiments.

To further determine if paracellular tight junctions were affected by WT SMase, a calcein flux permeability assay was performed (305; 306). WT SMase treatment over the course of 1 hr did not affect calcein permeability (Figure 2.11C). To evaluate how these fluxes compared to those under conditions

Figure 2.11. SMase does not affect baseline transepithelial conductance or calcein flux. Transepithelial conductances of nHBE cells (a single biological replicate, but n=4 technical replicates) were measured by Ussing Chamber under symmetric chloride conditions. Cells were allowed to stabilize for 30 min, after which 1 $\mu\text{g}/\text{mL}$ enzyme-dead H322A (black, n=4) or WT (grey, n=4) SMase was added to the basolateral side for 30 min. After this, 20 μM amiloride was added apically, followed by 10 μM forskolin added to both sides. After this forskolin-elicited current stabilized, 10 μM INH172 was added apically to inhibit CFTR. The conductances after (A) 20 μM amiloride and (B) 10 μM INH172 apically are shown. Data were analyzed by unpaired two-tailed *t* tests, which indicate that WT SMase did not affect post-amiloride or post-INH172 conductances ($p=0.1171$, $p=0.4561$). Paracellular flux of calcein in nHBE cells was determined as described in section 2.2.7. (C) The assay involved adding 1 $\mu\text{g}/\text{mL}$ H322A (black, n=7) or WT (grey, n=6-7) SMase basolaterally and 20 $\mu\text{g}/\text{mL}$ calcein apically. (D) To determine maximal paracellular flux, tight junctions were disrupted with 3 mM EGTA. These EGTA-treated cells secondarily were treated with either H322A (open black) or WT (open grey) SMase. Data were analyzed by a two-way ANOVA for the EGTA treatment, and a mixed-effects analysis for the no-EGTA treatment due to missing values. In both cases, there were repeated measures over time. These analyses indicate SMase does not affect transepithelial calcein flux under normal conditions ($F=0.4586$, $p=0.2983$), and that an increase in paracellular flux could have been detected. Mass spectrometry analysis of (E) sphingomyelins and (F) ceramides in Calu-3 cells treated as in the nHBE calcein flux experiments indicated that in the presence of 3 mM EGTA in KRH buffer, WT SMase retained its ability to hydrolyze sphingomyelin into ceramide. The normalized area of all sphingomyelins or ceramides were added together and reported here. Two-way ANOVAs with multiple comparisons and Tukey correction were used to analyze the data. As seen previously, WT SMase (grey) decreased sphingomyelins and increased ceramides relative to H322A SMase (black) (** $p=0.0003$; **** $p<0.0001$). Similarly, in 3 mM EGTA conditions, WT SMase (open grey circles) decreased sphingomyelins and increased ceramides relative to H322A SMase (open black circles) (** $p=0.0002$; **** $p<0.0001$). There was no significant difference in sum of the normalized area of sphingomyelins or ceramides in cells treated with WT SMase, regardless of EGTA treatment ($p=0.1644$; $p=0.6282$).



facilitating maximal paracellular flux, we treated one group of Transwells with 3 mM EGTA to allow unencumbered paracellular movement through tight junctions (Figure 2.11D). This group of wells was further subdivided into samples treated with either H322A or WT SMase. Treatment with 3 mM EGTA allowed for an approximate 100-fold increase in the flux of calcein through the nHBE cells, and WT SMase treatment did not affect this, indicating that an increase in flux from the untreated cells would have been detectable. We also confirmed via lipidomics analysis of Calu-3 bronchial epithelial cells that WT SMase was still active in the presence of 3 mM EGTA in KRH (Figure 2.11E-F). These results indicate that, over the time course used, WT SMase did not affect paracellular permeability. As such, our assumptions for fitting impedance data are supported, and the conclusion that WT SMase inhibits apical and basolateral membrane conductance in nHBE cells can be maintained.

2.3.6 *WT SMase inhibits CFTR current and conductance in cfHBE cells*

In order to determine if WT SMase similarly inhibited CFTR-mediated transepithelial current and conductance in cells from people with CF, and to determine if current FDA-approved CFTR modulators could overcome WT SMase-mediated inhibition of CFTR, these experiments were repeated on cfHBE cells homozygous for the $\Delta F508$ -CFTR mutation. The $\Delta F508$ mutation results in an unfolded CFTR protein that does not traffic to the cell surface. Trafficking of $\Delta F508$ -CFTR to the cell membrane can be rescued (corrected) by temperature shift to 27 °C; by treatment with FDA-approved correctors such as VX809 (lumacaftor) (76), VX661 (tezacaftor), or VX445 (elexacaftor) (85; 317); or by a combination of these drugs. Once at the surface, $\Delta F508$ -CFTR still has difficulty opening, and requires potentiators such as VX770 (Ivacaftor) to elicit more current. We have shown previously that WT SMase inhibits transepithelial currents in cfHBE cells corrected by temperature shift alone (266), but have not determined if correction with VX809 or VX445/VX661 can prevent WT SMase-mediated inhibition of CFTR-mediated transepithelial currents in cfHBE cells.

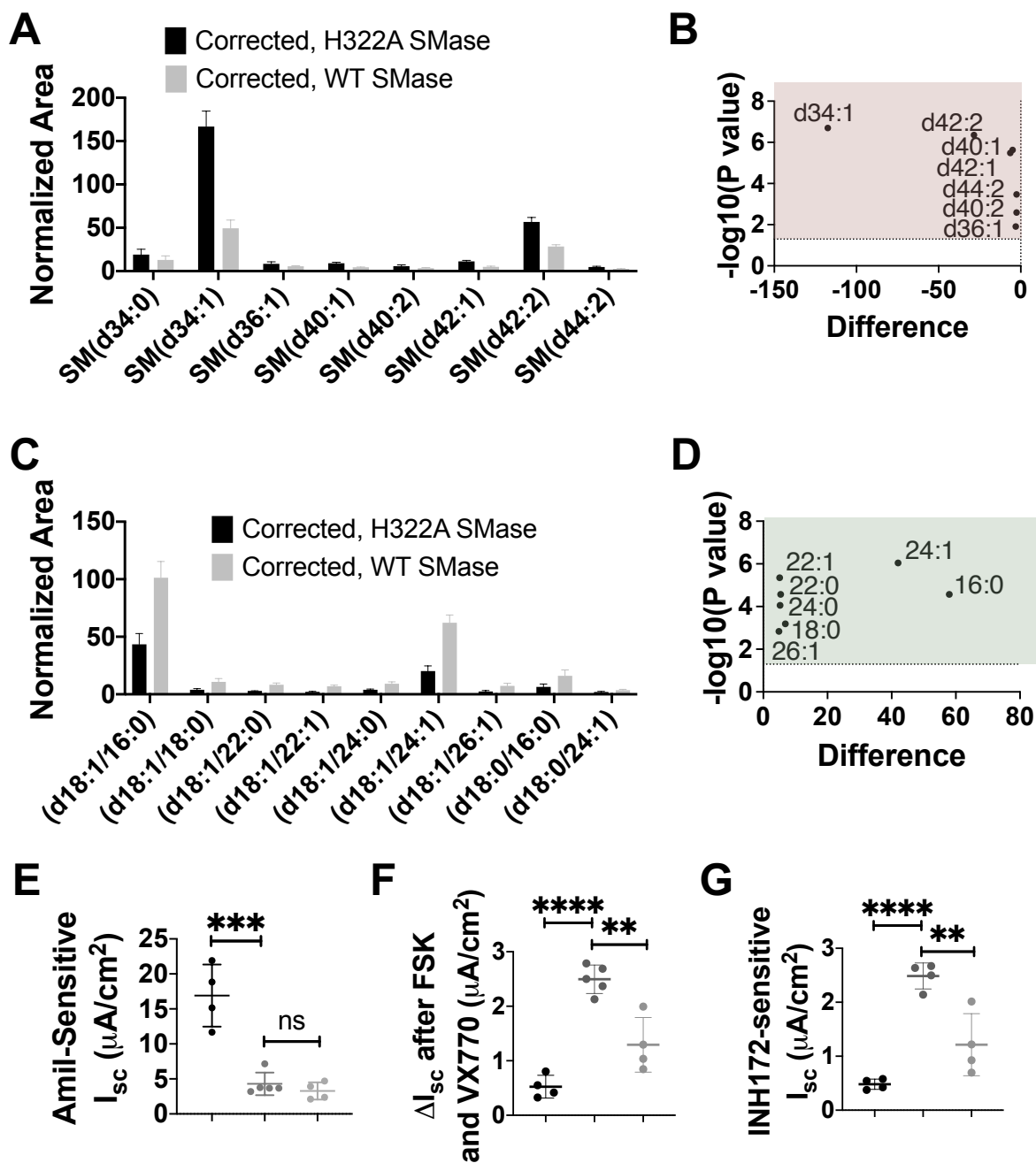
We first confirmed that WT SMase affected sphingolipids similarly in VX809-corrected cfHBE cells as in nHBE cells (Figure 2.12A-D). Then, we performed short-circuit current experiments on cfHBE

cells corrected with 3 μM VX809 and temperature shift to 27 $^{\circ}\text{C}$ for 24 hr (Figure 2.12E-G). Correction significantly reduced the amount of amiloride-sensitive ENaC current in cfHBE cells (Figure 2.12E). This makes sense, given that ENaC is overactive in CF compared to non-CF cells (15). Interestingly, WT SMase treatment did not affect the ENaC currents in these corrected cells, contrary to in nHBE cells (Figure 2.6). VX809- and temperature-shift correction did not rescue forskolin-elicited currents alone (*data not shown*) but did rescue VX770-potentiated and INH172-sensitive currents (Figure 2.12F). WT SMase decreased the VX770-potentiated and INH172-sensitive currents in corrected cfHBE cells (Figure 2.12F,G).

The more clinically relevant drugs in the current Trikafta[®] therapy, VX445 and VX661, were evaluated as well. In this case, cfHBE cells were treated with 5 μM VX445 and 18 μM VX661 for 48 hr (Figure 2.13). As in the VX809- and temperature-corrected cfHBE cells, VX445/VX661 correction decreased amiloride-sensitive ENaC currents (Figure 2.13C). However, this may have been in part due to an elevated post-amiloride baseline current in these corrected cells (Figure 2.13B). This elevated baseline remained even after INH172 addition at the end of the experiment, indicating that it was not CFTR currents (Figure 2.13F). The origin of this elevated baseline current has not yet been explored. Corrected VX445/VX661-corrected cfHBE cells also had more forskolin-elicited, VX770-potentiated, and INH172-sensitive current than their uncorrected counterparts (Figure 2.13D,E,G). The corrected cfHBE cells treated with H322A SMase were then compared to corrected cfHBE cells treated with WT SMase. In cfHBE cells corrected with VX445/VX661, WT SMase decreased the forskolin-elicited, VX770-potentiated, and INH172-sensitive CFTR currents from $13.17 \pm 2.96 \mu\text{A}/\text{cm}^2$ to $6.26 \pm 1.86 \mu\text{A}/\text{cm}^2$, from $12.34 \pm 2.90 \mu\text{A}/\text{cm}^2$ to $5.06 \pm 4.01 \mu\text{A}/\text{cm}^2$, and from $20.11 \pm 3.35 \mu\text{A}/\text{cm}^2$ to $13.39 \pm 5.78 \mu\text{A}/\text{cm}^2$, respectively (Figure 2.13D,E,G). These reductions are similar to those seen in nHBE cells, and again indicate that WT SMase reduces CFTR-mediated transepithelial currents in cfHBE cells corrected with current FDA-approved CFTR modulators.

In continuing to compare the effects of WT SMase on cfHBE cells to the effects on nHBE cells, we used impedance analysis to determine the effects of WT SMase treatment on apical and basolateral membrane conductances in cfHBE cells with the VX809 analog C18 (6 μM for 24 hr). Note that at baseline,

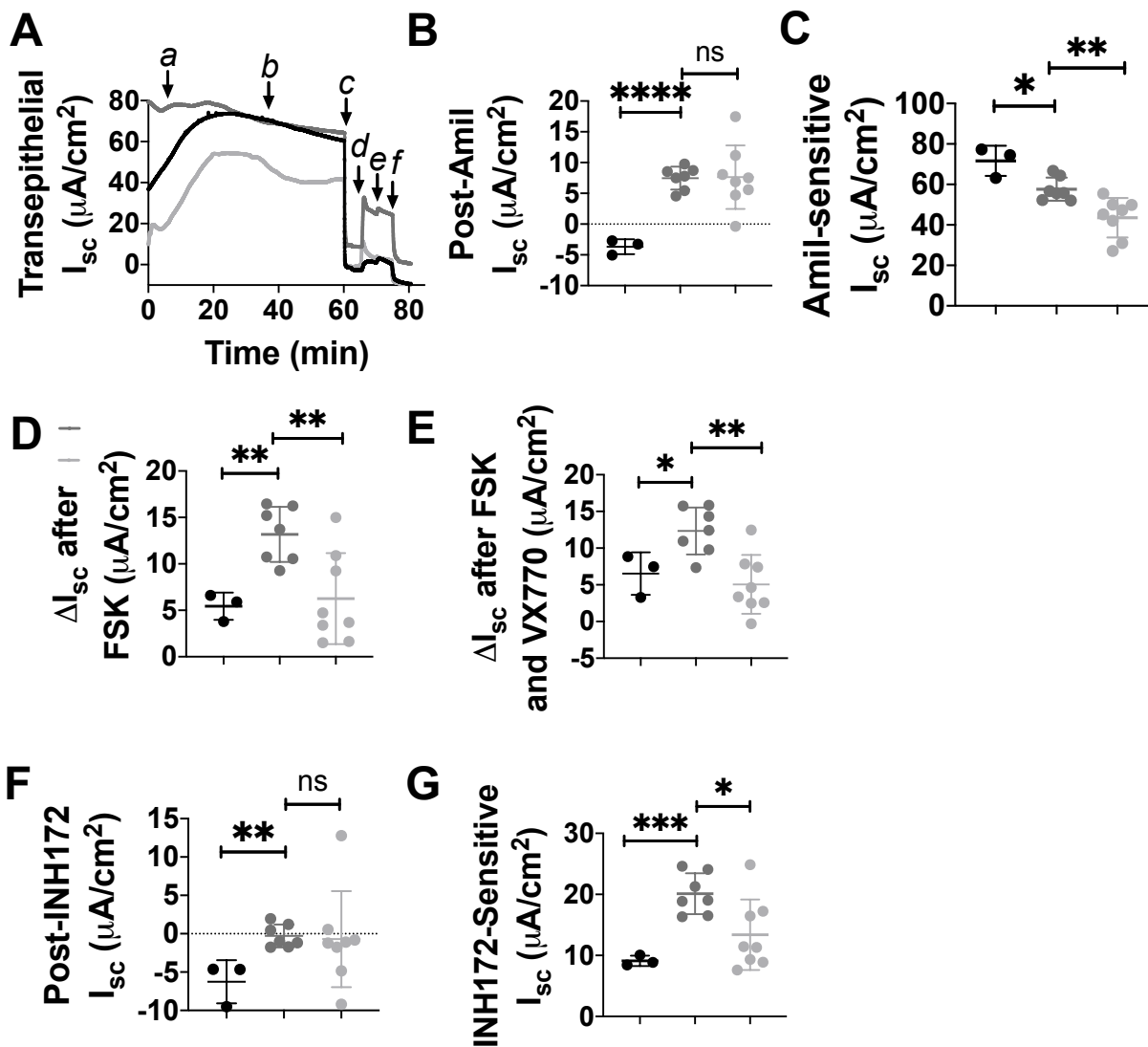
Figure 2.12. SMase modulates sphingolipids and transepithelial currents similarly in VX809-corrected cfHBE cells as in nHBE cells. In VX809-corrected cfHBE cells, SMase (grey, n=6) **(A,B)** decreased all sphingomyelins and **(C,D)** increased all ceramides of interest compared to enzyme-dead H322A SMase control (black, n=5). SMase treatment of cfHBE cells either uncorrected (black, n=4) or corrected (grey) with 3 μM VX-809 and temperature shift to 27 $^{\circ}\text{C}$ for 24 hr showed changes in short-circuit currents, as measured by an Ussing Chamber in symmetric chloride conditions. Basolaterally, 1 $\mu\text{g}/\text{mL}$ enzyme-dead H322A (dark grey, n=5) or WT SMase (light grey, n=4) was added for 30 min. After this, 20 μM amiloride was added apically, followed by 10 μM forskolin, and then 1 μM VX770. After this current stabilized, 10 μM INH172 was added apically. All data from these experiments were analyzed by unpaired two-tailed t tests. **(E)** Correction significantly decreased the amount of amiloride-sensitive ENaC current ($***p=0.0006$), and SMase did not further affect this ($p=0.3357$). Correction significantly increased the amount of **(F)** VX770-potentiated ($****p<0.0001$) and **(G)** INH172-sensitive ($****p<0.0001$) currents in cfHBE cells. SMase significantly decreased both the VX770-potentiated ($**p=0.0023$) and INH172-sensitive ($**p=0.0065$) currents. SMase decreased the maximal CFTR currents and INH172-sensitive currents to 52% and 49% of the corrected control cells, respectively.



- uncorrected, H322A SMase
- corrected, H322A SMase
- corrected, WT SMase

Figure 2.13. SMase modulates transepithelial currents similarly in VX445/VX661-corrected cfHBE cells as in nHBE cells.

(A-D) Transepithelial currents of cfHBE cells (single biological replicate), either uncorrected (black) or corrected with 5 μM VX445 and 18 μM VX661 for 48 hr (grey), were measured using an Ussing Chamber. **(A)** An example trace is shown. At the beginning of the experiment, *(a)* the correctors or vehicle were added to the appropriate cells. The cfHBE cells were stabilized for 30 min, at which point *(b)* 1 $\mu\text{g/mL}$ enzyme-dead H322A (uncorrected, black, $n=4$; corrected, dark grey, $n=5$) or WT SMase (corrected, light grey, $n=4$) was added basolaterally. After 30 min, *(c)* 20 μM amiloride was added apically, then *(d)* 10 μM forskolin was added. These forskolin-elicited CFTR currents were potentiated by addition of *(e)* 1 μM VX770. Finally, CFTR currents were inhibited by apical addition of *(f)* 10 μM INH172. All currents were analyzed by unpaired two-tailed *t* tests. Analysis of the absolute currents after **(B)** amiloride and after **(F)** INH172 indicate that VX445/VX661-mediated correction of cfHBE cells significantly increased these baseline currents (**** $p<0.0001$, ** $p=0.0019$). However, WT SMase did not affect these baseline currents in the corrected cfHBE cells ($p=0.9423$, $p=0.8678$). **(C)** Analysis of the amiloride-sensitive current indicates that correction significantly reduced ENaC currents (* $p=0.0114$). WT SMase further decreased these ENaC currents in VX445/VX661-corrected cfHBE cells (** $p=0.0052$). **(D)** Analysis of the changes in current from the post-amiloride current to the post-forskolin current indicates that correction significantly rescued forskolin-elicited currents (** $p=0.0030$). WT SMase significantly decreased these currents (** $p=0.0064$). **(E)** Analysis of the changes in current from the post-amiloride current to the post-VX770 current indicates that correction significantly rescued VX770-potentiated currents (* $p=0.0274$). However, WT SMase significantly decreased these currents (** $p=0.0020$). **(G)** Analysis of the changes in current from the post-VX770 current to the post-INH172 current indicates that correction significantly rescued INH172-sensitive currents (**** $p=0.0006$). However, WT SMase significantly decreased these currents (* $p=0.0183$). Altogether, this suggests that correction was effective, but that WT SMase still inhibited CFTR-mediated currents in VX445/VX661-corrected cfHBE cells.

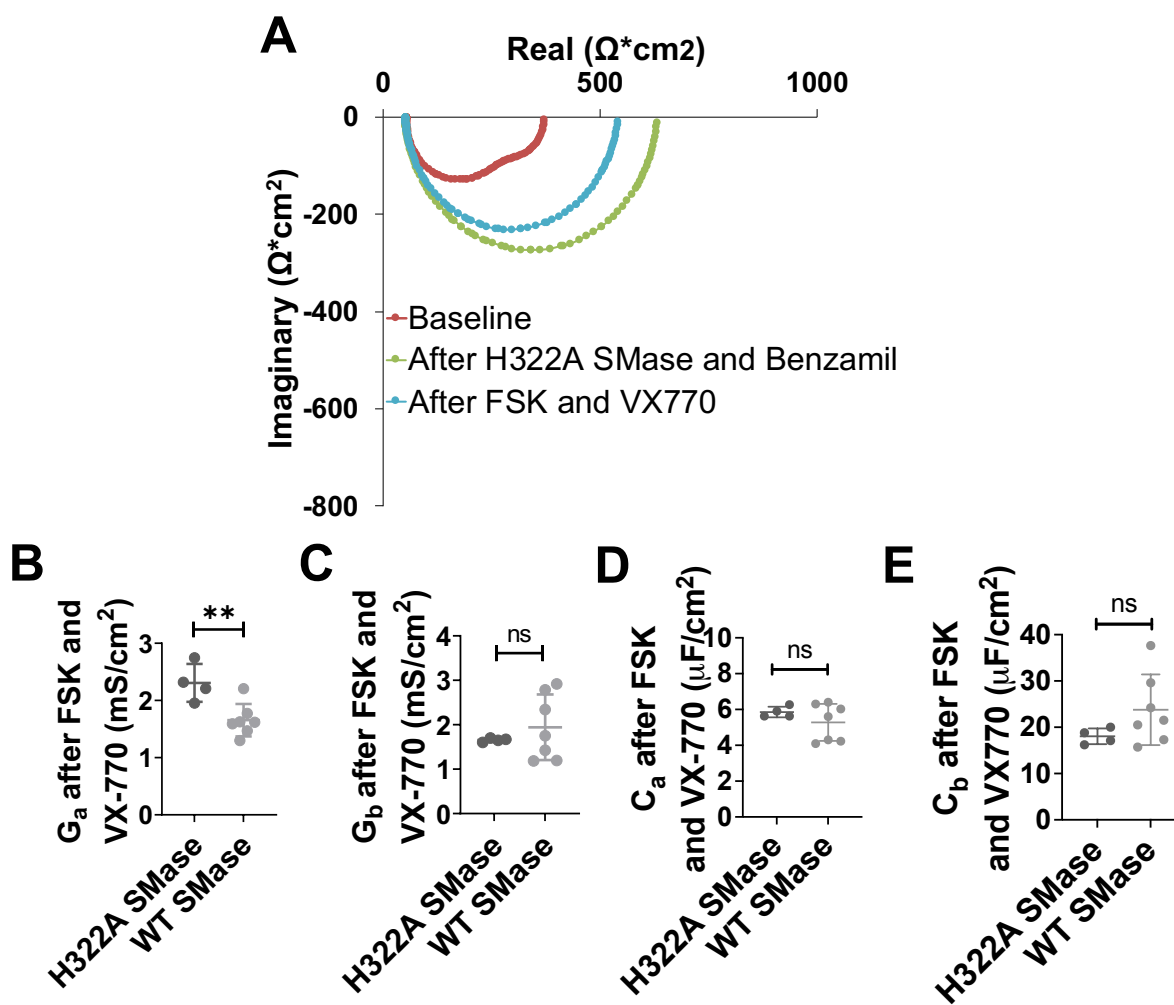


the Nyquist Plot of the corrected cfHBE cells appeared as two distinct semi-circles (Figure 2.14A). This phenomenon occurred in the uncorrected cfHBE cells as well (*data not shown*) but did not occur in the nHBE cells (Figure 2.10A). The presence of two semi-circles at baseline in the corrected cfHBE cells suggests that the apical and basolateral membrane have very different time constants. Furthermore, in corrected cfHBE cells, the plots following forskolin and VX770 addition appear as a single semi-circle (Figure 2.14A). This is contrary to nHBE cells, which did show two distinct semi-circles following forskolin and VX770 (Figure 2.10A). Similar to the nHBE cells, though, in C18-corrected cfHBE cells, apical conductance again was decreased by WT SMase from 2.31 ± 0.33 mS/cm² to 1.66 ± 0.28 mS/cm², a 28% decrease (Figure 2.14B). This indicates that WT SMase inhibited CFTR-mediated apical membrane conductance in cfHBE cells corrected and potentiated by FDA-approved small molecule modulators. Interestingly, though, the mean of the basolateral conductance was not affected by WT SMase, even though the variability increased relative to the control (Figure 2.14C). Furthermore, SMase did not affect the capacitance at either the apical or the basolateral membrane (Figure 2.14D-E). This does not match what was seen in nHBE cells, where conductance at both membranes was inhibited and the capacitance at both membranes was affected. More work is necessary to understand these discrepancies.

2.4 Discussion

The data presented here indicate that acute basolateral exposure to WT SMase decreases transepithelial CFTR currents in nHBE cells, nHTE cells, and chemically corrected cfHBE cells. Furthermore, as found previously (266), VX770 did not recover currents in nHBE cells or corrected cfHBE cells treated with WT SMase. It remains to be determined if these reduced currents were due to decreased secretion of chloride, bicarbonate, or both. Note that we distinguish between a reduction of current (indicative of the net vectorial movement of ions) and an inhibition of membrane conductance (indicative of the potential for total movement of ions in both directions). Reduced transepithelial currents can be caused by reduced apical membrane conductance, reduced basolateral membrane conductance, reduced paracellular conductance, or any combination of these.

Figure 2.14. Apical conductance (G_a) was decreased but basolateral conductances (G_b) was unaffected by WT SMase in C18-corrected cfHBE cells (a single biological replicate), as determined by impedance analysis. (A) A representative Nyquist Plot is shown of cfHBE cells corrected with 6 μM C18 for 24 hr at baseline (red), after 30 min of 1 $\mu\text{g/mL}$ enzyme-dead H322A SMase basolaterally and 6 μM benzamil apically (green), and after 10 μM forskolin and 1 μM VX770 (blue). The (B) G_a and (C) G_b after forskolin and VX770 in these C18-corrected cfHBE cells treated basolaterally with either 1 $\mu\text{g/mL}$ H322A (black, $n=4$) or WT SMase (grey, $n=7$) were analyzed by unpaired two-tailed t tests. These analyses indicate that WT SMase significantly decreased G_a (** $p=0.0072$) but did not affect G_b ($p=0.4369$).



We determined in this study that WT SMase does not affect paracellular flux, leaving only apical and/or basolateral conductance as the causes of changes to transepithelial current. While previous work in Calu-3 cells attempted to isolate the apical and basolateral membrane conductances by utilizing the pore-forming antifungal nystatin (269), we chose not to use this technique. Since both WT SMase and nystatin perturb lipid rafts, with WT SMase disrupting sphingomyelin and nystatin disrupting cholesterol, the use of both could cause competition between them (280; 318). Instead, we utilized the non-destructive impedance analysis method to study intact epithelia.

Using impedance analysis, we found that WT SMase decreased transepithelial CFTR currents in part by inhibiting CFTR-mediated apical membrane conductance in nHBE cells and corrected cfHBE cells. Furthermore, in nHBE cells, impedance analysis revealed that WT SMase decreased basolateral membrane conductance. This decreased basolateral conductance likely was due to decreased activity of potassium channels, which contribute to transepithelial anion secretion by repolarizing the membrane potential thereby driving anions out of the cell across the apical membrane. Thus, in future experiments to understand the mechanism of WT SMase-mediated inhibition of CFTR current in nHBE cells, it will be important to perform impedance analysis experiments to distinguish effects at the apical vs the basolateral membrane. Interestingly, though, decreased basolateral conductance was not seen in cfHBE cells. These results suggest that WT SMase acts on both apical and basal membrane conductance in nHBE cells but only the apical membrane conductance of corrected cfHBE cells. The reason for this discrepancy remains to be explored.

In apparent contradiction to our findings, it was found that treating CFBE410^o and nHBE cells acutely with the acid-SMase inhibitor amitriptyline reduced sequential VIP and forskolin-elicited transepithelial currents (280). Abu-Arish *et al.* found that VIP stimulation resulted in an acid-SMase-dependent increase in ceramide, which formed platforms where CFTR clustered. Furthermore, VIP stimulation caused an increase in surface expression of CFTR. Acute amitriptyline treatment, without affecting the surface expression of acid-SMase, prevented both the acid-SMase-dependent generation of ceramide and the increased surface expression of CFTR caused by VIP stimulation (280). While this appears to conflict with our results obtained with bacterial WT SMase, these authors did not evaluate

forskolin treatment independent of VIP treatment, which is what we evaluated here. Furthermore, amitriptyline causes a functional inhibition of acid-SMase by accumulating in the lysosome and inducing dissociation of acid-SMase from the lysosomal membrane, resulting in its proteolysis (319). Amitriptyline is not specific to acid-SMase in this mechanism of lysosomal membrane dissociation and subsequent proteolysis (197; 198; 320), and thus has off-target effects that need to be considered. Furthermore, it does not make mechanistic sense for amitriptyline to have affected surface acid SMase activity without affecting its expression, again, since amitriptyline causes the degradation of acid SMase in the lysosome, not at the surface of the cell.

Given the data presented thus far, it is relevant to determine the mechanism of WT SMase-mediated decreases in CFTR activity in HBES. Our observed lack of acute-VX770-mediated recovery in cells treated with WT SMase does give some insight into the mechanism of inhibition. The fact that VX770 does not rescue the decreased forskolin-elicited or INH172-sensitive current or conductance indicates that WT SMase does not reduce CFTR-mediated currents and conductances by reducing PKA-mediated phosphorylation. As we showed in nHBE cells, a reduced level of PKA phosphorylation allows for greater VX770-mediated potentiation of CFTR-mediated currents, not less (73). Thus, if WT SMase was inhibiting CFTR activity by decreasing PKA phosphorylation, VX770 would have recovered the CFTR-mediated current and conductance. Similarly, we showed that WT SMase inhibits CFTR channels made independent of PKA-mediated phosphorylation by removal of the regulatory (R-) domain – which bears the sites phosphorylated by PKA – when these channels are expressed in *Xenopus* oocytes (266). A mechanism unrelated to PKA-mediated phosphorylation must be involved, and this mechanism must be determined to develop potential therapeutic strategies to negate WT SMase-mediated decreases in CFTR currents in bronchial epithelial cells.

It is also important to determine the clinical relevance of the effects of WT SMase on these cells. This includes determining the imbalance of sphingolipids as well as sphingolipid modulating enzymes in cfHBE cells compare to nHBE cells. Recent evidence from multiple laboratories using multiple methods, including thin-layer chromatography and mass spectrometry, has indicated that ceramides are increased in

polarized bronchial epithelial cells from people living with CF (homozygous or heterozygous for the $\Delta F508$ -CFTR mutation), as compared to cells from non-CF subjects (193; 194). One of these papers suggested that this imbalance could be due to decreased activity of acid-CDase, though increased acid-SMase activity was also observed (194). However, conflicting data also has been found in which overall ceramide levels are decreased in CF cells compared to non-CF cells, though the ratio of long-chain ceramides to very-long-chain ceramides is increased (146). Due to this conflicting data, it will be important for other groups to evaluate sphingolipid imbalances in cfHBE cells compared to nHBE cells.

CHAPTER 3 – MECHANISTIC ANALYSIS AND SIGNIFICANCE OF SMASE-MEDIATED DECREASES IN TRANSEPITHELIAL CFTR CURRENTS IN HBE CELLS

Preface: Much of the text and figures presented here are reproduced from a portion of a manuscript submitted to *American Journal of Physiology: Lung, Cellular, and Molecular Physiology* in April 2021, which was transferred to *Physiological Reports* in June 2021 and is currently in revision. There were multiple goals for this manuscript, including 1) determining the mechanism by which SMase decreases transepithelial CFTR currents in bronchial epithelial cells and 2) determining the clinical relevance of sphingolipid imbalances as SMase enzyme activity in CF. I performed all experiments, in some cases with assistance from co-authors or Cores. I also analyzed all data and wrote the manuscript.

It is important to acknowledge the lab of Dr. Joanna Goldberg for the use of their cooled incubator, sonicator, and centrifuge to purify SMase. This work was supported by Georgia Institute of Technology's Systems Mass Spectrometry Core Facility, which performed mass spectrometry lipidomics experiments that I then analyzed. This work also was supported by the CF@LANTA Biorepository and Experimental Models Core, which collected, grew, and differentiated primary pulmonary epithelial cells. These were the cells used for the vast majority of the experiments in this chapter, with the exception of the AMPK inhibitor experiments which utilized cells grown in the Dr. Robert Bridges laboratory.

- **Cottrill KA**, Giacalone VD, Margaroli C, Bridges RJ, Koval M, Tirouvanziam, & McCarty NA. 2021. Mechanistic analysis and significance of sphingomyelinase-mediated decreases in transepithelial CFTR currents in nHBES. *Physiol Report*. In revision.

3.1 Introduction

As stated multiple times thus far, CF is caused by loss of function in CFTR, an apically located

chloride and bicarbonate ion channel in airway epithelial cells (38; 39). CFTR is activated by PKA-mediated phosphorylation of its R-domain and is gated by the binding and hydrolysis of ATP (15; 41). Currently, most people living with CF succumb to pulmonary failure caused in part by chronic airway obstruction, immune cell infiltration, and lung infections (21; 283).

Fortunately, highly effective modulator therapies have been developed recently that target the primary CFTR defect (284; 285), as discussed in section 1.3. However, we have shown in chapter 2 that these modulator therapies are unable to recover a loss of CFTR currents and CFTR-mediated apical membrane conductance following exposure to the bacterial virulence factor SMase (266; 321). SMase converts sphingomyelin into ceramide and phosphocholine. Sphingolipids are well known to be involved in CF inflammatory lung disease, as has been detailed elsewhere (289). Harmful stimuli such as oxidative stress, tumor necrosis factor α , and lipopolysaccharide, all associated with the CF lung (290; 291), can increase the activity of endogenous neutral-SMase as well as the secretion and activity of endogenous acid-SMase in lung epithelial cells (292-295). Furthermore, *P. aeruginosa* and *S. aureus*, the two bacteria most commonly found in CF airways (21), both secrete enzymes with SMase activity (296; 297).

To add to the relevance of this question, much work has been done recently that identifies sphingolipid imbalances in CF bronchial epithelial cells compared to non-CF controls, as reviewed in section 1.5. Dihydroceramides increase under hypoxic conditions and are increased in bronchial epithelial cell models of CF (189; 322). Furthermore, multiple groups have found that ceramides are increased in primary cfHBE cells (homozygous or heterozygous for the $\Delta F508$ -CFTR mutation), as compared to nHBE cells (193; 194). Importantly, however, conflicting data also has been found in which overall ceramide levels are decreased in CF cells compared to non-CF cells. In this instance, it was also found that the ratio of long-chain ceramides to very-long-chain ceramides was increased (146). The reason for this discrepancy in results between labs can only be speculated upon at this time.

Given the relevance of these sphingolipid imbalances and their modulating enzymes, more work is needed to understand the mechanism of SMase-mediated inhibition of transepithelial CFTR currents. Decreased transepithelial anion current after SMase treatment could be due to the loss of sphingomyelin,

the production of phosphocholine or ceramide, the production of ceramide derivatives such as sphingosine-1-phosphate, some combination of these, or some other effect of SMase. Furthermore, lipids have the potential to affect membrane channel activity by a number of means (Figure 1.7), namely: modulating membrane mechanics, directly interacting with the channel and affecting its structure/function, changing surface localization of the channel (either total surface localization or microdomain localization), and initiating signaling cascades that result in modifications to the channel (323).

One of the goals of the work presented here was to understand in more detail the mechanism by which SMase decreased transepithelial anion currents in primary airway epithelial cells. Another goal was to determine the sphingolipid imbalance in CF airway epithelial cells as compared to non-CF control cells, given the conflicting current literature discussed above. Furthermore, we were interested in the effects of relevant CFTR modulators on this sphingolipid imbalance, because again conflicting literature exists (146; 324). Lastly, we sought to determine the relevance of acid-SMase secretion from bronchial epithelial cells, as well as from airway-like neutrophils, which are prevalent in the CF lung (325).

3.2 Materials and methods

Unless otherwise specified, chemical reagents were purchased from MilliporeSigma.

3.2.1 Airway epithelial cells from human donors

Two different methods for preparing and culturing primary airway epithelial cells were used, as described in section 2.2.1. For CF cells (cfHBE, cfHNE), which were homozygous for the $\Delta F508$ -CFTR mutation, CFTR was corrected by either 3 μM VX809 for 24 hr, 5 μM VX445 plus 18 μM VX661 for 48 hr, or 5 μM VX445 plus 18 μM VX661 and 1 μM VX770 for 48 hr (all VX compounds were from Selleckchem). For these treatments, medium with drugs was replenished every 24 hr.

3.2.2 Purification of bacterial SMase

Recombinant *S. aureus* SMase were purified as described in section 2.2.3.

3.2.3 *Lipidomics mass spectrometry*

Lipidomics mass spectrometry was performed as described in section 2.2.4.

3.2.4 *Short-circuit current measurements*

Short-circuit current experiments using an Ussing chamber were performed as described in section 2.2.5. To inhibit CDase, 4 μ M ceranib-1 (Tocris) was added. To inhibit AMPK, 20 μ M BML-275 (Tocris) was added. The currents elicited by each treatment were calculated as the average of the final ten seconds prior to the next treatment.

3.2.5 *Analysis of surface expression of CFTR in nHBE cells*

Cells were first washed with Dulbecco's PBS with calcium and magnesium (DPBS), then equilibrated in normal chloride buffer, treated with 1 μ g/mL SMase basolaterally for 30 min, then with 20 μ M amiloride apically, and lastly treated with 10 μ M forskolin. Cells were washed with ice cold DPBS and incubated with 0.5 mg/mL cell-impermeable EZ-LinkTM Sulfo-NHS-SS-Biotin (Thermo Fisher) apically on ice for 45 min. The biotinylation solution was removed, and excess Sulfo-NHS-SS-Biotin was quenched with ice cold solutions of 50 mM Tris (pH 7.4), 100 mM glycine in 50 mM Tris, and 1 mM oxidized glutathione (Acros Organics) in DPBS. Cells were scraped from the filter and lysed for 30 min on ice in RIPA buffer (Boston BioProducts) with 3 mM EDTA and 1:100 protease inhibitor cocktail specific for CFTR (5 mg/mL AEBSF, 250 μ g/mL chymostatin, 500 μ g/mL E64, 1.25 mg/mL leupeptin, 1.25 mg/mL pepstatin (VWR), 17.4 mg/mL PMSF (Amresco), 250 μ g/mL bestatin, 36 mg/mL benzamidine)) (326). Cell debris was pelleted at 5,000 xg for 5 min at 4 °C, and the supernatant was retained as the total cell lysate. This cell lysate was incubated overnight at 4 °C with Protein A/G beads (Santa Cruz) coupled to CFTR antibody 24-1 (R&D) according to the manufacturer's protocol. Beads were pelleted at 1,000 xg for 1 min, washed with DPBS three times, and protein was eluted in 2x sample buffer without any reducing

agent at 37 °C for 30 min.

3.2.6 *Neutrophil transmigration*

Neutrophils were isolated from blood of non-CF donors under a protocol approved by the Emory University IRB and were transmigrated through H441 epithelial cell monolayers using leukotriene B4 (LTB4) as a chemoattractant on the apical side, as described (327).

Briefly, 250,000 H441 cells were cultured on Alvetex[®] membranes (ReproCell) coated with 3 mg/mL of rat tail collagen I, with DMEM + 10% FBS + 1% penicillin/streptomycin (pen/strep) + 1% L-glutamine. The next day, cells were transitioned to ALI by removing apical medium and replacing basolateral medium with DMEM/F12 + 2% Ultrosor-G (Crescent Chemicals) + 1% pen/strep + 1% L-glutamine. Neutrophil transmigration assays were performed 14 days after establishing H441 cells at ALI.

For neutrophil isolation, blood was collected into K2-EDTA tubes, layered onto PolymorphPrep[™] (Progen), then centrifuged at 400 xg for 45 min at 21 °C. The neutrophil band was collected with a Pasteur pipet, then washed in 0.45% NaCl and centrifuged at 800 xg for 5 min at room temperature. Remaining erythrocytes were lysed by hypotonic shock. Neutrophils were resuspended in RPMI medium + 10% FBS, then counted and assessed for purity and viability with ethidium bromide + acridine orange staining. Our experiments showed > 95% viability and <1% contamination of the neutrophil sample with other cells.

For transmigration, filters with H441 cells were inverted, LTB4 (100 nM) was added to the bottom RPMI medium (the apical side of the cells), and neutrophils (1.5 million/well) were added to the top RPMI medium (basolateral side of the cells). Transmigration was allowed to progress for 6 hr at 37 °C in a cell culture incubator with 5% CO₂, at which point transmigrated neutrophils were collected from the apical medium by centrifugation at 800 x g for 10 min at 4°C. Cells were then counted and assessed for viability and epithelial cell contamination. Our experiments showed > 95% viability and <1% contamination of the neutrophil sample with epithelial cells.

Where indicated, transmigrated neutrophils were allowed to condition medium (RPMI + 10% FBS, 4 million cells/mL) for 4 hr at 37 °C in a cell culture incubator. Conditioned medium was collected and

centrifuged at 800 xg for 5 min at 4 °C to separate out the neutrophils. The cell-free supernatant (conditioned medium) had protease inhibitor cocktail and EDTA added, then was flash frozen in liquid nitrogen and stored at -80 °C for further analysis. The neutrophil pellet was resuspended, and neutrophils were counted and evaluated for cell death. Our experiments showed ~7% cell death after 4 hr of incubation in conditioning medium. Neutrophils then were re-pelleted and flash frozen in liquid nitrogen, then stored at -80 °C for further analysis. For analysis, they were lysed in RIPA buffer with protease inhibitor cocktail and EDTA.

3.2.7 *Western blot analysis*

For analysis of acid-SMase in HBE cells, 6x sample buffer and 48 mM DTT were added to the samples. For biotinylation experiments and analysis of acid-SMase in neutrophils, no DTT was added. Samples then were boiled at 95 °C for 10 min. Samples then were run by sodium dodecyl sulfate-polyacrylamide gel electrophoresis using Bio-Rad, Mini-PROTEAN TGX, 4-15% gels. The gel was transferred to a nitrocellulose membrane (Bio-Rad, 0.2 µM), which then was blocked in Licor® Intercept™ buffer. All subsequent probing agents were maintained in blocking buffer with 0.01% Tween 20.

Biotinylated CFTR was evaluated using a Licor® IRDye® 680LT Streptavidin probe incubated at 1:5,000 overnight at 4 °C. The blot was imaged on a Licor® Odyssey, then stripped using Licor® NewBlot™ Nitro Stripping buffer according to the manufacturer's protocol. The blot was reimaged to confirm sufficient removal of the original probe, re-blocked, then incubated with 1:1,500 anti-CFTR 596 antibody (University of North Carolina) at room temperature for 2 hr. The blot was then washed three times in PBS with 0.01% Tween 20 and incubated with 1:10,000 Licor® goat anti-mouse 680 antibody for 1 hr at room temperature. The blot was washed and again imaged to evaluate total CFTR in the eluate.

Acid-SMase was also analyzed in nHBE and cfHBE cells. Basolateral medium was collected 72 hr after addition of fresh medium to the cells, except in the case of cfHBE cells treated with correctors, in which the medium was changed every 24 hr. Cells were collected and pooled from six Transwells and lysed as indicated above. Acid-SMase and total protein were evaluated in both lysates and medium. Cellular and

secreted acid-SMase was evaluated by a similar protocol as above using 1:200 anti-SMPD1 AF5348 antibody (R&D) overnight at 4 °C, followed by 1:5,000 Licor[®] donkey anti-goat 680 antibody for 1 hr at room temperature. Total protein was probed with Ponceau S staining of the nitrocellulose blot for 1 min, followed by a PBS wash. In the cell lysate lanes, acid-SMase density was normalized to a prominent Ponceau-stained band. In the basolateral medium lanes, acid-SMase density was normalized to the most prominent Ponceau-stained band, likely corresponding to BSA at 66 kDa.

Image J software was used to conduct densitometry analysis on the appropriate bands of interest. Biotinylation bands of interest were determined by visual alignment with the corresponding CFTR bands.

3.2.8 *Statistical analyses*

Data were exported to and processed in Excel, unless otherwise noted. Statistical analyses were conducted and graphs were made using GraphPad PRISM software, with α set at 0.05 according to common practice. Data were excluded based on Grubb's outlier tests with α set at 0.05, or in cases of technical experimental issues. In all cases, data are represented as the mean and standard deviation. In many cases, the individual data points are plotted. Specific statistical tests as well as the significance values are listed in the figure legends, but included unpaired, two-tailed *t* tests; multiple *t* tests without correction; and two-way ANOVAs, utilizing the Tukey correction recommended by PRISM if multiple comparisons were used.

3.3 **Results**

3.3.1 *Inhibiting CDases with ceranib-1 affects CFTR currents similarly to WT SMase*

We have shown in section 2.3.2 that acute basolateral WT SMase treatment decreases transepithelial CFTR currents in nHBE, nHTE, and nHAE cells (266; 321). We sought to determine whether the decreased CFTR currents after WT SMase treatment were due to decreased sphingomyelin, increased ceramide, or increased ceramide derivatives such as sphingosine or sphingosine-1-phosphate. To determine if any ceramide break-down product was the cause for reduced CFTR currents following WT SMase treatment, we minimized the conversion of ceramide into sphingosine by treating nHAE cells acutely with

the CDase inhibitor ceranib-1 while evaluating short-circuit currents.

First, we replicated our previous results showing that WT SMase decreases transepithelial CFTR currents (Figure 3.1A). Specifically, in nHAE cells, 30-minute treatment with 1 $\mu\text{g}/\text{mL}$ WT SMase decreased the maximum forskolin-elicited currents from $27.1 \pm 1.4 \mu\text{A}/\text{cm}^2$ to $18.6 \pm 1.3 \mu\text{A}/\text{cm}^2$ (approximate 31.5% decrease), decreased VX770-potentiated currents from $27.4 \pm 1.3 \mu\text{A}/\text{cm}^2$ to $18.2 \pm 1.7 \mu\text{A}/\text{cm}^2$ (approximate 33.6% decrease), and decreased INH172-sensitive current from $26.2 \pm 3.0 \mu\text{A}/\text{cm}^2$ to $18.1 \pm 1.6 \mu\text{A}/\text{cm}^2$ (approximate 30.6% decrease), as compared to the enzyme-dead H322A SMase control (Figure 3.1B-D). Preventing the conversion of ceramide into sphingosine (and other derivatives) by treating with ceranib-1 did not mitigate WT SMase-mediated decreases in forskolin-elicited, VX770-potentiated, or INH172-sensitive CFTR currents (Figure 3.1B-D). This suggests that a ceramide derivative is not the cause of SMase-mediated inhibition of CFTR currents.

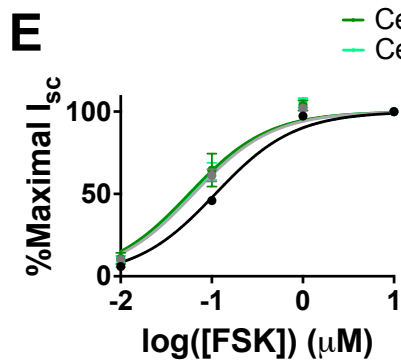
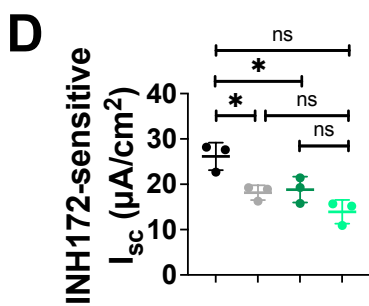
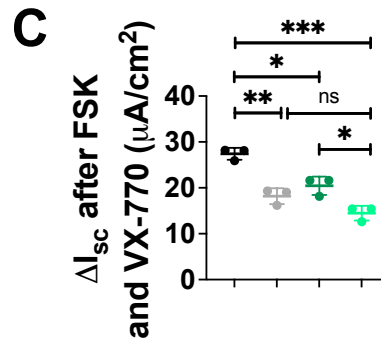
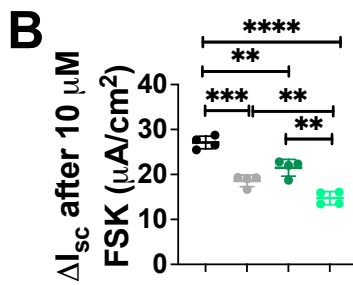
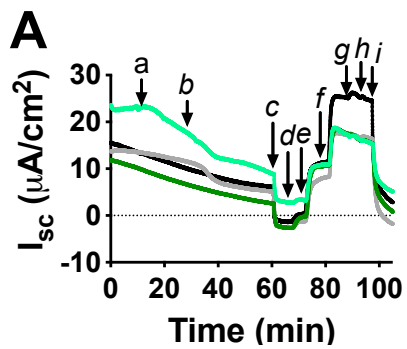
In fact, ceranib-1 treatment exacerbated the WT SMase-mediated decrease of forskolin-elicited currents, relative to WT SMase or ceranib-1 treatment alone (Figure 3.1B). Note that while this trend remained in the VX770-potentiated and INH172-sensitive currents, the results did not reach statistical significance, likely due to a smaller number of replicates. Relatedly, though, 1 hr ceranib-1 treatment alone decreased the maximum forskolin-elicited currents to $21.5 \pm 1.9 \mu\text{A}/\text{cm}^2$ (approximate 20.8% decrease), decreased VX770-potentiated currents to $20.5 \pm 2.0 \mu\text{A}/\text{cm}^2$ (approximate 25.3% decrease), and decreased INH172-sensitive current to $18.8 \pm 2.8 \mu\text{A}/\text{cm}^2$ (approximate 28.0% decrease), as compared to the DMSO with H322A SMase control (Figure 3.1B-D). This was similar to the DMSO with WT SMase treatments.

These data indicate that ceranib-1 and WT SMase each decrease CFTR currents, but the question remained whether they utilize the same mechanism or different mechanisms to facilitate this reduction of current. Analysis of the forskolin-mediated activation of CFTR indicated that WT SMase, ceranib-1, and the combination of these treatments shifted the dose-response curve left relative to the control treatment (Figure 3.1E). Interestingly, data from all three of these treatments could be fit with the same curve, suggesting that the ability to activate CFTR (dependent on adenylyl cyclase, PKA, and ATP) was the same following SMase treatment, ceranib-1 treatment, and dual treatment of SMase and ceranib-1. This indicates

Figure 3.1. Inhibiting CDases with ceranib-1 caused a decrease in CFTR currents and enhanced the

WT SMase-mediated inhibition of CFTR. (A) A representative example of an Ussing chamber trace of

area-corrected short-circuit currents from nHAE cells is shown. Cells stabilized for 5-10 min, at which point (a) 4 μ M ceranib-1 or an equivalent volume of DMSO was added. At the 30-minute timepoint, (b) 1 μ g/mL enzyme-dead H322A (with DMSO control, black, n=3-4; with ceranib-1 treatment, dark green, n=3-4) or WT SMase (with DMSO control, grey, n=3-4; with ceranib-1 treatment, light green, n=3-4) was added basolaterally. After 30 min, (c) 20 μ M amiloride was added apically. Then, (d-g) 0.01, 0.1, 1, and 10 μ M forskolin was added. Currents were potentiated by (h) 1 μ M VX770, and finally were inhibited by (i) 10 μ M INH172. Changes in current were evaluated by unpaired two-tailed *t* tests. (B) The change from the post-amiloride current to the current after the final dose of forskolin (forskolin-elicited) was decreased by WT SMase alone (dark grey vs black, ****p*=0.0010) and ceranib-1 alone (medium grey vs black, ***p*=0.0029). Ceranib-1 did not prevent WT SMase-mediated decreases in currents (light grey vs black, *****p*<0.0001), but rather enhanced them (light grey vs dark grey, ***p*=0.0076). In addition, WT SMase enhanced the ceranib-1-mediated decreases in current (light grey vs medium grey, ***p*=0.0013). (C) The change from the post-amiloride current to the current after VX770 (VX770-potentiated) was decreased by WT SMase alone (***p*=0.0018) and ceranib-1 alone (***p*=0.0073). Ceranib-1 did not prevent WT SMase-mediated decreases in currents (****p*=0.0001). Significance was not quite reached to determine that ceranib-1 enhanced WT SMase-mediated decreases in current (*p*=0.0529), but WT SMase did enhance ceranib-1-mediated decreases in current (**p*=0.0156). (D) The change from the post-VX770 current to the current after INH172 (INH172-sensitive) was reduced by WT SMase alone (**p*=0.0157) and ceranib-1 alone (**p*=0.0377). Lastly, (E) forskolin dose-response curves were generated by normalizing forskolin-elicited currents to the current elicited by the maximum concentration of forskolin within each replicate, and then fitting points with a non-linear fit of log(agonist) vs. normalized response using Prism. A comparison of fits determined that one equation could fit the data for DMSO+H322A SMase, and a different equation fit the data for all the other treatments. This indicates that CFTR is in one activatable state under control conditions, but a different and common activatable state under the other conditions.



— DMSO and H322A SMase
 — DMSO and WT SMase
 — Ceranib-1 and H322A SMase
 — Ceranib-1 and WT SMase

that WT SMase and ceranib-1 likely decrease CFTR currents via the same mechanism, especially given that dual SMase and ceranib-1 treatment did not further shift the dose-response curve from either treatment alone. However, it is still possible that they elicit their effects via different mechanisms. More work is necessary to determine the specific mechanisms of SMase- and ceranib-1-mediated decreases in transepithelial CFTR currents.

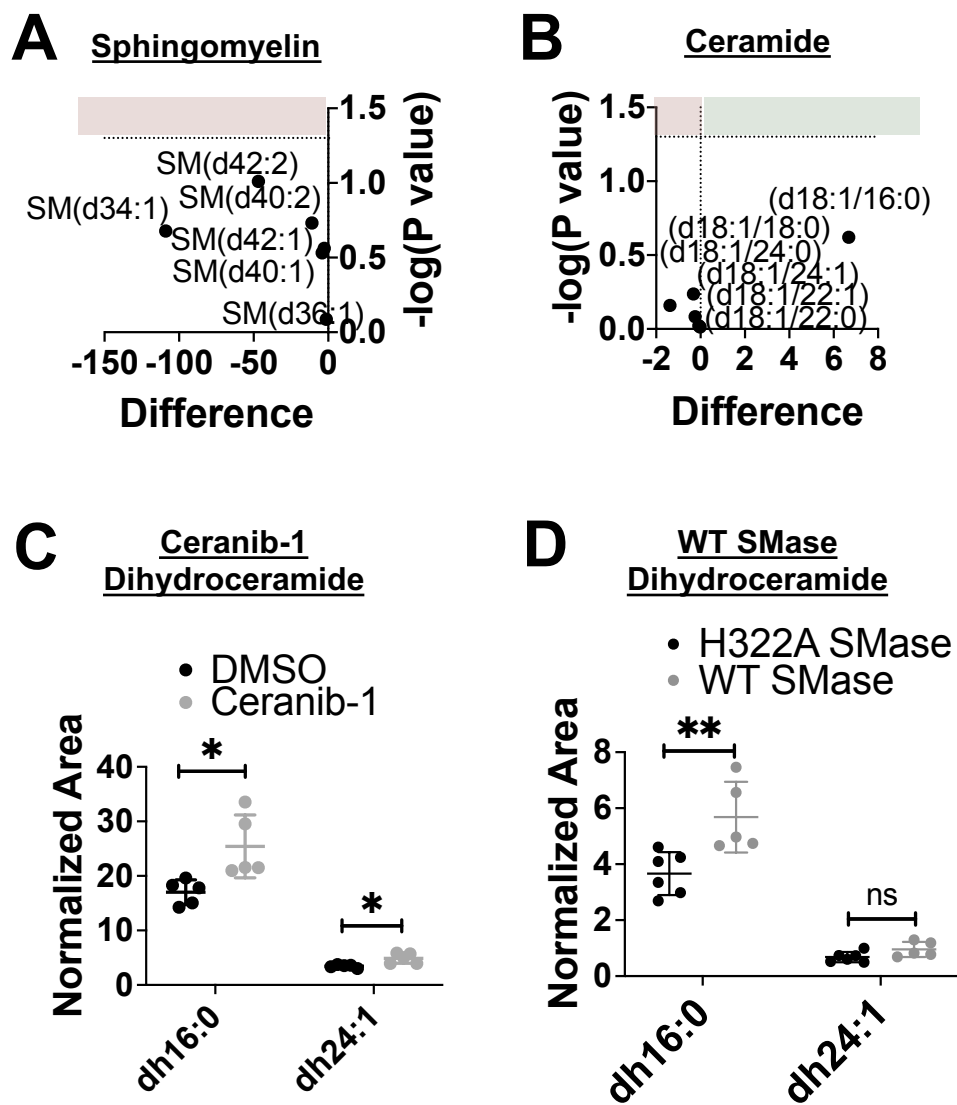
3.3.2 Ceranib-1 affects total cellular dihydroceramides, as does SMase

In order to determine if WT SMase and ceranib-1 treatment generated similar changes in sphingolipids, we performed lipidomics mass spectrometry analysis. We have shown that WT SMase treatment decreases all sphingomyelins and increases all ceramides of interest (section 2.3.1). Analysis of nHAE cells acutely treated with ceranib-1 indicated that ceranib-1 caused no significant effect on bulk cellular sphingomyelins or ceramides (Figure 3.2A-B). Localized effects on sphingomyelin and ceramide cannot be ruled out, though, and future experiments should evaluate plasma membrane sphingolipids specifically. However, it was determined that ceranib-1 significantly increased two dihydroceramides (dh16:0 and dh24:1) which correspond to the two highest abundance ceramides (Figure 3.2C). Interestingly, WT SMase treatment also increased the dh16:0 dihydroceramide in nHBE cells, and almost significantly increased the dh24:1 dihydroceramide (Figure 3.2D). Thus, ceranib-1 shares a mechanism with WT SMase either by increasing dihydroceramides, or by increasing ceramides in a localized manner undetectable by whole-cell lipidomics analysis, or both.

3.3.3 No decrease in relative CFTR surface expression was detected following SMase treatment

To continue to explore how WT SMase decreases transepithelial CFTR currents, we assessed potential effects on surface expression. Utilizing the cell-impermeable Sulfo-NHS-SS-Biotin compound, we labeled all apical membrane proteins at the surface of nHBE cells to compare the abundance of surface-CFTR following treatment with either H322A or WT SMase. Note that DTT was not used in these experiments, as it would cleave the disulfide bond and remove the biotin label. Representative figures for

Figure 3.2. Lipidomics mass spectrometry analysis indicated that ceranib-1 increased dihydroceramides. The (A) sphingomyelin and (B) ceramide data were analyzed by multiple *t* tests. These data are plotted as volcano plots, with the difference in normalized peak area on the x-axis, and the $-\log(P)$ value on the y-axis. Anything in the green box was increased by ceranib-1, whereas anything in the red box was decreased by ceranib-1. Sphingomyelins and ceramides were unaffected by ceranib-1 treatment over this time course. However, (C) two dihydroceramide species were increased by ceranib-1 treatment (grey, $n=5$) as compared to DMSO control (black, $n=5$) (dh16:0, $*p=0.0161$; dh24:1, $*p=0.0105$). (D) WT SMase (grey, $n=5$) increased the dh16:0 dihydroceramide compared to the enzyme-dead H322A SMase control (black, $n=6$) ($**p=0.0095$), but not quite the dh24:1 species ($p=0.0780$).



total CFTR and biotinylated surface CFTR are shown (Figure 3.3A-B). Biotinylated CFTR density was normalized to total CFTR density to account for differential effects of cell collection, lysis, and loading. WT SMase caused relative surface CFTR to be $104 \pm 19\%$ of the H322A SMase treated control group. This was not statistically different from 100%, indicating that WT SMase did not cause a decrease in CFTR abundance at the apical surface of nHBE cells relative to total CFTR. This is consistent with our previous experiments in *Xenopus* oocytes and rules out decreased CFTR surface expression as the means by which basolateral WT SMase decreases apical membrane conductance (266). However, it is important to note that CFTR was not visible enough in the cell lysate lanes to be able to quantify total cellular CFTR. Thus, it remains possible that while surface expression of CFTR relative to total immunoprecipitated CFTR remains unchanged, overall levels of both surface-expressed and total cellular CFTR could be decreased by SMase. This would result in decreased transepithelial CFTR currents, and future experiments should determine if there is a change in total cellular CFTR following SMase treatment.

3.3.4 *AMPK is not involved in the WT SMase-mediated decrease in transepithelial CFTR currents*

In *Xenopus* oocytes, we found that intracellular components were necessary for a decrease in CFTR-mediated current following WT SMase treatment, indicating that a signaling mechanism was involved (266). Based on the above surface expression data in nHBE cells indicating a lack of SMase-induced internalization of CFTR, it is likely that a signaling mechanism is involved in nHBE cells as well. Both ceramide and dihydroceramide are known to activate AMPK (328; 329), which phosphorylates the CFTR R-domain at the inhibitory S737 and S768 sites (277; 330). Thus, we hypothesized that AMPK activation via the generation of ceramide and/or dihydroceramide was involved in WT SMase-mediated decreases in transepithelial CFTR current. In order to test this, we utilized the AMPK inhibitor dorsomorphin dihydrochloride (BML-275) (Figure 3.4).

We found that inhibiting AMPK with BML-275 did not prevent WT SMase-mediated reductions in the forskolin-elicited or INH172-sensitive currents in nHBE cells (Figure 3.4). Specifically, for the forskolin-elicited currents, within the control group WT SMase caused a 31% reduction of currents from

Figure 3.3. Surface biotinylation followed by a CFTR pull-down indicated that SMase did not decrease CFTR surface expression. Representative blots for (A) total loaded CFTR and (B) surface biotinylated CFTR are shown. (C) Densitometry analysis was performed, and total amount of biotinylated surface CFTR was normalized to the total amount of CFTR (n=3). A one-sample t test indicates no significant difference between these values and 100%, suggesting that WT SMase does not affect surface CFTR levels.

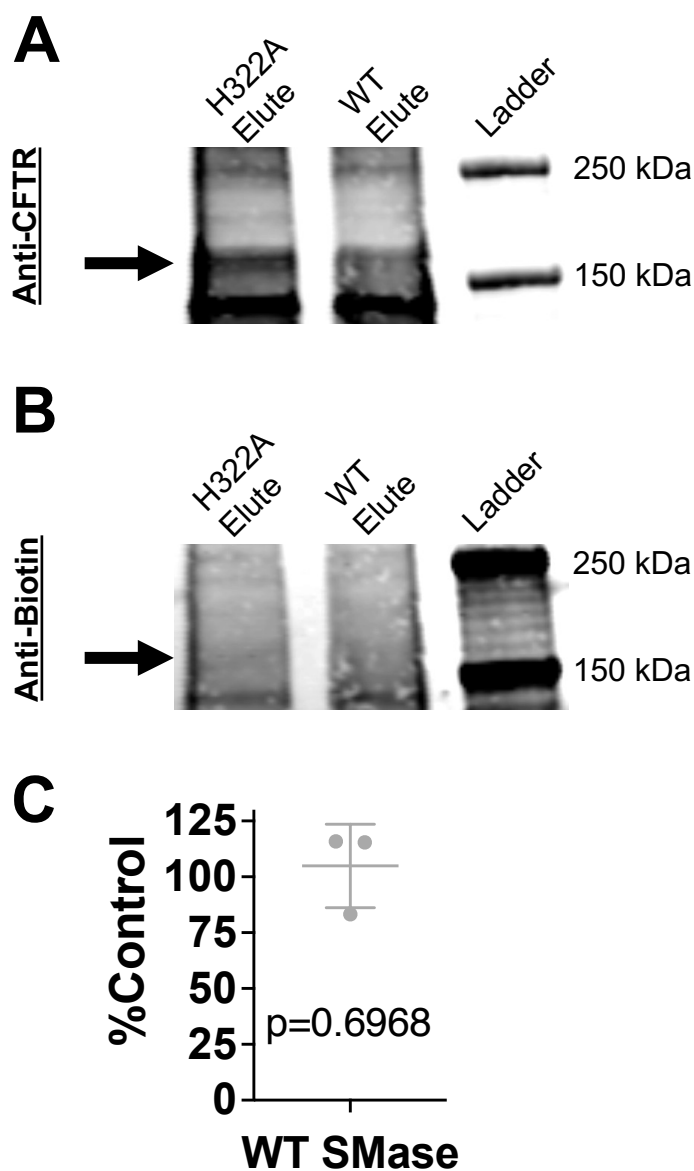
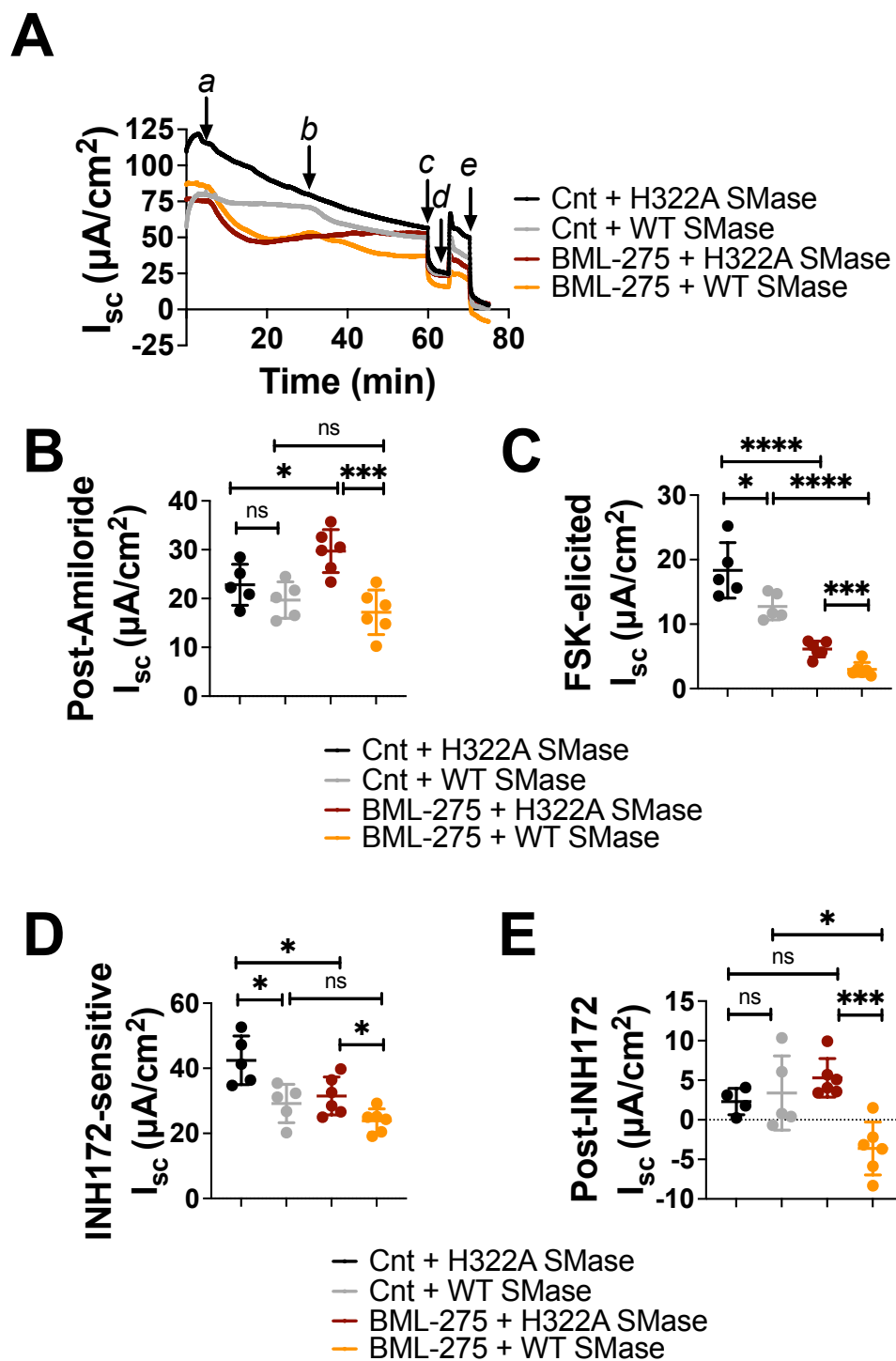


Figure 3.4. Inhibiting AMPK does not prevent WT SMase-mediated decreases in transepithelial

CFTR currents but does have other effects on currents. (A) An example area-corrected short-circuit current trace is shown of nHBE cells treated with either (a) 20 μ M BML-275 or vehicle control (Cnt), then (b) 1 μ g/mL either H322A (with Cnt, black, n=5; with BML-275 treatment, red, n=6) or WT SMase (with Cnt, grey, n=5; with BML-275 treatment, orange, n=6) basolaterally for 30 min. (c) ENaC was inhibited with 20 μ M amiloride apically, then (d) CFTR was activated with 10 μ M forskolin. Lastly, (e) CFTR was inhibited with 10 μ M INH172 apically. All data were analyzed by unpaired, two-tailed *t* tests. For these short circuit current analyses, n=4-6 for each group. (B) For the post-amiloride current, in the BML-275 group WT SMase caused a significant decrease ($***p=0.0007$), a phenomenon not seen in the control treatment ($p=0.2454$). However, BML-275 itself increased the post-amiloride current in the H322A SMase group ($*p=0.0267$). (C) For the forskolin-elicited current, the control and BML-275 groups both showed a WT SMase-mediated decrease in current ($*p=0.0302$; $***p=0.0008$). However, BML-275 itself decreased the forskolin-elicited currents in both the H322A and WT SMase groups ($****p<0.0001$). (D) For the INH172-sensitive current, both the control and BML-275 groups showed a WT SMase-mediated decrease in current ($*p=0.0144$; $*p=0.0218$). However, BML-275 itself decreased the INH172-sensitive currents in the H322A SMase group ($*p=0.0229$). (E) For the post-INH172 current, within the BML-275 group, there was a significant decrease caused by WT SMase ($***p=0.0007$), a phenomenon not seen in the control group ($p=0.2454$). However, BML-275 itself caused an almost significant increase in the post-INH172 current in the H322A SMase group ($p=0.0667$). Conversely, BML-275 caused a significant decrease in the post-INH172 currents in the WT SMase group ($*p=0.0177$).



$18.7 \pm 4.9 \mu\text{A}/\text{cm}^2$ to $12.9 \pm 1.9 \mu\text{A}/\text{cm}^2$, whereas in the BML-275 group WT SMase caused a 51% reduction of currents from $6.1 \pm 1.2 \mu\text{A}/\text{cm}^2$ to $3.0 \pm 1.1 \mu\text{A}/\text{cm}^2$. For the INH172-sensitive currents, within the control group WT SMase caused a 26% reduction of currents from $42.7 \pm 8.6 \mu\text{A}/\text{cm}^2$ to $31.5 \pm 8.0 \mu\text{A}/\text{cm}^2$, whereas in the BML-275 group WT SMase caused a similar 22% reduction of currents from $30.6 \pm 4.6 \mu\text{A}/\text{cm}^2$ to $23.8 \pm 3.6 \mu\text{A}/\text{cm}^2$. These data suggest that AMPK is not involved in the signaling pathway by which WT SMase decreases transepithelial CFTR currents. However, it is important to note that BML-275 had other effects on the cells, such as increasing the post-amiloride baseline current (Figure 3.4B), decreasing the forskolin-elicited current (Figure 3.4C), decreasing the INH172-sensitive current (Figure 3.4D), and affecting the post-INH172 current (Figure 3.4E); these findings suggest that the inhibitor was used at an effective concentration. While these effects must be considered when interpreting the data, we remain confident that inhibiting AMPK does not prevent WT SMase-mediated decreases in CFTR currents in nHBE cells.

3.3.5 *Ceramide and dihydroceramide levels in cfHBE compared to nHBE cells*

While some work already has been done to identify ceramide and dihydroceramide imbalances in CF bronchial epithelial cells compared to non-CF bronchial epithelial cells (189; 193; 194), much of the data is conflicting. Thus, we thought it important to assess these imbalances within our own cells and to determine the potential impact of culture conditions that may explain differences in results between laboratories.

First, we analyzed nHBE cells grown on T25 flasks for 7 days, Transwells for 8 days, and Transwells for 14 days to determine if ceramide or dihydroceramide levels changed over the course of differentiation. These data indicate that differentiation affects sphingolipid profiles, and that time on the Transwell is an important factor to control for when comparing cfHBE to nHBE cells (Figure 3.5). Keeping this in mind, we compared the sphingomyelin, ceramide, and dihydroceramide levels of multiple Transwells of a single biological replicate of cfHBE cells (homozygous for $\Delta\text{F508-CFTR}$) to multiple Transwells of a single biological replicate of nHBE cells (Figure 3.6A-D). In cfHBE cells relative to nHBE, four

Figure 3.5. Lipidomics analysis reveals that time on the Transwell affects the ceramides and dihydroceramide profiles of nHBE cells. Cells grown either on T25 flasks (black, n=6), on Transwells for 8 days (dark grey, n=4), or on Transwells for 14 days (light grey, n=4).

(A) A bar graph of normalized areas for each sphingolipid of interest is shown. (B-D) Data were analyzed by multiple t tests as described in Methods, and volcano plots were created. Lipids in the green box are increased in the comparative treatment, while lipids in the pink box are decreased. (B) All dihydroceramides and most ceramides increased when transitioning the cells from a T25 flask to a Transwell for 8 days. The exceptions were one decreased ceramide, and one ceramide that was unchanged. (C) By 14 days on the Transwell, this unchanged ceramide was found to be significantly decreased as compared to the T25 cells. (D) Also, by 14 days, one ceramide had further increased, one ceramide had further decreased, and dihydroceramide had decreased as compared to cells that were on the Transwells for 8 days. This indicates that time on the Transwell affects the sphingolipid profile. This must be taken into consideration during future experiments.

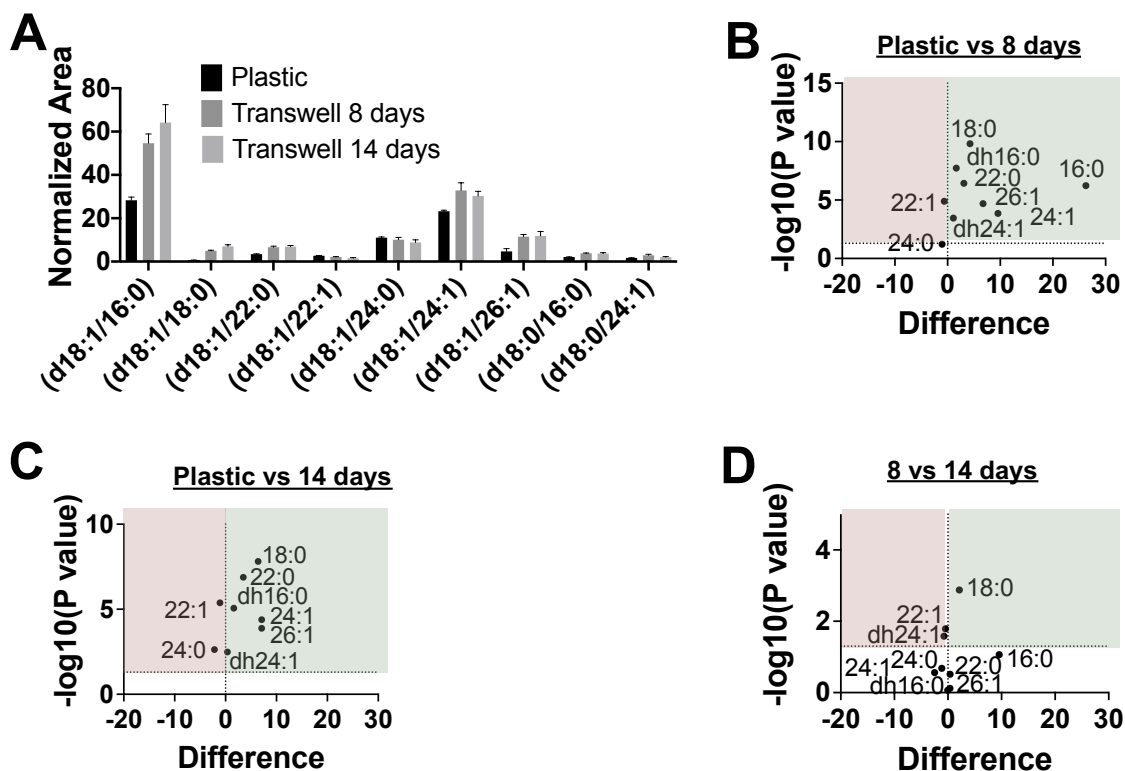
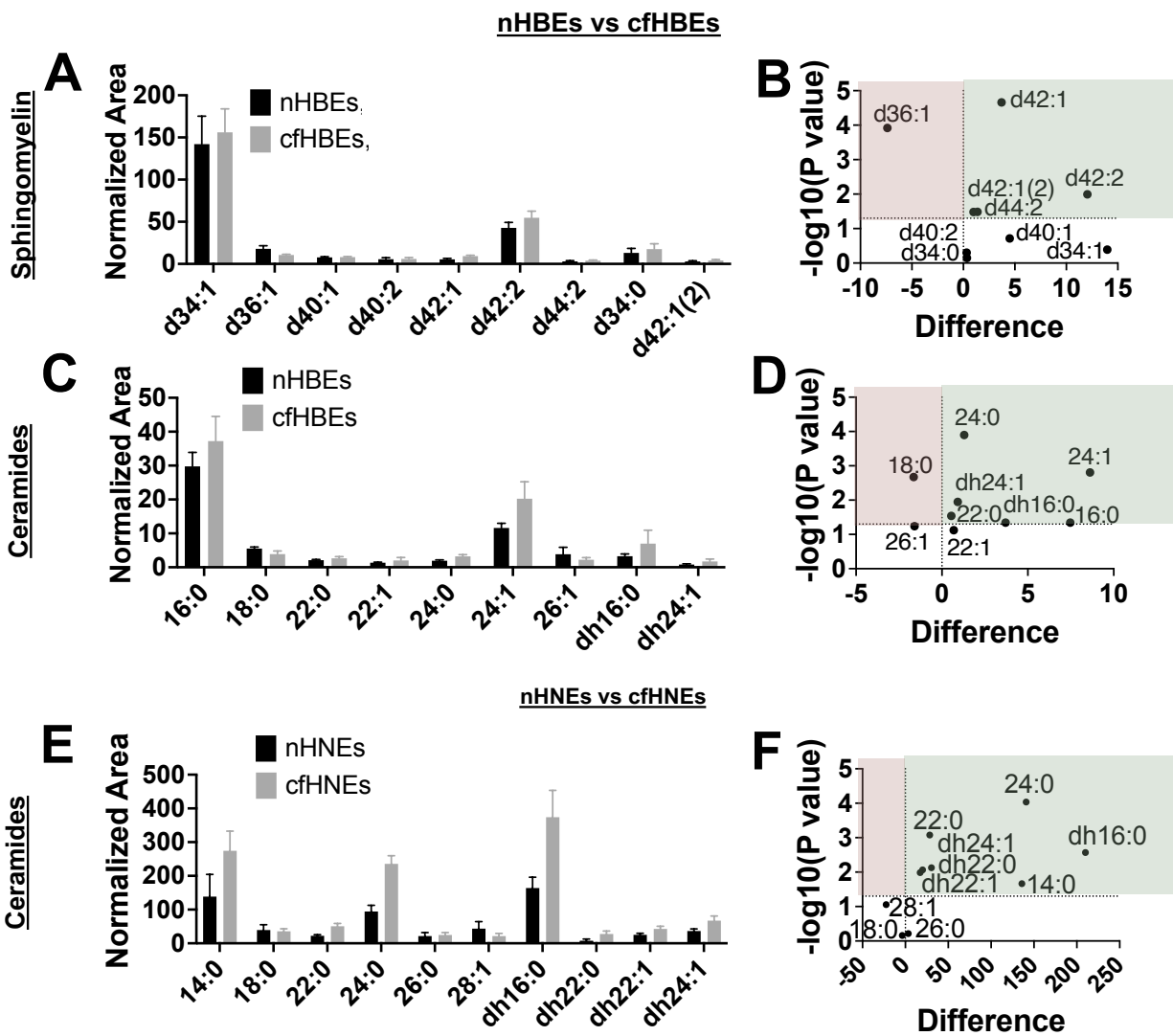


Figure 3.6. Lipidomics analysis of sphingolipid species in HBE and HNE cells indicate many increased sphingomyelins, ceramides, and dihydroceramides in the CF group. Bar graphs and volcano plots of the sphingolipid species are shown. For the volcano plots, anything in the green box was increased in the CF group, whereas anything in the pink box was decreased. Lipidomics analysis of a single biological replicate of cfHBE cells (n=8 Transwells) as compared to a single biological replicate of nHBE cells (n=6 Transwells) (a single biological replicate of each) was used to evaluate **(A-B)** sphingomyelins as well as **(C-D)** ceramides and dihydroceramides. Many sphingomyelins were increased, though one was decreased in cfHBE relative to nHBE cells. Most ceramides were increased, one ceramide was decreased, and two dihydroceramides were increased. **(E-F)** Lipidomics analysis of a single biological replicate of cf (n=4 Transwells) as compared to a single biological replicate of n (n=4 Transwells) indicated that most ceramides were increased, and all dihydroceramides were increased in cfHNE relative to nHNE cells, similar to the phenomenon seen in HBE cells.



sphingomyelins were increased (d42:1, d42:1 (2), d42:2, and d44:2). Based on the ceramides and dihydroceramides present, these likely correspond to 24:0 ceramide, dh24:1 dihydroceramide, 24:1 ceramide, and 26:1 ceramide, though this cannot be confirmed given our current methods. Simultaneous with these increases, a single sphingomyelin was decreased (d36:1). In cfHBE relative to nHBE cells, four ceramides were increased (16:0, 22:0, 24:0, 24:1). These included the two most abundant ceramides, 16:0 and 24:1, and include both long-chain and very-long-chain ceramides. Both dihydroceramides also were increased (dh16:0, dh24:1), each corresponding to the most abundant ceramide species. Some of these increased ceramides and dihydroceramides likely correspond to the increased sphingomyelins. Specifically, 24:0 ceramide and dh24:1 dihydroceramides could each be one of the d42:1 sphingomyelins, and 24:1 ceramide could be d42:2 sphingomyelin. Simultaneous with these increases in ceramide, one ceramide was decreased (18:0), which likely corresponds to the one decreased sphingomyelin (d36:1). Importantly, broadly comparing the downregulated ceramide to the upregulated ceramides does not indicate a differential effect on long-chain versus very-long-chain ceramides, as had been seen by another group (146). Furthermore, the fact that both sphingomyelins and ceramides largely are increased in cfHBE relative to nHBE cells suggests that the increase in ceramides is not due to increased breakdown of sphingomyelin in cfHBE cells solely.

What is important to keep in mind when working with primary cfHBE cells is that they are obtained from lungs of patients with disease state advanced enough to warrant a lung transplant. We were interested in analyzing an airway cell type that could be collected at any stage of CF, and that could be age and gender-matched to “healthy” controls, rather than other non-CF lung transplant cells. Thus, we evaluated sphingolipid imbalances in primary nasal epithelia (HNE), as well. We evaluated nHNE cells from a 25-year-old female donor, and cfHNE cells from a 23-year-old female donor homozygous for the $\Delta F508$ -CFTR mutation (Figure 3.6E-F). The most abundant sphingomyelins were a dihydrosphingomyelin (fully saturated) and an odd-chained sphingomyelin (*data not shown*). As such, we did not think it appropriate to compare the sphingomyelins of HNE cells to those of HBE cells. Interestingly, the most prominent ceramides and dihydroceramides were different in these HNE than in the HBE cells, though certainly less

so than the sphingomyelins. Most notably, 14:0 and 24:0 were the most prominent ceramides rather than 16:0 and 24:1. Similarly to HBE cells, though, lipidomics analysis revealed that cfHNE cells, as compared to nHNE, had increased levels of many ceramides (14:0, 22:0, 24:0). This includes the two most prominent ceramides as well as long-chain and very-long-chain ceramides. Note, also, that the 22:0 and 24:0 ceramides were increased in the cfHBE cells as well. Along with these increases in ceramide, all four dihydroceramides (dh16:0, dh22:0, dh22:1, dh24:1) were increased in cfHNE cells. No ceramides were decreased. Again, this indicates no differential effect on long-chain versus very-long-chain ceramides, as had been seen by another group (146). Thus, when considering the ceramide and dihydroceramide data gathered in HBE as well as HNE cells, it appears that the general trend is an increase in ceramides and dihydroceramides in CF cells.

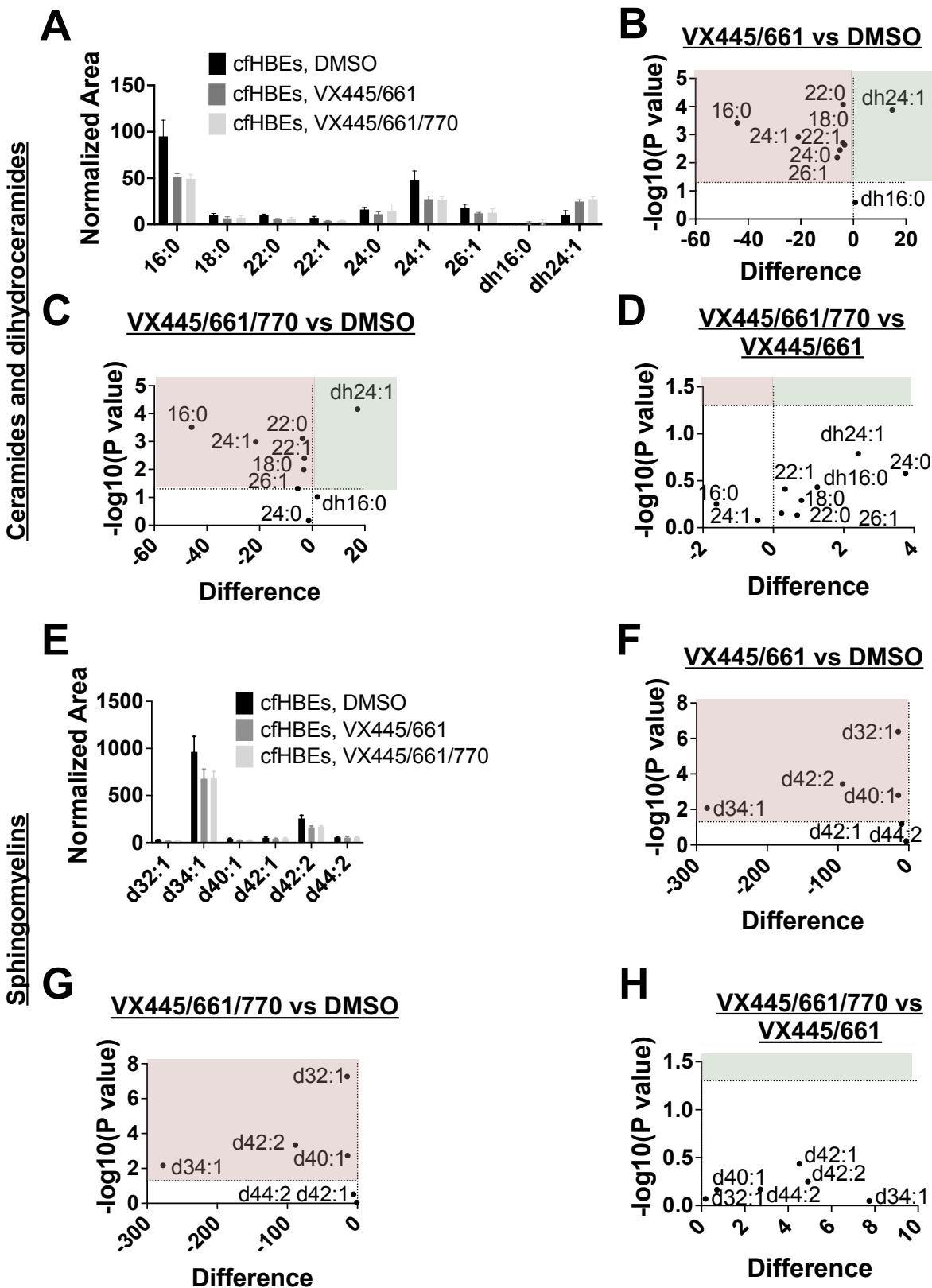
3.3.6 *Effects of modulator therapy on sphingolipids in cfHBE cells*

Given our own data and previous literature (189; 193; 194), cfHBE cells have increased ceramides and dihydroceramides compared to nHBE cells. However, many CF patients are approved for treatment with CFTR modulators, so it is important to determine if these modulators rescue sphingolipid imbalances.

We first treated cfHBE cells with VX809 for 24 hr and found no effects on ceramides or dihydroceramides (*data not shown*). We then treated cfHBE cells either with VX445+VX661 or with VX445+VX661+VX770 for 48 hr (Figure 3.7). These treatments rescue either CFTR trafficking or CFTR trafficking and activity, respectively, allowing us to begin to distinguish the effects of accumulated unfolded protein as compared to a loss of CFTR activity. Lipidomics analysis of these cfHBE cells indicated that, compared to DMSO-treated cells, VX445+VX661 decreased all ceramides of interest and increased one dihydroceramide (dh24:1) (Figure 3.7B). Treating cells with VX445+VX661+VX770 decreased all but one ceramide of interest (24:0) and increased the same dihydroceramide (Figure 3.7C). No significant difference was found between the two different treatments (Figure 3.7D).

In an effort to understand if this effect was due to decreased sphingomyelin breakdown, we evaluated the effects of these drugs on sphingomyelin levels as well (Figure 3.7E-H). Interestingly,

Figure 3.7. Lipidomics analysis indicates that the newest FDA-approved correctors can affect the sphingolipid imbalances in cfHBE cells. Any sphingolipid in a pink box was significantly decreased by treatments, whereas any sphingolipid in a green box was significantly increased by treatments. **(A-D)** In cfHBE cells, 48 hr treatment with VX445+VX661 (n=5) or VX445+VX661+VX770 (n=5) decreased all ceramides of interest except for one ceramide in the VX445+VX661+VX770 treatment group, though no difference was found between treatments. Four of these ceramides were significantly increased in cfHBE compared to nHBE cells, so modulators corrected these imbalances. Simultaneously, VX445+VX661 and VX445+VX661+VX770 treatments both increased one dihydroceramide, again with no difference between the two treatments. This dihydroceramide was already increased in cfHBE as compared to nHBE cells, indicating that treatment pushed this dihydroceramide even further away from the nHBE levels. **(E-H)** In regard to sphingomyelin, both VX445+VX661 and VX445+VX661+VX770 decreased four sphingomyelins of interest, with no difference between the two treatments.



VX445+VX661 alone as well as VX445+VX661+VX770 for 48 hr decreased four sphingomyelins (d32:1, d34:1, d40:1, and d42:2), with no difference between the two treatments. One of these sphingomyelins (d42:2) was identified above as being increased in cfHBE relative to nHBE cells. Given that these drugs decreased sphingomyelins as well as ceramides, it is unlikely that the decrease in ceramide is due to a decrease in conversion of sphingomyelin into ceramide. An alternative pathway that can explain a reduced presence of both sphingolipids must be involved and should be identified.

3.3.7 *Imbalance of acid-SMase in cfHBE cells and the effects of modulators*

Though the above lipidomics data suggests that increased breakdown of sphingomyelin alone cannot explain increased ceramide levels in CF airway cells, differential activity of acid-SMase could at least partially be involved still. Previous literature has indicated elevated levels of SMase activity on the surface of cfHBE compared to nHBE cells, though the same study found no increase in cellular mRNA or protein levels of acid-SMase (194). Thus, we sought to evaluate cellular and extracellular levels of acid-SMase protein in nHBE and cfHBE cells using western blot and densitometry analysis on a single biological replicate. Importantly, note that lysosomal and secreted acid-SMase, though arising from the same gene, are distinct (181; 295; 331-333).

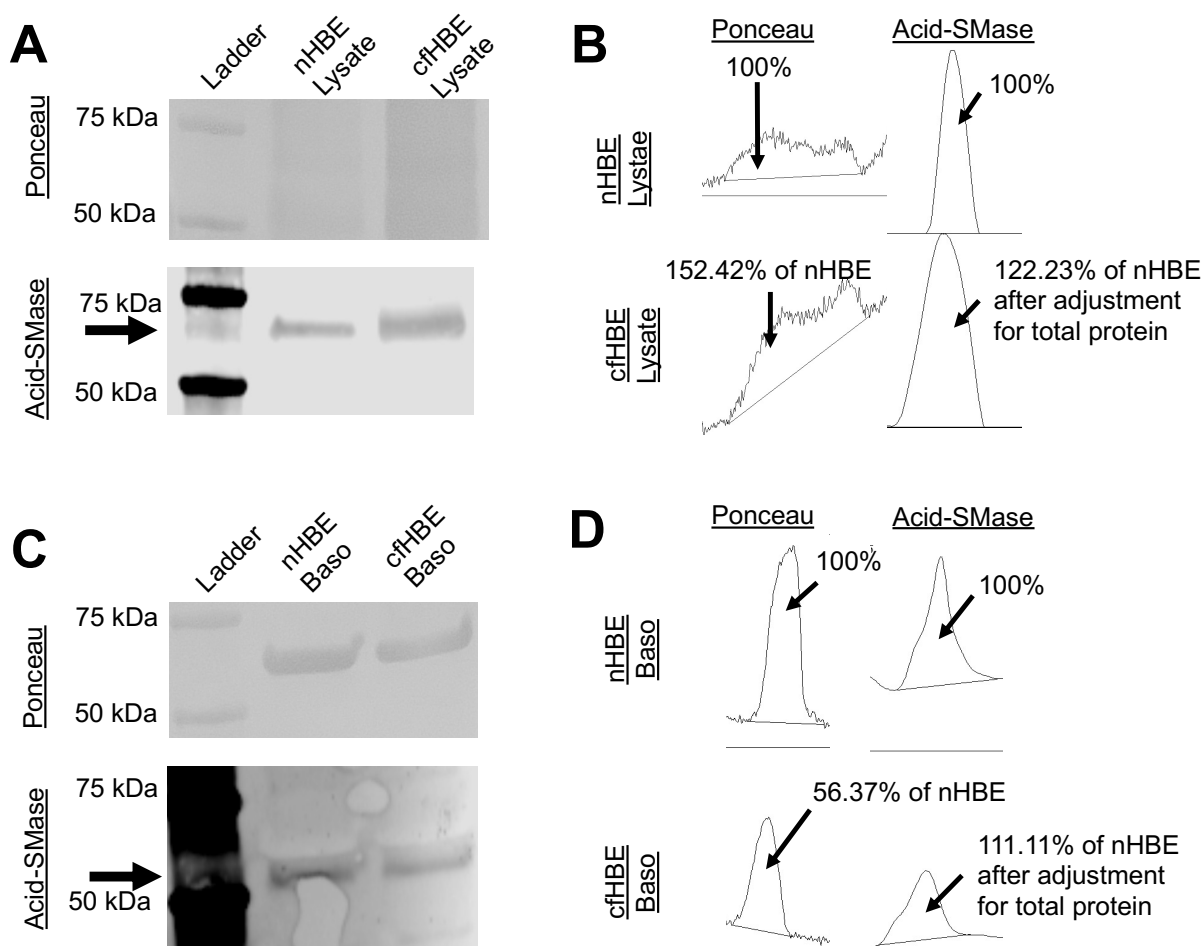
Following normalization to Ponceau staining, these analyses indicated that cfHBE cells had 22% more cellular acid-SMase (~70 kDa band) than nHBE cells (Figure 3.8A-B), and about 11% more extracellular acid-SMase (~57 kDa band) (Figure 3.8C-D). Confidence in our conclusions is enhanced by the finding that both total cellular and extracellular acid-SMase levels were increased in cfHBE cells. While increased acid-SMase levels in cfHBE cells could explain increases in some of the ceramide levels in cfHBE compared to nHBE cells, further studies blocking acid-SMase activity would need to be performed to confirm this.

3.3.8 *LTB4-transmigrated neutrophils secrete acid-SMase*

Everything evaluated thus far has been in CF and non-CF primary airway epithelial cells in an

Figure 3.8. Western blot and densitometry analyses indicate imbalances in acid-SMase protein

expression and secretion in cfHBE as compared to nHBEs cell. (A-B) Cell lysate of cfHBE cells had 52% more protein than nHBE cells. When correcting for this loading control, cfHBE cell lysate still had 22% more acid-SMase protein expression than nHBE controls. **(C-D)** Basolateral medium of cfHBE cells had 44% less protein than nHBE cells (100%-56%). When correcting for this loading control, basolateral medium from cfHBE cells still had 11% more acid-SMase protein expression than nHBE controls.



isolated laboratory setting. However, the lung environment is much more complicated. Endogenously, HBE cells scaffold on top of basal cells and fibroblasts, and immune cells such as macrophages and neutrophils are recruited through the HBE cells into the airspace. Previous work has shown that macrophages, among many other cell types, secrete acid-SMase (181). However, no one to our knowledge has evaluated acid-SMase secretion from neutrophils. Neutrophils are important to the pulmonary pathophysiology of CF and are present in much higher abundance in CF airways than other immune cells (325). Thus, we resolved to determine the presence of cellular and secreted acid-SMase in transmigrated neutrophils. Neutrophils were collected from subjects without CF and transmigrated across non-CF epithelial cells in response to chemoattraction using LTB₄, then allowed to condition the apical medium for 4 hr. These cells and the medium they conditioned were then separated and analyzed for acid-SMase (Figure 3.9). Acid-SMase was detectible in the cellular lysate of these neutrophils, at the approximate molecular weight expected for lysosomal acid-SMase (~60 kDa). Furthermore, acid-SMase was detectible in the conditioned medium of these neutrophils, at the approximate molecular weight for dimerized secreted acid-SMase (~150 kDa), since DTT was not added in this experiment. Thus, these results show that LTB₄-transmigrated neutrophils are an endogenous source of acid-SMase in the lung environment. The effects of this secretion should be characterized in future work.

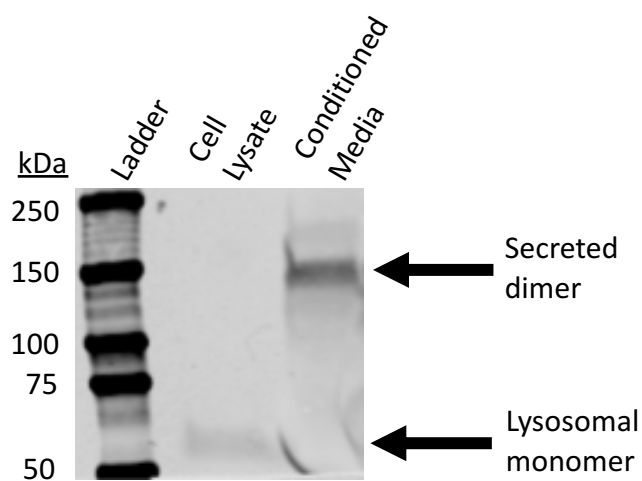
3.4 Discussion

In this study, we found that inhibiting ceramide breakdown by treating nHAE cells with ceranib-1 decreased the forskolin dose-response curve similarly to WT SMase, suggesting that these treatments decreased CFTR currents via the same mechanism. Long-term treatment with ceranib-1 increases ceramide levels and theoretically would not affect sphingomyelin or phosphocholine levels (334). Importantly, lipidomics analysis of nHBE cells treated with ceranib-1 for 1-2 hr, as in our experiments, showed no apparent effect on total cellular sphingomyelins or ceramides.

Instead, we detected an increase in two dihydroceramides, one of which was also found to be increased by WT SMase treatment alone. Dihydroceramides are a step in the *de novo* ceramide synthesis

Figure 3.9. Neutrophils transmigrated through H441 cells by LTB₄ stimulation secrete acid-SMase.

Neutrophils were evaluated for cellular and secreted acid-SMase after 4 hr of media conditioning following transmigration. In the left lane, a protein standard ladder is shown with labeled molecular weights. In the middle lane, cellular lysate of the transmigrated neutrophils shows lysosomal acid-SMase around 60 kDa. In the right lane, conditioned medium shows secreted acid-SMase dimer around 150 kDa. Transmigrated neutrophils secrete acid-SMase. DTT was not added in this experiment.



pathway and are converted into ceramide in the ER by dihydroceramide desaturase (335). Since both WT SMase and ceranib-1 treatment increase these lipids, dihydroceramides could be the commonality between the inhibitory mechanisms of these two treatments. It is also possible that ceranib-1 caused localized changes in ceramide that were not detected when evaluating total cellular lipids. More experiments evaluating the specific changes in plasma membrane ceramides along with experiments acutely adding ceramide and dihydroceramide are necessary to determine if accumulation of ceramide, dihydroceramide, both, or neither is the mechanism underlying WT SMase- and ceranib-1-mediated inhibition of CFTR.

The potential effects of ceramide and dihydroceramide on CFTR activity are relevant to many inflammatory lung diseases, and to CF in particular (188; 322; 336). Multiple groups have identified an increase in ceramides in CF airway cells as compared to non-CF controls (193; 194), though one group found an overall decrease in ceramides with a simultaneous increase in the ratio of long-chain- to very-long-chain ceramides (146). Dihydroceramides also have been found to be increased in immortalized CF cell line models (189). We report within this study that many ceramides and dihydroceramides are increased in cfHBE cells compared to nHBE controls. We also found this phenomenon in cfHNE cells as compared to age- and sex-matched nHNE controls, which can be collected non-invasively at any stage of CF and from healthy non-CF donors. Evaluations on sphingolipids in cfHNE cells has not been reported to our knowledge. Interestingly, in HBE cells, this increase in ceramides was accompanied by an increase in sphingomyelins as well. This suggests that increased acid-SMase activity alone cannot explain the increased ceramide levels, as decreased sphingomyelin levels would be expected in that case.

There are current FDA-approved modulators to address the mistrafficking and reduced activity of CFTR, so it was important to evaluate the effects of these drugs on the sphingolipid profile of cfHBE cells. In this study, we found that treatments with 24 hr VX809 treatment had no effect on sphingolipid profiles. This is consistent with previous work in CFBE41o- cells (36) but is not consistent with previous work in cfHBE cells that shows a slight decrease in a ceramide species not found at a large abundance in the cfHBE cells in this study (14:0) (55).

We also found that 48 hr VX445+VX661 alone decreased all ceramides of interest. Importantly,

effects of this treatment, which only facilitates rescue of misfolding and trafficking of $\Delta F508$ -CFTR, were no different than effects of 48 hr treatment with VX445+VX661+VX770, which facilitates rescue of misfolding, trafficking, and activity of $\Delta F508$ -CFTR. The observed effects of VX445+VX661+VX770 on ceramides in cfHBE cells are consistent with previous work in CFBE41o- cells (36) but is not consistent with previous work in cfHBE cells which found that VX445+VX661+VX770 treatment increased total ceramide levels (55). No previous work to our knowledge has evaluated separately the effects of these correctors alone on the sphingolipid profiles of homozygous $\Delta F508$ -CFTR cfHBE cells as compared to the correctors plus the potentiator VX770. Our results suggest that the unfolded protein response due to mistrafficked $\Delta F508$ -CFTR may be the cause of ceramide imbalances, rather than a loss of CFTR function. Of note, though, is that modulator therapy further exacerbated the increase in one very-long-chain dihydroceramide (dh24:1) in cfHBE cells, which could prove problematic if this dihydroceramide has detrimental effects on the cells. Furthermore, many sphingomyelins were decreased by VX445+VX661 or VX445+VX661+VX770 treatment. This suggests that the decrease in ceramides caused by these treatments is not due to decreased acid-SMase activity alone, as increased sphingomyelin levels would be expected in this case. Another mechanism must be involved.

In order to begin to understand if acid-SMase could be involved in increased ceramides in cfHBE cells, we evaluated acid-SMase protein levels in cfHBE and nHBE cells and conditioned medium thereof, given that increased surface acid-SMase activity has been identified in cfHBE cells (194). A single biological replicate of our cfHBE cells showed increased protein levels of both cellular and secreted acid-SMase as compared to nHBE cells. While the increased total cellular protein levels of acid-SMase in cfHBE cells appears inconsistent with previous literature that identified no difference, this previous literature did not normalize to a loading control as was done here, which is a more accurate method (194). Furthermore, this previous work did not evaluate extracellular acid-SMase levels as we did here. However, of note, this work did provide evidence suggesting that decreased CDase activity was the cause for increased ceramide levels in cfHBE compared to nHBE cells. This mechanism would be consistent with our observation that

sphingomyelin levels are also increased in cfHBE cells.

To provide even further physiological context to our work, we also determined within this study that LTB₄-transmigrated neutrophils secrete acid-SMase. Neutrophils are present at high numbers in the CF lung, and thus this secretion of acid-SMase is relevant to understanding the disease state of CF (325). These results, along with the existing literature, suggest that determining the mechanism of WT SMase-mediated decreases in CFTR activity in HBE cells is quite relevant.

This study has shown that accumulation of ceramides and/or dihydroceramides underly the proximal mechanism by which SMase reduces CFTR activity in airway cells. However, the next steps in the mechanism by which ceramide and/or dihydroceramide could be affecting CFTR-mediated conductance still remain to be understood completely. There are four ways that lipids can affect a membrane protein's activity: direct allosteric interaction, changing surface localization, changing signaling cascades, and membrane mechanics (Figure 1.7) (323). Our prior experiments in *Xenopus* oocytes showed that WT SMase applied directly to an excised patch of membrane did not inhibit CFTR channels within the patch (266). This indicated that direct allosteric interaction and membrane mechanics affected by the loss of sphingomyelin and accumulation of ceramide and phosphocholine did not underly the inhibition of CFTR conductance. This theoretically will be true regardless of cell type. Further experimentation in *Xenopus* oocytes showed that WT SMase did not change surface expression of CFTR, a phenomenon that we confirmed in nHBE cells in this study, using surface biotinylation and normalization to total immunoprecipitated CFTR. Instead, we found in *Xenopus* oocytes that intracellular components were necessary to facilitate WT SMase-mediated decreases in CFTR currents, indicating that a signaling mechanism was involved (266). It is likely that a signaling mechanism is involved in HBE cells as well.

As we established within this study and previously (266) (section 2.3.2), VX770 does not rescue WT SMase-mediated decreases in CFTR currents or conductances in nHBE cells. We also have shown in nHBE cells that potentiation of CFTR currents by VX770 is greater when CFTR has reduced levels of PKA phosphorylation (73). Therefore, if WT SMase inhibited CFTR activity by decreasing PKA phosphorylation, we would expect that VX770 treatment would have recovered the CFTR-mediated current

and conductance, which was not the case. Furthermore, we previously showed that in *Xenopus* oocytes, WT SMase inhibits CFTR channels without the R-domain, the location of the PKA phosphorylation sites (266). A signaling mechanism unrelated to PKA-mediated phosphorylation must be involved.

Both ceramide and dihydroceramide activate AMPK (328; 329), which inhibits CFTR by phosphorylating S737 and S768 in the R-domain. We utilized the AMPK inhibitor BML-275 to determine its involvement in the mechanism of action of SMase and found that WT SMase decreased CFTR-mediated currents to a similar degree even with this inhibitor present. This indicates that AMPK is not involved. Ceramide is known to initiate many other signaling cascades, though, including those involving protein phosphatases 2A and 2C (PP2A (271), PP2C (337)). PP2A and PP2C inhibit CFTR by dephosphorylating the R-domain's stimulatory phosphorylation sites, thus inactivating CFTR (272; 273; 338). This is functionally the same as reduced PKA phosphorylation, so we can hypothesize based on the lack of VX770-mediated recovery that PP2A and PP2C are involved in the inhibitory mechanism. However, we again note that the effect of SMase in *Xenopus* oocytes did not require the R-domain.

There are still alternative mechanisms to explore. Ceramide inhibits certain protein kinase C isoforms (339). PKC has differential effects on CFTR, depending on which site it phosphorylates (274). In Calu-3 cells, the PKC activator phorbol 12-myristate 13-acetate did not recover the WT SMase-mediated decrease in cAMP-activated transepithelial anion currents (269), although we have shown that WT SMase does not affect CFTR currents in the same manner in Calu-3s as in nHBE cells (section 2.3.3). Future work should activate protein kinase C to determine if this enzyme is involved in WT SMase-mediated inhibition of CFTR in nHBE cells. Dihydroceramides are also known to decrease ATP levels (329; 340), which could decrease CFTR-mediated conductance since ATP is required for CFTR gating (41). Thus, along with the remainder of the future experiments suggested in this paper, future work should evaluate ATP levels to determine if these enzymes are involved in WT SMase-mediated inhibition of CFTR in nHBE cells.

3.4.1 Limitations

A limitation of this study is that the effects of ceranib-1 and BML-275 were evaluated only in

regard to transepithelial currents. Future work should re-evaluate these treatments in regard to their effects on apical and basolateral conductance. Furthermore, this study is limited in that only a single biological replicate was used to determine the imbalance of ceramides and dihydroceramides in CF airway cells as compared to non-CF controls. However, we are confident in the results presented here because similar trends were found in cfHBEs and cfHNEs as compared to nHBEs and nHNEs, all from different donors, and since previous literature has reported similar findings. This study is also limited in that only a single neutrophil donor was used to evaluate protein expression of acid-SMase in neutrophils. Future work should evaluate acid-SMase expression in neutrophils from multiple donors. Lastly, we were unable to evaluate total CFTR cellular protein expression following SMase treatments.

CHAPTER 4 – DETERMINING THE EFFECTS OF CHOLESTEROL EXTRACTION ON CFTR CHANNEL ACTIVITY

Preface: Some of the text (in particular the methods section) and much of the figures presented here are reproduced from a portion of a manuscript published in *Frontiers in Physiology* in May 2021. The goal of this manuscript was to determine the effects of modulating cholesterol levels on WT- and P67L-CFTR activity in the context of patch clamp experiments as well as epithelial cell monolayers, including bronchial epithelial cells. For the purposes of this chapter, I focus only on WT-CFTR. For this chapter, I re-wrote the introduction, results, and discussion. Also, I remade each of the figures independently. The project was conceptualized by Drs. Nael McCarty and Guiying Cui. Figure legends give credit to the researcher who performed the experiments. Most experiments were conducted by Dr. Cui (Figures 4.1-4.3). I did some preliminary Ussing Chamber work in 16HBE cells and some preliminary microscopy work in FRT cells (*data not shown*). I also performed Ussing Chamber experiments and analyses on nHBE cells (Figure 4.4).

- Cui G, Cottrill KA, Strickland KM, Mashburn SA, Koval M, & McCarty NA. 2021. Alteration of membrane cholesterol content plays a key role in regulation of CFTR channel activity. *Front Physiol.* Accepted.

4.1 Introduction

Cholesterol is an important biological lipid with many relevant functions. It is the precursor for many physiological vitamins and hormones. It also constitutes a large percentage of the lipid mass of the plasma membrane, has a large influence on the fluidity of the membrane, and clusters with sphingomyelin to form lipid rafts (151). As outlined in section 1.5.2, there is much evidence to suggest increased

cholesterol levels in CF airway epithelial cells as compared to non-CF cells (155-157; 159; 161). These data warrant studies to determine the effects of cholesterol imbalance on CFTR activity. Furthermore, there are many diseases aside from CF in which cholesterol is imbalanced. For example, Niemann-Pick Disease type C (NPC) is a lysosomal storage disorder caused by mutations to the *NPC1* or *NPC2* genes that results in cholesterol accumulation in cells. Interestingly, people with NPC develop a severe pulmonary phenotype, including recurrent pneumonia and pulmonary fibrosis (341; 342). Understanding how cholesterol imbalances affect CFTR activity could inform the pulmonary phenotype in this and other diseases with cholesterol imbalance, since cholesterol is known to affect membrane protein activity by a variety of mechanisms.

CFTR has been found to reside in cholesterol-rich lipid rafts, as determined by colocalization with the GM1 marker cholera toxin and by identification of CFTR by western blot in detergent-resistance membranes (281; 282). Furthermore, in a recent cryo-EM structure of ATP-bound (outward facing) human CFTR in detergent (PDB: 6MSM) (43), a cholesterol-shaped density was resolved in the structure (Figure 1.8). This density is either a cholesterol copurified with CFTR or CHS with an unresolved succinate region, which was introduced during the purification process. Aside from this structural data, cholesterol was found to copurify with CFTR purified with amphipol A8-35 (343). This suggests a strong binding association between CFTR and these cholesterol. Interestingly, though, while molecular docking simulations against the inward-facing zebrafish CFTR predicted eight cholesterol binding sites (253), none of these sites match the site of bound cholesterol observed in the outward-facing human CFTR structure.

Overall, there is a strong potential for an effect of cholesterol on CFTR structure and activity. Thus, we conducted studies to determine the effects of reducing cholesterol levels on CFTR activity.

4.2 Methods

4.2.1 FRT cells

FRT cells stably expressing WT-CFTR were kindly provided by the Sorscher lab. For short-circuit current analysis, cells were plated at a density of 1,000,000 cells/well on Corning 3470 Transwells (6.5 mm

diameter) in Coon's modified Ham's F12 medium. Cells were maintained at liquid-liquid interface in a 37 °C incubator with 95:5% O₂:CO₂. CFTR was activated by increasing concentrations of forskolin bilaterally and was inhibited by 10 μM INH172 apically. For other experiments, the description of the treatment of the FRT cells is included in the method.

4.2.2 *Primary bronchial epithelial cells*

Primary nHBE cells were handled as described in section 2.2.1, using the modified UNC method developed in the Koval laboratory (137). Prior to CFTR activation, ENaC was inhibited with 20 μM amiloride apically. CFTR was activated by increasing concentrations of forskolin bilaterally and was inhibited by 10 μM INH172 apically.

4.2.3 *Transepithelial short-circuit current analysis*

Transepithelial short-circuit currents were obtained using an Ussing Chamber system, as described in section 2.2.5. However, recording solutions were different. The Normal Chloride Basolateral buffer was 140 mM NaCl, 5 mM KCl, 0.36 mM K₂HPO₄, 0.44 mM KH₂PO₄, 0.5 mM MgCl₂, 1.3 mM CaCl₂, 4.2 mM NaHCO₃, 10 mM glucose, 10 mM HEPES, pH 7.4. The Low Chloride Apical buffer was 133 mM Na gluconate, 5 mM K gluconate, 2.5 mM NaCl, 0.36 mM K₂HPO₄, 0.44 mM KH₂PO₄, 0.5 mM MgCl₂, 5.7 mM CaCl₂, 4.2 mM NaHCO₃, 10 mM mannitol, 10 mM HEPES, pH 7.4.

4.2.4 *Cholesterol staining with filipin III*

Filipin III was used to stain for cholesterol in FRT cells. Rather than growing on Transwells, FRT cells for this experiment were cultured for 2-4 days on cover slips coated with 20 μg/mL collagen I. Cells were washed with PBS then treated with either 5 mM mannitol (control) or 5 mM MβCD diluted in normal chloride buffer for 1 hr in the cell culture incubator. Following treatment, cells were washed with PBS, fixed in 4% paraformaldehyde for 20 min, then washed with PBS again. For staining, cells were incubated

with 10 $\mu\text{l}/\text{mL}$ filipin III in PBS for 1 hr. Cells were washed again with PBS, Vectashield[®] mounting media without 4',6-diamidino-2-phenylindole (DAPI) (Vector Laboratories) was applied, and a coverslip was added. Images were taken at 20x magnification using a widefield fluorescence microscope with an ultraviolet filter. Using ImageJ, the average filipin staining intensity at the cell surface was determined by evaluating the average fluorescence around the border of a subset of randomly selected cells.

4.2.5 *Mass spectrometry analysis of cholesterol*

FRT cells were cultured for 3 days in 60 mm cell culture dishes. Cells were washed with PBS, then were treated with either 5 mM mannitol (control) or 5 mM M β CD in normal chloride buffer for 1 hr in the cell culture incubator. Following treatment, cells were washed with PBS and detached with 0.25 % trypsin/EDTA, then collected by centrifugation. The supernatant was removed, and the cell pellet was washed once with PBS. Cell pellets were stored at -80 °C for subsequent analysis.

Primary cells were cultured as described above. These cells then were treated with either 5 mM mannitol or 5 mM M β CD in normal chloride buffer for 1 hr in the cell culture incubator. Following treatment, cells were washed with PBS, scraped with a pipet tip off the Transwell, and then collected by centrifugation. The supernatant was removed, and cell pellets were stored at -80 °C for subsequent analysis.

Mass spectrometry analysis was performed similarly to what was described in section 2.2.4. Briefly, samples were removed from -80 °C and thawed on ice. A 1 mL aliquot of IPA containing 5 μM deuterated cholesterol was added to each sample, except the blank, which received exclusively IPA. Samples were submerged in liquid nitrogen until frozen and then thawed and sonicated in an ice bath for 3 min. This freeze-thaw cycle was repeated 3 times. Samples were centrifuged at 10,000 x g for 8 min. A pool was made from 100 μL aliquots from each sample. The pool and samples were transferred to liquid chromatography vials and stored at 4 °C until analysis. A Reverse Phase Accucore C30, 2.6 μm , 150x2.1 mm column was used. Mobile Phase A was 40% H₂O / 60% ACN, 10 mM ammonium formate, 0.1% formic acid. Mobile Phase B was 10% ACN / 90% IPA, 10 mM ammonium formate, 0.1% formic acid. The column temperature was 50 °C. The resolution was 240,000. The scan range was 150-1500 m/z.

Samples were injected at 5 μ L.

4.3 Results

4.3.1 *M β CD extracts cholesterol from FRT and nHBE cells*

Prior to determining the effects of M β CD on CFTR currents, it was important to determine an appropriate concentration and incubation time for M β CD to extract cholesterol. We began with FRT cells expressing WT-CFTR. Cells were treated with either 5 mM mannitol or 5 mM M β CD for 1 hr, then were stained for cholesterol using filipin III, as described in section 4.2.4. Representative images are shown (Figure 4.1A,B). The average fluorescence of the cell borders was obtained to quantify the relative amount of filipin staining in these cells. This analysis indicated that M β CD decreased filipin staining by 38% (Figure 4.1C). Mass spectrometry, a more powerful technique, was also used to quantify extraction of cholesterol following M β CD treatment in FRT as well as nHBE cells (Figure 4.1D,E). These analyses indicated that in FRT cells, M β CD extracted 66% of cholesterol, from 3.84 ± 0.16 normalized area to 1.31 ± 0.07 normalized area. Similarly, in nHBE cells, M β CD extracted 48% of cholesterol, from 7.96 ± 1.04 normalized area to 4.17 ± 1.31 normalized area. Together, these data suggest that 5 mM M β CD treatment for 1 hr extracts a large amount of cholesterol from FRT and nHBE cells. As such, this concentration and incubation time was used in subsequent experiments.

4.3.2 *M β CD shifts the forskolin dose-response curve of CFTR to the right in FRT cells*

To understand the effects of cholesterol extraction on CFTR ion channel activation, we utilized FRT cells stably expressing WT-CFTR, a common cell line used in CF research. Cells were treated with either 5 mM mannitol (control) or 5 mM M β CD, and CFTR activation by forskolin and inhibition by INH172 was subsequently evaluated by transepithelial short-circuit current analysis (Figure 4.2). A forskolin dose-response curve was generated by normalizing changes in current following increasing concentrations of forskolin to the change in current following either 11 μ M (control) or 71 μ M (M β CD)

Figure 4.1: M β CD extracts cholesterol from FRT and nHBE cells. WT-CFTR-expressing FRT cells were treated with either (A) 5 mM mannitol (control, black) or (B) 5 mM M β CD (grey) at 37 °C for 1 hr. Cells were then stained with filipin III to probe for cholesterol and microscopically analyzed. Representative images are shown, with a scale bar of 100 μ m. (C) A bar graph of the fluorescence intensity for the control- and M β CD-treated groups (n=6), normalized to the average intensity of the control group, is shown. Data were compared by an unpaired two-tailed *t* test. M β CD-treated (D) CFTR-expressing FRT cells and (E) nHBE cells treated with mannitol (black; FRT cells, n=3; nHBE cells, n=5) or M β CD (grey; FRT cells, n=3; nHBE cells, n=6) were also collected for lipidomics analysis. Note that these data only were normalized to blank controls. Cholesterol peak intensities were compared by an unpaired two-tailed *t* test and indicated that M β CD significantly decreased cholesterol levels in both cell types (****p<0.0001, ***p=0.00272). Credit to Dr. Guiying Cui.

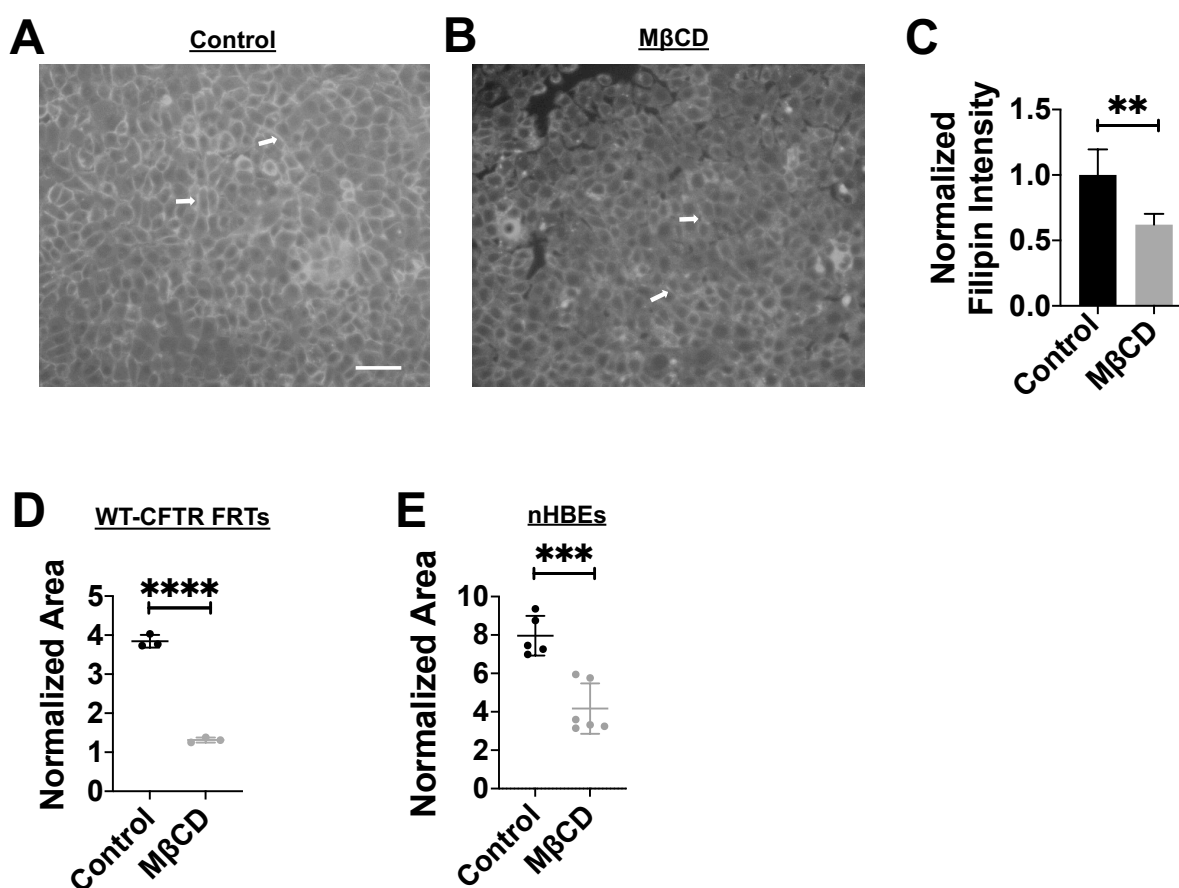
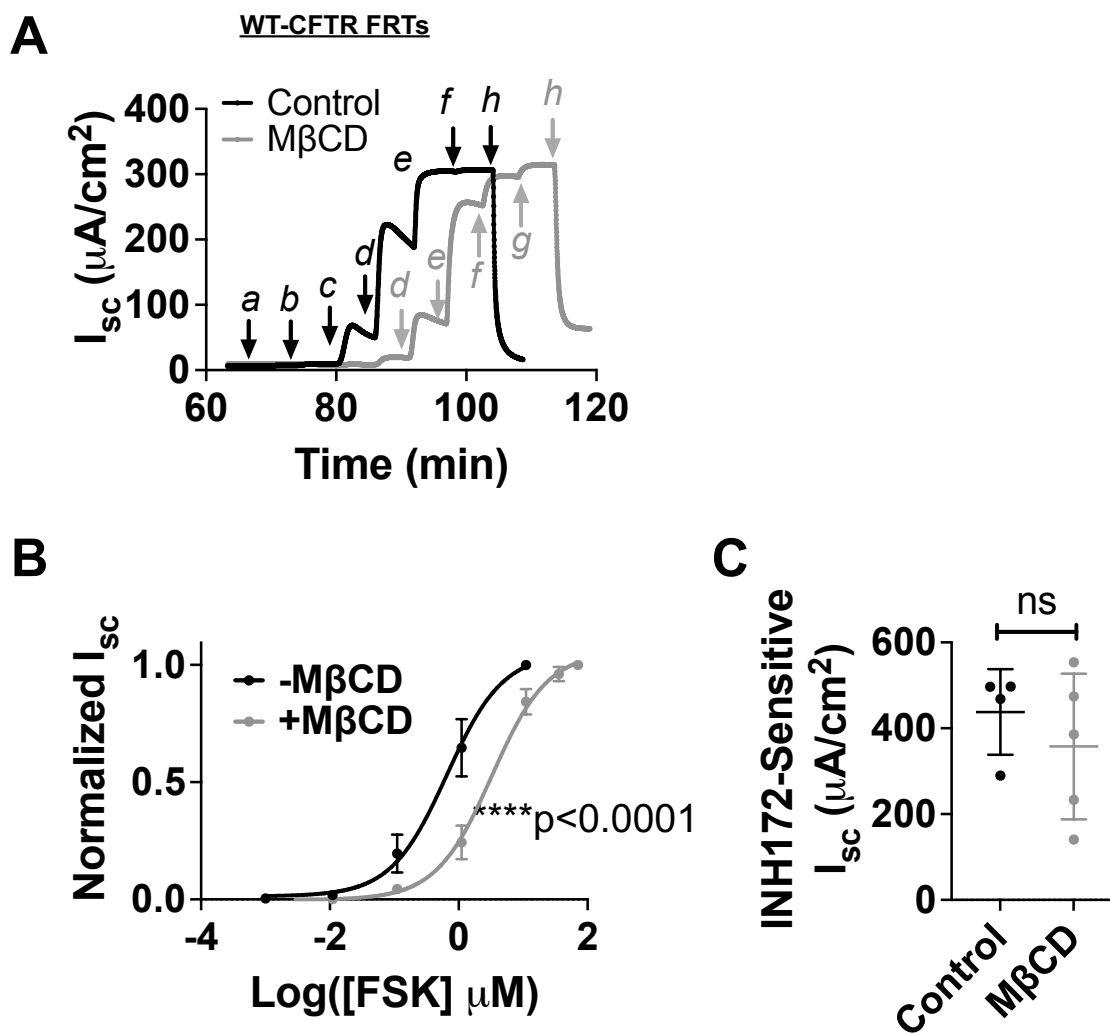


Figure 4.2: M β CD affects the forskolin dose-response curve in FRT cells expressing CFTR. (A)

Representative traces of CFTR-expressing FRT cells treated for 1 hr with either 5 mM mannitol (control, black, n=4) or 5 mM M β CD (grey, n=5) at 37 °C are shown. After approximately 1 hr of treatment, CFTR was activated by (a) 1 nM, (b) 11 nM, (c) 111 nM, (d) 1 μ M, (e) 11 μ M, (f) and 36 μ M forskolin. For the M β CD group, (g) an additional 71 μ M forskolin was used. Lastly, CFTR was inhibited with (h) 10 μ M INH172 apically. (B) The changes in current after the different concentrations of forskolin were normalized to the change in current following 11 μ M forskolin for the untreated cells and 71 μ M forskolin for the M β CD-treated cells. PRISM was used to apply a non-linear fit of log(agonist) vs. response to each group. The effective concentration for half-maximal activation (EC_{50}) in the control group was 0.658 μ M forskolin, whereas in the M β CD treatment group it was 3.277 μ M forskolin. These were significantly different from one another, indicating that M β CD causes a significant rightward shift of the forskolin dose-response curve (**** p <0.0001). (C) The change in current from the post-forskolin current to the post-INH172 current was compared by an unpaired two-tailed t test, which indicated that M β CD had no significant effect on these INH172 sensitive currents (p =0.4327). Credit to Dr. Guiying Cui.



forskolin, based on the maximum amount of forskolin necessary to elicit the maximum amount of current in each group. A non-linear fit of log(agonist) vs. response was generated based on the data for each group, which provided an EC_{50} value for forskolin activation of CFTR current (Figure 4.2B). The EC_{50} for the control group was 0.658 μM forskolin. However, in the M β CD treatment group, this EC_{50} was significantly increased 5-fold to 3.277 μM forskolin. Importantly, analysis of the INH172-sensitive current showed that M β CD treatment did not affect the maximal amount of transepithelial CFTR current (Figure 4.2C).

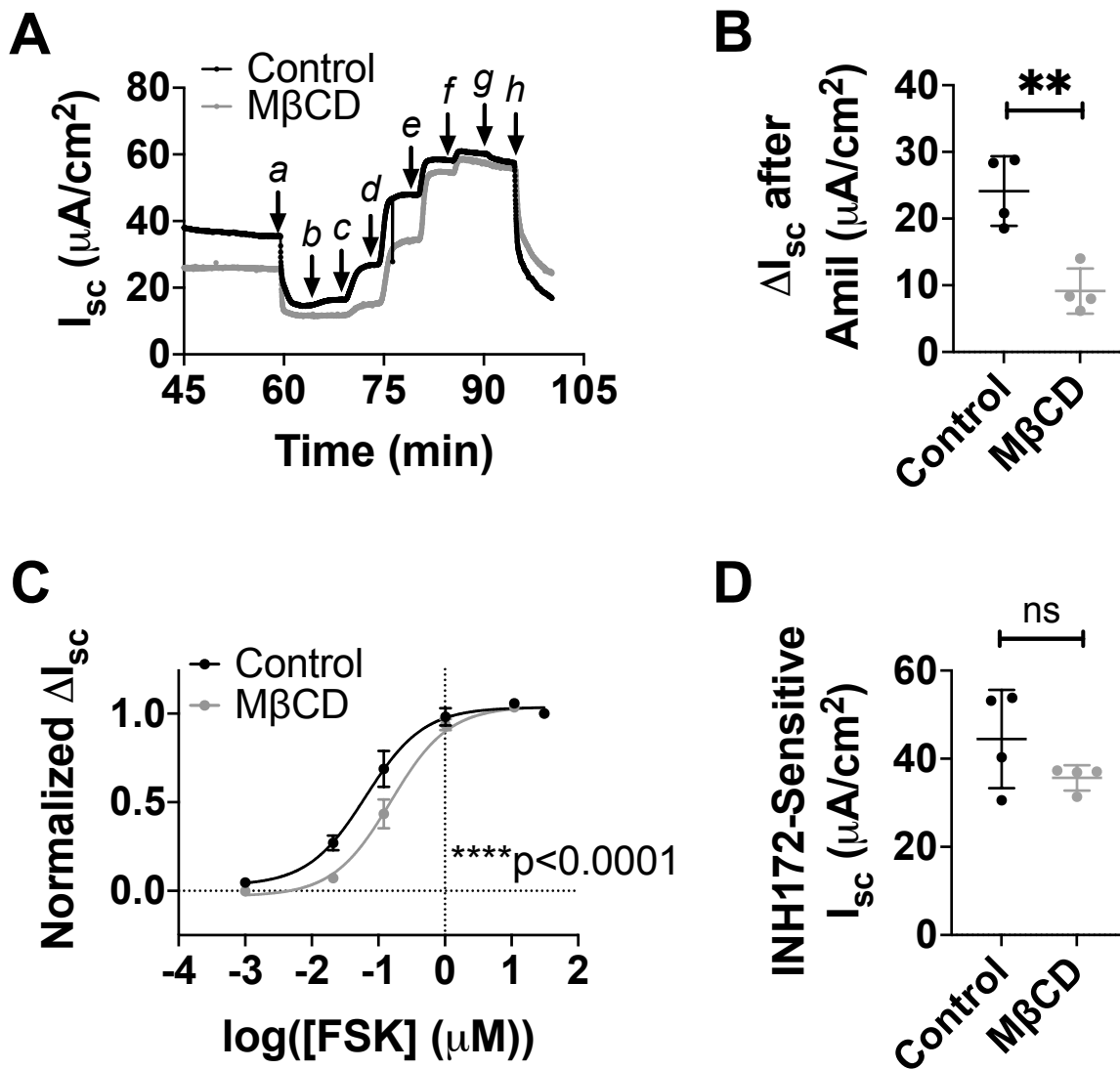
This rightward shift of the forskolin dose response curve indicates that in the M β CD treatment group, more forskolin is necessary to activate CFTR to a similar degree as the control treatment group. The lack of difference in INH172-sensitive current suggests that the total potential amount of CFTR current is not affected, though. Thus, based on these data, in FRT cells expressing WT-CFTR, M β CD decreases the activatability of CFTR by forskolin.

4.3.3 *M β CD shifts the forskolin dose-response curve of CFTR to the right in nHBE cells*

In order to understand if the effects of M β CD on CFTR activation were translatable, we repeated these experiments on nHBE cells (Figure 4.3). These cells express ENaC, whereas FRT cells do not, so it was important to inhibit ENaC currents with amiloride prior to CFTR activation with forskolin. Interestingly, M β CD treatment significantly decreased the amount of amiloride-sensitive current in these nHBE cells (Figure 4.3B). This phenomenon has been observed in other cell types, with data implicating decreased surface expression of ENaC following M β CD treatment as the cause for decreased ENaC current (225; 344).

Following amiloride treatment, CFTR was activated with increasing concentrations of 0.001 to 51 μM forskolin. A dose response curve was generated by normalizing changes in currents after each concentration of forskolin to the change in current after 51 μM forskolin, which elicited the maximum amount of current. Again, a non-linear fit of log(agonist) vs. response was generated based on the data for each group, which provided an EC_{50} value for forskolin activation of CFTR current (Figure 4.3C). The EC_{50} for the control group was 0.0653 μM (65.3 nM) forskolin. However, in the M β CD treatment group, this

Figure 4.3: M β CD affects ENaC and CFTR currents in nHBE cells. (A) A representative trace of nHBE cells treated for an hour with either 5 mM mannitol (control, black, n=4) or with 5 mM M β CD (grey, n=4) is shown. At 1 hr (a) 20 μ M amiloride was added apically to inhibit ENaC. Following this, CFTR was activated with (b) 1 nM, (c) 11 nM, (d) 111 nM, (e) 1 μ M, (f) 11 μ M, and (g) 51 μ M forskolin. Lastly, CFTR was inhibited with (h) 10 μ M INH172 apically. (B) The change in current from the pre- to the post-amiloride currents was calculated and analyzed by an unpaired two-tailed *t* test. This analysis indicates that M β CD decreased amiloride-sensitive currents (***p*=0.0029). (C) The changes in current from the post-amiloride current to the currents after the different concentrations of forskolin were normalized to the change in current following the maximum concentration of forskolin. PRISM was used to apply non-linear fit of log(agonist) vs response to each treatment group and indicates that the EC₅₀ in the control group was 64.5 nM forskolin, whereas in the M β CD treatment group it was 154.1 nM forskolin. These were significantly different from one another, indicating that M β CD causes a significant rightward shift of the forskolin dose-response curve (*****p*<0.0001). (D) The change in current from the post-forskolin current to the post-INH172 current was calculated and analyzed by an unpaired two-tailed *t* test. This analysis indicates that M β CD did not affect INH172-sensitive currents (*p*=0.1771).



EC_{50} was significantly increased 2.4-fold to 0.154 μ M (154 nM) forskolin. Importantly, analysis of the INH172-sensitive current showed that M β CD treatment did not affect the maximal amount of CFTR current (Figure 4.3D).

These effects of M β CD treatment on CFTR activation are consistent with those found in FRT cells. Given the translational relevance of nHBE cells as primary human bronchial epithelial cells, the mechanism by which M β CD changes the activatability of CFTR by forskolin is important to understand.

4.4 Discussion

We determined a concentration and incubation time of M β CD that extracts 40-70% of cholesterol from cells. In FRT cells expressing WT-CFTR, and in nHBE cells, this M β CD treatment increased the EC_{50} for forskolin for activating CFTR currents. There was no effect on the maximum amount of CFTR current.

The increase in EC_{50} for forskolin could be due to a decreased efficacy of forskolin on adenylyl cyclase to generate cAMP, a decreased efficacy of cAMP to generate active PKA, a decreased efficacy of active PKA to activate CFTR, a decreased responsiveness of CFTR to active PKA, or some combination of these. Interestingly, previous work has determined that M β CD treatment reduces the internalization rate of Δ F508-CFTR in primary HAE cells (345). Whether this would be translated to WT-CFTR, which is not as unstable at the cell surface as Δ F508-CFTR, is unclear. If reduced internalization had occurred in the WT-CFTR studies here, it would have been seen as increased maximum CFTR currents, though the chloride driving force across the membrane could have been a limiting factor that prevented this increase. Repletion of cholesterol to detergent-purified, pre-phosphorylated CFTR has also been found to increase CFTR ATPase activity (343). Though ATPase activity does not correlate directly to channel activity, this finding may suggest that cholesterol increases the channel activity of phosphorylated CFTR. However, if this was the case, depletion of cholesterol would have decreased maximal CFTR currents, which was not seen here. It is unclear if this phenomenon would cause a shift in the EC_{50} of forskolin activation of CFTR, since CFTR was phosphorylated prior to evaluation of ATPase activity.

An alternative hypothesis can be proposed based on the observation that M β CD decreases CFTR confinement to lipid rafts and increases lateral motility in the plasma membrane (178). In addition, adenylyl cyclase localizes to lipid rafts (346). PKA also localizes to lipid rafts,(347; 348) and M β CD decreases PKA-mediated phosphorylation of other target proteins (347). Thus, since lipid rafts normally would serve to immobilize adenylyl cyclase, PKA, and CFTR into close proximity to one another, disruption of these lipid rafts with M β CD likely decreases the potential for interaction between these proteins. Ultimately, this would lead to decreased activation of PKA at a given submaximal forskolin concentration, compounded by decreased PKA phosphorylation of CFTR at the same forskolin concentration relative to control treated cells. Individually, and certainly in combination, this would manifest as an increase in the EC₅₀ for forskolin-mediated activation of CFTR. More experiments, such as determining PKA activation and CFTR phosphorylation at the various concentrations of forskolin, would be necessary to determine the mechanism causing this shifted forskolin dose-response curve following M β CD treatment in FRT and nHBE cells.

CHAPTER 5 – UTILIZATION OF THE PLANAR LIPID BILAYER TECHNIQUE TO STUDY SINGLE-CHANNEL CFTR ACTIVITY

Preface: Part of the text presented here is reproduced from a portion of a methods chapter published in *Methods in Molecular Biology* in April 2021 regarding the planar lipid bilayer (PLB) technique. The goal of this chapter was to review various electrophysiological methods by which to study ion channels. For the methods chapter, Dr. McCarty wrote the introduction, Drs. McCarty and Cui wrote sections involving *Xenopus* oocytes – such as two-electrode voltage clamp and patch clamp analysis – and I wrote sections involving Ussing Chamber analysis and the PLB. I generated and analyzed all data.

- Cui G, Cottrill KA, & McCarty NA. 2021. Electrophysiological Approaches for the Study of Ion Channel Function. *Methods Mol Biol* 2302:49-67

Part of the text presented here is based on a portion of a methods chapter published by Dr. Kerry Strickland, a former graduate student in the McCarty lab, in *Methods in Molecular Biology* in April 2021. However, I wrote all text of this chapter independently. Dr. Strickland developed the techniques for maintaining His-CFTR-expressing BHK cells, generating His-CFTR microsomes, and purifying His-CFTR into proteoliposomes. I established the PLB reconstitution technique in our laboratory and performed all experiments and analyses on the PLB system.

- Strickland KM, Neselu K, Grant AJ, Espy CL, McCarty NA, & Schmidt-Krey I. 2021. Reconstitution of Detergent-Solubilized Membrane Proteins into Proteoliposomes and Nanodiscs for Functional and Structural Studies. *Methods Mol Biol* 2302:21-35

5.1 Introduction

PLB reconstitution is a technique originally developed in 1962 (349). In PLB, which at this point in time encompasses a few different techniques, an artificial bilayer is formed with a lipid mixture of known composition. Solutions containing lipids and channels of interest (generally in the form of cellular microsomes or reconstituted proteoliposomes) are added to the system, and the lipid-bound channels fuse to the artificial bilayer. Upon fusion, single-channel recordings can be obtained.

A benefit to this method is that the lipid composition of the artificial bilayer can be tightly controlled, which allows for studies in which the effects of lipid perturbation on channel activity can be studied directly. As it is, all studies on CFTR in which the lipid composition was specifically controlled evaluated only ATPase activity (255; 350). Specifically, these studies found PS to be important for stimulating ATPase activity. We were interested in determining how PS, and other common lipids, affect ion channel activity. Thus, we established the PLB method in our lab, and confirm here that we can record CFTR single-channel currents from microsomes and reconstituted proteoliposomes.

5.2 Methods

5.2.1 Growth and maintenance of BHK cells stably expressing His-tagged CFTR

BHK cells stably expressing C-terminally 6xHis-tagged CFTR first were cultured as adherent cells in T175 flasks in DMEM/F12 with 10% FBS, 1 % pen/strep, and 500 μ M methotrexate (the selection agent). Once 100% confluence was reached, adherent cells were subjected to daily trypsinization with subsequent resettling into the same flask for 4 days. Following this, cells were removed from the flask by trypsinization, then transferred to a glass spinner flask and grown in the same media, supplemented with 10% Pluronic F-

68 (Invitrogen). Cells were agitated at 60 rpm. After 2 days, the volume was doubled with media containing 10% Pluronic F-68. Agitation continued. After 4 days, an additional 500 μ M methotrexate was added.

5.2.2 *Generation of His-tagged CFTR microsomes from BHK cells*

Following 12 hr after this methotrexate addition, BHK cells were pelleted at 1000 xg for 10 min at 4 °C. Cell pellets were then resuspended in a buffer of 8 mM HEPES, 0.8 mM EDTA, 1 mM DTT (pH 7.2) with 1:100 protease inhibitor cocktail specific for CFTR described in section 3.2.5. Cells were lysed with a Dounce Homogenizer, then 1/7th of the volume was added of a buffer containing the above components along with 2 M sucrose (0.25 M sucrose final). After 10 min, cell lysate was centrifuged at 1000 xg for 10 min at 4 °C. The supernatant was collected and centrifuged again at 1000 xg for 10 min at 4 °C. The supernatant was collected and centrifuged using an XPN-100 Beckman Ultracentrifuge with a 70 Ti rotor at 100,000 xg for 1 hr at 4 °C with slow breaking. The pellet was resuspended in buffer containing 50 mM Tris-HCl, 500 mM NaCl, 10% glycerol, 1 mM DTT, and 1:100 protease inhibitor cocktail (pH 7.5). Again, this was centrifuged at 100,000 xg for 1 hr at 4 °C with slow breaking. The pellet was resuspended in buffer containing 10 mM HEPES, 5 mM MgCl₂, 300 mM sucrose, and 1 mM EGTA (pH 7.2). This microsome solution was flash frozen and stored at -80 °C.

5.2.3 *Purification of His-tagged CFTR from BHK cells and generation of proteoliposomes*

The protocol is as described in the method for the generation of microsomes above, but instead the pellet was resuspended in buffer containing 50 mM Tris-HCl, 500 mM NaCl, 10% glycerol (pH 8.0). This solution was stirred gently on ice while, slowly, 4-fold of this volume was added of a buffer as described in the previous step, but with 2.5 mM MgCl₂ and 1 mM ATP (2 mM and 0.8 mM final, respectively). To this solution, still stirring, slowly over the course of 30 min, a 10% DDM and 2% CHS solution was added to a final concentration of 0.1% and 0.02%, respectively. This solution was centrifuged for 30 min at 100,000 xg at 4 °C with slow breaking.

The supernatant was collected and incubated for 1 hr at 4 °C with Pierce Ni-NTA resin pre-equilibrated with buffer composed of 50 mM Tris-HCl, 150 mM NaCl, 2.5 mM MgCl₂, 10% glycerol, 1 mM ATP, 10 mM imidazole, 0.1% DDM, and 0.02% CHS (pH 7.5). Following this incubation, solution was added to a gravity flow column and the flow-through was collected. The resin was washed in two column volumes of buffer as described in the previous step, with increasing steps of imidazole from 10, to 25, to 75, to 125 mM. The resin was then resuspended in one column volume of buffer as described in the previous step, except with 450 mM imidazole. This step was repeated three additional times, with the elution fractions collected each time. The elution fractions from the first three elutions were pooled and concentrated to a final volume of 2 mL using an Amicon Ultra-2 centrifugal spin unit (100 kDa cutoff, 2 mL) centrifuged at 1000 xg for 20 min intervals at 4 °C.

The ÄKTA FPLC with associated size exclusion column (Superdex 200 10/300 GL) was pre-equilibrated with buffer composed of 50 mM Tris-HCl, 150 mM NaCl, 2.5 mM MgCl₂, 10% glycerol, 1 mM ATP, 0.1% DDM (n-Dodecyl β-D-maltoside), and 0.02% CHS (pH 7.5). The concentrated elution sample was then injected onto the loop immediately prior to the size exclusion column. The sample was run through the column at 0.25 mL/min, and elution fractions were collected. Fractions likely to contain CFTR based on ultraviolet peak and time on the column were pooled and concentrated using an Amicon[®] Ultra-2 centrifugal spin unit (100 kDa cutoff, 2 mL) centrifuged at 1000 xg for 10 min intervals at 4 °C.

A bicinchoninic acid assay was used to determine protein concentration in this concentrated CFTR fraction. DMPC (1,2-dimyristoyl-sn-glycero-3-phosphocholine)-CFTR proteoliposomes were generated by making a 100:1 (w/w) DMPC:purified-CFTR solution and dialyzing this solution in 50 mM Tris-HCl, 150 mM NaCl, 2.5 mM MgCl₂, 10% glycerol, 1 mM ATP for 8 hr at 4 °C three times. Proteoliposomes were concentrated 5-10-fold to at least 0.2 mg/mL using an Amicon[®] Ultra-2 centrifugal spin unit (100 kDa cutoff, 2 mL).

5.2.4 Planar Lipid Bilayer

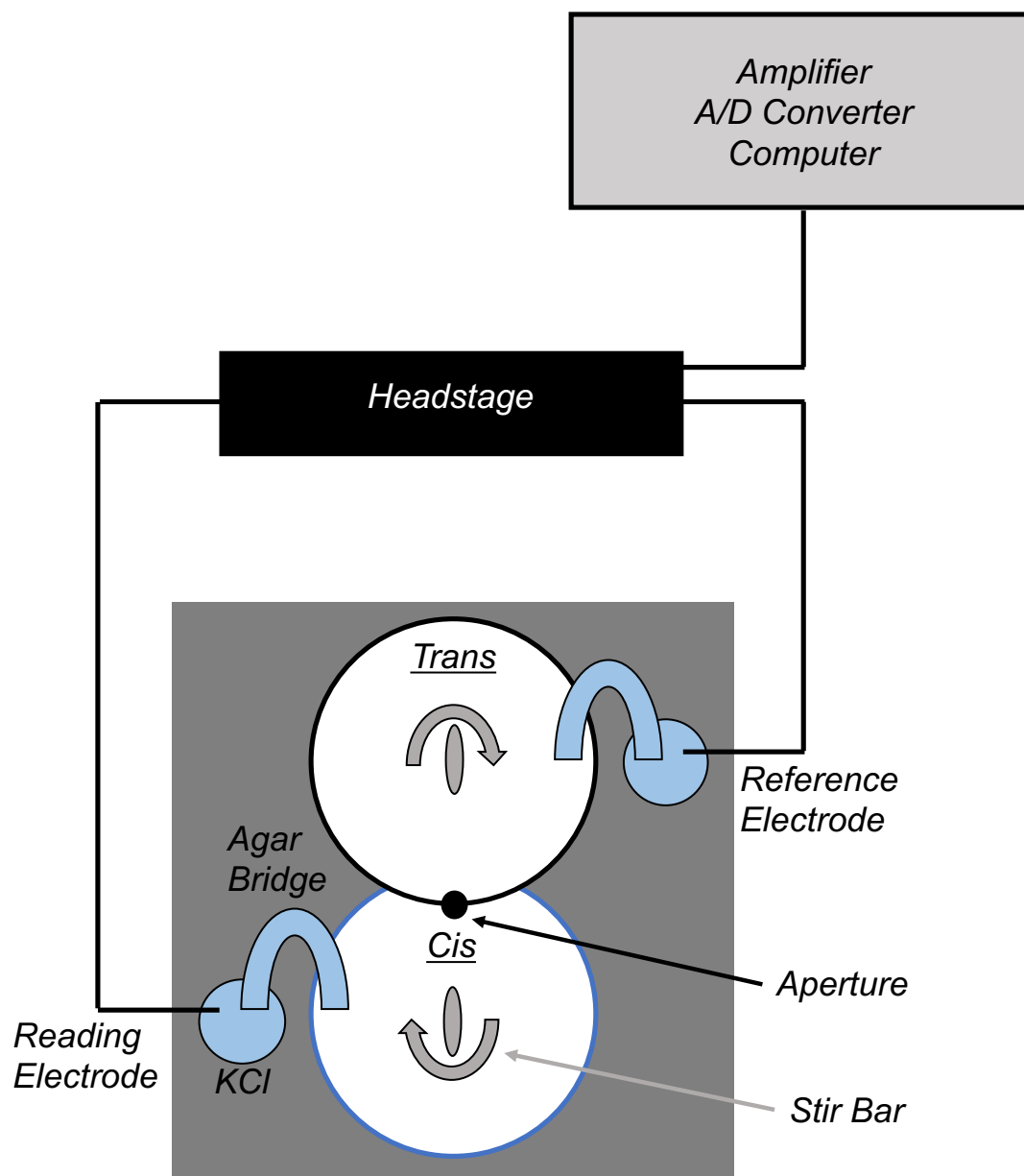
Electronics equipment for PLB experiments included an Axopatch 200B amplifier with a CV 203BU headstage (Molecular Devices), DigiData 1322A analog-to-digital interface (Molecular Devices), a TDS 1002 oscilloscope (Tektronix), an LPF-100B low-pass Bessel filter (Warner Instruments), a computer, and a monitor. The Clampex program within pClamp (Axon Instruments) was used for data acquisition, while the ClampFit program was used for data processing. Other equipment included an aluminum box, Spin-2 bilayer stirplate and controller, stir bars, and bilayer chambers (BCH-M13) and cuvettes (CD13A-200) from Warner Instruments. Lipids should be purchased from Avanti Polar Lipids. Glass rods with closed ends and agar bridges with 3% agar in 1 M KCl were prepared by hand.

For the amplifier, “Headstage cooling” should be turned on. Dials for “Zap”, “Pipette Capacitance Compensation”, “Series Resistance Compensation”, “Whole-cell Parameters”, and “Subtraction” should be turned as low as possible. The “Configuration” should be in “Patch $\beta=1$ ” for the capacitive headstage and in “Whole Cell $\beta=1$ ” for the resistive headstage. “Mode” should be set to “V-clamp”. The “Low-Pass Bessel Filter” and “Output Gain” should be set to values that are appropriate for the specific experiment. “Pipette Offset” should remain around 5, but this will be adjusted during the zeroing process.

Microsomes or proteoliposomes were pre-phosphorylated with 5 mM ATP and 100 U/mL PKA (Promega) for 15 min at room temperature. These samples were stored on ice otherwise. POPE and POPS lipid aliquots in chloroform in a glass vial (10 mg/mL) were brought to room temperature prior to opening the vial to prevent condensation on the inside of the vial. Using a glass syringe, an appropriate volume of lipids in chloroform were mixed into a new glass vial to produce 300 μg of a 7:3 POPE:POPS ratio (21 μL to get 210 μg POPE, 9 μL to get 90 μg POPS). This lipid mixture in chloroform was dried under a stream of nitrogen gas. Dried lipids were resuspended in 10 μL decane and vortexed briefly, making a final 30 mg/mL solution.

The chamber was assembled as shown in Figure 5.1. Lipids in decane were applied lightly around the aperture on the *cis* side of the PLB cup (“priming”) and the cup was replaced into the holder. To the

Figure 5.1: Diagram of the PLB setup, viewed from above. Two chambers (*cis*, white circle with blue outline; *trans*, white circle with black outline) are separated by a 200 μm diameter aperture (black circle). A stir bar (grey oval with black outline) is placed in each chamber. Adjacent to each chamber is a small cup (light blue circles with black outlines) filled with 1 M KCl. Agar bridges (light blue arches with black outlines) of 3% agar in 1 M KCl are used to connect the chambers to the cups with KCl. One electrode (black line) is placed in each KCl cup, and the electrodes are connected to the headstage (black rectangle). The headstage is connected to the amplifier, which is connected to the A/D converter, which is connected to the computer (grey box with black outline).



outer wells of the holder, 1 M KCl was added, and the agar bridges were used to connect these wells to the main chambers. The main chambers were filled with 900 μ L of recording solution comprised of 50 mM KCl, 10 mM MOPS, 1 mM MgCl₂, and 2 mM CaCl₂ (pH 6.9). Silver chloride pellet electrodes were connected to the headstage with the ground electrode connected to the *trans* chamber and the recording electrode connected to the *cis* chamber.

To establish a bilayer, a protocol was run that performed a voltage ramp from 0 mV to +200 mV to 0 mV over 1 s. The chamber was zeroed using “Pipette Offset” until the vertical current aligned with the start of the ramp up to +200 mV. As the protocol continued to run, additional lipids in decane were painted onto the aperture with the glass rod until the current trace appeared similar to a square wave. The capacitance of the membrane was determined by evaluating this wave via the equation

$$I_{cap} = C \frac{dv}{dt}$$

, where I_{cap} is the capacitive current at the end of the ramp up to 200 mV, C is the capacitance, and dv/dt is calculated from the protocol (0.2 V / 1 s). Bilayers were considered usable if they were >200 pF.

Once a viable bilayer was formed, to establish an ion gradient, 250 mM KCl was added to the *cis* chamber, with a concurrent amount of water added to the *cis* chamber. This chloride gradient established a -45 mV potential, *cis* relative to *trans*. Additionally, pre-phosphorylated microsomes or proteoliposomes (7-14 μ L), 100-500 μ M ATP, and 50 U/mL PKA were added to the *cis* chamber. An appropriate amount of relevant buffer was added to the *trans* chamber to compensate for these volumes added to the *cis* chamber.

To facilitate mixing and fusion, the system was stirred, and the protocol was switched to one that steps from 0 mV, to +100 mV, to -100 mV, back to 0 mV over 1.2 s. Once incorporation occurred, stirring and the protocol were stopped. A recording was started, and the system was subjected to a -45 mV applied potential (for -90 mV total electrochemical potential). After recording baseline currents, the applied voltage was removed, and 10 μ M INH172 was added bilaterally. The system was stirred briefly to facilitate mixing, then the stirring was turned off, the -45 mV potential was reapplied, and the recording was resumed.

Chambers were washed overnight in detergent water following addition of INH172.

5.3 Results

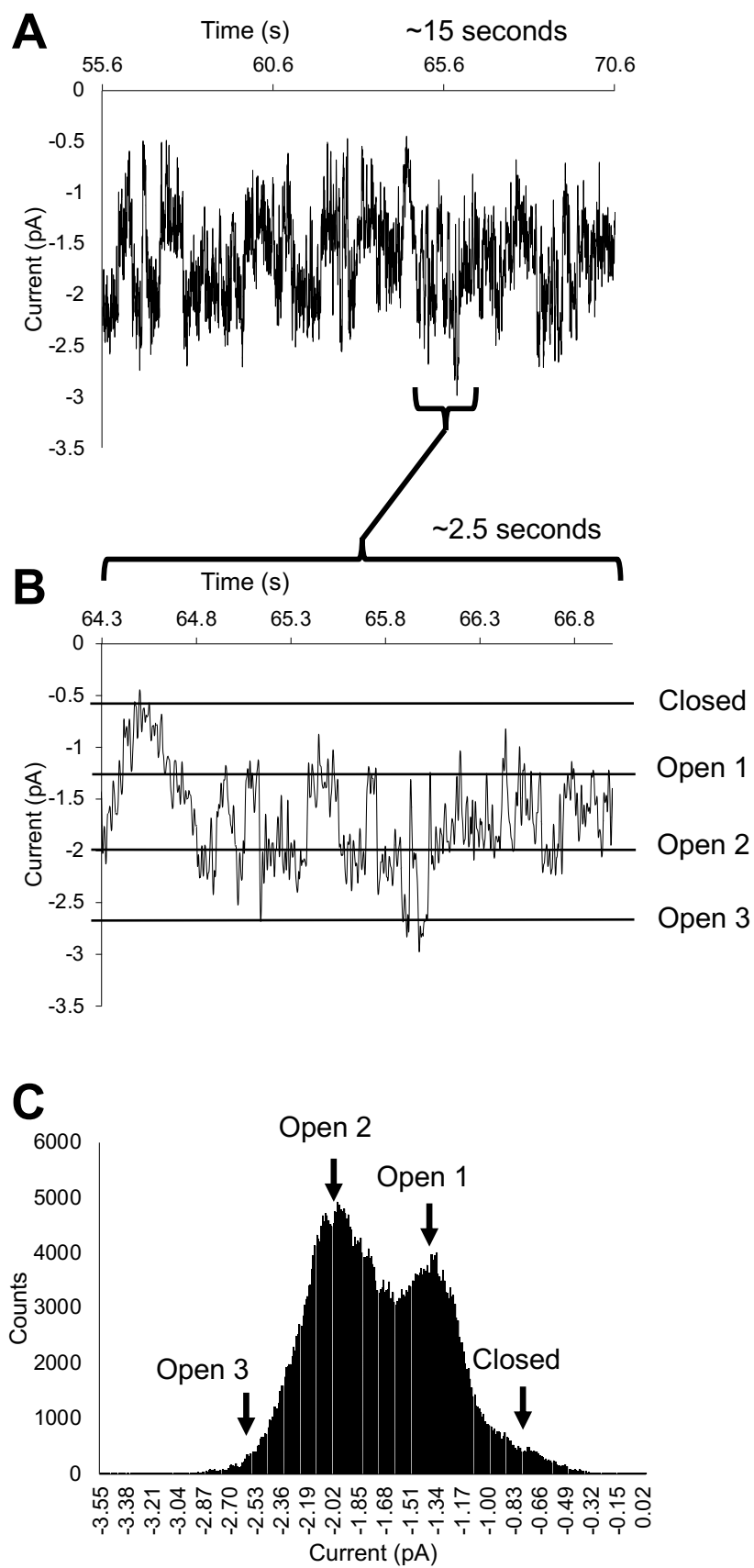
5.3.1 A CFTR-like current can be detected in His-CFTR-expressing BHK microsomes

Microsomes were generated from BHK cells expressing His-tagged CFTR, as described in section 5.2.2. The CFTR within these microsomes was then pre-phosphorylated with PKA and ATP. Importantly, note that within these microsomes, we do not know protein orientation. Only 50% of CFTR channels will have their intracellular R-domain facing outwards towards the bulk solution, whereas the other 50% will have their R-domain facing inwards towards the center of the microsome, which will be inaccessible to the PKA and ATP. Thus, only 50% of CFTR channels will be phosphorylated at this step. Phosphorylated microsomes were then added to the *cis* cup of the PLB chamber along with additional PKA and ATP. When fusion occurs, pre-phosphorylated CFTR channels positioned in the microsome such that their intracellular R-domain faces the bulk solution will establish an orientation in which this intracellular R-domain and intracellular NBDs face towards the *cis* cup, where the PKA and ATP are located. The CFTR channels that were not pre-phosphorylated due to an inverted positioning in the microsomes will fuse such that their intracellular R-domain faces towards the *trans* cup, which has no PKA or ATP. Thus, while CFTR channels will fuse in both orientations in the PLB, active channels will be represented by one orientation.

Three independent fusion events were detected and analyzed. A representative fusion event for His-tagged CFTR-expressing BHK microsomes is discussed (Figure 5.2). This particular fusion event contained three active channels, as determined by the maximum number of simultaneous openings in the current trace (Figure 5.2B), as well as analysis of the amplitude histogram distribution of currents (Figure 5.2C). Combining the analysis of the three separate traces, the conductance (G) and open probability ($P(o)$) of the channel was determined using ClampFit. Conductance was calculated by averaging the current for each channel opening for each trace and dividing by $-0.09 \mu\text{V}$ (the functional voltage across the PLB given the chloride gradient and applied voltage). $P(o)$ was calculated by dividing the total open probability by the number of channels present (taken as the largest number of simultaneously open channels). These combined

Figure 5.2: A CFTR-like current can be detected in His-CFTR-expressing BHK microsomes.

Microsomes from BHK cells expressing His-tagged CFTR were generated and then analyzed for single-channel CFTR activity as described in the PLB setup with ATP concentrations at 100-500 μM . **(A)** 15 seconds of an example trace at -45 mV applied voltage is shown. **(B)** An expansion of 2.5 seconds of this trace is also shown. Horizontal black lines indicate the closed, one-channel open, two-channels open, and three-channels open levels. **(C)** A histogram analysis of the currents over the entire trace prior to any drug additions is also shown.



analyses of all three traces indicate that the channel had a 6.85 ± 0.47 pS conductance and a 0.499 ± 0.097 P(o). These are similar to previously reported values for CFTR (351-353). Thus, we are confident that these channels are indeed CFTR channels.

5.3.2 *The CFTR current from His-CFTR-expressing BHK Microsomes is sensitive to INH172*

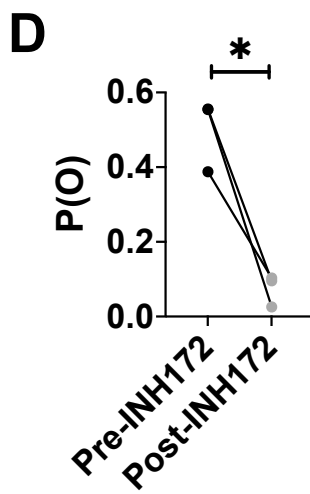
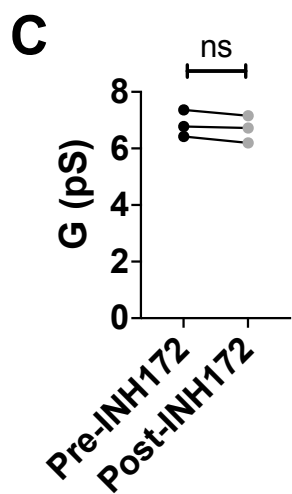
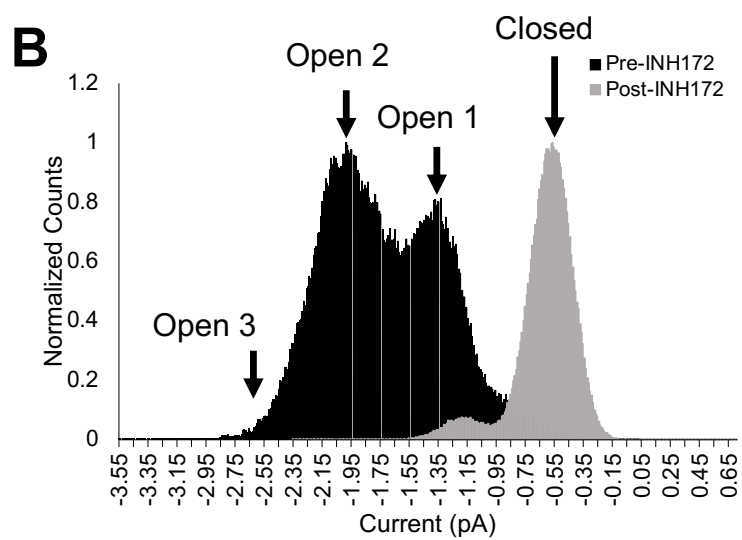
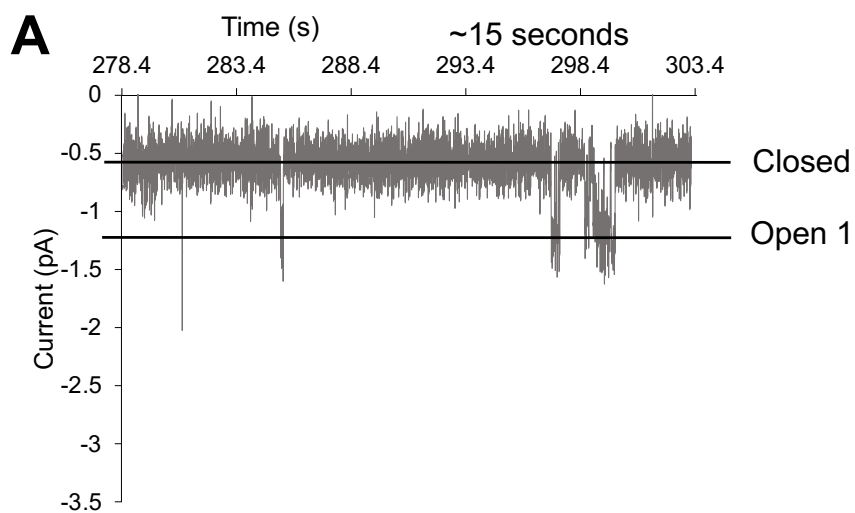
To further confirm if these channels were indeed CFTR, we applied the CFTR inhibitor INH172 bilaterally (10 mM) (312). INH172 is an effective, voltage-insensitive, closed-channel stabilizer (i.e., gating modifier; $K_i = 0.6 \mu\text{M}$) thought to bind at one of the TMDs of CFTR (354; 355). INH172 has been found not to affect CFTR single-channel conductance, but rather decrease the P(o) of CFTR channels (355).

The same fusion event reported above was analyzed following INH172 addition (Figure 5.3). Fewer events in which multiple channels were opened simultaneously were observed, as determined by the current trace (Figure 5.3A) and the shift in the histogram analysis towards the closed level (5.3B, grey). However, it can be assumed that the same three channels remain in the bilayer from the original analysis. Importantly, and consistent with previous reports (355), the average conductance of all three traces remained at 6.69 ± 0.48 pS (Figure 5.3C). This was not significantly different from the pre-INH172 conductance. However, the average P(o) decreased to 0.075 ± 0.04 (Figure 5.3D). This indicates an average 85.0% decrease in P(o) following 10 μM INH172, which is similar to previous reports (355). Overall, these data further confirm that this channel is CFTR.

5.3.3 *Purified CFTR proteoliposomes can be analyzed by PLB but are not as sensitive to INH172*

One consideration when evaluating CFTR in BHK microsomes is that the lipids from the BHK membrane are included during the fusion. Thus, the lipid composition is not as controlled. To circumvent this, one can use purified CFTR reconstituted into proteoliposomes of a known lipid composition. Note, however, that tightly bound lipids such as those seen in the cryo-EM structures for CFTR discussed in section 1.7.1 may still remain associated with CFTR after purification.

Figure 5.3: The CFTR-like current from His-CFTR-expressing BHK Microsomes is sensitive to INH172. Following collection of pre-drug data (Figure 5.2), 10 μ M INH172 was added to each chamber of the PLB setup. Data collection was then continued. **(A)** 15 seconds of an example trace at -45 mV applied voltage is shown. Horizontal black lines indicate the closed level and 1-channel open level. **(B)** A histogram analysis of the currents prior to INH172 addition (black) is also shown alongside a histogram of the currents following INH172 addition (grey). A clear shift to the closed level is apparent following INH172 addition. Combining the analysis of three separate traces, the **(C)** conductance and **(D)** P(o) of the channel was determined before and after INH172 addition as described in Methods. These analyses indicate that this channel had a 6.85 +/- 0.47 pS conductance and a 0.499 +/- 0.97 P(o) prior to INH172 addition, and a 6.69 +/- 0.48 pS conductance and a 0.075 +/- 0.04 P(o) following INH172 addition. These data were analyzed by paired two-tailed *t* tests, which indicate that while conductance was unaffected by INH172 treatment (p=0.0988), P(o) was significantly reduced (*p=0.0282).



We purified CFTR and reconstituted it into proteoliposomes, as described in section 5.2.3. These proteoliposomes share the same orientation issue for CFTR as described above for microsomes, but again this does not create a problem when evaluating CFTR in the PLB since we can ensure that only channels oriented with intracellular domains in the *cis* chamber are recorded from by only including ATP and PKA in that chamber. These CFTR-proteoliposomes were added to the *cis* cup of the PLB chamber and given time to fuse. While three fusion events occurred, two of these fusions displayed a double-conductance phenomenon (*data not shown*) seen previously with purified CFTR and proposed to be coordination between two CFTR channels (351). However, this double-conductance was not seen in any of the microsome fusions. Furthermore, these two varied conductances make analysis of the trace difficult.

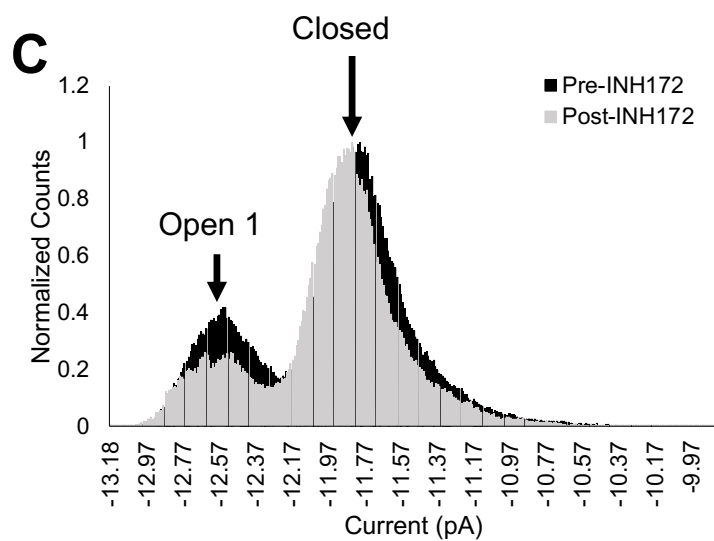
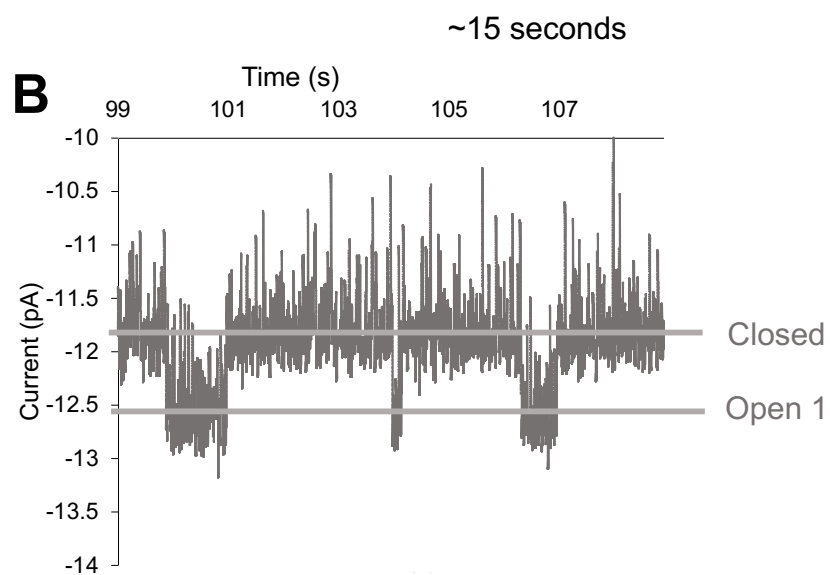
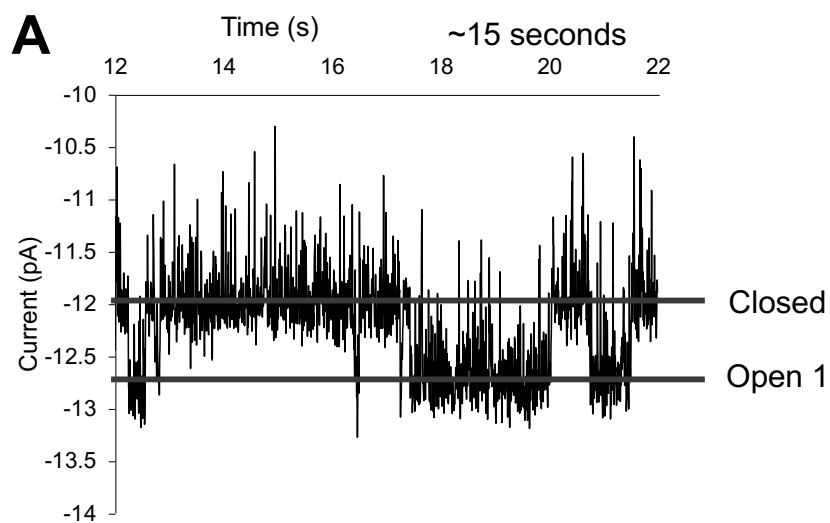
Thus, for the purposes of this work, we only considered the fusion in which a single conductance was observed (Figure 5.4). Importantly, only one active channel was present in this fusion event, as determined by the maximum number of open channels observed simultaneously over the trace (Figure 5.4A) and by analysis of the amplitude histogram (Figure 5.4C, black). Since only one active channel was present, cooperation could not have occurred. This channel had a 7.69 pS conductance and a 0.318 P(o), which is similar to what was observed for the CFTR in the BHK microsomes.

Interestingly, bilateral addition of 10 μ M INH172 did not seem to have a dramatic effect on the channel P(o) (Figure 5.4B-C). Following INH172 addition, the channel maintained a 8.04 pS conductance, with a slightly decreased P(o) of 0.214. This indicates a 32.7% reduction in P(o), which is far less than the 85.0% reduction in BHK microsomes. The reason for this discrepancy requires further investigation.

5.4 Discussion

We have shown that we can record CFTR single-channel currents from microsomes generated from BHK cells expressing His-tagged CFTR and from DMPC proteoliposomes containing His-tagged CFTR purified from BHK cells. This technique will be critical in the future for evaluating the effects of various lipids on CFTR ion channel activity, as thus far, studies have been limited to evaluating CFTR ATPase activity in controlled lipid environments.

Figure 5.4: Purified CFTR proteoliposomes can be analyzed by PLB but are not as sensitive to INH172. Proteoliposomes were generated from purified CFTR and then analyzed for single-channel CFTR activity via the PLB setup, with ATP concentrations at 500 μ M. An example trace (15 sec) at -45 mV applied voltage **(A)** prior to and **(B)** following 10 μ M INH172 addition is shown. **(C)** An amplitude histogram analysis of the currents prior to INH172 addition (black) is also shown alongside a histogram of the currents following INH172 addition (grey). While a slight shift to the closed level appears, the shift is not substantial.



Interestingly, we found that the CFTR from BHK microsomes was sensitive to INH172 inhibition, though the reconstituted CFTR proteoliposomes were not. This could be due to a number of reasons. One potential hypothesis is that the purification process affected the structure of CFTR such that it was no longer sensitive to INH172. However, the similarity in conductance and open probability between the purified CFTR proteoliposomes and the BHK-CFTR microsomes does not seem to support this hypothesis, though it cannot be ruled out. As an alternative hypothesis, it is possible that purification removed a critical lipid involved in the binding and/or inhibitory mechanism of INH172. Future experiments should be conducted to evaluate the effects of repleting specific lipids into the proteoliposomes and/or planar lipid bilayer to determine if these lipids recover INH172 sensitivity.

CHAPTER 6 – THE EFFECTS OF LONG-TERM HYPERGLYCEMIA ON TIGHT JUNCTION FIDELITY IN NON- CF AND CF 16HBE CELLS

Preface: The work presented here is planned to contribute to a publication once further experiments have been conducted. I wrote all text written independently. I collected the majority of the data and generated all figures. The only data not collected by me are included in figure 6.1, with these data being collected by Dr. Guiying Cui.

6.1 Introduction

As clinical care for CF has improved, and as the life expectancy of people with CF has increased, comorbidities have become an important consideration for disease management. The most common comorbidity in people living with CF is CFRD (356). CFRD is defined as a 2 hr post-prandial plasma glucose level >200 mg/dL either with or without fasting glucose levels >126 mg/dL. It is present in approximately 20% of adolescents with CF, increasing in prevalence to approximately 50% in adults over 30. The predominant defect in CFRD is impaired insulin secretion due to pancreatic damage (357; 358). This can be managed with insulin injections, which lead to health improvements including increased pulmonary function and survival (359). However, there is also some degree of insulin resistance in CF, which can worsen during episodes of infection and inflammation (357; 358; 360; 361).

The CFRD comorbidity is important to the health of people with CF, as numerous studies have found decreased lung function, increased frequency of pulmonary exacerbations, and increased mortality in people with CFRD as compared to people with CF without CFRD (356; 362-365). Mortality in CFRD generally is due to pulmonary failure, as opposed to other complications associated with Type 1 and Type 2 diabetes such as cardiovascular disease. While pulmonary manifestations generally are not discussed in non-CF diabetes, there is evidence that pulmonary function is negatively impacted in non-CF diabetes (366;

367). Specifically, both forced vital capacity and FEV1 were decreased in people with type 2 diabetes relative to their non-diabetes controls, even after adjusting for many potential confounders such as adiposity, smoking, and physical activity (368).

Understanding the connection between CF, CFRD, and worsened airway function is critical for developing new treatment strategies for the aging CF population. The airways of people with CF without CFRD were found to have increased glucose relative to non-CF controls, as analyzed via exhaled breath condensate (369). Even more precisely, the ratio between airway glucose and blood glucose was significantly higher in CF relative to control (369). People with CF with CFRD had even more increased airway glucose levels and ratios of airway to blood glucose than their non-CFRD CF controls. In a gut-corrected CFTR knockout mouse model, CF mice with diabetes exhibited a worsened ability to clear a pulmonary infection of *P. aeruginosa* than CF mice without diabetes (370). Importantly, *P. aeruginosa* and *S. aureus* grew better in media containing glucose concentrations present in the CF airway than in media containing glucose concentrations present in the non-CF airway (371). This seems to have clinical relevance, as co-infection with both of these pathogens is correlated with decreased lung function, and people with CFRD are more likely to have co-infection than non-CFRD CF controls (372). Thus, cumulatively, these data suggest that an increased bacterial burden in the CFRD lung is possibly due to increased growth of the bacteria in the elevated glucose environment that cannot not be overcome by the body's clearance mechanisms. Understanding the mechanism by which increased glucose levels exist in the CF airway, especially in the CFRD airway, is the next step to determining effective treatment strategies to mitigate these deleterious effects.

Previous work in NuLi and CuFi cells, which are telomerase-immortalized cell lines representing non-CF and CF airway epithelial cells, respectively, has indicated reduced transepithelial resistance (TER) and increased paracellular flux of glucose-sized molecules in CuFi cells as compared to NuLi cells (373). This was confirmed in cfHBE (homozygous $\Delta F508$ -CFTR) compared to nHBE cells as well (374). Interestingly, insulin treatment can affect the TER and paracellular flux of these cells. In nHBE, cfHBE, NuLi, and CuFi cells, insulin receptor was expressed mostly apically (374). In nHBE and NuLi cells, insulin

increased TER. Contrarily, TER was unaffected by insulin treatment in cHBEs and CuLi cells. In NuLi cells, insulin decreased paracellular flux of small molecules such as calcein, whereas in CuFi cells, insulin increased paracellular flux of small molecules (374).

This increased paracellular flux of small molecules in CF cells has important implications on glucose flux, and it was confirmed that glucose flux is increased in CuFi cells as compared to NuLi cells (374). In addition, in nHBEs and NuLi cells, but not in cHBEs or CuFi cells, insulin stimulated glucose uptake, mostly through the apical membrane (374). The combined increased paracellular glucose flux and decreased insulin-responsive glucose-uptake in CF airway cells could explain the increased levels of airway glucose in the CF lung.

While dysfunctional PI3-kinase/protein kinase B has been implicated in the lack of response to insulin in CF cells (374), the reason for diminished barrier function in CF cells at baseline is not well understood yet. We sought to determine if an imbalance of tight junction protein expression or localization was the cause for impaired barrier function in CF airway cells, and if chronic hyperglycemic conditions affected the expression of these proteins.

6.2 Methods

6.2.1 16HBE cells

16HBE cells, expressing either WT-CFTR or Δ F508-CFTR, were grown as described in section 2.2.2. Cells were plated at 250,000 cells/well on 3460 Transwells for the purposes of qRT-PCR experiments. Two days following plating onto the Transwells, cells were either transitioned to media containing 17.5 mM glucose (316 mg/dL) or were maintained in media with 5.5 mM glucose (90 mg/dL). Media was changed every day following this step for five days, at which point the cells were analyzed.

6.2.2 Transepithelial short-circuit current analysis

Transepithelial short-circuit currents were obtained using an Ussing Chamber system, as described

in section 2.2.5. However, recording solutions were different. The normal chloride basolateral buffer was 140 mM NaCl, 5 mM KCl, 0.36 mM K₂HPO₄, 0.44 mM KH₂PO₄, 0.5 mM MgCl₂, 1.3 mM CaCl₂, 4.2 mM NaHCO₃, 10 mM glucose, 10 mM HEPES, pH 7.4. The low chloride apical buffer was 133 mM Na gluconate, 5 mM K gluconate, 2.5 mM NaCl, 0.36 mM K₂HPO₄, 0.44 mM KH₂PO₄, 0.5 mM MgCl₂, 5.7 mM CaCl₂, 4.2 mM NaHCO₃, 10 mM mannitol, 10 mM HEPES, pH 7.4.

6.2.3 *Transcriptional expression analysis*

All solutions (except PBS) for these experiments were handled carefully and separately from general supplies to prevent contamination with RNAses for these real-time quantitative reverse transcription polymerase chain reaction (qRT-PCR) experiments.

Cells from two 3460 wells were scraped into PBS and centrifuged at 500 xg for 10 min. PBS supernatant was removed, and the cell pellet was resuspended in 300 µL TRIzol™ (Thermo Scientific). This was left at room temperature for 5 min, at which point the TRIzol™ mixture was stored at -20 °C. To extract RNA, this TRIzol™ mixture was thawed, and mixed with 60 µL chloroform, vortexed, and left at room temperature for 2-3 min. The mixture was centrifuged at 12,000 xg for 15 min at 4 °C. The upper aqueous phase containing RNA was collected into a new tube, to which 150 µL isopropanol was added. This mixture remained at room temperature for 10 min, and then was centrifuged at 12,000 xg for 15 min at 4 °C. The supernatant was removed, and the pellet was resuspended in 1 mL of cold 70% ethanol by vortexing. After 10 min, the solution was centrifuged at 7,500 xg for 10 min at 4 °C, and the wash of the pellet was repeated twice more. Following the final wash, the ethanol was removed, and the pellet was dried in a fume hood.

The pellet was resuspended in 25 µL ZymoPURE™ Elution Buffer (Zymo Research), and the concentration and integrity of the sample was obtained using a NanoDrop ND-1000 Spectrophotometer. Following this, the QuantiTech Reverse Transcription Kit (Qiagen) was used according to the manufacturer's protocol to remove genomic DNA and convert the RNA into cDNA. The generated cDNA

was then diluted 1:10 in RNase-free water, then mixed 1:1 with 2x Power SYBR[®] Green Master Mix (Thermo Scientific). This mixture (40 μ L/well) was added to a predesigned and prevalidated BioRad PCR primer plate, which was then sealed with Microamp Optical Adhesive Tape (Thermo Scientific) and centrifuged sideways to push all contents to the bottom of the well. Each plate contained wells for three replicates of each gene, so each experimental condition was given an entire plate for analysis to allow for triplicate in most genes.

A StepOnePlus[™] Real-Time PCR System (Thermo Scientific) was used to perform the analysis. The plate was maintained at 95 °C for 10 min. Then, 40 cycles of a 15 sec hold at 95 °C followed by a step to 60 °C were run. Following these amplification cycles, a melt curve analysis was performed to determine the fidelity of the primers. This melt curve analysis maintained a temperature of 95 °C for 15 sec, then stepped to 60 °C for 1 min, then took 0.3 °C steps up to 95 °C every 15 sec.

Any gene with a cycle threshold (C_T) greater than 35, with a melt curve with multiple prominent peaks, or with a melt curve without a prominent peak, was not considered for analysis. HPRT1 was used as the housekeeping gene to calculate ΔC_T , the difference between the C_T of the gene of interest and that of the normalization housekeeper gene. The WT-16HBE 5.5 mM glucose group was grown and run separately from the other treatment groups. Upon analysis, the WT-16HBE 5.5 mM glucose group had an average ΔC_T over all 21 viable genes of interest that was approximately 1 less than the other groups, which were all within 0.4 of each other. Because this group was grown and analyzed separately, an adjustment was made to each ΔC_T of the WT-16HBE 5.5 mM glucose group such that its average ΔC_T matched the average ΔC_T of the other three groups combined. Note that this adjustment caused a loss of significant difference in 6 genes when comparing WT-16HBE 5.5 mM glucose to 17.5 mM glucose, while only gaining significance in 1 gene. Similarly, it caused a loss of significant difference in 7 genes when comparing WT-16HBE to Δ F508-16HBE 5.5 mM glucose, while only gaining significance in 2 genes. Thus, for the most part, this adjustment biases our results towards the null.

The ΔC_T values for each group were compared by multiple t tests and are plotted as volcano plots

with the $-\log(\text{P value})$ on the y-axis, and the $\log_2(\text{fold difference})$ in transcript levels is on the x-axis. Recall that a difference in ΔC_T of 1 is an approximate two-fold difference between transcript levels, so the x-axis can be viewed as the $-\Delta\Delta C_T$, the difference in ΔC_T between groups. Note that though SLC2A glucose transporters were evaluated, they are not reported in this work.

6.2.4 *Immunofluorescence staining*

All steps were performed at room temperature, unless otherwise noted. Cells on Transwells were washed 3 times with ice-cold PBS, then fixed in ice-cold 100% methanol for 10 min. Cells were washed 3 times with PBS, then were permeabilized with 0.2% Triton X-100 for 15 min. Cells were washed 3 times with PBS, then nuclei were stained with 10 $\mu\text{g/mL}$ DAPI for 5 min. Cells were washed 3 times with PBS, then were blocked for 1 hr in PBS + 2% BSA. Cells were then incubated with primary antibodies in PBS/BSA overnight at 4 °C. The antibodies for claudin-1 (CLDN1) (Fisher Scientific, 51-900-0), claudin-3 (CLDN3) (Thermo Scientific, 34-1700), and claudin-4 (CLDN4) (Thermo Scientific, 36-4800) were diluted at 1:100, while the antibody for claudin-7 (CLDN7) (Fisher Scientific, 34-910-0) was diluted at 1:200. Cells were washed 3 times in PBS/BSA, then were incubated with 1:500 Alexafluor 594 anti-rabbit antibody (Thermo Scientific) in PBS/BSA for 1 hr. Cells then were washed 3 times in PBS/BSA, followed by 3 washes in PBS. A razor was used to separate the flexible plastic support for the cells from the firm plastic structure of the Transwells. These cells were then placed on a cover slide and ProLong Gold Antifade mounting media (Thermo Scientific) was added to the cells. Lastly, a cover slip was placed on top and sealed with clear nail polish.

Slides were imaged on an FV1000 confocal microscope maintained at the Emory Integrated Cellular Imaging Core. A 40x objective with oil, a step size of 1 μm , and Kalman filter mode were used. Each set of samples for a given claudin was imaged with the same laser intensities, HV, gain, and offset on the same day. Images were then analyzed using FIJI. Specifically, a Z-projection of either the maximum intensity or the average intensity was generated depending on which claudin was being analyzed. The image

was divided into nine equal boxes, and the average intensity of each box was recorded. If the claudin localized to the tight junctions such that a clear cobblestone outline of the cells was apparent, each cell capable of being outlined was numbered, and a random number list generator was used to select 10 of those cells. The segmented line tool was used to outline the selected cells, and the average intensity over that outline was recorded. If a clear cobblestone outline was not apparent, only the average fluorescence over the nine equal boxes was calculated.

6.3 Results

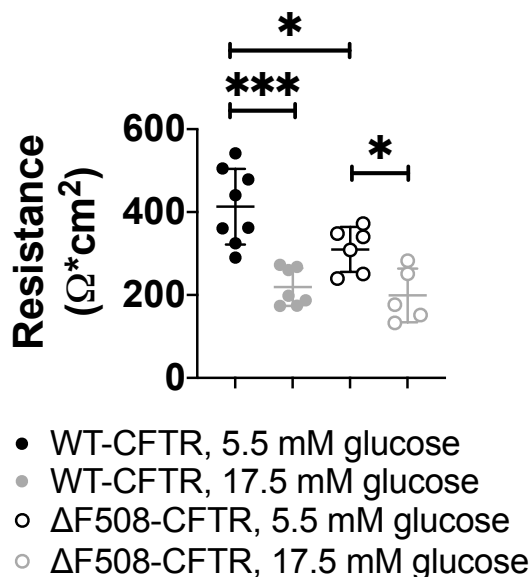
6.3.1 CFTR mutation and long-term glucose growth affect TER in 16HBE cells

While it has been shown that CuFi cells have decreased TER compared to NuLi cells (373), we were interested in confirming this phenomenon in SV40-immortalized 16HBE cells since the latter are available bearing a variety of CFTR mutations (127). Using chamber analysis of 16HBE cells expressing Δ F508-CFTR revealed that these CF cells had decreased TER as compared to WT-CFTR-expressing cells (Figure 6.1). This is consistent with the NuLi and CuFi cells. We then went on to evaluate the effects of chronic hyperglycemia on these TER values. Importantly, in both WT-CFTR- and Δ F508-CFTR-expressing 16HBE cells, growth at 17.5 mM glucose (316 mg/dL) instead of 5.5 mM glucose (90 mg/dL) for 5 days resulted in decreased TER.

6.3.2 CFTR mutation and chronic hyperglycemia affect mRNA expression of tight junction proteins

To begin to understand the origin of the altered TER in CF cells and after chronic hyperglycemic conditions, we performed qRT-PCR analysis evaluating various tight junction proteins. CLDN1 was the most abundantly expressed claudin, followed by CLDN7. CLDN3 and CLDN4 were also detected, but in much lower abundance than CLDN1 and CLDN7. CLDN5 was not detected in these 16HBE cells. Gap junction protein B2 (GJB2) was the most abundantly expressed gap junction protein, followed by GJB5, GJB4, and GJA3. GJB1 was not detected.

Figure 6.1: TER is lower in CF cells and following hyperglycemic conditions, as determined by an Ussing Chamber. The data represent WT-CFTR 16HBE cells grown in either 5.5 mM (closed black, n=8) or 17.5 mM glucose (closed grey, n=7), and Δ F508-CFTR 16HBE cells grown in either 5.5 mM (open black, n=6) or 17.5 mM glucose (open grey, n=5). Data were analyzed by unpaired two-tailed *t* tests. Within WT-CFTR and Δ F508-CFTR 16HBE cells, 17.5 mM glucose decreased TER (***p*=0.0002, **p*=0.0128). Comparing WT-CFTR to Δ F508-CFTR 16HBE cells grown in 5.5 mM glucose, Δ F508-CFTR 16HBE cells had significantly decreased TER (**p*=0.0308). Credit to Dr. Cui.



Within WT-CFTR 16HBE cells, hyperglycemic conditions caused a decrease in transcript levels of the tight junction proteins CLDN3, CLDN4, and connexin 30.3 (GJB4) (Figure 6.2A). Simultaneously, there was an increase in transcript levels of connexin 31.1 (GJB5) and SRY-box transcription factor 7 (SOX7). None of these same alterations were found in Δ F508-CFTR 16HBE cells under chronic hyperglycemic conditions. Instead, GJB4 transcript levels were increased while GJB5 levels were decreased (Figure 6.2B). Furthermore, transcript levels for CLDN1, CLDN7, and insulin receptor were decreased in CF cells grown under hyperglycemic conditions.

Evaluation of the differential transcript levels in WT-CFTR and Δ F508-CFTR 16HBE cells also revealed some interesting imbalances. Specifically, Δ F508-CFTR 16HBE cells had lower expression of CLDN3, CLDN4, and GJB4 concomitantly with increased expression of GJB5, similarly to WT-CFTR cells under hyperglycemic conditions (Figure 6.2C). However, contrary to hyperglycemic WT-CFTR cells, Δ F508-CFTR cells under normal glucose conditions had decreased SOX7 transcript levels. Furthermore, Δ F508-CFTR cells under normal glucose conditions had increased connexin 26 (GJB2) and connexin 31 (GJB3) transcript levels relative to WT-CFTR cells under normal glucose conditions.

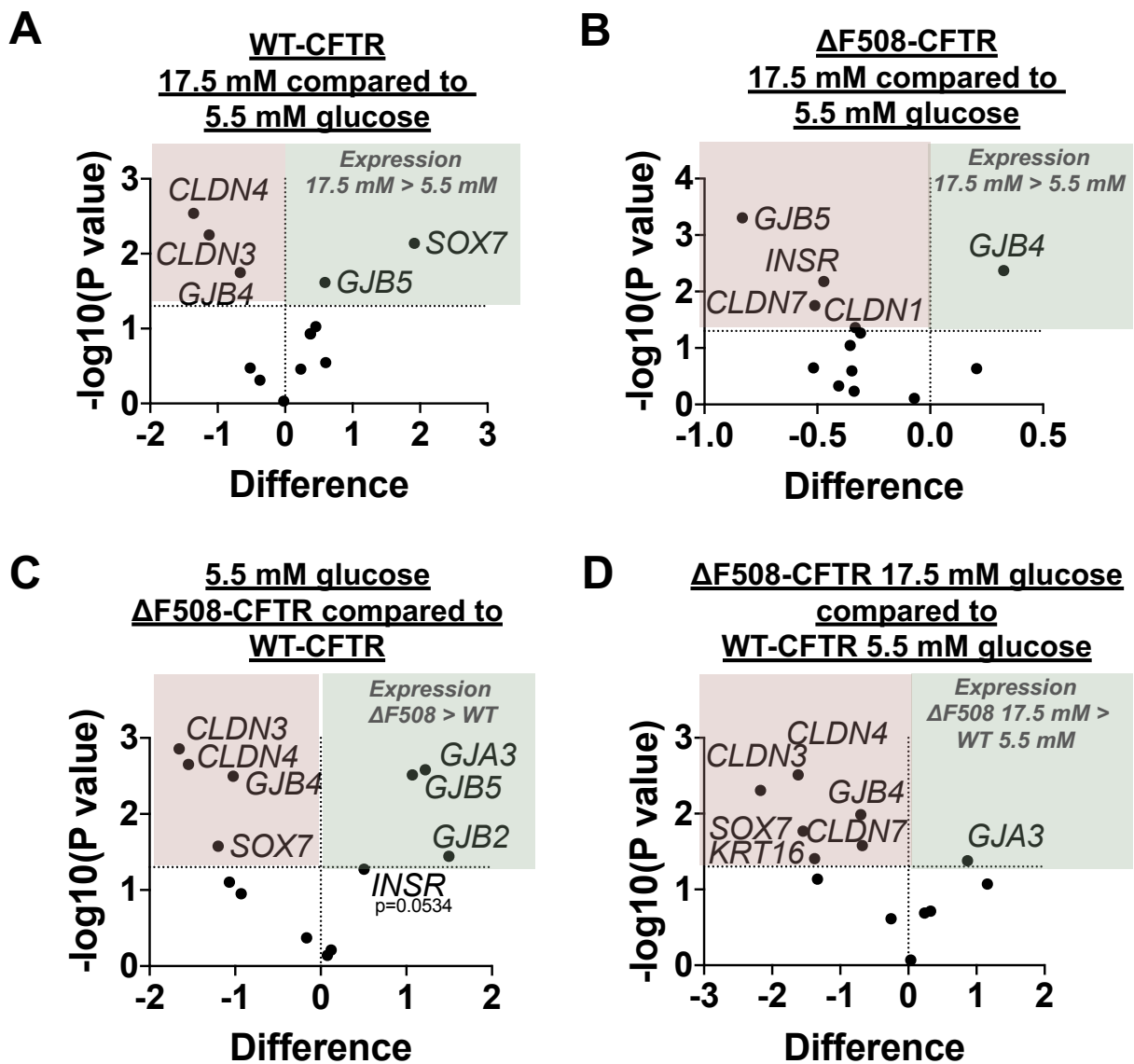
Interestingly, comparison of WT-CFTR cells grown under normal glucose conditions and Δ F508-CFTR cells grown under hyperglycemic conditions indicated that hyperglycemia in Δ F508-CFTR cells recovered some of the imbalances found in Δ F508-CFTR cells under normal glucose conditions. Specifically, GJB2 and GJB5 were no longer differentially expressed (Figure 6.2D). However, CLDN7 and keratin-16 (KRT16) became significantly decreased relative to control.

Importantly, transcript levels do not necessarily correlate with protein levels, and protein levels do not indicate anything about proper trafficking or localization of proteins. Thus, immunofluorescence studies determining the protein abundance and localization of the claudins of interest were performed.

6.3.3 *CFTR mutation and long-term hyperglycemia affect CLDN1 protein expression*

Confocal analysis, in particular evaluation of the orthogonal views of the cells, suggested that

Figure 6.2: PCR analysis of WT- and Δ F508-CFTR-expressing 16HBE cells indicate different gene expression in CF cells and differential adaptations to hyperglycemia. WT-CFTR and Δ F508-CFTR 16HBE cells were grown in either 5.5 mM or 17.5 mM glucose for 5 days, then were collected and analyzed by qRT-PCR. ΔC_T was calculated for each gene, using HPRT1 as the housekeeping gene. These ΔC_T values were compared by multiple *t* tests, with data represented as volcano plots with the difference in ΔC_T on the x-axis and the $-\log(P \text{ value})$ on the y-axis. Genes that were decreased in the comparison group appear in the pink box, whereas genes that were increased appear in the green box. **(A)** Comparing WT-CFTR 16HBE cells grown in 5.5 mM and 17.5 mM glucose, transcript levels for CLDN3, CLDN4, and GJB4 were decreased in the 17.5 mM condition, whereas SOX7 and GJB5 were increased. **(B)** Comparing Δ F508-CFTR 16HBE cells grown in 5.5 mM and 17.5 mM glucose, transcript levels for CLDN1, CLDN7, GJB5, and INSR were decreased in the 17.5 mM condition, whereas GJB4 was increased. **(C)** Comparing WT-CFTR to Δ F508-CFTR 16HBE cells grown in 5.5 mM glucose, transcript levels for CLDN3, CLDN4, GJB4, and SOX7 were decreased in the Δ F508-CFTR 16HBE cells, whereas GJA3, GJB2, and GJB5 were increased. **(D)** Comparing WT-CFTR 16HBE cells grown in 5.5 mM glucose to Δ F508-CFTR 16HBE cells grown in 17.5 mM glucose, transcript levels for CLDN3, CLDN4, CLDN7, GJB4, SOX7, and KRT16 were decreased in the Δ F508-CFTR 16HBE cells, whereas GJA3 was increased.



CLDN1 was evenly distributed throughout the plasma membrane of WT-CFTR 16HBE cells (Figure 6.3A). This does not seem consistent with previous reports, though differential growth methods may be the reason (375; 376). Because of this even distribution, we chose to assemble for analysis a Z-projection based on the average fluorescence over the Z-stack (Figure 6.3A-D). Since the cells were not able to be outlined reliably, the average fluorescence over this Z-projection was calculated as described in section 6.2.4.

Analyses indicated that WT-CFTR cells grown in hyperglycemic conditions, as well as Δ F508-CFTR cells grown in normal or hyperglycemic conditions, have significantly reduced CLDN1 staining compared to WT-CFTR cells grown in normal glucose conditions (Figure 6.3E). Within the Δ F508-CFTR cells, hyperglycemia did increase the CLDN1 levels relative to normal glucose treatment but did not recover these levels to those of the WT-CFTR cells in normal glucose conditions.

6.3.4 *CFTR mutation and long-term glucose growth affect CLDN3 protein expression and localization*

Evaluation of the orthogonal views of the confocal analysis of 16HBE cells suggested that CLDN3 localized very specifically to an apical location between cells, with minimal distribution throughout the remainder of the membrane. As such, we chose to assemble for analysis a Z-projection based on the maximum fluorescence over the Z-stack, since this would best capture localized structures (Figure 6.4A-D). Indeed, a Z-projection of the maximum intensity provided an image with clear outlines of the cells. The membrane localization of CLDN3 (Figure 6.4E) as well as the average fluorescence over the entire image (Figure 6.4F) were analyzed as described in section 6.2.4.

Analyses of the membrane fluorescence of CLDN3 revealed that while hyperglycemic conditions decrease CLDN3 expression in WT-CFTR cells, these same conditions increased expression in Δ F508-CFTR cells (Figure 6.4E). Importantly, the membrane fluorescence of CLDN3 was not significantly different between WT-CFTR cells in normal chloride conditions and Δ F508-CFTR cells in either glucose condition. However, it is vital to note that the number of cells with definable outlines was

Figure 6.3: CLDN1 fluorescence is affected by CFTR expression and glucose growth. Confocal microscopy images were and (A-D) Z-projections of the maximum intensity are shown for WT-CFTR or Δ F508-CFTR 16HBE cells grown in 5.5 mM or 17.5 mM glucose for 5 days. (A) Orthogonal views of the Z-stack also are shown for the WT-CFTR cells grown in 5.5 mM glucose, as a representation of the localization of the claudin along the z-axis. (E) Because CLDN1 is dispersed around the edges of the cells, as can be seen in the orthogonal views, a Z-projection of the average intensity of each pixel over each slice was created and used for analysis in FIJI. The image was divided into 9 equal grid sections, and the average fluorescence intensity of the Z-projection in each section was obtained and analyzed by unpaired two-tailed *t* tests. The data represent WT-CFTR (filled) or Δ F508-CFTR (open) cells grown in 5.5 mM (black) or 17.5 mM glucose (grey). Within the WT-CFTR 16HBE cells, CLDN1 was decreased by growth in 17.5 mM glucose (**** $p < 0.0001$). Within the Δ F508-CFTR 16HBE cells, CLDN1 was increased by growth in 17.5 mM glucose (** $p < 0.098$). When comparing WT-CFTR cells grown in 5.5 mM glucose to Δ F508-CFTR cells, grown in either 5.5 mM or with 17.5 mM glucose, a significant decrease was found in CLDN1 staining (**** $p < 0.0001$).

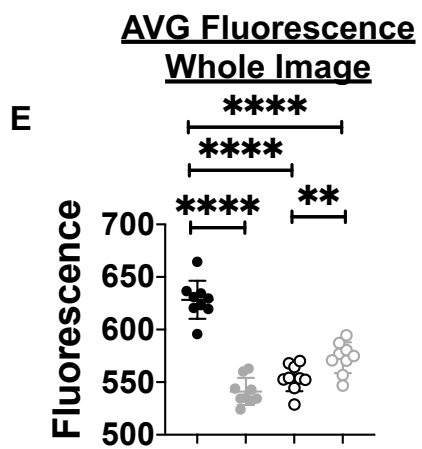
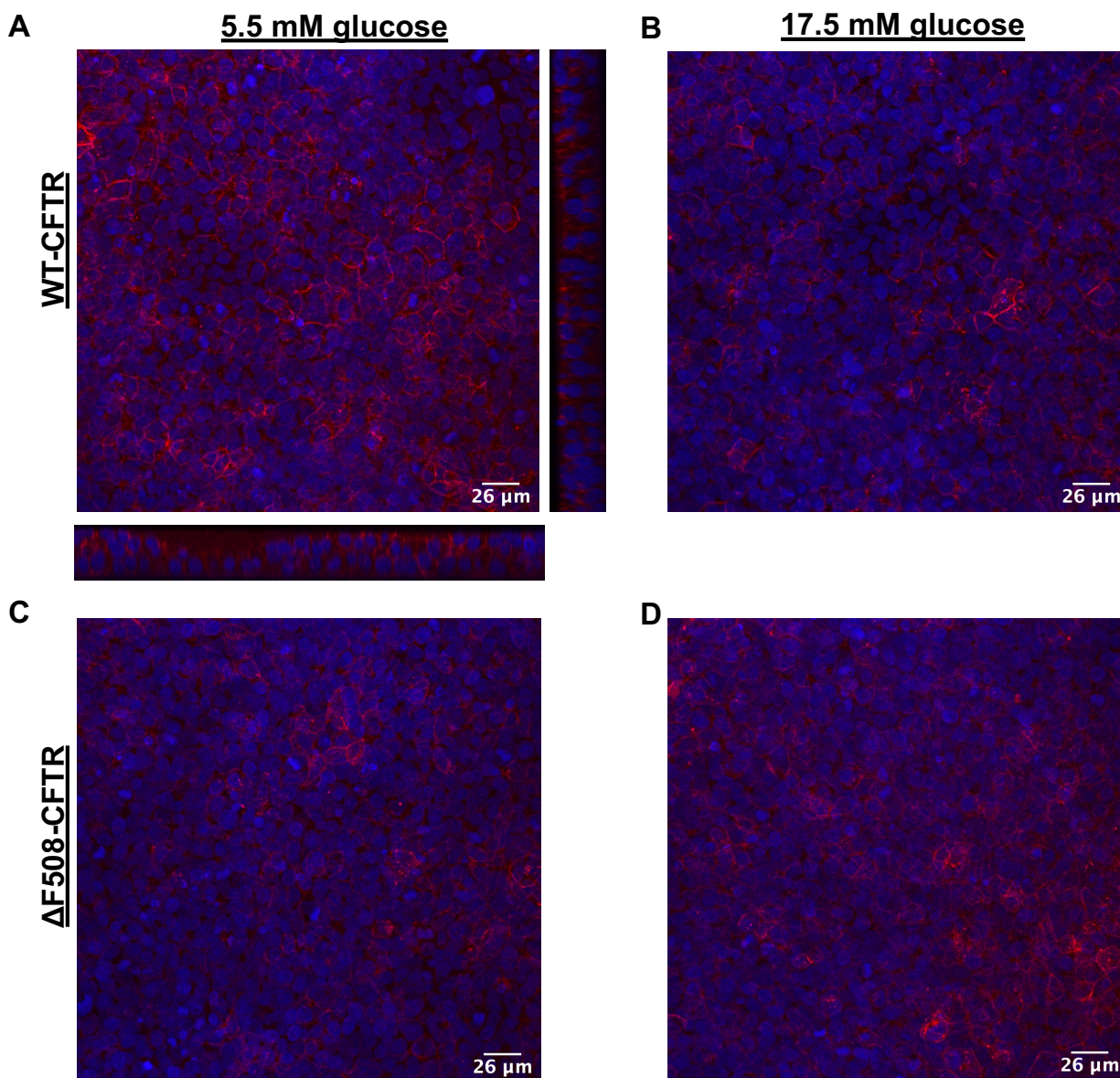
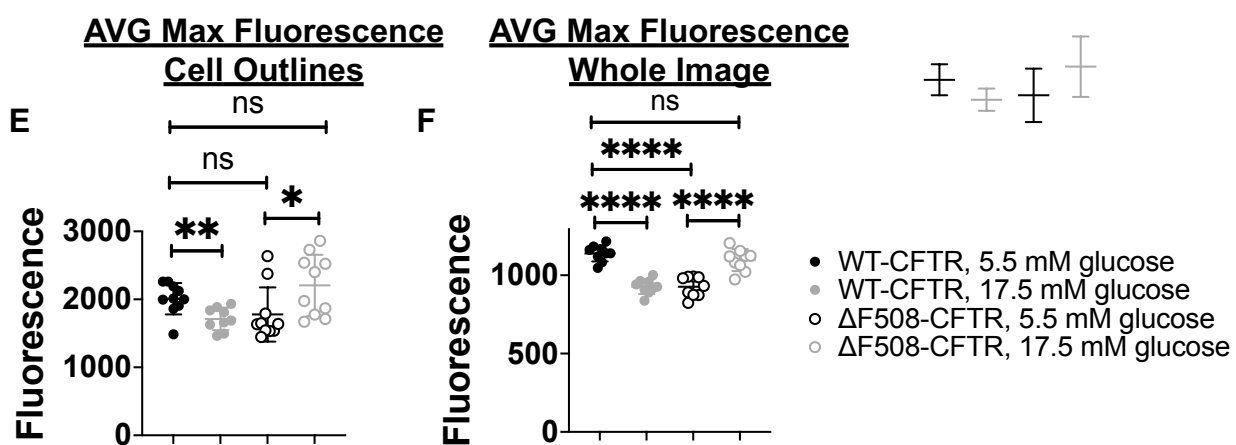
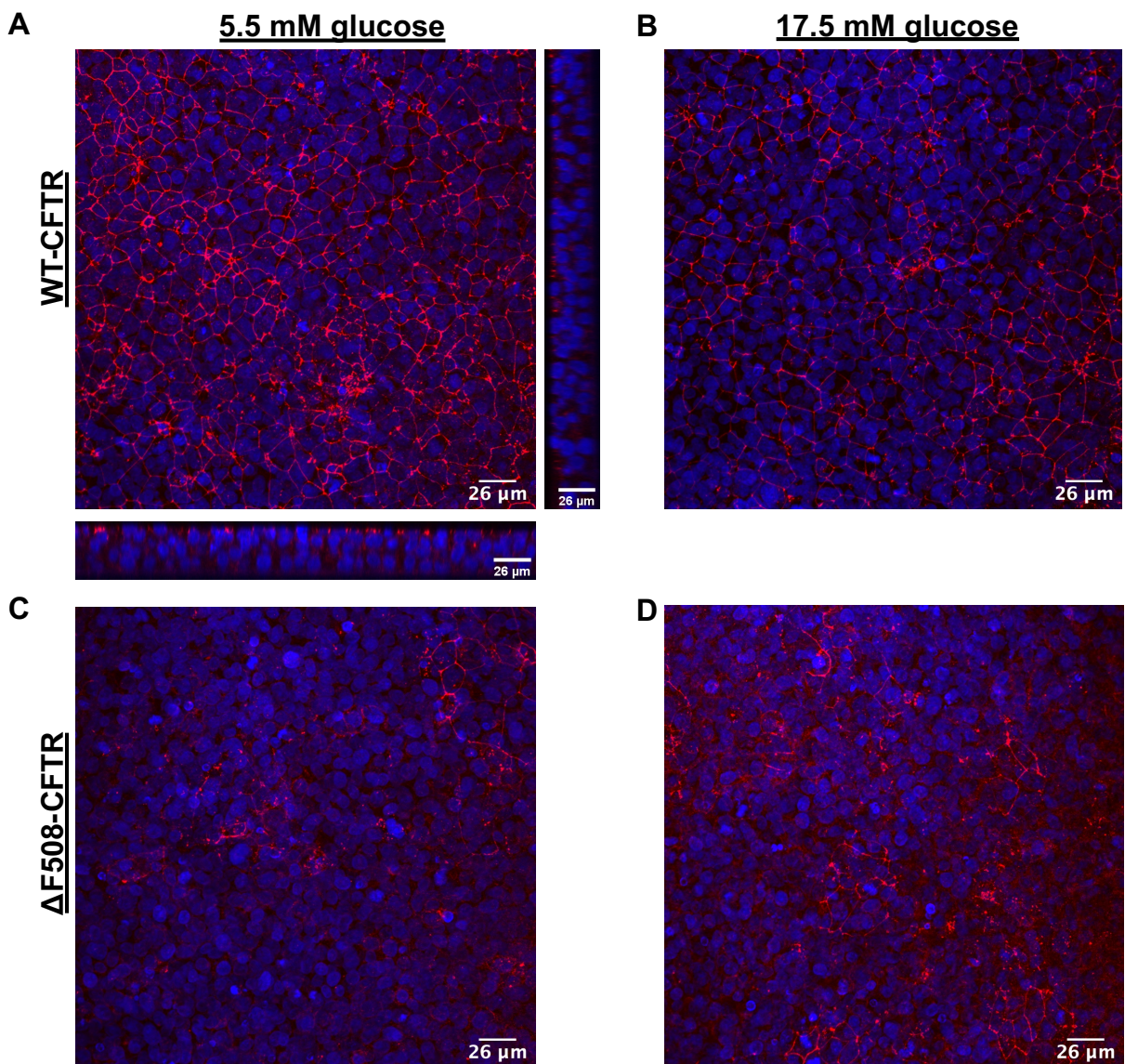


Figure 6.4: CLDN3 fluorescence is affected by CFTR expression and glucose growth. Confocal microscopy images were obtained and (A-D) Z-projections of the maximum intensity are shown for WT-CFTR or Δ F508-CFTR 16HBE cells grown in 5.5 mM or 17.5 mM glucose for 5 days. (A) Orthogonal views of the Z-stack also are shown for the WT-CFTR cells grown in 5.5 mM glucose, as a representation of the localization of the claudin along the z-axis. (E-F) Because CLDN3 is localized to the tight junctions toward the apical side of the cell, these Z-projections of the maximum intensity were used for quantification of staining. The data represent 16HBE cells expressing WT-CFTR (filled) or Δ F508-CFTR (open) and grown in 5.5 mM (black) or 17.5 mM glucose (grey). Cells were defined by an outline of claudin staining. Interestingly, for WT-CFTR cells grown in 5.5 mM or 17.5 mM glucose, 421 and 365 cells (respectively) could be counted definitively. However, in the Δ F508-CFTR cells, only 30 and 40 cells (respectively) could be counted. (E) The average fluorescence intensity over the cell border (defined by the claudin staining) was analyzed by unpaired two-tailed *t* tests. Within WT-CFTR 16HBE cells, border CLDN3 staining was decreased by growth in 17.5 mM glucose treatment (** $p=0.0053$). Contrarily, in Δ F508-CFTR cells, border CLDN3 staining was increased by growth in 17.5 mM glucose treatment (* $p=0.0378$). When comparing to WT-CFTR cells grown in 5.5 mM glucose, Δ F508-CFTR cells grown in either 5.5 mM or 17.5 mM glucose showed no significant difference in border CLDN3 staining ($p=0.1298$, $p=0.2374$). (F) The average fluorescence intensity over nine sections of the Z-projection image was analyzed by unpaired two-tailed *t* tests. Within the WT-CFTR and the Δ F508-CFTR cells, CLDN3 staining was decreased by growth in 17.5 mM glucose (**** $p<0.0001$). A significant decrease was found in CLDN3 staining in Δ F508-CFTR compared to WT-CFTR cells grown in 5.5 mM glucose (**** $p<0.0001$). When comparing WT-CFTR cells grown in 5.5 mM glucose to Δ F508-CFTR cells grown in 17.5 mM glucose, no significant difference was found in CLDN3 staining ($p=0.1585$), suggesting that 17.5 mM glucose in Δ F508-CFTR cells facilitates recovery of CLDN3 expression.



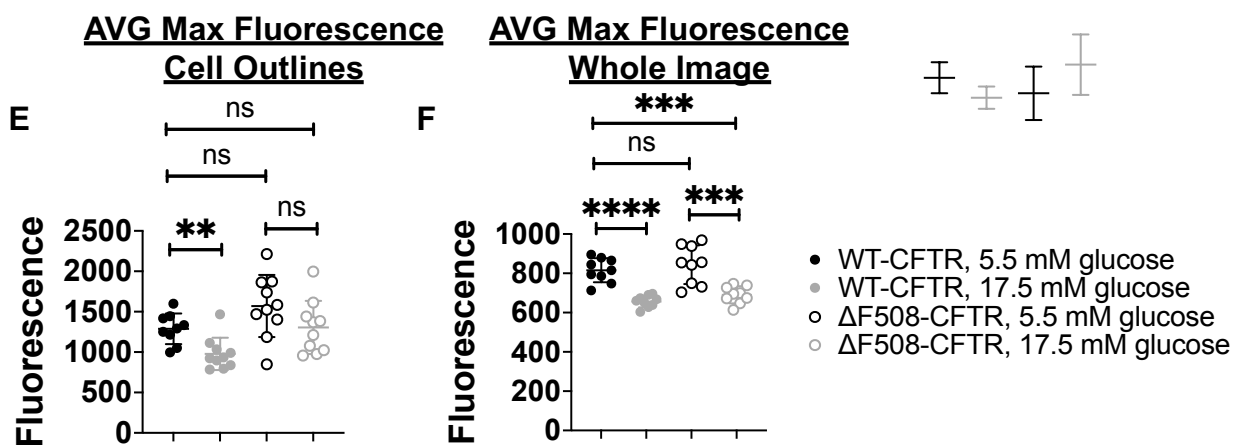
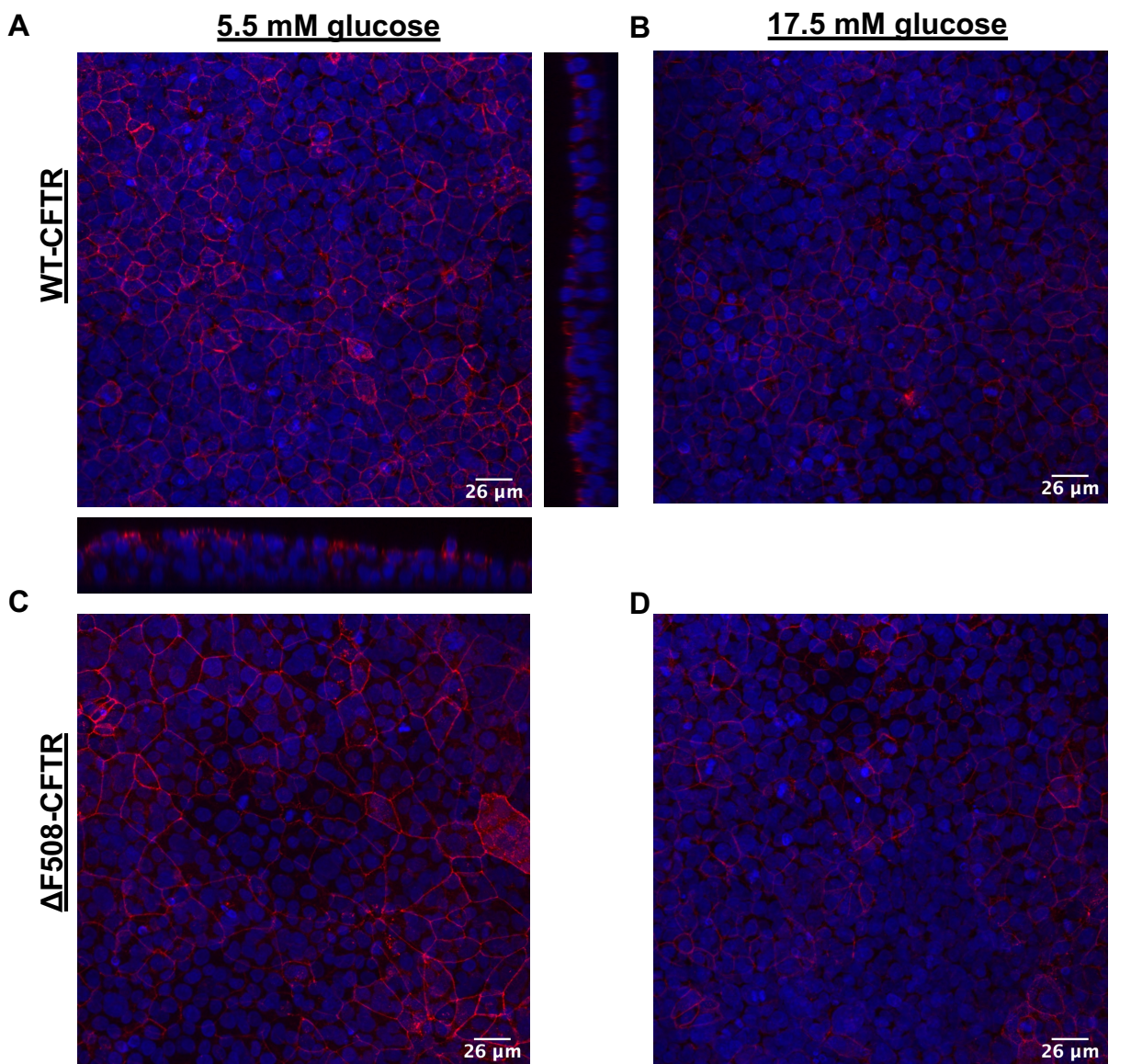
reduced in the Δ F508-CFTR group. The WT-CFTR group in normal and hyperglycemic conditions had 421 and 365 countable outlines, respectively, while the Δ F508-CFTR group in these same conditions had 30 and 40 cells, respectively. This indicates an approximate 10-fold reduction in the number of cells expressing and localizing CLDN3 correctly in the Δ F508-CFTR groups. This is reflected partially in the analyses of the total fluorescence over the image. WT-CFTR cells in hyperglycemic conditions and Δ F508-CFTR cells in normal glucose conditions had significantly reduced overall CLDN3 staining relative to WT-CFTR cells in normal glucose conditions (Figure 6.4F). Interestingly, Δ F508-CFTR cells in hyperglycemic conditions did not have differential expression of CLDN3 compared to WT-CFTR cells in normal glucose conditions. Again, though, the number of cells in which CLDN3 was correctly localized was significantly decreased in these cells, and thus the CLDN3 likely is not able to elicit its normal function.

6.3.5 *CFTR mutation and long-term glucose growth affect CLDN4 protein expression and localization*

Evaluation of the orthogonal views of the confocal analysis of 16HBE cells suggested that CLDN4 localized to an apical location between cells, with minimal distribution throughout the remainder of the membrane. As such, we chose to assemble a Z-projection based on the maximum fluorescence over the Z-stack for analysis, which did provide an image with clear outlines of the cells (Figure 6.5A-D). The membrane localization of CLDN4 (Figure 6.5E) as well as the average fluorescence over the entire image (Figure 6.5F) were analyzed as described in section 6.2.4.

Analyses of the membrane fluorescence of CLDN4 revealed that while hyperglycemic conditions decrease CLDN4 expression in WT-CFTR cells, these same conditions did not affect expression in Δ F508-CFTR cells (Figure 6.5E). Importantly, the membrane outline fluorescence of CLDN4 was not significantly different between WT-CFTR and Δ F508-CFTR cells in normal chloride conditions and Δ F508-CFTR cells in either glucose condition. Interestingly, analyses of the total fluorescence over the image resulted in slightly different comparisons. As in the cell outline data, WT-CFTR cells in hyperglycemic conditions had significantly reduced overall CLDN4 staining while Δ F508-CFTR cells in normal glucose were not

Figure 6.5: CLDN4 fluorescence is affected by CFTR expression and glucose growth. Confocal microscopy images were obtained, and (A-D) Z-projections of the maximum intensity are shown for WT-CFTR or Δ F508-CFTR 16HBE cells grown in 5.5 mM or 17.5 mM glucose for 5 days. (A) Orthogonal views of the Z-stack also are shown for the WT-CFTR cells grown in 5.5 mM glucose, as a representation of the localization of the claudin along the z-axis. (E-F) Because CLDN4 is localized to the tight junctions toward the apical side of the cell, these Z-projections of the maximum intensity were used for quantification of staining. The data represent 16HBE cells expressing WT-CFTR (filled) or Δ F508-CFTR (open) and grown in 5.5 mM (black) or 17.5 mM glucose (grey). (E) The cell border (defined by the claudin staining) was outlined using the segmented line tool, and the average fluorescence intensity over that outline was obtained for each of 10 randomly selected cells. These cell border intensities were analyzed by unpaired two-tailed *t* tests. Within the WT-CFTR 16HBE cells, border CLDN4 staining was decreased by 5-day growth in 17.5 mM glucose (** $p=0.0030$). However, no difference was found within the Δ F508-CFTR cells based on glucose growth conditions ($p=0.1140$). When comparing WT-CFTR cells grown in 5.5 mM glucose to Δ F508-CFTR cells, grown in either 5.5 mM or 17.5 mM glucose, no significant difference was found in border CLDN4 staining ($p=0.0635$, $p=0.9013$). (F) The image was also divided into 9 equal sections, and the average fluorescence intensity of each section was obtained and analyzed by unpaired two-tailed *t* tests. Within the WT-CFTR and the Δ F508-CFTR 16HBE cells, CLDN4 staining was decreased by 5-day growth in 17.5 mM glucose (**** $p<0.0001$, *** $p=0.0006$). When comparing WT-CFTR to Δ F508-CFTR cells grown in 5.5 mM glucose, no significant decrease was found in CLDN4 staining ($p=0.4768$). However, when comparing WT-CFTR cells grown in 5.5 mM glucose to Δ F508-CFTR cells grown in 17.5 mM glucose, a significant decrease was found in CLDN4 staining (*** $p=0.0001$).



different from WT-CFTR cells in normal glucose (Figure 6.5F). However, unlike in the cell outline data, Δ F508-CFTR cells in hyperglycemic conditions also had significantly reduced overall CLDN4 staining compared to Δ F508-CFTR and WT-CFTR cells in normal glucose.

6.3.6 *CFTR mutation and long-term glucose growth affect CLDN7 protein expression and localization*

Evaluation of the orthogonal views of the confocal analysis of 16HBE cells suggested that CLDN7 localized very specifically to an apical location between cells, with minimal distribution throughout the remainder of the membrane. As such, we chose to assemble a Z-projection based on the maximum fluorescence over the Z-stack for analysis, which did provide an image with clear outlines of the cells (Figure 6.6A-D). The membrane localization of CLDN7 (Figure 6.6E) as well as the average fluorescence over the entire image (Figure 6.6F) were analyzed as described in section 6.2.4.

Analyses of the membrane fluorescence of CLDN7 revealed that hyperglycemic conditions did not affect CLDN7 expression in WT-CFTR cells, but increased expression in Δ F508-CFTR cells (Figure 6.6E). The membrane fluorescence of CLDN7 was significantly decreased in Δ F508-CFTR cells compared to WT-CFTR in normal chloride conditions, but was increased in Δ F508-CFTR cells in hyperglycemic conditions. Analyses of the total fluorescence over the image resulted in the same comparisons (Figure 6.6F).

6.4 Discussion

A summary of the data presented here is provided in Figure 6.7. We found that hyperglycemic conditions and CFTR mutation each decreased TER. PCR analysis determined many imbalances in claudin and gap junction proteins. Immunofluorescence evaluation of these claudin proteins revealed different imbalances than were identified by PCR. This immunofluorescence data is more informative than the PCR data since it indicates actual protein expression and localization.

The claudins explored here have been found previously in bronchial epithelial cells (377). In our

Figure 6.6: CLDN7 fluorescence is affected by CFTR expression and glucose growth. Confocal microscopy images were obtained and (A-D) Z-projections of the maximum intensity of each pixel over each slice were created and are shown for WT-CFTR or Δ F508-CFTR 16HBE cells grown in 5.5 mM or 17.5 mM glucose for 5 days. (A) Orthogonal views of the Z-stack also are shown for the WT-CFTR cells grown in 5.5 mM glucose, as a representation of the localization of the claudin along the z-axis. (E-F) Because CLDN7 is localized to the tight junctions toward the apical side of the cell, Z-projections of the maximum intensity were used for quantification of staining. The data represent 16HBE cells expressing WT-CFTR (filled) or Δ F508-CFTR (open) and grown in 5.5 mM (black) or 17.5 mM glucose (grey). (E) The average fluorescence intensity over the cell border (defined by claudin staining) was obtained for each of 10 randomly selected cells. These cell border intensities were analyzed by unpaired two-tailed *t* tests. Within the WT-CFTR 16HBE cells, CLDN7 border staining was not affected by growth in 17.5 mM glucose ($p=0.0694$). However, within the Δ F508-CFTR cells, growth in 17.5 mM glucose increased CLDN7 border staining ($***p=0.0003$). When comparing WT-CFTR to Δ F508-CFTR cells grown in 5.5 mM glucose, a decrease in border CLDN7 staining in the F508-CFTR cells was found ($**p=0.0050$). Conversely, when comparing WT-CFTR cells grown in 5.5 mM glucose to Δ F508-CFTR cells grown in 17.5 mM glucose, an increase in border CLDN7 staining in the F508-CFTR cells was found ($*p=0.0269$). (F) The Z-projection was also divided into 9 equal sections, and the average fluorescence intensity of the sections was analyzed by unpaired two-tailed *t* tests. Within the WT-CFTR 16HBE cells, CLDN7 staining was not affected by growth in 17.5 mM glucose ($p=0.4626$). However, within the Δ F508-CFTR 16HBE cells, CLDN7 staining was increased by growth in 17.5 mM glucose ($****p<0.0001$). A significant decrease was found in CLDN7 staining in Δ F508-CFTR compared to WT-CFTR cells grown in 5.5 mM ($***p=.0008$). However, when comparing WT-CFTR cells grown in 5.5 mM glucose to Δ F508-CFTR cells grown in 17.5 mM glucose, a significant increase was found in CLDN7 staining in Δ F508-CFTR cells ($*p=0.0155$).

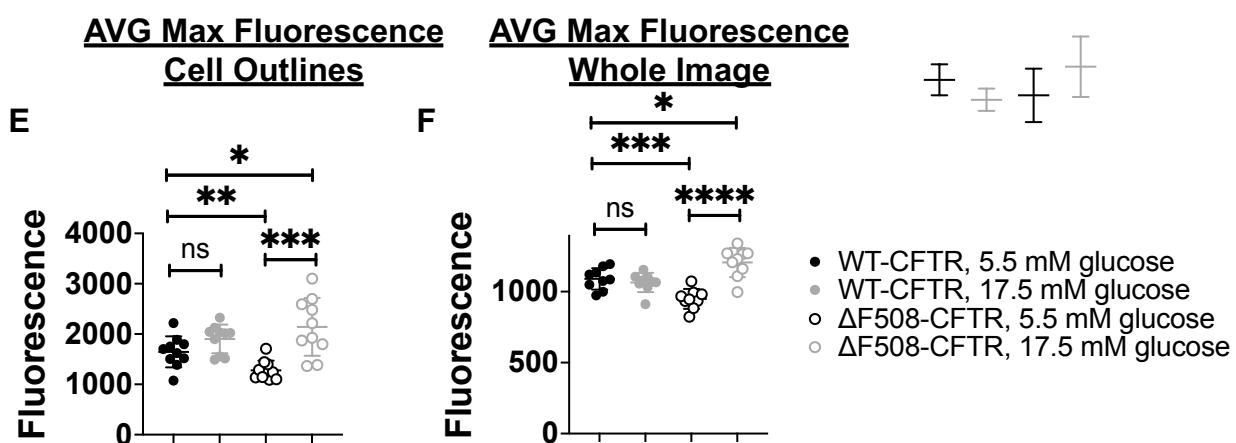
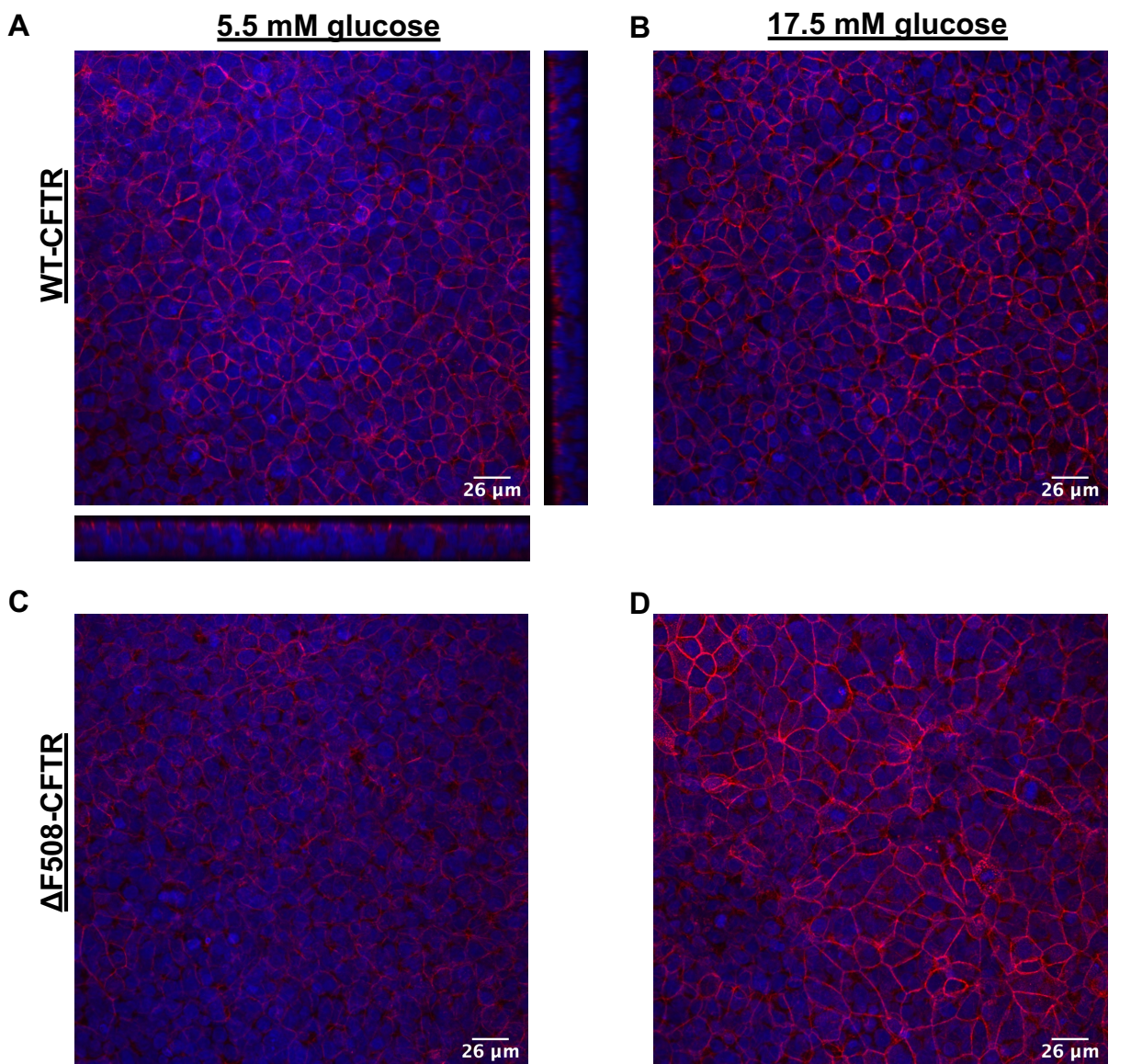
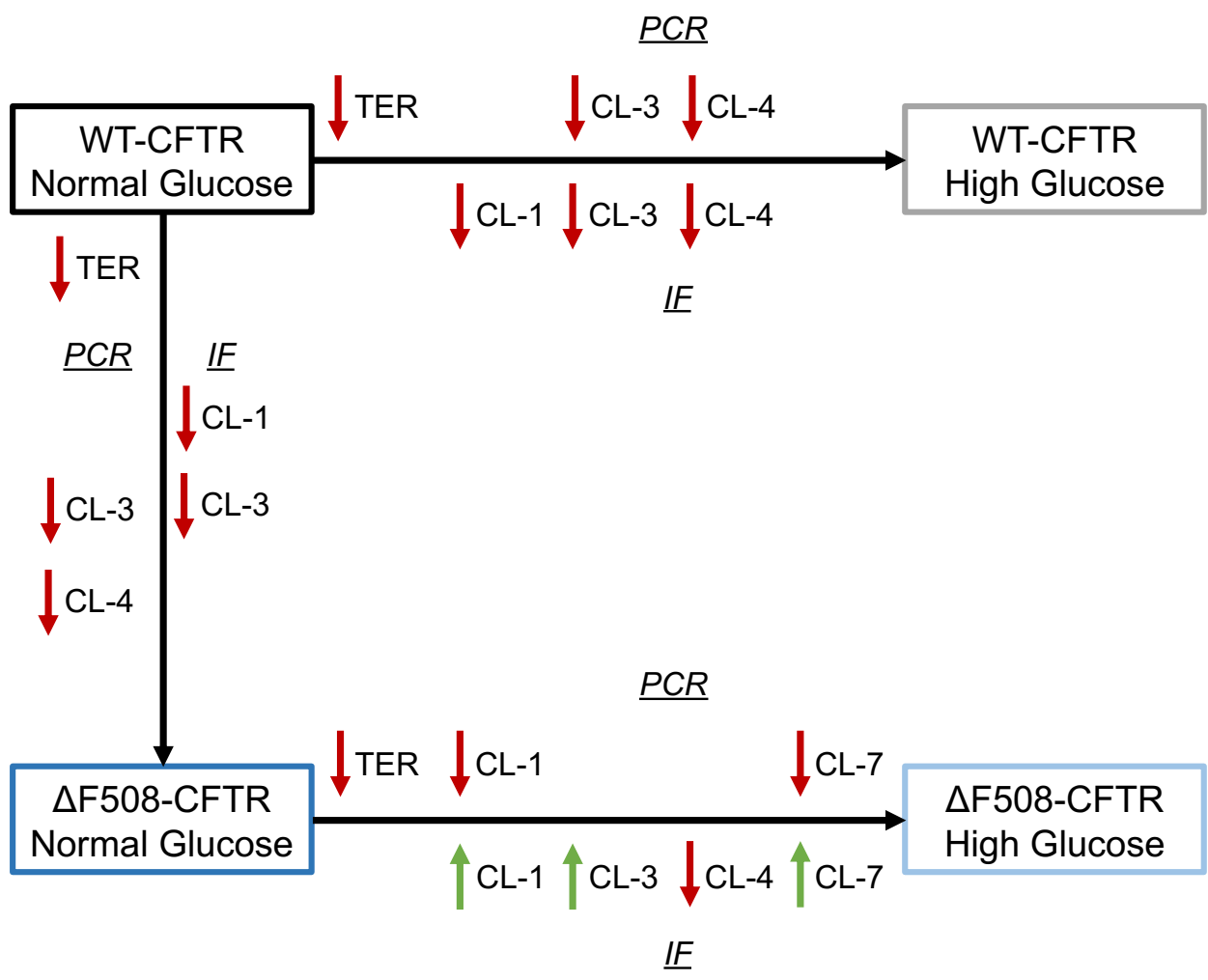


Figure 6.7: A graphical representation of the results. TER is transepithelial resistance. IF is immunofluorescence. Width and length of the arrows are not proportional to anything. Red, downward pointing arrows indicate decreased values/expression in the second group (where the black arrow is pointing) compared to the first groups (where the black arrow originates). Green, upward arrows indicate increased values/expression in the second group compared to the first group.



experiments, these claudins localize to the tight junction as expected (except for CLDN1) (378). Interestingly, some studies have found that CLDN7 is basolaterally distributed. Each of the claudins analyzed by immunofluorescence (CLDN1, -3, -4, -7) are generally considered sealing claudins, meaning that increased expression should indicate increased paracellular resistance (377). However, there has been some debate as to whether CLDN4 and CLDN7 can function as anion pores in some situations (377; 379; 380). If all of the claudins were indeed barrier forming, since TER was decreased by hyperglycemia and CFTR mutation, it would be expected that cumulative claudin protein abundance would be decreased in these conditions. For the most part, this was indeed the case; WT-CFTR cells in hyperglycemia showed reduced CLDN1, -3, and -4 protein levels, while $\Delta F508$ -CFTR cells in normal glucose conditions showed reduced CLDN3 and -4 protein levels. However, when evaluating the $\Delta F508$ -CFTR cells in hyperglycemic conditions relative to the $\Delta F508$ -CFTR cells in normal glucose conditions, CLDN1, -3, and -7 protein abundances were increased, though CLDN4 was still decreased. The reason for these increases in claudin protein expression despite decreased TER has yet to be determined, but could indicate that in this situation, these claudins are not all barrier forming.

While tight junctions and claudins are important for controlling ion permeability, gap junctions and connexins are important for both ion and metabolite permeability (373). Importantly, mRNA analysis of some of these gap junction proteins has indicated an imbalance in CF airway cells as compared to non-CF cells (373). We also identified some imbalances in gap junction proteins here, though the degree of overlap in the specific findings is unclear. Future work should evaluate the protein expression and localization of these gap junction proteins.

The data outlined here are helpful for understanding the effects of hyperglycemia and CFTR mutation on tight junction fidelity. However, future work should be done in primary bronchial epithelial cells from lung explant tissue since these are not immortalized cells. Overall, it is clear that evaluation of tight junction and gap junction proteins could lead to a better understanding of increased glucose permeability in CF cells relative to non-CF cells.

CHAPTER 7 – CONCLUSIONS

We have determined here that lipid modulation can affect the activity of the membrane channel CFTR and its response to the FDA-approved VX770 potentiator in primary airway epithelial cells.

In regards to sphingolipids, we have found that the bacterial virulence factor SMase decreases transepithelial CFTR currents when applied basolaterally to primary bronchial and tracheal epithelial cells. VX770 could not recover this effect. Importantly, paracellular tight junction fidelity remained intact following SMase treatment, allowing us to perform non-destructive impedance analysis experiments to determine the effects of basolateral SMase on apical and basolateral membrane conductance and capacitance. These data indicate that the SMase-mediated reduction in forskolin-and-VX770-elicited current was caused in part by decreased apical membrane conductance through the cells. Since CFTR is the only apical channel activated by forskolin and VX770, these data indicate that basolateral SMase can inhibit CFTR's ability to conduct ions on a population level.

With this information, we conducted more experiments to determine if this inhibition of CFTR population conductance was due to changes in the amount of CFTR protein at the surface of the cell available for conductance of ions, or if changes to the single-channel conductance of CFTR was implicated instead. Surface biotinylation experiments found no change in surface expression of CFTR, normalized to total cellular amount of CFTR. Based on previous work in *Xenopus* oocytes, changes in membrane mechanics or direct lipid interactions were not the cause of SMase-mediated inhibition of CFTR. Thus, the only remaining possibility is that SMase treatment initiated a signaling cascade that inhibited CFTR ion channel activity. Based on the inability for VX770 to recover SMase-mediated decreases in currents, a decrease in PKA activity or an increase in PP1A/B activity is not involved. Furthermore, we have found that increased AMPK activity is not involved, as inhibiting AMPK did not prevent SMase-mediated decreases in transepithelial CFTR currents. The exact cascade involved in SMase-mediated inhibition of CFTR has yet to be determined, and future experiments should work towards this understanding.

We also found that SMase-mediated reduction of CFTR currents involves either the generation of

dihydroceramide or ceramide, based on equivalent inhibitory effects on CFTR when inhibiting CDase with ceranib-1. Acute ceranib-1 treatment did not increase global ceramides, but rather increased two dihydroceramides. However, localized changes in ceramide cannot be ruled out. Analysis of the signaling cascades known to be activated or inactivated specifically by these lipids can inform future studies to determine the enzymes involved in SMase-mediated inhibition of CFTR.

Importantly, the inhibitory effects of SMase on CFTR current and conductance found in non-CF airway cells were maintained in $\Delta F508$ -CFTR cells corrected with multiple FDA-approved drugs. These currents and conductances also were not rescued by VX770 potentiation. Determination of the mechanism by which SMase inhibits CFTR is vital, as we and others have found that many ceramides and dihydroceramides are increased in $\Delta F508$ -CFTR airway cells. While we and others have found that correction of CFTR with FDA-approved drugs recovers increased ceramide levels in $\Delta F508$ -CFTR cell, we found that these drugs simultaneously exacerbate the increased levels of dihydroceramides. This could be detrimental if dihydroceramide is indeed the lipid causing decreased CFTR activity. In addition to these sphingolipid imbalances, we have found that endogenous acid-SMase is secreted by primary airway epithelial cells into the basolateral space. Importantly, this secretion is increased in $\Delta F508$ -CFTR as compared to non-CF airway cells. Additionally, we have found for the first time that airway-like neutrophils secrete acid-SMase. This could serve as another source of SMase in the CF lung, which has an increased neutrophil burden compared to the non-CF lung, in addition to the bacteria in the CF lung that secrete bacterial SMases.

Overall for this project, which represents the main focus of this thesis, we have determined not only that sphingolipid imbalances, in particular increased either ceramides, dihydroceramides, or both, can negatively impact the function of CFTR ion channels in airway epithelial cells. We have also confirmed that these sphingolipids are already increased in $\Delta F508$ -CFTR airway cells, and have data suggesting that acid-SMase is increased in $\Delta F508$ -CFTR cells. Thus, the mechanism of this inhibition is relevant to determine, though future work should also evaluate sphingolipid and SMase imbalances in cells with CFTR

mutations other than $\Delta F508$, preferably examining the range of mutation classes.

In addition to effects of sphingolipid modulation on CFTR activity, we have found that cholesterol modulation can affect CFTR activity in airway epithelial cells. Specifically, we have found that reduction of membrane cholesterol via treatment with M β CD shifts the forskolin dose-response curve for activation of CFTR to the right, without affecting the maximum current elicited at maximal CFTR activation. This rightward shift indicates increased difficulty in activating CFTR with forskolin, which could be due to effects on the ability of forskolin to activate adenylyl cyclase, adenylyl cyclase to generate cAMP, cAMP to activate PKA, PKA to phosphorylate CFTR, or could be due to direct effects on CFTR activity. Future experiments should determine the exact mechanism by which cholesterol depletion negatively impacts CFTR activation. This work also should evaluate the effects of increasing cholesterol concentration on CFTR activation with forskolin, which could increase the efficacy of forskolin. This is all important understanding to have, as previous work has identified cholesterol as a copurified lipid with CFTR, suggesting its importance in CFTR function. Furthermore, other work has found increased levels of cholesterol in the cell membrane of CF cells. If cholesterol binding is necessary for proper CFTR functioning, and/or if increased cholesterol shifts the forskolin dose-response curve for CFTR activation to the left (indicating increased ease in activating CFTR) it is possible that this cholesterol increase in CF cells is beneficial to people living with CF. Though forskolin is not used as a therapeutic, it mimics activation of adenylyl cyclase that is endogenously caused by activation of the β_2 adrenergic receptor. Thus, a shift in forskolin efficacy potentially indicates a shift in β_2 adrenergic receptor activation efficacy, which would have important clinical implications.

While manipulation of lipids in whole tissue, as has been discussed so far, is beneficial for understanding more complete systems, there are benefits to evaluating lipid modulation at a single-protein level. As such, we established the planar lipid bilayer technique in our lab. With this technique, we can evaluate single-channel events for CFTR in an environment with controlled lipid compositions. This lipid environment can be controlled even further by evaluating detergent-purified CFTR that has been

reconstituted into proteoliposomes, rather than CFTR from cellular microsomes. We show here that we can evaluate CFTR from microsomes and proteoliposomes in a planar lipid bilayer setup. Interestingly, the preliminary data from these experiments suggest that purification of CFTR with detergent and subsequent reconstitution into POPC proteoliposomes resulted in a decreased responsiveness of CFTR to its specific inhibitor, INH172. Whether or not this decreased INH172 efficacy was due to a loss in endogenous lipids that are important for INH172 function or due to structural deformations in CFTR caused by the purification process is yet unknown. However, further studies are warranted, as it is possible that certain lipids are necessary for the proper structure, function, and drug sensitivity of CFTR. These studies can include manipulation of the lipid composition of the planar lipid bilayer and/or the proteoliposome, followed by analysis in changing activity and drug sensitivity of CFTR.

Overall, these projects, though evaluating separate lipids, indicate an importance for future studies to consider the membrane lipid environment when evaluating CFTR activity, CFTR modulators, and additional therapies for CF. More work is necessary to evaluate all lipid imbalances in CF cells, to determine if these imbalances are corrected with FDA-approved modulator therapy, and to determine if these imbalances are beneficial or detrimental to CFTR activity as well as modulator efficacy. Furthermore, it should be determined if these lipid imbalances lead to any of the negative pulmonary phenotypes associated with CF, and whether correction of these lipids imbalances improves patient outcomes.

In addition to lipid imbalances, future work should evaluate the effects of hyperglycemia on airway epithelial cell function. CFRD is the most common co-morbidity in CF, resulting in persistent hyperglycemia. We and others have found that CFTR mutation decreases tight junction fidelity in airway epithelial cells, in some cases directly translating to increased glucose flux into the airspace. This glucose can act as a food source for bacteria, potentially explaining increased bacterial colonization of the CF airways, in turn potentially explaining the even greater pulmonary decline experienced by people with CFRD as compared to people with CF but no CFRD. We have found that tight junction fidelity is decreased by both CFTR mutation ($\Delta F508$) and hyperglycemia 16HBEs. While we have begun working to identify specific tight junction and gap junction proteins that are imbalanced by CFTR mutation and hyperglycemia,

more work is necessary to confirm the functional consequences of each imbalance, and these imbalances need to be confirmed in primary airway epithelial cells. Additionally, mutations besides $\Delta F508$ should be tested, for while $\Delta F508$ is the most commonly found mutation in CF, there are many patients without this mutation. It is important to determine if the mutations found in these people have similar effects as the $\Delta F508$ mutation.

Though substantial and commendable improvements have been made to the lives of many people with CF recently, more work is still necessary to more fully understand this disease, its current therapies, and its future therapies. This work should consider the lipid and glucose imbalances in CF, and how these imbalances impact CFTR and airway epithelial cells as a whole.

CHAPTER 8 – APPENDIX OF ADDITIONAL PROJECTS

Preface: This section serves to briefly outline additional projects in which I was involved to varying degrees.

8.1 Identification of CFTR in lamprey intestine

For this section, I contributed lamprey intestine microdissection as well as short-circuit current analysis in the Ussing Chamber. This work resulted in a publication in *Developmental Cell* in 2019 (381).

Prior to our work, the oldest known CFTR ortholog was from the dogfish, which arose 150 million years ago. In this study, CFTR was found to be highly expressed in the distal intestines of the dogfish (382). Interestingly, though, there was genetic evidence that CFTR, a member of the ABCC family, could exist in sea lamprey, which arose even farther in the past than dogfish (500 million years ago) (383).

We identified the CFTR gene in lamprey, though many important differences were noted, such as a reduced number of PKA phosphorylation sites and no F508 residue (the deletion of which constitutes the most common CFTR mutation found in people with CF). Furthermore, lamprey CFTR was also found to have altered activation kinetics, altered single-channel properties, and minimal responsiveness to traditional CFTR blockers as well as the CFTR potentiator VX770 as compared to human CFTR.

In addition to this, we found via PCR, western blotting, and immunohistochemistry that lamprey CFTR was highly expressed in the distal intestine of the lamprey. Many attempts were made to functionally evaluate CFTR expression in the distal intestine using short-circuit current analysis in an Ussing Chamber. This required microdissection of the lamprey intestine, as well as manipulation of the Ussing Chamber to evaluate extremely small sections of tissue. The Ussing Chamber manipulation were found to be effective when recording from mouse intestine, validating this approach. However, lamprey intestine was never sufficiently stable to reliably evaluate CFTR ion channel activity.

8.2 Development of the Programmable Automated Cell Culture System (PACCS)

This work was done in collaboration with a graduate student researcher and an undergraduate

researcher at Emory University.

Traditional methods of cell culture involved media with exorbitant concentrations of glucose, with this media being replenished every 2 days. However, this is a non-physiological pattern of glucose exposure for cells. In the non-diabetic human blood, glucose spikes in the two hours following a meal, though these spikes still do not reach the concentrations found in cell culture media. Approximately 2 hours after the meal, glucose levels return to a stable baseline concentration that is far lower than traditional cell culture media.

It is unknown if or how traditional cell culture methods change the epigenetics, gene expression, and protein expression of cells in laboratory culture relative to cells in the body. However, these changes could change our understanding of the normal activity of these cells. This is especially important in diabetes research, in which increased blood glucose is a major symptom of the disease. It has become necessary to evaluate the effects of traditional cell culture methods on cell culture phenotypes, and to transition to a more physiologically relevant feeding schedule for these cells.

Humans typically have three meals per day. To replicate this, cells would experience baseline glucose, elevated glucose for 2 hours to represent the post-breakfast spike, baseline glucose, elevated glucose for 2 hours to represent the post-lunch spike, baseline glucose, elevated glucose for 2 hours to represent the post-dinner spike, and finally baseline glucose again. However, this is extremely expensive in regard to manpower and time. To circumvent this, the McCarty lab is developing the PACCS system to automate this feeding.

Since in bronchial epithelial cell research, cells are grown on Transwells, and since these Transwells are each supported by individual and non-continuous wells, we first needed to develop a plate with a contiguous well system that could support Transwells. Utilizing the 3D-printing facilities at Emory University, we have gone through many iterations of this plate. The current design involves a plate with columns on the bottom to fill in some negative space and reduce media usage, along with a removable Transwell support plate and a lid.

We evaluated Calu-3 cells grown in the PACCS system vs traditional wells, via Ussing Chamber.

In both setups, media was changed daily. Unfortunately, the cells grown in the PACCS systems had low resistances, such that they could not be well evaluated in the Ussing Chamber. Upon visual inspection, the cells appeared to be largely detached from the Transwell support filter, with an interesting pattern of degree of detachment based on geographical location in the PACCS system. We hypothesized that unequal media exchanged was occurring to cause these geographical differences in cell detachment.

To evaluate the media exchange in the PACCS system, we added two different dyes to two different bottles of glucose water. One bottle had low glucose, and one had high glucose. A simple program was run in which media was switch from the low- to high- back to low-glucose water three times. The water in each well was collected after each exchange, and the relative amount of low- vs high-glucose water was evaluated by absorbance spectroscopy (since each had a different dye color). Importantly, we found that while adequate media exchange occurred at the input valves of the PACCS plate, media exchange at the other end with the output valve was not sufficient. Future work will adjust program parameters to exchange media more adequately in the PACCS plate.

8.3 Expanding the applicability of a new impedance analysis technology

This work was done in collaboration with a graduate student researcher at the Georgia Institute of Technology.

Impedance analysis has been described previously in this work (section 2.2.6). While it is a powerful tool, in part because it is non-destructive for the tissue, two-membrane impedance analysis requires specialized equipment and analyses that are uncommon in biomedical research. As such, researchers at the Georgia Institute of Technology are working to develop an impedance analysis technique that they can utilize in their own laboratory. The main focus of this research is on eye epithelial cells, but the laboratory wants to expand the relevance of their technique to other fields. We have provided expertise of the electrical circuitry and biological components comprising this circuitry in bronchial epithelial cells. Furthermore, we will be supplying bronchial epithelial cells to this laboratory.

8.4 Determining the impacts of β 2AR agonists on VX770-mediated potentiation of CFTR

This work was part of a summer experience with an undergraduate researcher from the University of Georgia.

Many people with CF are prescribed short- and or long-acting β 2AR agonists as part of their treatment regiment (384). Note that there is an important clinical difference between short- and long-acting β 2AR agonists. Short-acting β 2AR agonists are for emergency use, in part because they cause have rates of desensitization. Conversely, long-acting β 2AR agonists are for daily use and cause decreased rates of desensitization. While these β 2AR agonists typically are administered to open airways by eliciting bronchodilation via activation of β 2AR in the smooth muscle cells surrounding the airway, these agonists will also activate CFTR in the epithelial cells. As we have shown previously, the CFTR potentiator VX770 is less efficacious when CFTR is highly activated due to the ceiling effect (73). Thus, it stands to reason that CFTR activation with β 2AR agonists follows the same principle, reducing the apparent efficacy of VX770 if the β 2AR agonists dose is too high.

First, we determined the dose-response curves for the short-acting β 2AR agonist albuterol and the long-acting β 2AR agonist formoterol in Calu-3, 16HBE, and nHAE cells. Interestingly, the EC_{50} for these drugs was different between the cell types. The nHAE cells exhibited the highest EC_{50} concentrations for both drugs, while Calu-3 cells exhibited similar or 2x lower concentrations and 16HBE cells exhibited 4-5x lower concentrations than nHAE cells.

Utilizing the dose-response curves to determine EC_{10} and EC_{90} values, we determined in 16HBE cells that VX770 elicits a decreased fold-change in CFTR currents following acute CFTR activation with the EC_{90} concentrations of albuterol or formoterol, compared to their EC_{10} concentrations. We confirmed this for albuterol in nHAE cells as well. Future work will establish the effects of long-term albuterol and formoterol treatment on VX770 potentiation in these airway cell models, as long-term treatment is more clinically relevant, at least for the long-acting agonist.

8.5 Evaluating the importance of cholesterol on CLC channels

This work was performed in collaboration with an undergraduate student at Emory University as a part of this student's Honors Thesis. I contributed to the design of the project, the development of all computational analyses, and the analysis of two-electrode voltage clamp data. This work resulted in a thesis that received Highest Honors from Emory's Neuroscience and Behavioral Biology program.

The ultimate goal was to evaluate the effects of cholesterol on CLC channel activity in order to inform how cholesterol imbalances in the human body could affect CLC channels. We began by identifying potential cholesterol binding motifs in the primary amino sequences of various CLC channels. This was accomplished by developing an R script that scanned the amino acid sequence for canonical CRAC and CARC motifs (known cholesterol binding motifs) (224; 385). In each CLC protein evaluated, 6-9 potential CRAC and 11-14 potential CARC motif were found.

These motifs are not truly CRAC or CARC motifs if they do not exist within the transmembrane portion of the protein, though, where cholesterol could bind. Given that there is a solved cryo-EM structure of CLC-1 (386), we chose to map the potential CRAC and CARC motif for CLC-1 onto this 3D model to narrow down sites that potentially bind cholesterol. Importantly, this narrowed our pool of potential cholesterol binding sites to 5 CRAC and 5 CARC motifs.

In addition to evaluation of localization to the transmembrane domain, it is important to evaluate the accessibility of the motif to the bulk lipid solution. To begin to understand accessibility of the proposed CRAC and CARC motifs on CLC-1, we performed molecular docking simulations using AutoDock Vina (387). Importantly, some proposed CRAC and CARC motifs could be excluded as potential cholesterol binding sites, due to an inability of cholesterol to interface with the amino acids based on steric hindrance of other parts of the protein. While these initial binding studies were sufficient to determine amino acid accessibility, they do not provide reliable binding energies or poses for cholesterol binding, as the protein is not given the freedom or energy to move along with the cholesterol. Still, these initial docking studies are useful for providing a starting point from which more advanced molecular dynamics simulation can be run. These molecular dynamics simulation will give a better understanding of probable cholesterol binding,

and should be performed as a future experiment.

As another means by which to increase our confidence that these proposed cholesterol binding motifs are indeed important to the protein's structure/function, we performed multiple sequence alignment on all human CLC channel proteins (CLC-1, CLC-2, CLC-Ka, and CLC-Kb) along with rabbit CLC-2, which was used for electrophysiological studies to be described below. This was done using Clustal Omega.(388) This alignment method identified 5 CRAC and 4 CARC motifs that were 100% conserved between all 5 protein sequences evaluated, suggesting extreme importance of these amino acids to the structure and function of the CLC channel proteins.

Lastly, we evaluated the effects of extracting membrane cholesterol on rabbit CLC-2 channel activity, using two-electrode voltage clamp. Experiments were performed to determine an efficacious concentration, time, and temperature of M β CD treatment was determined by filipin III staining. *Xenopus* oocytes that were injected with CLC-2 RNA successfully expressed CLC-2 protein, as seen by significantly increased currents at hyperpolarizing voltages as compared to un-injected oocytes. However, treatment with M β CD ablated all CLC-2 currents down to un-injected levels. Importantly, M β CD had no effect on currents in un-injected oocytes, so the decrease in current in CLC-2-expressing oocytes can be attributed to a loss of CLC-2 function. More experiments are necessary to determine if this phenomenon exists for human CLC-2 and for all other human CLC channel proteins. Furthermore, it is important to determine if these effects are caused by bulk membrane mechanics or more specific mechanisms. If specific cholesterol-CLC interactions are implicated, future directions should utilize site-directed mutagenesis, guided by the computational results outlined above, to determine if any one cholesterol binding motif is involved in this loss of CLC-2 activity.

CHAPTER 9 – APPENDIX OF DETAILED ELECTROPHYSIOLOGY METHODS

Preface: The text within this chapter is directly reproduced from a portion of a methods chapter published in *Methods in Molecular Biology* in April 2021. I wrote these sections, which relate to Ussing Chamber analysis and the PLB technique.

- Cui G, Cottrill KA, & McCarty NA. 2021. Electrophysiological Approaches for the Study of Ion Channel Function. *Methods Mol Biol* 2302:49-67

9.1 Ussing chamber analysis

9.1.1 Recording solutions

All chemicals are purchased from Sigma, unless otherwise noted. Experiments in the Ussing Chamber can be conducted either in symmetric chloride conditions, or under a chloride gradient in which apical chloride has been depleted. Both have their advantages, in that symmetric chloride conditions allow the user to ascertain more information about the system through determining the conductance, while imposing a chloride gradient can increase the magnitude of the currents observed. In some cases, for example in 16HBES, a gradient is necessary to be able to observe any cAMP-activated chloride currents. The typical solution for the Ussing Chamber is Ringers: (in mM) 140 NaCl, 5 KCl, 0.36 K₂HPO₄, 0.44 KH₂PO₄, 1.3 CaCl₂, 0.5 MgCl₂, 4.2 NaHCO₃, 10 NaHEPES, 10 Glucose, pH 7.4 (266). If interested in a chloride gradient, the apical solution can be replaced with low-chloride Ringers: (in mM) 133.33 Na gluconate, 5 K gluconate, 2.5 NaCl, 0.36 K₂HPO₄, 0.44 KH₂PO₄, 5.7 CaCl₂, 0.5 MgCl₂, 4.2 NaHCO₃, 10 NaHEPES, 10 Mannitol, pH 7.4. Note that mannitol is substituted for glucose in this buffer to maintain the osmolarity of the solution, and to prevent obtrusive currents from the sodium glucose cotransporter located

on the apical side of bronchial epithelial cells.

9.1.2 Sources of reagents and equipment

Ussing Chamber equipment and Acquire & Analyze software are purchased from Physiologic Instruments (San Diego, CA) unless otherwise noted. A VCC-MC6 voltage/current clamp amplifier is used to control the electrodes, collect data, and output that data to the computer. Each chamber in the experiment, which is connected to an individual amplifier and control panel on the VCC-MC6, is connected to a DM-MC6 input module and dummy membrane. The DM-MC6 serves as an integration point for the four P202-S electrodes, two voltage-sensing and two current-passing, that are connected on either side of the P2300 chamber secured into an EM-RSYS-2 mount. The electrodes are secured into P2023 electrode tips that are filled with 3 M KCl 3% agar on the tip and backfilled with 3 M KCl. The two sides of the chamber are separated by a P2302T slider with a Transwell filter inserted into the center.

9.1.3 Setting up and running the experiment

1. Turn on the water bath to 42°C to make the chamber 37°C
2. Place recording solution(s) in a 37°C water bath and chambers in a 37°C incubator
3. Make electrode tips
 - a. Melt 3% agar in 3M KCl in a beaker of water on a heating/stir plate
 - b. Pull some of the agar solution into a small syringe
 - c. Place the tip of the electrode into the end of the syringe and inject some agar
 - d. Immediately put this tip into a beaker of 3M KCl
 - i. Note: Tips can dry out easily, so minimize air exposure
 - e. Once the agar has solidified, use a syringe with a long needle to fill the rest of the tip with 3M KCl
 - i. Note: Ensure that there are no bubbles in the agar once it is in the tip
4. Assemble the chambers with a slider containing a blank filter

5. Insert electrodes in tips into the chambers
 - a. Long, white current-passing electrodes go on the outside of the chamber
 - b. Short, black voltage-sensing electrodes go on the inside of the chamber
 - c. Make sure that the paired electrode leads are on the same side of the chamber, and that the same pair is on the same side of each chamber in the series
 - i. Note: Paired electrodes have either black tape or no tape around them
 - ii. Note: Switching sides will make the current go in the opposite direction
6. Fill each chamber with 4 mL of solution on each side
 - i. Note: Make sure that there are no bubbles at the end of the electrode tips or inside the chambers
7. Put the gas lines into each chamber
8. Turn on the Blood Gas (95%:5%, O₂:CO₂) tank and adjust the nobs on the top of the chambers until the bubbling rate is appropriate for mixing the solution without being too vigorous
9. Turn on the amplifier and computer
10. Correct the Electrode Offset Potential
 - a. Make sure the “Meter” is set to “V”
 - b. Press the “Function” button to read “Open”.
 - i. Note: The display will show the difference potential between the pairs of voltage-sensing electrodes
 - c. Use the “Offset” button and dial to adjust until the meter reads “0.0”.
 - i. Note: The offset dial can only adjust +/- 10, so if the offset is greater than that, the electrodes may need to be switched out, or there may be a bubble somewhere in the circuit
11. Correct the Fluid Resistance Compensation
 - a. Make sure the “Meter” is set to “I”
 - b. Press and hold the “Push to Adj” button to pass current across the fluid in the chamber.

15. Create a new experiment file in the Acquire & Analyze software
16. Select the chambers for data collection and the surface area of the filters
17. Reference tissues (“Acquire” tab, then “Reference” subtab)
 - a. Boxes should remain white to indicate no issues
 - i. Yellow indicates a small offset issue. If any box turns yellow, wait 30 seconds and try to re-reference to determine if the system stabilizes
 - ii. Red indicates a significant offset. Something is very wrong with the setup in this case and must be rectified immediately
 - iii. Note: If the problem cannot be determined, unselect the chamber in Acquire and Analyze, unselect “Rem”, take the chamber off “Clamp” mode, and flip both switches on the DM-MC6 box to “Test” to make a dummy membrane
18. Begin data acquisition

9.1.4 *Application notes*

- a. If the electrodes become white, they should be re-chlorided by carefully submerging the silver-chloride part in bleach for 1 hr
- b. To wash chambers, soaked overnight in detergent solution (Contrad 70; Decon Labs, Inc; King of Prussia, PA), rinse three times with tap water, then rinse with distilled water.

9.2 PLB analysis

9.2.1 *Sources of reagents and equipment*

This protocol assumes the use of an Axopatch 200B amplifier and DigiData 1322A analog-to-digital (A/D) interface, both from Molecular Devices, and a Spin-2 bilayer stirplate and controller, stir bars, and bilayer chambers (BCH-M13) and cuvettes (CD13A-200) from Warner Instruments. Lipids should be purchased from Avanti Polar Lipids (Alabaster, AL), either in powder form or already dissolved in

chloroform. Lipids are water-sensitive, so before opening any vial, let the vial warm to room temperature to prevent condensation on the inside of the vial. Furthermore, once lipids are dissolved in chloroform and opened, lipids should be aliquoted with glass syringes into glass vials with appropriate chloroform-resistant lids and stored at $-80\text{ }^{\circ}\text{C}$. Note that glass syringes are important as chloroform dissolves plastic, so using standard plastic pipettes will contaminate the lipids. Furthermore, note that chloroform is highly volatile, carcinogenic, and lethal if acutely exposed at high concentrations. Always work with chloroform under a chemical fume hood.

9.2.2 *Electrophysiology Physical Setup*

The Spin-2 stir plate should be placed inside of a solid aluminum box (grounded), which is inside of a Faraday cage on a floating antivibration table (also grounded). A foam mat should be placed on top of the stirplate to buffer the planar lipid bilayer chamber from the stirplate. The stir plate should be connected to the Spin-2 controller, which also should be grounded. It is important to use the power supply that comes with the Spin-2 stirplate, as using generic commercially available external power supplies may introduce noise into the system.

The amplifier and oscilloscope (*e.g.*, TDS 1002, Tektronix, Beaverton, OR) should be grounded. The headstage should run through the Faraday cage and into the aluminum box. From the amplifier, telegraph outputs “Gain,” “Frequency,” and “Mode” should be connected to the Telegraph inputs “0,” “1,” and “2” on the back of the A/D converter. On the rear of the amplifier, “scaled output” should connect to the “input” of the low-pass Bessel filter (*e.g.*, LPF-100B, Warner Instruments), the “10 mV output” should connect to “Analog In 1” and “Ext. Command Input Front Switched” should connect to “Analog Out 0” of the A/D converter. On the front of the amplifier, the “scaled output” should be connected to “CH 1” of the oscilloscope with a T connection, with the connection continuing to “Analog In 0” of the A/D converter. The “output” of the low-pass Bessel filter should be connected to “CH 2” of the oscilloscope with a T connection, with the connection continuing to “Analog In 2” of the A/D converter. Some of these connections can be adjusted, moved, or eliminated, but be sure to keep track of the connections when

configuring the lab bench in Clampex (discussed below).

On the back of the amplifier, “Headstage cooling” should be turned to the “on” position. “Pipette Offset” should remain around 5. Dials for “Zap”, “Pipette Capacitance Compensation”, “Series Resistance Compensation”, “Whole-cell Parameters”, and “Subtraction” should be turned all the way to the left. The “Configuration” should be in “Patch $\beta=1$ ” for the capacitive headstage and should be in “Whole Cell $\beta=1$ ” for the resistive headstage. “Mode” should be set to “V-clamp”. The “Low-Pass Bessel Filter” and “Output Gain” should be set to values that are appropriate for the specific experiment.

We use the Clampex program within pClamp for data acquisition. Configure the lab bench to understand the connections and scaling factors. Given the setup outlined above,

- “Analog IN #0” (ultimately connected to the “scaled output” of the amplifier) would be in units of pA. The scale factor would be based on the configuration (β) and the output gain (α) of the amplifier. Specifically, given that the amplifier is in “V-clamp” mode, the scaling factor is $\alpha*\beta$ mV/pA or $\alpha*\beta/1000$ V/pA. If the amplifier was set up for configuration “Patch $\beta=1$ ” and output gain $\alpha=10$, the scale factor would be 0.01 V/pA.
- “Analog In #2” (ultimately connected to the “output” of the low-pass Bessel filter) would also be in units of pA. But this time, the scale factor is 0.1 V/pA.
- “Analog In #1” (connected to the “10 mV output”) would be in units of mV, and the scale factor would be 0.01 V/mV (10 mV/mV) (provided that the “Gain” on the low-pass Bessel filter is at “1”).

9.2.3 *Running an Experiment*

Experiments can be run on cell lysate membrane fraction, proteoliposomes, and (in one reported case) nanodiscs (though it was unclear if proteoliposomes were an unintended byproduct of their nanodisc formation since the sample was not imaged) (389).

1. Prepare any glass rods needed to paint the lipids onto the aperture
 - a. Use a Bunsen burner to melt the end of a capillary tube into a rounded end (with no hole) and give a slight curve to this knob

2. Prepare any agar bridges needed to connect the electrodes to the recording solution
 - a. Use a Bunsen burner to bend a capillary tube into a small arch that fits between the well for the electrode and the well for the recording solution
 - b. Trim the tube to be the correct length using a diamond-tipped pen
 - c. Melt 3% agar in 1 M KCl
 - d. Hook the capillary arch on the rim of a small beaker
 - e. Pour the melted agar into the beaker so that capillary action draws the agar into the arch
 - f. Put the agar bridge into a solution of 1 M KCl to cool
3. Prepare the lipids
 - a. Protocols use anywhere between 10 and 50 $\mu\text{g}/\text{mL}$ lipids in decane as the final concentration for painting a bilayer on the aperture. Chose the concentration and composition that is relevant to the experiment planned
 - b. Using a glass syringe, cleaned three times with chloroform, collect the appropriate volume of lipids and dispense it into a glass reactivial
 - i. Note: If using multiple lipids, be sure to wash the syringe with chloroform between each lipid
 - c. Using N_2 gas, gently dry the lipids in the reactivial, making sure that all chloroform is gone
 - d. Using a clean glass syringe, collect the appropriate amount of decane and dispense it onto the dried lipids in the reactivial
 - e. Vortex the vial briefly to dissolve any lipids that dried to the walls of the reactivial
4. Set up the PLB chamber
 - a. On the outside of the removable cup (the outside of the cup is the *cis* chamber, and the inside is the *trans* chamber), paint a little bit of lipids onto the aperture, use the pressure of your thumb to push air through the aperture, and allow the lipids to dry for one minute
 - b. Put the removable cup into the larger chamber

- c. Add an appropriate volume of recording solution (keeping in mind the volumes of solutions that will need to be added later in the experiment and the capacity of the cups) into both chambers (~ 0.9 mL is normally appropriate)
 - i. Use the pressure of your thumb to force some solution through the aperture to remove any bubbles that have formed on either side of it
 - d. Add 1 M KCl to the outside wells for the electrodes
 - e. Add a stir bar to each side of the aperture, ensuring the magnets align with the chambers
 - f. Connect the electrodes to the headstage and place the electrodes into the outside wells (ground the headstage in the back next to the *trans* chamber)
 - i. Note: Dental gum can keep the electrode placement steady during the experiment
 - g. Connect the electrode wells to the recording chambers using the agar bridges
 - i. Note: Make sure the bridges do not have any bubbles
 - h. Turn on the amplifier, A/D converter, low-pass Bessel filter, and oscilloscope
5. Use Clampex to run a voltage ramp from 0 mV to +200 mV to 0 mV over 1 s
 - a. This protocol is used to evaluate the capacitance of the bilayer, using the equation

$$I_{cap} = C \frac{dv}{dt}$$

Where I_{cap} is the capacitive current, C is the capacitance, and dv/dt is calculated from the protocol (0.2 V / 1 s)
 6. Switch the “ext. command” to “on” and run the protocol, using the “pipet offset” dial to zero the setup as much as possible
 7. Continuing to run the protocol, use the glass bubble to paint on lipids (or smudge around the lipids that are already there) until a stable bilayer is formed
 - a. Note: Bilayer formation can be detected as a pseudo square-wave while the protocol runs
 8. Once a stable bilayer is formed, switch to a protocol that steps from 0 mV, to +100 mV, to -100 mV, back to 0 mV over 1.2 s

9. Very carefully, add the protein of interest (and any other necessary components) to the *cis* side, adding an equal volume of control buffer to the *trans* side
 - a. For example, for CFTR recordings, add to the *cis* side
 - i. 10 μ g of microsomes from BHKs overexpressing CFTR
 - ii. 500 μ M MgATP (to facilitate channel activity)
 - iii. 50 U/mL PKA (to activate CFTR)
 - iv. 300 mM KCl (up from the 50 mM base buffer) (to establish an ion gradient and therefore a voltage potential)
 - o Note: Some people add an ion gradient from *cis* to *trans* at this point to facilitate fusion. If they do this, they do not add an equal volume of control buffer to the *trans* side, but wait until incorporation occurs to add an equal volume of the ions to the *trans* side to abolish the gradient
10. Turn on the stirplate and wait for incorporation
 - a. An incorporation event can be detected as:
 - i. An out-of-place capacitance spike
 - ii. Unstable currents
 - iii. Increased leak current between the +100 mV and -100 mV holding currents
 - b. If no incorporation occurs after 20 min, break the bilayer by flicking the chamber. Quickly repainting the bilayer over the aperture, preferably without adding new lipids. Sometimes, an ion channel will be painted into the bilayer, and recording can begin immediately
11. Once incorporation has occurred, turn off the stirplate, stop the protocol, and begin recording
12. Switch the “ext. command” to “off” and the holding command to “+” or “-,” depending on the channel being studied
 - a. Note: you can set the holding potential first by switching the meter to “ $V_{\text{hold}}/I_{\text{hold}}$ ” and adjusting the holding potential to the desired voltage

- b. Bilayers can last anywhere between 10 seconds and 45 min, depending on the stability of the membrane, which is based on lipid composition, applied voltage, and other factors
13. After a while, if more than 5 or 6 swipes of lipid have been added to the aperture, discard everything, force some solution through the aperture, and try again to form a fresh bilayer
- a. Note: there will be some lipids left on the aperture, so the new membrane will not be fresh

REFERENCES

1. *About Cystic Fibrosis*. <https://www.cff.org/What-is-CF/About-Cystic-Fibrosis/>
2. Welsh MJ, Smith AE. 1995. Cystic fibrosis. *Sci Am* 273:52-9
3. Di Sant'Agnese PA, Darling RC, Perera GA, Shea E. 1953. Abnormal electrolyte composition of sweat in cystic fibrosis of the pancreas; clinical significance and relationship to the disease. *Pediatrics* 12:549-63
4. Quinton PM. 2007. Cystic fibrosis: lessons from the sweat gland. *Physiology (Bethesda)* 22:212-25
5. Mishra A, Greaves R, Massie J. 2005. The relevance of sweat testing for the diagnosis of cystic fibrosis in the genomic era. *Clin Biochem Rev* 26:135-53
6. Saint-Criq V, Gray MA. 2017. Role of CFTR in epithelial physiology. *Cell Mol Life Sci* 74:93-115
7. Reddy MM, Light MJ, Quinton PM. 1999. Activation of the epithelial Na⁺ channel (ENaC) requires CFTR Cl⁻ channel function. *Nature* 402:301-4
8. Reddy MM, Quinton PM. 2003. Functional interaction of CFTR and ENaC in sweat glands. *Pflugers Arch* 445:499-503
9. Quinton PM. 1983. Chloride impermeability in cystic fibrosis. *Nature* 301:421-2
10. Anderson DH. 1938. Cystic Fibrosis of the Pancreas and its Relation to Celiac Disease: A Clinical and Pathologic Study. *Am J Dis Child* 56:344-99
11. Andersen DH, Hodges RG. 1946. Celiac syndrome; genetics of cystic fibrosis of the pancreas, with a consideration of etiology. *Am J Dis Child* 72:62-80
12. Marino CR, Matovcik LM, Gorelick FS, Cohn JA. 1991. Localization of the cystic fibrosis transmembrane conductance regulator in pancreas. *J Clin Invest* 88:712-6
13. Kopelman H, Durie P, Gaskin K, Weizman Z, Forstner G. 1985. Pancreatic fluid secretion and protein hyperconcentration in cystic fibrosis. *N Engl J Med* 312:329-34

14. Gaskin KJ, Durie PR, Corey M, Wei P, Forstner GG. 1982. Evidence for a primary defect of pancreatic HCO₃-secretion in cystic fibrosis. *Pediatr Res* 16:554-7
15. Frizzell RA, Hanrahan JW. 2012. Physiology of epithelial chloride and fluid secretion. *Cold Spring Harb Perspect Med* 2:a009563
16. Castellani C, Assael BM. 2017. Cystic fibrosis: a clinical view. *Cell Mol Life Sci* 74:129-40
17. Davis PB. 2006. Cystic fibrosis since 1938. *Am J Respir Crit Care Med* 173:475-82
18. Wilcken B, Brown AR, Urwin R, Brown DA. 1983. Cystic fibrosis screening by dried blood spot trypsin assay: results in 75,000 newborn infants. *J Pediatr* 102:383-7
19. Cipolli M, Castellani C, Wilcken B, Massie J, McKay K, et al. 2007. Pancreatic phenotype in infants with cystic fibrosis identified by mutation screening. *Arch Dis Child* 92:842-6
20. 2016. 2016 Patient Registry Annual Data Report, Cystic Fibrosis Foundation
21. 2018. 2018 Patient Registry Annual Report, Cystic Fibrosis Foundation, Bethesda, MD
22. Engelhardt JF, Yankaskas JR, Ernst SA, Yang Y, Marino CR, et al. 1992. Submucosal glands are the predominant site of CFTR expression in the human bronchus. *Nat Genet* 2:240-8
23. Kreda SM, Mall M, Mengos A, Rochelle L, Yankaskas J, et al. 2005. Characterization of wild-type and deltaF508 cystic fibrosis transmembrane regulator in human respiratory epithelia. *Mol Biol Cell* 16:2154-67
24. Plasschaert LW, Zilionis R, Choo-Wing R, Savova V, Knehr J, et al. 2018. A single-cell atlas of the airway epithelium reveals the CFTR-rich pulmonary ionocyte. *Nature* 560:377-81
25. Danahay HL, Lilley S, Fox R, Charlton H, Sabater J, et al. 2020. TMEM16A Potentiation: A Novel Therapeutic Approach for the Treatment of Cystic Fibrosis. *Am J Respir Crit Care Med* 201:946-54
26. Matsui H, Randell SH, Peretti SW, Davis CW, Boucher RC. 1998. Coordinated clearance of periciliary liquid and mucus from airway surfaces. *J Clin Invest* 102:1125-31
27. Tarran R. 2004. Regulation of airway surface liquid volume and mucus transport by active ion transport. *Proc Am Thorac Soc* 1:42-6

28. Stutts MJ, Canessa CM, Olsen JC, Hamrick M, Cohn JA, et al. 1995. CFTR as a cAMP-dependent regulator of sodium channels. *Science* 269:847-50
29. Donaldson SH, Boucher RC. 2007. Sodium channels and cystic fibrosis. *Chest* 132:1631-6
30. Burrows EF, Southern KW, Noone PG. 2014. Sodium channel blockers for cystic fibrosis. *Cochrane Database Syst Rev*:CD005087
31. Matsui H, Grubb BR, Tarran R, Randell SH, Gatzky JT, et al. 1998. Evidence for periciliary liquid layer depletion, not abnormal ion composition, in the pathogenesis of cystic fibrosis airways disease. *Cell* 95:1005-15
32. Wark P, McDonald VM. 2018. Nebulised hypertonic saline for cystic fibrosis. *Cochrane Database Syst Rev* 9:CD001506
33. De Lisle RC, Borowitz D. 2013. The cystic fibrosis intestine. *Cold Spring Harb Perspect Med* 3:a009753
34. Anguiano A, Oates RD, Amos JA, Dean M, Gerrard B, et al. 1992. Congenital bilateral absence of the vas deferens. A primarily genital form of cystic fibrosis. *JAMA* 267:1794-7
35. Bombieri C, Claustres M, De Boeck K, Derichs N, Dodge J, et al. 2011. Recommendations for the classification of diseases as CFTR-related disorders. *J Cyst Fibros* 10 Suppl 2:S86-102
36. Yu J, Chen Z, Ni Y, Li Z. 2012. CFTR mutations in men with congenital bilateral absence of the vas deferens (CBAVD): a systemic review and meta-analysis. *Hum Reprod* 27:25-35
37. Hughan KS, Daley T, Rayas MS, Kelly A, Roe A. 2019. Female reproductive health in cystic fibrosis. *J Cyst Fibros* 18 Suppl 2:S95-S104
38. Rommens JM, Iannuzzi MC, Kerem B, Drumm ML, Melmer G, et al. 1989. Identification of the cystic fibrosis gene: chromosome walking and jumping. *Science* 245:1059-65
39. Riordan JR, Rommens JM, Kerem B, Alon N, Rozmahel R, et al. 1989. Identification of the cystic fibrosis gene: cloning and characterization of complementary DNA. *Science* 245:1066-73
40. Kerem B, Rommens JM, Buchanan JA, Markiewicz D, Cox TK, et al. 1989. Identification of the cystic fibrosis gene: genetic analysis. *Science* 245:1073-80

41. Berger HA, Anderson MP, Gregory RJ, Thompson S, Howard PW, et al. 1991. Identification and regulation of the cystic fibrosis transmembrane conductance regulator-generated chloride channel. *J Clin Invest* 88:1422-31
42. Liu F, Zhang Z, Csanady L, Gadsby DC, Chen J. 2017. Molecular Structure of the Human CFTR Ion Channel. *Cell* 169:85-95 e8
43. Zhang Z, Liu F, Chen J. 2018. Molecular structure of the ATP-bound, phosphorylated human CFTR. *Proc Natl Acad Sci U S A* 115:12757-62
44. Cheng SH, Rich DP, Marshall J, Gregory RJ, Welsh MJ, Smith AE. 1991. Phosphorylation of the R domain by cAMP-dependent protein kinase regulates the CFTR chloride channel. *Cell* 66:1027-36
45. Berger HA, Travis SM, Welsh MJ. 1993. Regulation of the cystic fibrosis transmembrane conductance regulator Cl⁻ channel by specific protein kinases and protein phosphatases. *J Biol Chem* 268:2037-47
46. Csanady L, Chan KW, Seto-Young D, Kopsco DC, Nairn AC, Gadsby DC. 2000. Severed channels probe regulation of gating of cystic fibrosis transmembrane conductance regulator by its cytoplasmic domains. *J Gen Physiol* 116:477-500
47. Winter MC, Welsh MJ. 1997. Stimulation of CFTR activity by its phosphorylated R domain. *Nature* 389:294-6
48. Chang XB, Tabcharani JA, Hou YX, Jensen TJ, Kartner N, et al. 1993. Protein kinase A (PKA) still activates CFTR chloride channel after mutagenesis of all 10 PKA consensus phosphorylation sites. *J Biol Chem* 268:11304-11
49. Moran O. 2017. The gating of the CFTR channel. *Cell Mol Life Sci* 74:85-92
50. Chappe V, Hinkson DA, Zhu T, Chang XB, Riordan JR, Hanrahan JW. 2003. Phosphorylation of protein kinase C sites in NBD1 and the R domain control CFTR channel activation by PKA. *J Physiol* 548:39-52

51. Zhang Z, Liu F, Chen J. 2017. Conformational Changes of CFTR upon Phosphorylation and ATP Binding. *Cell* 170:483-91 e8
52. Aleksandrov L, Aleksandrov AA, Chang XB, Riordan JR. 2002. The First Nucleotide Binding Domain of Cystic Fibrosis Transmembrane Conductance Regulator Is a Site of Stable Nucleotide Interaction, whereas the Second Is a Site of Rapid Turnover. *J Biol Chem* 277:15419-25
53. Carson MR, Travis SM, Welsh MJ. 1995. The two nucleotide-binding domains of cystic fibrosis transmembrane conductance regulator (CFTR) have distinct functions in controlling channel activity. *J Biol Chem* 270:1711-7
54. 31 July 2020. *CFTR2 Variant List History*. https://www.cftr2.org/mutations_history
55. Veit G, Avramescu RG, Chiang AN, Houck SA, Cai Z, et al. 2016. From CFTR biology toward combinatorial pharmacotherapy: expanded classification of cystic fibrosis mutations. *Mol Biol Cell* 27:424-33
56. De Boeck K, Amaral MD. 2016. Progress in therapies for cystic fibrosis. *Lancet Respir Med* 4:662-74
57. Hamosh A, Rosenstein BJ, Cutting GR. 1992. CFTR nonsense mutations G542X and W1282X associated with severe reduction of CFTR mRNA in nasal epithelial cells. *Hum Mol Genet* 1:542-4
58. Will K, Dork T, Stuhmann M, von der Hardt H, Ellemunter H, et al. 1995. Transcript analysis of CFTR nonsense mutations in lymphocytes and nasal epithelial cells from cystic fibrosis patients. *Hum Mutat* 5:210-20
59. Serohijos AW, Hegedus T, Aleksandrov AA, He L, Cui L, et al. 2008. Phenylalanine-508 mediates a cytoplasmic-membrane domain contact in the CFTR 3D structure crucial to assembly and channel function. *Proc Natl Acad Sci U S A* 105:3256-61
60. Cheng SH, Gregory RJ, Marshall J, Paul S, Souza DW, et al. 1990. Defective intracellular transport and processing of CFTR is the molecular basis of most cystic fibrosis. *Cell* 63:827-34

61. Logan J, Hiestand D, Daram P, Huang Z, Muccio DD, et al. 1994. Cystic fibrosis transmembrane conductance regulator mutations that disrupt nucleotide binding. *J Clin Invest* 94:228-36
62. Bompadre SG, Sohma Y, Li M, Hwang TC. 2007. G551D and G1349D, two CF-associated mutations in the signature sequences of CFTR, exhibit distinct gating defects. *J Gen Physiol* 129:285-98
63. Van Goor F, Yu H, Burton B, Hoffman BJ. 2014. Effect of ivacaftor on CFTR forms with missense mutations associated with defects in protein processing or function. *J Cyst Fibros* 13:29-36
64. Cebotaru L, Rapino D, Cebotaru V, Guggino WB. 2014. Correcting the cystic fibrosis disease mutant, A455E CFTR. *PLoS One* 9:e85183
65. Silvis MR, Picciano JA, Bertrand C, Weixel K, Bridges RJ, Bradbury NA. 2003. A mutation in the cystic fibrosis transmembrane conductance regulator generates a novel internalization sequence and enhances endocytic rates. *J Biol Chem* 278:11554-60
66. Van Goor F, Hadida S, Grootenhuis PD, Burton B, Cao D, et al. 2009. Rescue of CF airway epithelial cell function in vitro by a CFTR potentiator, VX-770. *Proc Natl Acad Sci U S A* 106:18825-30
67. Eckford PD, Li C, Ramjeesingh M, Bear CE. 2012. Cystic fibrosis transmembrane conductance regulator (CFTR) potentiator VX-770 (ivacaftor) opens the defective channel gate of mutant CFTR in a phosphorylation-dependent but ATP-independent manner. *J Biol Chem* 287:36639-49
68. Cui G, McCarty NA. 2015. Murine and human CFTR exhibit different sensitivities to CFTR potentiators. *Am J Physiol Lung Cell Mol Physiol* 309:L687-99
69. Jih KY, Hwang TC. 2013. Vx-770 potentiates CFTR function by promoting decoupling between the gating cycle and ATP hydrolysis cycle. *Proc Natl Acad Sci U S A* 110:4404-9
70. Liu F, Zhang Z, Levit A, Levring J, Touhara KK, et al. 2019. Structural identification of a hotspot on CFTR for potentiation. *Science* 364:1184-8

71. Byrnes LJ, Xu Y, Qiu X, Hall JD, West GM. 2018. Sites associated with Kalydeco binding on human Cystic Fibrosis Transmembrane Conductance Regulator revealed by Hydrogen/Deuterium Exchange. *Sci Rep* 8:4664
72. Laselva O, Qureshi Z, Zeng Z-W, Petrotchenko EV, Ramjeesingh M, et al. 2021. Identification of binding sites for ivacaftor on the cystic fibrosis transmembrane conductance regulator. *iScience* 24
73. Cui G, Stauffer BB, Imhoff BR, Rab A, Hong JS, et al. 2019. VX-770-mediated potentiation of numerous human CFTR disease mutants is influenced by phosphorylation level. *Sci Rep* 9:13460
74. Accurso FJ, Rowe SM, Clancy JP, Boyle MP, Dunitz JM, et al. 2010. Effect of VX-770 in persons with cystic fibrosis and the G551D-CFTR mutation. *N Engl J Med* 363:1991-2003
75. Ramsey BW, Davies J, McElvaney NG, Tullis E, Bell SC, et al. 2011. A CFTR potentiator in patients with cystic fibrosis and the G551D mutation. *N Engl J Med* 365:1663-72
76. Van Goor F, Hadida S, Grootenhuis PD, Burton B, Stack JH, et al. 2011. Correction of the F508del-CFTR protein processing defect in vitro by the investigational drug VX-809. *Proc Natl Acad Sci U S A* 108:18843-8
77. He L, Kota P, Aleksandrov AA, Cui L, Jensen T, et al. 2013. Correctors of DeltaF508 CFTR restore global conformational maturation without thermally stabilizing the mutant protein. *FASEB J* 27:536-45
78. Okiyoneda T, Veit G, Dekkers JF, Bagdany M, Soya N, et al. 2013. Mechanism-based corrector combination restores DeltaF508-CFTR folding and function. *Nat Chem Biol* 9:444-54
79. Hudson RP, Dawson JE, Chong PA, Yang Z, Millen L, et al. 2017. Direct Binding of the Corrector VX-809 to Human CFTR NBD1: Evidence of an Allosteric Coupling between the Binding Site and the NBD1:CL4 Interface. *Mol Pharmacol* 92:124-35
80. Molinski SV, Shahani VM, Subramanian AS, MacKinnon SS, Woollard G, et al. 2018. Comprehensive mapping of cystic fibrosis mutations to CFTR protein identifies mutation clusters and molecular docking predicts corrector binding site. *Proteins* 86:833-43

81. Wainwright CE, Elborn JS, Ramsey BW, Marigowda G, Huang X, et al. 2015. Lumacaftor-Ivacaftor in Patients with Cystic Fibrosis Homozygous for Phe508del CFTR. *N Engl J Med* 373:220-31
82. Cholon DM, Quinney NL, Fulcher ML, Esther CR, Jr., Das J, et al. 2014. Potentiator ivacaftor abrogates pharmacological correction of DeltaF508 CFTR in cystic fibrosis. *Sci Transl Med* 6:246ra96
83. Veit G, Avramescu RG, Perdomo D, Phuan PW, Bagdany M, et al. 2014. Some gating potentiators, including VX-770, diminish DeltaF508-CFTR functional expression. *Sci Transl Med* 6:246ra97
84. Taylor-Cousar JL, Munck A, McKone EF, van der Ent CK, Moeller A, et al. 2017. Tezacaftor-Ivacaftor in Patients with Cystic Fibrosis Homozygous for Phe508del. *N Engl J Med* 377:2013-23
85. Keating D, Marigowda G, Burr L, Daines C, Mall MA, et al. 2018. VX-445-Tezacaftor-Ivacaftor in Patients with Cystic Fibrosis and One or Two Phe508del Alleles. *N Engl J Med* 379:1612-20
86. Veit G, Roldan A, Hancock MA, Da Fonte DF, Xu H, et al. 2020. Allosteric folding correction of F508del and rare CFTR mutants by elexacaftor-tezacaftor-ivacaftor (Trikafta) combination. *JCI Insight* 5
87. 2020. NDA/BLA Multi-disciplinary Review and Evaluation {NDA 212273} {TRIKAFTA, elexacaftor/tezacaftor/ivacaftor}. *Rep. 212273*, Center for Drug Evaluation and Research
88. Heijerman HGM, McKone EF, Downey DG, Van Braeckel E, Rowe SM, et al. 2019. Efficacy and safety of the elexacaftor plus tezacaftor plus ivacaftor combination regimen in people with cystic fibrosis homozygous for the F508del mutation: a double-blind, randomised, phase 3 trial. *Lancet* 394:1940-8
89. Middleton PG, Mall MA, Drevinek P, Lands LC, McKone EF, et al. 2019. Elexacaftor-Tezacaftor-Ivacaftor for Cystic Fibrosis with a Single Phe508del Allele. *N Engl J Med* 381:1809-19

90. Kerem E, Hirawat S, Armoni S, Yaakov Y, Shoseyov D, et al. 2008. Effectiveness of PTC124 treatment of cystic fibrosis caused by nonsense mutations: a prospective phase II trial. *Lancet* 372:719-27
91. Sermet-Gaudelus I, Boeck KD, Casimir GJ, Vermeulen F, Leal T, et al. 2010. Ataluren (PTC124) induces cystic fibrosis transmembrane conductance regulator protein expression and activity in children with nonsense mutation cystic fibrosis. *Am J Respir Crit Care Med* 182:1262-72
92. Alton E, Armstrong DK, Ashby D, Bayfield KJ, Bilton D, et al. 2015. Repeated nebulisation of non-viral CFTR gene therapy in patients with cystic fibrosis: a randomised, double-blind, placebo-controlled, phase 2b trial. *Lancet Respir Med* 3:684-91
93. Fajac I, De Boeck K. 2017. New horizons for cystic fibrosis treatment. *Pharmacol Ther* 170:205-11
94. Tata F, Stanier P, Wicking C, Halford S, Kruyer H, et al. 1991. Cloning the mouse homolog of the human cystic fibrosis transmembrane conductance regulator gene. *Genomics* 10:301-7
95. Snouwaert JN, Brigman KK, Latour AM, Malouf NN, Boucher RC, et al. 1992. An animal model for cystic fibrosis made by gene targeting. *Science* 257:1083-8
96. Wilke M, Buijs-Offerman RM, Aarbiou J, Colledge WH, Sheppard DN, et al. 2011. Mouse models of cystic fibrosis: phenotypic analysis and research applications. *J Cyst Fibros* 10 Suppl 2:S152-71
97. McCarron A, Parsons D, Donnelley M. 2021. Animal and Cell Culture Models for Cystic Fibrosis: Which Model Is Right for Your Application? *Am J Pathol* 191:228-42
98. Semaniakou A, Croll RP, Chappe V. 2018. Animal Models in the Pathophysiology of Cystic Fibrosis. *Front Pharmacol* 9:1475
99. Kent G, Oliver M, Foskett JK, Frndova H, Durie P, et al. 1996. Phenotypic abnormalities in long-term surviving cystic fibrosis mice. *Pediatr Res* 40:233-41
100. Cottart CH, Bonvin E, Rey C, Wendum D, Bernaudin JF, et al. 2007. Impact of nutrition on phenotype in CFTR-deficient mice. *Pediatr Res* 62:528-32

101. Grubb BR, Vick RN, Boucher RC. 1994. Hyperabsorption of Na⁺ and raised Ca(2⁺)-mediated Cl⁻ secretion in nasal epithelia of CF mice. *Am J Physiol* 266:C1478-83
102. Knowles M, Gatzky J, Boucher R. 1981. Increased bioelectric potential difference across respiratory epithelia in cystic fibrosis. *N Engl J Med* 305:1489-95
103. Grubb BR, Paradiso AM, Boucher RC. 1994. Anomalies in ion transport in CF mouse tracheal epithelium. *Am J Physiol* 267:C293-300
104. Benedetto R, Ousingsawat J, Wanitchakool P, Zhang Y, Holtzman MJ, et al. 2017. Epithelial Chloride Transport by CFTR Requires TMEM16A. *Sci Rep* 7:12397
105. Clarke LL, Grubb BR, Yankaskas JR, Cotton CU, McKenzie A, Boucher RC. 1994. Relationship of a non-cystic fibrosis transmembrane conductance regulator-mediated chloride conductance to organ-level disease in Cfr(-/-) mice. *Proc Natl Acad Sci U S A* 91:479-83
106. Zhou L, Dey CR, Wert SE, DuVall MD, Frizzell RA, Whitsett JA. 1994. Correction of lethal intestinal defect in a mouse model of cystic fibrosis by human CFTR. *Science* 266:1705-8
107. Dorin JR, Dickinson P, Alton EW, Smith SN, Geddes DM, et al. 1992. Cystic fibrosis in the mouse by targeted insertional mutagenesis. *Nature* 359:211-5
108. French PJ, van Doorninck JH, Peters RH, Verbeek E, Ameen NA, et al. 1996. A delta F508 mutation in mouse cystic fibrosis transmembrane conductance regulator results in a temperature-sensitive processing defect in vivo. *J Clin Invest* 98:1304-12
109. van Doorninck JH, French PJ, Verbeek E, Peters RH, Morreau H, et al. 1995. A mouse model for the cystic fibrosis delta F508 mutation. *EMBO J* 14:4403-11
110. Bose SJ, Bijvelds MJC, Wang Y, Liu J, Cai Z, et al. 2019. Differential thermostability and response to cystic fibrosis transmembrane conductance regulator potentiators of human and mouse F508del-CFTR. *Am J Physiol Lung Cell Mol Physiol* 317:L71-L86
111. Mall M, Grubb BR, Harkema JR, O'Neal WK, Boucher RC. 2004. Increased airway epithelial Na⁺ absorption produces cystic fibrosis-like lung disease in mice. *Nat Med* 10:487-93

112. Mall MA, Harkema JR, Trojanek JB, Treis D, Livraghi A, et al. 2008. Development of chronic bronchitis and emphysema in beta-epithelial Na⁺ channel-overexpressing mice. *Am J Respir Crit Care Med* 177:730-42
113. Sun X, Yan Z, Yi Y, Li Z, Lei D, et al. 2008. Adeno-associated virus-targeted disruption of the CFTR gene in cloned ferrets. *J Clin Invest* 118:1578-83
114. Sun X, Sui H, Fisher JT, Yan Z, Liu X, et al. 2010. Disease phenotype of a ferret CFTR-knockout model of cystic fibrosis. *J Clin Invest* 120:3149-60
115. Sun X, Olivier AK, Liang B, Yi Y, Sui H, et al. 2014. Lung phenotype of juvenile and adult cystic fibrosis transmembrane conductance regulator-knockout ferrets. *Am J Respir Cell Mol Biol* 50:502-12
116. Rosen BH, Evans TIA, Moll SR, Gray JS, Liang B, et al. 2018. Infection Is Not Required for Mucoinflammatory Lung Disease in CFTR-Knockout Ferrets. *Am J Respir Crit Care Med* 197:1308-18
117. Margaroli C, Garratt LW, Horati H, Dittrich AS, Rosenow T, et al. 2019. Elastase Exocytosis by Airway Neutrophils Is Associated with Early Lung Damage in Children with Cystic Fibrosis. *Am J Respir Crit Care Med* 199:873-81
118. Rogers CS, Abraham WM, Brogden KA, Engelhardt JF, Fisher JT, et al. 2008. The porcine lung as a potential model for cystic fibrosis. *Am J Physiol Lung Cell Mol Physiol* 295:L240-63
119. Ostedgaard LS, Rogers CS, Dong Q, Randak CO, Vermeer DW, et al. 2007. Processing and function of CFTR-DeltaF508 are species-dependent. *Proc Natl Acad Sci U S A* 104:15370-5
120. Rogers CS, Hao Y, Rokhlina T, Samuel M, Stoltz DA, et al. 2008. Production of CFTR-null and CFTR-DeltaF508 heterozygous pigs by adeno-associated virus-mediated gene targeting and somatic cell nuclear transfer. *J Clin Invest* 118:1571-7
121. Stoltz DA, Rokhlina T, Ernst SE, Pezzulo AA, Ostedgaard LS, et al. 2013. Intestinal CFTR expression alleviates meconium ileus in cystic fibrosis pigs. *J Clin Invest* 123:2685-93

122. Ostedgaard LS, Meyerholz DK, Chen JH, Pezzulo AA, Karp PH, et al. 2011. The DeltaF508 mutation causes CFTR misprocessing and cystic fibrosis-like disease in pigs. *Sci Transl Med* 3:74ra24
123. Stoltz DA, Meyerholz DK, Pezzulo AA, Ramachandran S, Rogan MP, et al. 2010. Cystic fibrosis pigs develop lung disease and exhibit defective bacterial eradication at birth. *Sci Transl Med* 2:29ra31
124. Cozens AL, Yezzi MJ, Chin L, Simon EM, Finkbeiner WE, et al. 1992. Characterization of immortal cystic fibrosis tracheobronchial gland epithelial cells. *Proc Natl Acad Sci U S A* 89:5171-5
125. Gruenert DC, Basbaum CB, Welsh MJ, Li M, Finkbeiner WE, Nadel JA. 1988. Characterization of human tracheal epithelial cells transformed by an origin-defective simian virus 40. *Proc Natl Acad Sci U S A* 85:5951-5
126. Sommerhoff CP, Finkbeiner WE. 1990. Human tracheobronchial submucosal gland cells in culture. *Am J Respir Cell Mol Biol* 2:41-50
127. Cozens AL, Yezzi MJ, Kunzelmann K, Ohnishi T, Chin L, et al. 1994. CFTR expression and chloride secretion in polarized immortal human bronchial epithelial cells. *Am J Respir Cell Mol Biol* 10:38-47
128. Valley HC, Bukis KM, Bell A, Cheng Y, Wong E, et al. 2019. Isogenic cell models of cystic fibrosis-causing variants in natively expressing pulmonary epithelial cells. *J Cyst Fibros* 18:476-83
129. Bruscia E, Sangiuolo F, Sinibaldi P, Goncz KK, Novelli G, Gruenert DC. 2002. Isolation of CF cell lines corrected at DeltaF508-CFTR locus by SFHR-mediated targeting. *Gene Ther* 9:683-5
130. Bebok Z, Collawn JF, Wakefield J, Parker W, Li Y, et al. 2005. Failure of cAMP agonists to activate rescued deltaF508 CFTR in CFBE41o- airway epithelial monolayers. *J Physiol* 569:601-

131. Zeitlin PL, Lu L, Rhim J, Cutting G, Stetten G, et al. 1991. A cystic fibrosis bronchial epithelial cell line: immortalization by adeno-12-SV40 infection. *Am J Respir Cell Mol Biol* 4:313-9
132. Flotte TR, Afione SA, Conrad C, McGrath SA, Solow R, et al. 1993. Stable in vivo expression of the cystic fibrosis transmembrane conductance regulator with an adeno-associated virus vector. *Proc Natl Acad Sci U S A* 90:10613-7
133. Shen BQ, Finkbeiner WE, Wine JJ, Mrsny RJ, Widdicombe JH. 1994. Calu-3: a human airway epithelial cell line that shows cAMP-dependent Cl⁻ secretion. *Am J Physiol* 266:L493-501
134. Haws C, Finkbeiner WE, Widdicombe JH, Wine JJ. 1994. CFTR in Calu-3 human airway cells: channel properties and role in cAMP-activated Cl⁻ conductance. *Am J Physiol* 266:L502-12
135. ATCC. *Calu-3 (ATCC® HTB-55™)*. <https://www.atcc.org/products/all/HTB-55.aspx>
136. Zabner J, Karp P, Seiler M, Phillips SL, Mitchell CJ, et al. 2003. Development of cystic fibrosis and noncystic fibrosis airway cell lines. *Am J Physiol Lung Cell Mol Physiol* 284:L844-54
137. Fulcher ML, Gabriel S, Burns KA, Yankaskas JR, Randell SH. 2005. Well-differentiated human airway epithelial cell cultures. *Methods Mol Med* 107:183-206
138. Neuberger T, Burton B, Clark H, Van Goor F. 2011. Use of primary cultures of human bronchial epithelial cells isolated from cystic fibrosis patients for the pre-clinical testing of CFTR modulators. *Methods Mol Biol* 741:39-54
139. van Meer G, de Kroon AI. 2011. Lipid map of the mammalian cell. *J Cell Sci* 124:5-8
140. Rhodes B, Nash EF, Tullis E, Pencharz PB, Brotherwood M, et al. 2010. Prevalence of dyslipidemia in adults with cystic fibrosis. *J Cyst Fibros* 9:24-8
141. Vandebrouck C, Ferreira T. 2020. Glued in lipids: Lipointoxication in cystic fibrosis. *EBioMedicine* 61:103038
142. Zarate R, El Jaber-Vazdekis N, Tejera N, Perez JA, Rodriguez C. 2017. Significance of long chain polyunsaturated fatty acids in human health. *Clin Transl Med* 6:25
143. Freedman SD, Blanco PG, Zaman MM, Shea JC, Ollero M, et al. 2004. Association of cystic fibrosis with abnormalities in fatty acid metabolism. *N Engl J Med* 350:560-9

144. Al-Turkmani MR, Andersson C, Alturkmani R, Katrangi W, Cluette-Brown JE, et al. 2008. A mechanism accounting for the low cellular level of linoleic acid in cystic fibrosis and its reversal by DHA. *J Lipid Res* 49:1946-54
145. Andersson C, Al-Turkmani MR, Savaille JE, Alturkmani R, Katrangi W, et al. 2008. Cell culture models demonstrate that CFTR dysfunction leads to defective fatty acid composition and metabolism. *J Lipid Res* 49:1692-700
146. Veltman M, De Sanctis JB, Stolarczyk M, Klymiuk N, Bahr A, et al. 2021. CFTR Correctors and Antioxidants Partially Normalize Lipid Imbalance but not Abnormal Basal Inflammatory Cytokine Profile in CF Bronchial Epithelial Cells. *Front Physiol* 12:619442
147. Njoroge SW, Laposata M, Katrangi W, Seegmiller AC. 2012. DHA and EPA reverse cystic fibrosis-related FA abnormalities by suppressing FA desaturase expression and activity. *J Lipid Res* 53:257-65
148. Umunakwe OC, Seegmiller AC. 2014. Abnormal n-6 fatty acid metabolism in cystic fibrosis is caused by activation of AMP-activated protein kinase. *J Lipid Res* 55:1489-97
149. Lopez-Neyra A, Suarez L, Munoz M, de Blas A, Ruiz de Valbuena M, et al. 2020. Long-term docosahexaenoic acid (DHA) supplementation in cystic fibrosis patients: a randomized, multi-center, double-blind, placebo-controlled trial. *Prostaglandins Leukot Essent Fatty Acids* 162:102186
150. Watson H, Stackhouse C. 2020. Omega-3 fatty acid supplementation for cystic fibrosis. *Cochrane Database Syst Rev* 4:CD002201
151. Simons K, Ikonen E. 1997. Functional rafts in cell membranes. *Nature* 387:569-72
152. Martin MG, Pfrieder F, Dotti CG. 2014. Cholesterol in brain disease: sometimes determinant and frequently implicated. *EMBO Rep* 15:1036-52
153. Ernst WL, Shome K, Wu CC, Gong X, Frizzell RA, Aridor M. 2016. VAMP-associated Proteins (VAP) as Receptors That Couple Cystic Fibrosis Transmembrane Conductance Regulator (CFTR) Proteostasis with Lipid Homeostasis. *J Biol Chem* 291:5206-20

154. Gentsch M, Choudhury A, Chang XB, Pagano RE, Riordan JR. 2007. Misassembled mutant DeltaF508 CFTR in the distal secretory pathway alters cellular lipid trafficking. *J Cell Sci* 120:447-55
155. White NM, Corey DA, Kelley TJ. 2004. Mechanistic similarities between cultured cell models of cystic fibrosis and Niemann-Pick type C. *Am J Respir Cell Mol Biol* 31:538-43
156. White NM, Jiang D, Burgess JD, Bederman IR, Previs SF, Kelley TJ. 2007. Altered cholesterol homeostasis in cultured and in vivo models of cystic fibrosis. *Am J Physiol Lung Cell Mol Physiol* 292:L476-86
157. Lu B, Li L, Schneider M, Hodges CA, Cotton CU, et al. 2019. Electrochemical measurement of membrane cholesterol correlates with CFTR function and is HDAC6-dependent. *J Cyst Fibros* 18:175-81
158. Kreiselmeier NE, Kraynack NC, Corey DA, Kelley TJ. 2003. Statin-mediated correction of STAT1 signaling and inducible nitric oxide synthase expression in cystic fibrosis epithelial cells. *Am J Physiol Lung Cell Mol Physiol* 285:L1286-95
159. Fang D, West RH, Manson ME, Ruddy J, Jiang D, et al. 2010. Increased plasma membrane cholesterol in cystic fibrosis cells correlates with CFTR genotype and depends on de novo cholesterol synthesis. *Respir Res* 11:61
160. Teichgraber V, Ulrich M, Endlich N, Riethmuller J, Wilker B, et al. 2008. Ceramide accumulation mediates inflammation, cell death and infection susceptibility in cystic fibrosis. *Nat Med* 14:382-91
161. Slomiany A, Murty VL, Aono M, Snyder CE, Herp A, Slomiany BL. 1982. Lipid composition of tracheobronchial secretions from normal individuals and patients with cystic fibrosis. *Biochim Biophys Acta* 710:106-11
162. Hartmann D, Lucks J, Fuchs S, Schiffmann S, Schreiber Y, et al. 2012. Long chain ceramides and very long chain ceramides have opposite effects on human breast and colon cancer cell growth. *Int J Biochem Cell Biol* 44:620-8

163. Gault CR, Obeid LM, Hannun YA. 2010. An overview of sphingolipid metabolism: from synthesis to breakdown. *Adv Exp Med Biol* 688:1-23
164. Bartke N, Hannun YA. 2009. Bioactive sphingolipids: metabolism and function. *J Lipid Res* 50 Suppl:S91-6
165. Hannun YA, Obeid LM. 2008. Principles of bioactive lipid signalling: lessons from sphingolipids. *Nat Rev Mol Cell Biol* 9:139-50
166. Laviad EL, Kelly S, Merrill AH, Jr., Futerman AH. 2012. Modulation of ceramide synthase activity via dimerization. *J Biol Chem* 287:21025-33
167. Petrache I, Kamocki K, Poirier C, Pewzner-Jung Y, Laviad EL, et al. 2013. Ceramide synthases expression and role of ceramide synthase-2 in the lung: insight from human lung cells and mouse models. *PLoS One* 8:e62968
168. Hanada K, Kumagai K, Tomishige N, Kawano M. 2007. CERT and intracellular trafficking of ceramide. *Biochim Biophys Acta* 1771:644-53
169. Tam C, Idone V, Devlin C, Fernandes MC, Flannery A, et al. 2010. Exocytosis of acid sphingomyelinase by wounded cells promotes endocytosis and plasma membrane repair. *J Cell Biol* 189:1027-38
170. Tepper AD, Ruurs P, Wiedmer T, Sims PJ, Borst J, van Blitterswijk WJ. 2000. Sphingomyelin hydrolysis to ceramide during the execution phase of apoptosis results from phospholipid scrambling and alters cell-surface morphology. *J Cell Biol* 150:155-64
171. Mao C, Obeid LM. 2008. Ceramidases: regulators of cellular responses mediated by ceramide, sphingosine, and sphingosine-1-phosphate. *Biochim Biophys Acta* 1781:424-34
172. Kitatani K, Idkowiak-Baldys J, Hannun YA. 2008. The sphingolipid salvage pathway in ceramide metabolism and signaling. *Cell Signal* 20:1010-8
173. Gulbins E, Kolesnick R. 2003. Raft ceramide in molecular medicine. *Oncogene* 22:7070-7
174. Grassme H, Jekle A, Riehle A, Schwarz H, Berger J, et al. 2001. CD95 signaling via ceramide-rich membrane rafts. *J Biol Chem* 276:20589-96

175. Grassme H, Cremesti A, Kolesnick R, Gulbins E. 2003. Ceramide-mediated clustering is required for CD95-DISC formation. *Oncogene* 22:5457-70
176. Grassme H, Jendrossek V, Riehle A, von Kurthy G, Berger J, et al. 2003. Host defense against *Pseudomonas aeruginosa* requires ceramide-rich membrane rafts. *Nat Med* 9:322-30
177. Dudez T, Borot F, Huang S, Kwak BR, Bacchetta M, et al. 2008. CFTR in a lipid raft-TNFR1 complex modulates gap junctional intercellular communication and IL-8 secretion. *Biochim Biophys Acta* 1783:779-88
178. Abu-Arish A, Pandzic E, Goepf J, Matthes E, Hanrahan JW, Wiseman PW. 2015. Cholesterol modulates CFTR confinement in the plasma membrane of primary epithelial cells. *Biophys J* 109:85-94
179. Garić D DSJ, Shah J, Dumut DC, Radzioch D. 2019. Biochemistry of very-long-chain and long-chain ceramides in cystic fibrosis and other diseases: The importance of side chain. *Progress in Lipid Research*:130-44
180. Di A, Brown ME, Deriy LV, Li C, Szeto FL, et al. 2006. CFTR regulates phagosome acidification in macrophages and alters bactericidal activity. *Nat Cell Biol* 8:933-44
181. Schissel SL, Schuchman EH, Williams KJ, Tabas I. 1996. Zn²⁺-stimulated sphingomyelinase is secreted by many cell types and is a product of the acid sphingomyelinase gene. *J Biol Chem* 271:18431-6
182. He X, Okino N, Dhami R, Dagan A, Gatt S, et al. 2003. Purification and characterization of recombinant, human acid ceramidase. Catalytic reactions and interactions with acid sphingomyelinase. *J Biol Chem* 278:32978-86
183. Haggie PM, Verkman AS. 2009. Defective organellar acidification as a cause of cystic fibrosis lung disease: reexamination of a recurring hypothesis. *Am J Physiol Lung Cell Mol Physiol* 296:L859-67

184. Barriere H, Bagdany M, Bossard F, Okiyoneda T, Wojewodka G, et al. 2009. Revisiting the role of cystic fibrosis transmembrane conductance regulator and counterion permeability in the pH regulation of endocytic organelles. *Mol Biol Cell* 20:3125-41
185. Guilbault C, De Sanctis JB, Wojewodka G, Saeed Z, Lachance C, et al. 2008. Fenretinide corrects newly found ceramide deficiency in cystic fibrosis. *Am J Respir Cell Mol Biol* 38:47-56
186. Garic D, De Sanctis JB, Wojewodka G, Houle D, Cupri S, et al. 2017. Fenretinide differentially modulates the levels of long- and very long-chain ceramides by downregulating Cers5 enzyme: evidence from bench to bedside. *J Mol Med (Berl)* 95:1053-64
187. Duchesneau P, Besla R, Derouet MF, Guo L, Karoubi G, et al. 2017. Partial Restoration of CFTR Function in cftr-Null Mice following Targeted Cell Replacement Therapy. *Mol Ther* 25:654-65
188. Ghidoni R, Caretti A, Signorelli P. 2015. Role of Sphingolipids in the Pathobiology of Lung Inflammation. *Mediators Inflamm* 2015:487508
189. Hamai H, Keyserman F, Quittell LM, Worgall TS. 2009. Defective CFTR increases synthesis and mass of sphingolipids that modulate membrane composition and lipid signaling. *J Lipid Res* 50:1101-8
190. Caretti A, Bragonzi A, Facchini M, De Fino I, Riva C, et al. 2014. Anti-inflammatory action of lipid nanocarrier-delivered myriocin: therapeutic potential in cystic fibrosis. *Biochim Biophys Acta* 1840:586-94
191. Mingione A, Dei Cas M, Bonezzi F, Caretti A, Piccoli M, et al. 2020. Inhibition of Sphingolipid Synthesis as a Phenotype-Modifying Therapy in Cystic Fibrosis. *Cell Physiol Biochem* 54:110-25
192. Brodlie M, McKean MC, Johnson GE, Gray J, Fisher AJ, et al. 2010. Ceramide is increased in the lower airway epithelium of people with advanced cystic fibrosis lung disease. *Am J Respir Crit Care Med* 182:369-75
193. Loberto N, Mancini G, Bassi R, Carsana EV, Tamanini A, et al. 2020. Sphingolipids and plasma membrane hydrolases in human primary bronchial cells during differentiation and their altered patterns in cystic fibrosis. *Glycoconj J*

194. Gardner AI, Haq IJ, Simpson AJ, Becker KA, Gallagher J, et al. 2020. Recombinant Acid Ceramidase Reduces Inflammation and Infection in Cystic Fibrosis. *Am J Respir Crit Care Med*
195. Riethmuller J, Anthonysamy J, Serra E, Schwab M, Doring G, Gulbins E. 2009. Therapeutic efficacy and safety of amitriptyline in patients with cystic fibrosis. *Cell Physiol Biochem* 24:65-72
196. Adams C, Icheva V, Deppisch C, Lauer J, Herrmann G, et al. 2016. Long-Term Pulmonary Therapy of Cystic Fibrosis-Patients with Amitriptyline. *Cell Physiol Biochem* 39:565-72
197. Kolzer M, Werth N, Sandhoff K. 2004. Interactions of acid sphingomyelinase and lipid bilayers in the presence of the tricyclic antidepressant desipramine. *FEBS Lett* 559:96-8
198. Elojeimy S, Holman DH, Liu X, El-Zawahry A, Villani M, et al. 2006. New insights on the use of desipramine as an inhibitor for acid ceramidase. *FEBS Lett* 580:4751-6
199. Santana P, Pena LA, Haimovitz-Friedman A, Martin S, Green D, et al. 1996. Acid sphingomyelinase-deficient human lymphoblasts and mice are defective in radiation-induced apoptosis. *Cell* 86:189-99
200. Esen M, Schreiner B, Jendrossek V, Lang F, Fassbender K, et al. 2001. Mechanisms of Staphylococcus aureus induced apoptosis of human endothelial cells. *Apoptosis* 6:431-9
201. Fisher-Wellman KH, Hagen JT, Neuffer PD, Kassai M, Cabot MC. 2021. On the nature of ceramide-mitochondria interactions - Dissection using comprehensive mitochondrial phenotyping. *Cell Signal* 78:109838
202. Ziobro R, Henry B, Edwards MJ, Lentsch AB, Gulbins E. 2013. Ceramide mediates lung fibrosis in cystic fibrosis. *Biochem Biophys Res Commun* 434:705-9
203. Zhang Y, Li X, Grassme H, Doring G, Gulbins E. 2010. Alterations in ceramide concentration and pH determine the release of reactive oxygen species by Cfr-deficient macrophages on infection. *J Immunol* 184:5104-11

204. Becker KA, Riethmuller J, Luth A, Doring G, Kleuser B, Gulbins E. 2010. Acid sphingomyelinase inhibitors normalize pulmonary ceramide and inflammation in cystic fibrosis. *Am J Respir Cell Mol Biol* 42:716-24
205. Krivan HC, Ginsburg V, Roberts DD. 1988. *Pseudomonas aeruginosa* and *Pseudomonas cepacia* isolated from cystic fibrosis patients bind specifically to gangliotetraosylceramide (asialo GM1) and gangliotriaosylceramide (asialo GM2). *Arch Biochem Biophys* 260:493-6
206. Bryan R, Kube D, Perez A, Davis P, Prince A. 1998. Overproduction of the CFTR R domain leads to increased levels of asialoGM1 and increased *Pseudomonas aeruginosa* binding by epithelial cells. *Am J Respir Cell Mol Biol* 19:269-77
207. Itokazu Y, Pagano RE, Schroeder AS, O'Grady SM, Limper AH, Marks DL. 2014. Reduced GM1 ganglioside in CFTR-deficient human airway cells results in decreased beta1-integrin signaling and delayed wound repair. *Am J Physiol Cell Physiol* 306:C819-30
208. Pewzner-Jung Y, Tavakoli Tabazavareh S, Grassme H, Becker KA, Japtok L, et al. 2014. Sphingoid long chain bases prevent lung infection by *Pseudomonas aeruginosa*. *EMBO Mol Med* 6:1205-14
209. Grassme H, Henry B, Ziobro R, Becker KA, Riethmuller J, et al. 2017. beta1-Integrin Accumulates in Cystic Fibrosis Luminal Airway Epithelial Membranes and Decreases Sphingosine, Promoting Bacterial Infections. *Cell Host Microbe* 21:707-18 e8
210. Veltman M, Stolarczyk M, Radzioch D, Wojewodka G, De Sanctis JB, et al. 2016. Correction of lung inflammation in a F508del CFTR murine cystic fibrosis model by the sphingosine-1-phosphate lyase inhibitor LX2931. *Am J Physiol Lung Cell Mol Physiol* 311:L1000-L14
211. Pyne S, Pyne NJ. 2000. Sphingosine 1-phosphate signalling in mammalian cells. *Biochem J* 349:385-402
212. Chen LY, Woszczek G, Nagineni S, Logun C, Shelhamer JH. 2008. Cytosolic phospholipase A2alpha activation induced by S1P is mediated by the S1P3 receptor in lung epithelial cells. *Am J Physiol Lung Cell Mol Physiol* 295:L326-35

213. Boujaoude LC, Bradshaw-Wilder C, Mao C, Cohn J, Ogretmen B, et al. 2001. Cystic fibrosis transmembrane regulator regulates uptake of sphingoid base phosphates and lysophosphatidic acid: modulation of cellular activity of sphingosine 1-phosphate. *J Biol Chem* 276:35258-64
214. Huang HW. 1986. Deformation free energy of bilayer membrane and its effect on gramicidin channel lifetime. *Biophys J* 50:1061-70
215. Andersen OS, Koeppe RE, 2nd. 2007. Bilayer thickness and membrane protein function: an energetic perspective. *Annu Rev Biophys Biomol Struct* 36:107-30
216. Phillips R, Ursell T, Wiggins P, Sens P. 2009. Emerging roles for lipids in shaping membrane-protein function. *Nature* 459:379-85
217. Lee AG. 2004. How lipids affect the activities of integral membrane proteins. *Biochim Biophys Acta* 1666:62-87
218. Norimatsu Y, Hasegawa K, Shimizu N, Toyoshima C. 2017. Protein-phospholipid interplay revealed with crystals of a calcium pump. *Nature* 545:193-8
219. Romanenko VG, Fang Y, Byfield F, Travis AJ, Vandenberg CA, et al. 2004. Cholesterol sensitivity and lipid raft targeting of Kir2.1 channels. *Biophys J* 87:3850-61
220. Romanenko VG, Rothblat GH, Levitan I. 2002. Modulation of endothelial inward-rectifier K⁺ current by optical isomers of cholesterol. *Biophys J* 83:3211-22
221. Rosenhouse-Dantsker A, Noskov S, Durdagi S, Logothetis DE, Levitan I. 2013. Identification of novel cholesterol-binding regions in Kir2 channels. *J Biol Chem* 288:31154-64
222. Picazo-Juarez G, Romero-Suarez S, Nieto-Posadas A, Llorente I, Jara-Oseguera A, et al. 2011. Identification of a binding motif in the S5 helix that confers cholesterol sensitivity to the TRPV1 ion channel. *J Biol Chem* 286:24966-76
223. Singh AK, McMillan J, Bukiya AN, Burton B, Parrill AL, Dopico AM. 2012. Multiple cholesterol recognition/interaction amino acid consensus (CRAC) motifs in cytosolic C tail of Slo1 subunit determine cholesterol sensitivity of Ca²⁺- and voltage-gated K⁺ (BK) channels. *J Biol Chem* 287:20509-21

224. Fantini J, Barrantes FJ. 2013. How cholesterol interacts with membrane proteins: an exploration of cholesterol-binding sites including CRAC, CARC, and tilted domains. *Front Physiol* 4:31
225. Hill WG, Butterworth MB, Wang H, Edinger RS, Lebowitz J, et al. 2007. The epithelial sodium channel (ENaC) traffics to apical membrane in lipid rafts in mouse cortical collecting duct cells. *J Biol Chem* 282:37402-11
226. Liu X, Fuentes EJ. 2019. Emerging Themes in PDZ Domain Signaling: Structure, Function, and Inhibition. *Int Rev Cell Mol Biol* 343:129-218
227. Fanning AS, Anderson JM. 1999. Protein modules as organizers of membrane structure. *Curr Opin Cell Biol* 11:432-9
228. Sheng M, Sala C. 2001. PDZ domains and the organization of supramolecular complexes. *Annu Rev Neurosci* 24:1-29
229. Sheng R, Chen Y, Yung Gee H, Stec E, Melowic HR, et al. 2012. Cholesterol modulates cell signaling and protein networking by specifically interacting with PDZ domain-containing scaffold proteins. *Nat Commun* 3:1249
230. Haggie PM, Stanton BA, Verkman AS. 2004. Increased diffusional mobility of CFTR at the plasma membrane after deletion of its C-terminal PDZ binding motif. *J Biol Chem* 279:5494-500
231. Haggie PM, Kim JK, Lukacs GL, Verkman AS. 2006. Tracking of quantum dot-labeled CFTR shows near immobilization by C-terminal PDZ interactions. *Mol Biol Cell* 17:4937-45
232. Hida H, Takeda M, Soliven B. 1998. Ceramide inhibits inwardly rectifying K⁺ currents via a Ras- and Raf-1-dependent pathway in cultured oligodendrocytes. *J Neurosci* 18:8712-9
233. Neumann J, Rose-Sperling D, Hellmich UA. 2017. Diverse relations between ABC transporters and lipids: An overview. *Biochim Biophys Acta Biomembr* 1859:605-18
234. Tarling EJ, de Aguiar Vallim TQ, Edwards PA. 2013. Role of ABC transporters in lipid transport and human disease. *Trends Endocrinol Metab* 24:342-50
235. Sharom FJ. 2014. Complex Interplay between the P-Glycoprotein Multidrug Efflux Pump and the Membrane: Its Role in Modulating Protein Function. *Front Oncol* 4:41

236. Sharom FJ, Yu X, Chu JW, Doige CA. 1995. Characterization of the ATPase activity of P-glycoprotein from multidrug-resistant Chinese hamster ovary cells. *Biochem J* 308 (Pt 2):381-90
237. Garrigues A, Escargueil AE, Orlowski S. 2002. The multidrug transporter, P-glycoprotein, actively mediates cholesterol redistribution in the cell membrane. *Proc Natl Acad Sci U S A* 99:10347-52
238. Kimura Y, Kioka N, Kato H, Matsuo M, Ueda K. 2007. Modulation of drug-stimulated ATPase activity of human MDR1/P-glycoprotein by cholesterol. *Biochem J* 401:597-605
239. Clay AT, Lu P, Sharom FJ. 2015. Interaction of the P-Glycoprotein Multidrug Transporter with Sterols. *Biochemistry* 54:6586-97
240. Ambudkar SV, Lelong IH, Zhang J, Cardarelli C. 1998. Purification and reconstitution of human P-glycoprotein. *Methods Enzymol* 292:492-504
241. Hirayama H, Kimura Y, Kioka N, Matsuo M, Ueda K. 2013. ATPase activity of human ABCG1 is stimulated by cholesterol and sphingomyelin. *J Lipid Res* 54:496-502
242. Ahn J, Wong JT, Molday RS. 2000. The effect of lipid environment and retinoids on the ATPase activity of ABCR, the photoreceptor ABC transporter responsible for Stargardt macular dystrophy. *J Biol Chem* 275:20399-405
243. Pal A, Mehn D, Molnar E, Gedey S, Meszaros P, et al. 2007. Cholesterol potentiates ABCG2 activity in a heterologous expression system: improved in vitro model to study function of human ABCG2. *J Pharmacol Exp Ther* 321:1085-94
244. Telbisz A, Muller M, Ozvegy-Laczka C, Homolya L, Szenté L, et al. 2007. Membrane cholesterol selectively modulates the activity of the human ABCG2 multidrug transporter. *Biochim Biophys Acta* 1768:2698-713
245. Jackson SM, Manolaridis, I., Kowal, J., Zechner, M., Taylor, N.M.I., Bauer, S., Bartholomeus, R., Stahlberg, H., Bernhardt, G., Koenig, B., Buschauer, A., Altmann, K.H., Locher, K.P. Structure of an inhibitor-bound ABC transporter. *To Be Published*

246. Shintre CA, Pike AC, Li Q, Kim JI, Barr AJ, et al. 2013. Structures of ABCB10, a human ATP-binding cassette transporter in apo- and nucleotide-bound states. *Proc Natl Acad Sci U S A* 110:9710-5
247. O'Ryan L, Rimington T, Cant N, Ford RC. 2012. Expression and purification of the cystic fibrosis transmembrane conductance regulator protein in *Saccharomyces cerevisiae*. *J Vis Exp*
248. Ford RC, Birtley J, Rosenberg MF, Zhang L. 2011. CFTR three-dimensional structure. *Methods Mol Biol* 741:329-46
249. Rosenberg MF, Kamis AB, Aleksandrov LA, Ford RC, Riordan JR. 2004. Purification and crystallization of the cystic fibrosis transmembrane conductance regulator (CFTR). *J Biol Chem* 279:39051-7
250. Zhang L, Aleksandrov LA, Riordan JR, Ford RC. 2011. Domain location within the cystic fibrosis transmembrane conductance regulator protein investigated by electron microscopy and gold labelling. *Biochim Biophys Acta* 1808:399-404
251. Zhang ZR, Song B, McCarty NA. 2005. State-dependent chemical reactivity of an engineered cysteine reveals conformational changes in the outer vestibule of the cystic fibrosis transmembrane conductance regulator. *J Biol Chem* 280:41997-2003
252. Zhang Z, Chen J. 2016. Atomic Structure of the Cystic Fibrosis Transmembrane Conductance Regulator. *Cell* 167:1586-97 e9
253. Lee AG. 2018. A Database of Predicted Binding Sites for Cholesterol on Membrane Proteins, Deep in the Membrane. *Biophys J* 115:522-32
254. Yang Z, Wang C, Zhou Q, An J, Hildebrandt E, et al. 2014. Membrane protein stability can be compromised by detergent interactions with the extramembranous soluble domains. *Protein Sci* 23:769-89
255. Hildebrandt E, Khazanov N, Kappes JC, Dai Q, Senderowitz H, Urbatsch IL. 2017. Specific stabilization of CFTR by phosphatidylserine. *Biochim Biophys Acta* 1859:289-93

256. Lewis HA, Zhao X, Wang C, Sauder JM, Rooney I, et al. 2005. Impact of the deltaF508 mutation in first nucleotide-binding domain of human cystic fibrosis transmembrane conductance regulator on domain folding and structure. *J Biol Chem* 280:1346-53
257. Du K, Sharma M, Lukacs GL. 2005. The DeltaF508 cystic fibrosis mutation impairs domain-domain interactions and arrests post-translational folding of CFTR. *Nat Struct Mol Biol* 12:17-25
258. Anderson MP, Welsh MJ. 1990. Fatty acids inhibit apical membrane chloride channels in airway epithelia. *Proc Natl Acad Sci U S A* 87:7334-8
259. Zhou JJ, Linsdell P. 2007. Molecular mechanism of arachidonic acid inhibition of the CFTR chloride channel. *Eur J Pharmacol* 563:88-91
260. Linsdell P. 2005. Location of a common inhibitor binding site in the cytoplasmic vestibule of the cystic fibrosis transmembrane conductance regulator chloride channel pore. *J Biol Chem* 280:8945-50
261. Aubin CN, Linsdell P. 2006. Positive charges at the intracellular mouth of the pore regulate anion conduction in the CFTR chloride channel. *J Gen Physiol* 128:535-45
262. Zhou JJ, Fatehi M, Linsdell P. 2008. Identification of positive charges situated at the outer mouth of the CFTR chloride channel pore. *Pflugers Arch* 457:351-60
263. Li Y, Wang W, Parker W, Clancy JP. 2006. Adenosine regulation of cystic fibrosis transmembrane conductance regulator through prostenoids in airway epithelia. *Am J Respir Cell Mol Biol* 34:600-8
264. Cobb BR, Ruiz F, King CM, Fortenberry J, Greer H, et al. 2002. A(2) adenosine receptors regulate CFTR through PKA and PLA(2). *Am J Physiol Lung Cell Mol Physiol* 282:L12-25
265. Ramu Y, Xu Y, Lu Z. 2007. Inhibition of CFTR Cl⁻ channel function caused by enzymatic hydrolysis of sphingomyelin. *Proc Natl Acad Sci U S A* 104:6448-53
266. Stauffer BB, Cui G, Cottrill KA, Infield DT, McCarty NA. 2017. Bacterial Sphingomyelinase is a State-Dependent Inhibitor of the Cystic Fibrosis Transmembrane conductance Regulator (CFTR). *Sci Rep* 7:2931

267. Saslowky DE, Tanaka N, Reddy KP, Lencer WI. 2009. Ceramide activates JNK to inhibit a cAMP-gated K⁺ conductance and Cl⁻ secretion in intestinal epithelia. *FASEB J* 23:259-70
268. Mall M, Wissner A, Schreiber R, Kuehr J, Seydewitz HH, et al. 2000. Role of K(V)LQT1 in cyclic adenosine monophosphate-mediated Cl⁻ secretion in human airway epithelia. *Am J Respir Cell Mol Biol* 23:283-9
269. Ito Y, Sato S, Ohashi T, Nakayama S, Shimokata K, Kume H. 2004. Reduction of airway anion secretion via CFTR in sphingomyelin pathway. *Biochem Biophys Res Commun* 324:901-8
270. Chalfant CE, Szulc Z, Roddy P, Bielawska A, Hannun YA. 2004. The structural requirements for ceramide activation of serine-threonine protein phosphatases. *J Lipid Res* 45:496-506
271. Dobrowsky RT, Kamibayashi C, Mumby MC, Hannun YA. 1993. Ceramide activates heterotrimeric protein phosphatase 2A. *J Biol Chem* 268:15523-30
272. Luo J, Pato MD, Riordan JR, Hanrahan JW. 1998. Differential regulation of single CFTR channels by PP2C, PP2A, and other phosphatases. *Am J Physiol* 274:C1397-410
273. Thelin WR, Kesimer M, Tarran R, Kreda SM, Grubb BR, et al. 2005. The cystic fibrosis transmembrane conductance regulator is regulated by a direct interaction with the protein phosphatase 2A. *J Biol Chem* 280:41512-20
274. Chappe V, Hinkson DA, Howell LD, Evagelidis A, Liao J, et al. 2004. Stimulatory and inhibitory protein kinase C consensus sequences regulate the cystic fibrosis transmembrane conductance regulator. *Proc Natl Acad Sci U S A* 101:390-5
275. Malik FA, Meissner A, Semenkov I, Molinski S, Pasyk S, et al. 2015. Sphingosine-1-Phosphate Is a Novel Regulator of Cystic Fibrosis Transmembrane Conductance Regulator (CFTR) Activity. *PLoS One* 10:e0130313
276. Wilkinson DJ, Strong TV, Mansoura MK, Wood DL, Smith SS, et al. 1997. CFTR activation: additive effects of stimulatory and inhibitory phosphorylation sites in the R domain. *Am J Physiol* 273:L127-33

277. Kongsuphol P, Cassidy D, Hieke B, Treharne KJ, Schreiber R, et al. 2009. Mechanistic insight into control of CFTR by AMPK. *J Biol Chem* 284:5645-53
278. Neville DC, Rozanas CR, Price EM, Gruis DB, Verkman AS, Townsend RR. 1997. Evidence for phosphorylation of serine 753 in CFTR using a novel metal-ion affinity resin and matrix-assisted laser desorption mass spectrometry. *Protein Sci* 6:2436-45
279. Picciotto MR, Cohn JA, Bertuzzi G, Greengard P, Nairn AC. 1992. Phosphorylation of the cystic fibrosis transmembrane conductance regulator. *J Biol Chem* 267:12742-52
280. Abu-Arish A, Pandzic E, Kim D, Tseng HW, Wiseman PW, Hanrahan JW. 2019. Agonists that stimulate secretion promote the recruitment of CFTR into membrane lipid microdomains. *J Gen Physiol*
281. Kowalski MP, Pier GB. 2004. Localization of cystic fibrosis transmembrane conductance regulator to lipid rafts of epithelial cells is required for *Pseudomonas aeruginosa*-induced cellular activation. *J Immunol* 172:418-25
282. Wang D, Wang W, Duan Y, Sun Y, Wang Y, Huang P. 2008. Functional coupling of Gs and CFTR is independent of their association with lipid rafts in epithelial cells. *Pflugers Arch* 456:929-38
283. Elborn JS. 2016. Cystic fibrosis. *Lancet* 388:2519-31
284. Joshi D, Ehrhardt A, Hong JS, Sorscher EJ. 2019. Cystic fibrosis precision therapeutics: Emerging considerations. *Pediatr Pulmonol* 54 Suppl 3:S13-S7
285. Guimbellot J, Sharma J, Rowe SM. 2017. Toward inclusive therapy with CFTR modulators: Progress and challenges. *Pediatr Pulmonol* 52:S4-S14
286. Levitan I, Fang Y, Rosenhouse-Dantsker A, Romanenko V. 2010. Cholesterol and ion channels. *Subcell Biochem* 51:509-49
287. Bao HF, Zhang ZR, Liang YY, Ma JJ, Eaton DC, Ma HP. 2007. Ceramide mediates inhibition of the renal epithelial sodium channel by tumor necrosis factor- α through protein kinase C. *Am J Physiol Renal Physiol* 293:F1178-86

288. Spiegel S, Merrill AH, Jr. 1996. Sphingolipid metabolism and cell growth regulation. *FASEB J* 10:1388-97
289. Maceyka M, Spiegel S. 2014. Sphingolipid metabolites in inflammatory disease. *Nature* 510:58-67
290. Dua K, Malyla V, Singhvi G, Wadhwa R, Krishna RV, et al. 2019. Increasing complexity and interactions of oxidative stress in chronic respiratory diseases: An emerging need for novel drug delivery systems. *Chem Biol Interact* 299:168-78
291. van der Vliet A, Janssen-Heininger YMW, Anathy V. 2018. Oxidative stress in chronic lung disease: From mitochondrial dysfunction to dysregulated redox signaling. *Mol Aspects Med* 63:59-69
292. Chan C, Goldkorn T. 2000. Ceramide path in human lung cell death. *Am J Respir Cell Mol Biol* 22:460-8
293. Lavrentiadou SN, Chan C, Kawcak T, Ravid T, Tsaba A, et al. 2001. Ceramide-mediated apoptosis in lung epithelial cells is regulated by glutathione. *Am J Respir Cell Mol Biol* 25:676-84
294. Jenkins RW, Canals D, Idkowiak-Baldys J, Simbari F, Roddy P, et al. 2010. Regulated secretion of acid sphingomyelinase: implications for selectivity of ceramide formation. *J Biol Chem* 285:35706-18
295. Kornhuber J, Rhein C, Muller CP, Muhle C. 2015. Secretory sphingomyelinase in health and disease. *Biol Chem* 396:707-36
296. Barker AP, Vasil AI, Filloux A, Ball G, Wilderman PJ, Vasil ML. 2004. A novel extracellular phospholipase C of *Pseudomonas aeruginosa* is required for phospholipid chemotaxis. *Mol Microbiol* 53:1089-98
297. Huseby M, Shi K, Brown CK, Digre J, Mengistu F, et al. 2007. Structure and biological activities of beta toxin from *Staphylococcus aureus*. *J Bacteriol* 189:8719-26

298. Eckford PD, Ramjeesingh M, Molinski S, Pasyk S, Dekkers JF, et al. 2014. VX-809 and related corrector compounds exhibit secondary activity stabilizing active F508del-CFTR after its partial rescue to the cell surface. *Chem Biol* 21:666-78
299. Benjamini Y, Krieger, A. M., Yekutieli, D. 2006. Adaptive linear step-up procedures that control the false discovery rate. *Biometrika* 93
300. Singh AK, Singh S, Devor DC, Frizzell RA, van Driessche W, Bridges RJ. 2002. Transepithelial impedance analysis of chloride secretion. *Methods Mol Med* 70:129-42
301. Tamada T, Hug MJ, Frizzell RA, Bridges RJ. 2001. Microelectrode and impedance analysis of anion secretion in Calu-3 cells. *JOP* 2:219-28
302. Margineanu DG, Van Driessche W. 1990. Effects of millimolar concentrations of glutaraldehyde on the electrical properties of frog skin. *J Physiol* 427:567-81
303. Kreindler JL, Jackson AD, Kemp PA, Bridges RJ, Danahay H. 2005. Inhibition of chloride secretion in human bronchial epithelial cells by cigarette smoke extract. *Am J Physiol Lung Cell Mol Physiol* 288:L894-902
304. Gentet LJ, Stuart GJ, Clements JD. 2000. Direct measurement of specific membrane capacitance in neurons. *Biophys J* 79:314-20
305. Schlingmann B, Overgaard CE, Molina SA, Lynn KS, Mitchell LA, et al. 2016. Regulation of claudin/zonula occludens-1 complexes by hetero-claudin interactions. *Nat Commun* 7:12276
306. Stewart T, Koval WT, Molina SA, Bock SM, Lillard JW, Jr., et al. 2017. Calibrated flux measurements reveal a nanostructure-stimulated transcytotic pathway. *Exp Cell Res* 355:153-61
307. Bielawski J, Szulc ZM, Hannun YA, Bielawska A. 2006. Simultaneous quantitative analysis of bioactive sphingolipids by high-performance liquid chromatography-tandem mass spectrometry. *Methods* 39:82-91
308. Schymanski EL, Jeon J, Gulde R, Fenner K, Ruff M, et al. 2014. Identifying small molecules via high resolution mass spectrometry: communicating confidence. *Environ Sci Technol* 48:2097-8

309. Zehethofer N, Bermbach S, Hagner S, Garn H, Muller J, et al. 2015. Lipid Analysis of Airway Epithelial Cells for Studying Respiratory Diseases. *Chromatographia* 78:403-13
310. Petrache I, Natarajan V, Zhen L, Medler TR, Richter AT, et al. 2005. Ceramide upregulation causes pulmonary cell apoptosis and emphysema-like disease in mice. *Nat Med* 11:491-8
311. Bielawski J, Pierce JS, Snider J, Rembiesa B, Szulc ZM, Bielawska A. 2010. Sphingolipid analysis by high performance liquid chromatography-tandem mass spectrometry (HPLC-MS/MS). *Adv Exp Med Biol* 688:46-59
312. Ma T, Thiagarajah JR, Yang H, Sonawane ND, Folli C, et al. 2002. Thiazolidinone CFTR inhibitor identified by high-throughput screening blocks cholera toxin-induced intestinal fluid secretion. *J Clin Invest* 110:1651-8
313. Melis N, Tauc M, Cougnon M, Bendahhou S, Giuliano S, et al. 2014. Revisiting CFTR inhibition: a comparative study of CFTRinh -172 and GlyH-101 inhibitors. *Br J Pharmacol* 171:3716-27
314. Kelly M, Trudel S, Brouillard F, Bouillaud F, Colas J, et al. 2010. Cystic fibrosis transmembrane regulator inhibitors CFTR(inh)-172 and GlyH-101 target mitochondrial functions, independently of chloride channel inhibition. *J Pharmacol Exp Ther* 333:60-9
315. Kalsi KK, Jackson S, Baines DL. 2019. Effect of exogenous ceramide on barrier function of human airway epithelial cells. *Faseb Journal* 33
316. Flynn AN, Itani OA, Moninger TO, Welsh MJ. 2009. Acute regulation of tight junction ion selectivity in human airway epithelia. *Proc Natl Acad Sci U S A* 106:3591-6
317. FDA. 2019. Application Number: 212273Orig1s000. In *NDA/BLA Multi-disciplinary Review and Evaluation {NDA 212273}*, ed. CFDEa Research
318. Coutinho A, Silva L, Fedorov A, Prieto M. 2004. Cholesterol and ergosterol influence nystatin surface aggregation: relation to pore formation. *Biophys J* 87:3264-76

319. Kornhuber J, Tripal P, Reichel M, Terfloth L, Bleich S, et al. 2008. Identification of new functional inhibitors of acid sphingomyelinase using a structure-property-activity relation model. *J Med Chem* 51:219-37
320. Zeidan YH, Pettus BJ, Elojeimy S, Taha T, Obeid LM, et al. 2006. Acid ceramidase but not acid sphingomyelinase is required for tumor necrosis factor- α -induced PGE2 production. *J Biol Chem* 281:24695-703
321. Kirsten A, Cottrill RJP, Colby F, Lewallen, Michael Koval, Robert J. Bridges, Nael A. McCarty. 2021. Sphingomyelinase decreases transepithelial anion secretion in airway epithelial cells in part by inhibiting CFTR-mediated apical conductance. *Physiological Reports*
322. Devlin CM, Lahm T, Hubbard WC, Van Demark M, Wang KC, et al. 2011. Dihydroceramide-based response to hypoxia. *J Biol Chem* 286:38069-78
323. Cottrill KA, Farinha CM, McCarty NA. 2020. The bidirectional relationship between CFTR and lipids. *Commun Biol* 3:179
324. Liessi N, Pesce E, Braccia C, Bertozzi SM, Giraud A, et al. 2020. Distinctive lipid signatures of bronchial epithelial cells associated with cystic fibrosis drugs, including Trikafta. *JCI Insight* 5
325. Giacalone VD, Dobosh BS, Gaggar A, Tirouvanziam R, Margaroli C. 2020. Immunomodulation in Cystic Fibrosis: Why and How? *Int J Mol Sci* 21
326. Pollock N, Cant N, Rimington T, Ford RC. 2014. Purification of the cystic fibrosis transmembrane conductance regulator protein expressed in *Saccharomyces cerevisiae*. *J Vis Exp*
327. Forrest OA, Ingersoll SA, Preininger MK, Laval J, Limoli DH, et al. 2018. Frontline Science: Pathological conditioning of human neutrophils recruited to the airway milieu in cystic fibrosis. *J Leukoc Biol* 104:665-75
328. Ji C, Yang B, Yang YL, He SH, Miao DS, et al. 2010. Exogenous cell-permeable C6 ceramide sensitizes multiple cancer cell lines to Doxorubicin-induced apoptosis by promoting AMPK activation and mTORC1 inhibition. *Oncogene* 29:6557-68

329. Siddique MM, Li Y, Wang L, Ching J, Mal M, et al. 2013. Ablation of dihydroceramide desaturase 1, a therapeutic target for the treatment of metabolic diseases, simultaneously stimulates anabolic and catabolic signaling. *Mol Cell Biol* 33:2353-69
330. Hallows KR, Raghuram V, Kemp BE, Witters LA, Foskett JK. 2000. Inhibition of cystic fibrosis transmembrane conductance regulator by novel interaction with the metabolic sensor AMP-activated protein kinase. *J Clin Invest* 105:1711-21
331. Schissel SL, Keesler GA, Schuchman EH, Williams KJ, Tabas I. 1998. The cellular trafficking and zinc dependence of secretory and lysosomal sphingomyelinase, two products of the acid sphingomyelinase gene. *J Biol Chem* 273:18250-9
332. Jenkins RW, Idkowiak-Baldys J, Simbari F, Canals D, Roddy P, et al. 2011. A novel mechanism of lysosomal acid sphingomyelinase maturation: requirement for carboxyl-terminal proteolytic processing. *J Biol Chem* 286:3777-88
333. Qiu H, Edmunds T, Baker-Malcolm J, Karey KP, Estes S, et al. 2003. Activation of human acid sphingomyelinase through modification or deletion of C-terminal cysteine. *J Biol Chem* 278:32744-52
334. Draper JM, Xia Z, Smith RA, Zhuang Y, Wang W, Smith CD. 2011. Discovery and evaluation of inhibitors of human ceramidase. *Mol Cancer Ther* 10:2052-61
335. Siddique MM, Li Y, Chaurasia B, Kaddai VA, Summers SA. 2015. Dihydroceramides: From Bit Players to Lead Actors. *J Biol Chem* 290:15371-9
336. Chakinala RC, Khatri A, Gupta K, Koike K, Epelbaum O. 2019. Sphingolipids in COPD. *Eur Respir Rev* 28
337. Perry DM, Kitatani K, Roddy P, El-Osta M, Hannun YA. 2012. Identification and characterization of protein phosphatase 2C activation by ceramide. *J Lipid Res* 53:1513-21
338. Travis SM, Berger HA, Welsh MJ. 1997. Protein phosphatase 2C dephosphorylates and inactivates cystic fibrosis transmembrane conductance regulator. *Proc Natl Acad Sci U S A* 94:11055-60

339. Bourbon NA, Yun J, Berkey D, Wang Y, Kester M. 2001. Inhibitory actions of ceramide upon PKC-epsilon/ERK interactions. *Am J Physiol Cell Physiol* 280:C1403-11
340. Zheng W, Kollmeyer J, Symolon H, Momin A, Munter E, et al. 2006. Ceramides and other bioactive sphingolipid backbones in health and disease: lipidomic analysis, metabolism and roles in membrane structure, dynamics, signaling and autophagy. *Biochim Biophys Acta* 1758:1864-84
341. Staretz-Chacham O, Aviram M, Morag I, Goldbart A, HersHKovitz E. 2018. Pulmonary involvement in Niemann-Pick C type 1. *Eur J Pediatr* 177:1609-15
342. Patterson MC, Hendriksz CJ, Walterfang M, Sedel F, Vanier MT, et al. 2012. Recommendations for the diagnosis and management of Niemann-Pick disease type C: an update. *Mol Genet Metab* 106:330-44
343. Chin S, Ramjeesingh M, Hung M, Ereno-Oreba J, Cui H, et al. 2019. Cholesterol Interaction Directly Enhances Intrinsic Activity of the Cystic Fibrosis Transmembrane Conductance Regulator (CFTR). *Cells* 8
344. Zhai YJ, Liu BC, Wei SP, Chou CF, Wu MM, et al. 2018. Depletion of Cholesterol Reduces ENaC Activity by Decreasing Phosphatidylinositol-4,5-Bisphosphate in Microvilli. *Cell Physiol Biochem* 47:1051-9
345. Cholon DM, O'Neal WK, Randell SH, Riordan JR, Gentsch M. 2010. Modulation of endocytic trafficking and apical stability of CFTR in primary human airway epithelial cultures. *Am J Physiol Lung Cell Mol Physiol* 298:L304-14
346. Ostrom RS, Bogard AS, Gros R, Feldman RD. 2012. Choreographing the adenylyl cyclase signalosome: sorting out the partners and the steps. *Naunyn Schmiedebergs Arch Pharmacol* 385:5-12
347. Fortalezas S, Marques-da-Silva D, Gutierrez-Merino C. 2018. Methyl-beta-Cyclodextrin Impairs the Phosphorylation of the beta(2) Subunit of L-Type Calcium Channels and Cytosolic Calcium Homeostasis in Mature Cerebellar Granule Neurons. *Int J Mol Sci* 19

348. Raslan Z, Magwenzi S, Aburima A, Tasken K, Naseem KM. 2015. Targeting of type I protein kinase A to lipid rafts is required for platelet inhibition by the 3',5'-cyclic adenosine monophosphate-signaling pathway. *J Thromb Haemost* 13:1721-34
349. Mueller P, Rudin DO, Tien HT, Wescott WC. 1962. Reconstitution of cell membrane structure in vitro and its transformation into an excitable system. *Nature* 194:979-80
350. Hildebrandt E, Zhang Q, Cant N, Ding H, Dai Q, et al. 2014. A survey of detergents for the purification of stable, active human cystic fibrosis transmembrane conductance regulator (CFTR). *Biochim Biophys Acta* 1838:2825-37
351. Bear CE, Li CH, Kartner N, Bridges RJ, Jensen TJ, et al. 1992. Purification and functional reconstitution of the cystic fibrosis transmembrane conductance regulator (CFTR). *Cell* 68:809-18
352. Tilly BC, Winter MC, Ostedgaard LS, O'Riordan C, Smith AE, Welsh MJ. 1992. Cyclic AMP-dependent protein kinase activation of cystic fibrosis transmembrane conductance regulator chloride channels in planar lipid bilayers. *J Biol Chem* 267:9470-3
353. Tabcharani JA, Chang XB, Riordan JR, Hanrahan JW. 1991. Phosphorylation-regulated Cl⁻ channel in CHO cells stably expressing the cystic fibrosis gene. *Nature* 352:628-31
354. Caci E, Caputo A, Hinzpeter A, Arous N, Fanen P, et al. 2008. Evidence for direct CFTR inhibition by CFTR(inh)-172 based on Arg347 mutagenesis. *Biochem J* 413:135-42
355. Taddei A, Folli C, Zegarra-Moran O, Fanen P, Verkman AS, Galiotta LJ. 2004. Altered channel gating mechanism for CFTR inhibition by a high-affinity thiazolidinone blocker. *FEBS Lett* 558:52-6
356. Moran A, Dunitz J, Nathan B, Saeed A, Holme B, Thomas W. 2009. Cystic fibrosis-related diabetes: current trends in prevalence, incidence, and mortality. *Diabetes Care* 32:1626-31
357. O'Riordan SM, Robinson PD, Donaghue KC, Moran A. 2009. Management of cystic fibrosis-related diabetes in children and adolescents. *Pediatr Diabetes* 10 Suppl 12:43-50

358. Stecenko AA, Moran A. 2010. Update on cystic fibrosis-related diabetes. *Curr Opin Pulm Med* 16:611-5
359. Moran A, Brunzell C, Cohen RC, Katz M, Marshall BC, et al. 2010. Clinical care guidelines for cystic fibrosis-related diabetes: a position statement of the American Diabetes Association and a clinical practice guideline of the Cystic Fibrosis Foundation, endorsed by the Pediatric Endocrine Society. *Diabetes Care* 33:2697-708
360. Mohan K, Miller H, Dyce P, Grainger R, Hughes R, et al. 2009. Mechanisms of glucose intolerance in cystic fibrosis. *Diabet Med* 26:582-8
361. Moran A, Becker D, Casella SJ, Gottlieb PA, Kirkman MS, et al. 2010. Epidemiology, pathophysiology, and prognostic implications of cystic fibrosis-related diabetes: a technical review. *Diabetes Care* 33:2677-83
362. Bismuth E, Laborde K, Taupin P, Velho G, Ribault V, et al. 2008. Glucose tolerance and insulin secretion, morbidity, and death in patients with cystic fibrosis. *J Pediatr* 152:540-5, 5 e1
363. Koch C, Rainisio M, Madessani U, Harms HK, Hodson ME, et al. 2001. Presence of cystic fibrosis-related diabetes mellitus is tightly linked to poor lung function in patients with cystic fibrosis: data from the European Epidemiologic Registry of Cystic Fibrosis. *Pediatr Pulmonol* 32:343-50
364. Marshall BC, Butler SM, Stoddard M, Moran AM, Liou TG, Morgan WJ. 2005. Epidemiology of cystic fibrosis-related diabetes. *J Pediatr* 146:681-7
365. Kelsey R, Manderson Koivula FN, McClenaghan NH, Kelly C. 2019. Cystic Fibrosis-Related Diabetes: Pathophysiology and Therapeutic Challenges. *Clin Med Insights Endocrinol Diabetes* 12:1179551419851770
366. Hsia CC, Raskin P. 2007. Lung function changes related to diabetes mellitus. *Diabetes Technol Ther* 9 Suppl 1:S73-82
367. Pitocco D, Fusco L, Conte EG, Zaccardi F, Condoluci C, et al. 2012. The diabetic lung--a new target organ? *Rev Diabet Stud* 9:23-35

368. Yeh HC, Punjabi NM, Wang NY, Pankow JS, Duncan BB, et al. 2008. Cross-sectional and prospective study of lung function in adults with type 2 diabetes: the Atherosclerosis Risk in Communities (ARIC) study. *Diabetes Care* 31:741-6
369. Baker EH, Clark N, Brennan AL, Fisher DA, Gyi KM, et al. 2007. Hyperglycemia and cystic fibrosis alter respiratory fluid glucose concentrations estimated by breath condensate analysis. *J Appl Physiol (1985)* 102:1969-75
370. Hunt WR, Zughaiier SM, Guentert DE, Shenep MA, Koval M, et al. 2014. Hyperglycemia impedes lung bacterial clearance in a murine model of cystic fibrosis-related diabetes. *Am J Physiol Lung Cell Mol Physiol* 306:L43-9
371. Brennan AL, Gyi KM, Wood DM, Johnson J, Holliman R, et al. 2007. Airway glucose concentrations and effect on growth of respiratory pathogens in cystic fibrosis. *J Cyst Fibros* 6:101-9
372. Limoli DH, Yang J, Khansaheb MK, Helfman B, Peng L, et al. 2016. Staphylococcus aureus and Pseudomonas aeruginosa co-infection is associated with cystic fibrosis-related diabetes and poor clinical outcomes. *Eur J Clin Microbiol Infect Dis* 35:947-53
373. Molina SA, Stauffer B, Moriarty HK, Kim AH, McCarty NA, Koval M. 2015. Junctional abnormalities in human airway epithelial cells expressing F508del CFTR. *Am J Physiol Lung Cell Mol Physiol* 309:L475-87
374. Molina SA, Moriarty HK, Infield DT, Imhoff BR, Vance RJ, et al. 2017. Insulin signaling via the PI3-kinase/Akt pathway regulates airway glucose uptake and barrier function in a CFTR-dependent manner. *Am J Physiol Lung Cell Mol Physiol* 312:L688-L702
375. Xu R, Li Q, Zhou J, Zhou XD, Perelman JM, Kolosov VP. 2013. The degradation of airway tight junction protein under acidic conditions is probably mediated by transient receptor potential vanilloid 1 receptor. *Biosci Rep* 33
376. Jia Z, Bao K, Wei P, Yu X, Zhang Y, et al. 2021. EGFR activation-induced decreases in claudin1 promote MUC5AC expression and exacerbate asthma in mice. *Mucosal Immunol* 14:125-34

377. Schlingmann B, Molina SA, Koval M. 2015. Claudins: Gatekeepers of lung epithelial function. *Semin Cell Dev Biol* 42:47-57
378. Gunzel D, Yu AS. 2013. Claudins and the modulation of tight junction permeability. *Physiol Rev* 93:525-69
379. Hou J, Gomes AS, Paul DL, Goodenough DA. 2006. Study of claudin function by RNA interference. *J Biol Chem* 281:36117-23
380. Hou J, Renigunta A, Yang J, Waldegger S. 2010. Claudin-4 forms paracellular chloride channel in the kidney and requires claudin-8 for tight junction localization. *Proc Natl Acad Sci U S A* 107:18010-5
381. Cui G, Hong J, Chung-Davidson YW, Infield D, Xu X, et al. 2019. An Ancient CFTR Ortholog Informs Molecular Evolution in ABC Transporters. *Dev Cell* 51:421-30 e3
382. Marshall J, Martin KA, Picciotto M, Hockfield S, Nairn AC, Kaczmarek LK. 1991. Identification and localization of a dogfish homolog of human cystic fibrosis transmembrane conductance regulator. *J Biol Chem* 266:22749-54
383. Ren J, Chung-Davidson YW, Yeh CY, Scott C, Brown T, Li W. 2015. Genome-wide analysis of the ATP-binding cassette (ABC) transporter gene family in sea lamprey and Japanese lamprey. *BMC Genomics* 16:436
384. Mogayzel PJ, Jr., Naureckas ET, Robinson KA, Mueller G, Hadjiliadis D, et al. 2013. Cystic fibrosis pulmonary guidelines. Chronic medications for maintenance of lung health. *Am J Respir Crit Care Med* 187:680-9
385. Li H, Papadopoulos V. 1998. Peripheral-type benzodiazepine receptor function in cholesterol transport. Identification of a putative cholesterol recognition/interaction amino acid sequence and consensus pattern. *Endocrinology* 139:4991-7
386. Wang K, Preisler SS, Zhang L, Cui Y, Missel JW, et al. 2019. Structure of the human ClC-1 chloride channel. *PLoS Biol* 17:e3000218

387. Trott O, Olson AJ. 2010. AutoDock Vina: improving the speed and accuracy of docking with a new scoring function, efficient optimization, and multithreading. *J Comput Chem* 31:455-61
388. Madeira F, Park YM, Lee J, Buso N, Gur T, et al. 2019. The EMBL-EBI search and sequence analysis tools APIs in 2019. *Nucleic Acids Res* 47:W636-W41
389. McCoy JG, Rusinova R, Kim DM, Kowal J, Banerjee S, et al. 2014. A KcsA/MloK1 chimeric ion channel has lipid-dependent ligand-binding energetics. *The Journal of biological chemistry* 289:9535-46